High angular resolution studies of the structure and evolution of protoplanetary disks

Thesis by

Joshua A. Eisner

In Partial Fulfillment of the Requirements

for the Degree of

Doctor of Philosophy

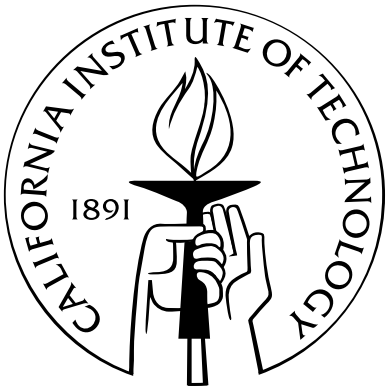

California Institute of Technology

Pasadena, California

2005

(Defended May 17, 2005)

Acknowledgements

The work presented in this thesis has benefited greatly from my interactions with many people. First and foremost are my advisors, Lynne Hillenbrand and Anneila Sargent. While working with two advisors is somewhat unusual, I found it it be an incredibly rewarding experience. Lynne and Anneila are both great scientists and teachers, and I learned a lot from them about the science of star and planet formation, as well as the techniques by which to study these subjects. I also fed off of their enthusiasm, and was often spurred onward by their suggestions and ideas.

There are several other people I would like to thank for their roles in my intellectual and professional development. Shri Kulkarni, my first advisor at Caltech, taught me a great deal about how to think and write about science, and this knowledge continues to serve me well. Ben Lane also played an important role in this thesis, teaching me many of the details of near-infrared interferometry, and working many a night with me at PTI. Two of the chapters in this thesis are co-authored by John Carpenter and myself, testifying to the large role he has played in my research. It has been a pleasure working with John and having the opportunity to absorb some of his ideas and approach. I would also like to thank my other collaborators and mentors, all of whom have been great to interact with and learn from: Rachel Akeson, Stuartt Corder, Lincoln Greenhill, James Herrnstein, Karl Menten, Stanimir Metchev, James Moran, Russel White, and Sebastian Wolf.

I am grateful to the staff at the Palomar and Keck observatories, the PTI collaboration, and the Robotic P60 team for all of their help. Without them, the data presented in this thesis would not have been obtained, and I greatly appreciate their efforts. I am also grateful for the friendship and good humor of those with whom I

have had the pleasure to observe. Kevin Rykoski in particular enriched my experience at Palomar. He taught me many subtleties of PTI, obtained some great data for me during his observing nights, and always kept his sense of humor, ensuring good spirits even on nights when everything else was going wrong.

The Caltech Astronomy department is a great place to learn about many different areas of astronomy, and to bounce ideas off of great astronomers. I am happy to have had the chance to interact with faculty, postdocs, and graduate students in the Robinson lounge and during informal office visits. Several conversations with Re'em Sari and Geoff Blake, among others, have helped me greatly to crystallize my understanding of issues related to this dissertation. I'm also indebted to my friends in the Caltech astronomy department (and the larger IPAC/JPL community), without whom maintaining my sanity during the more intense periods of my PhD career would have been substantially more difficult. So I whole-heartedly thank Josh, Kevin, Stan, Dave, Gordon, Dan, Don, Stefanie, and all the others who I haven't mentioned.

I also thank my family for their contributions to this work. My parents supported and encouraged me throughout my life, and helped me find a path to a life of intellectual pursuits. And my wife, Kelly, has been with me through thick and thin. She put up with me for five years of observing runs, late nights, and low income. The real thanks will be that I will now be able to keep her in the way to which she has become accustomed.

Finally, I gratefully acknowledge the financial support provided by the Michelson Graduate Fellowship program, which aims to advance the development and application of high angular resolution astronomical instruments, including optical/near-IR interferometry. This dissertation was performed in part under contract with the Jet Propulsion Laboratory (JPL) funded by NASA through the Michelson Fellowship Program. JPL is managed for NASA by the California Institute of Technology.

Abstract

Young stars are surrounded by massive, rotating disks of dust and gas, which supply a reservoir of material that may be incorporated into planets or accreted onto the central star. In this dissertation, I use high angular resolution observations at a range of wavelengths to understand the structure, ubiquity, and evolutionary timescales of protoplanetary disks.

First, I describe a study of Class I protostars, objects believed to be at an evolutionary stage between collapsing spherical clouds and fully-assembled young stars surrounded by protoplanetary disks. I use a Monte Carlo radiative transfer code to model new 0.9 μm scattered light images, 1.3 mm continuum images, and broadband spectral energy distributions. This modeling shows that Class I sources are probably surrounded by massive protoplanetary disks embedded in massive infalling envelopes. For the best-fitting models of the circumstellar dust distributions, I determine several important properties, including envelope and disk masses, mass infall rates, and system inclinations, and I use these results to constrain the evolutionary stage of these objects.

Second, I discuss observations of the innermost regions of more evolved disks around T Tauri and Herbig Ae/Be stars, obtained with the Palomar Testbed and Keck Interferometers. I constrain the spatial and temperature structure of the circumstellar material at sub-AU radii, and demonstrate that lower-mass stars are surrounded by inclined disks with puffed-up inner edges 0.1-1 AU from the star. In contrast, the truncated inner disks around more massive stars may not puff-up, indicating that disk structure depends on stellar properties. I discuss the implications of these results for disk accretion, terrestrial planet formation and giant planet migration.

Finally, I put these detailed studies of disk structure into a broader context by constraining the mass distribution and evolutionary timescales of circumstellar disks. Using the Owens Valley Millimeter Array, I mapped the millimeter continuum emission toward > 300 low-mass stars in the NGC 2024 and Orion Nebula clusters. These observations demonstrate that the average disk mass in each cluster is comparable to the "minimum-mass protosolar nebula", and that there may be disk evolution on one million year timescales.

Contents

List of Tables

List of Figures

Chapter 1

Introduction

Some of the central questions in astronomy, and indeed human inquiry in general, revolve around the formation of our solar system. How did our sun form? How did planets form out of the primordial circumstellar disk? Is the formation process universal, or is it unique to our own system? The answers to these questions are an integral part of understanding our place in the Universe.

With the discovery of a planet orbiting a main-sequence star other than our own sun (Mayor & Queloz 1995), and the subsequent discovery of over 100 extra-solar planets including multiple-planet systems (e.g., Marcy & Butler 2000; Butler et al. 1999), it is clear that planets are not unique to our own solar system. However, these extra-solar planets have properties that differ substantially from planets in our solar system, suggesting that the conditions that gave rise to our own system may not be universal. Studying the initial conditions of star and planet formation is crucial to understanding how planetary systems are created.

Direct observations of young stars and planets are difficult because of the small angular sizes of these objects and the high brightness contrast between stars and planets, especially at optical wavelengths. While astronomical instruments are now on the horizon that will allow a direct view of young stars and planets in formation, with current telescopes we are still limited to indirect observations. We therefore focus on the study of primordial material associated with forming stars and planets, which is more easily observed with current instruments.

As originally suggested by Kant, and later Laplace, the fact that the planets

in our solar system lie in a common orbital plane suggests that our system formed out of a flattened, rotating, disk-like structure. It is believed that protoplanetary disks provide the birth-sites for planetary systems around other stars as well, and the fairly recent discovery of dust and gas-rich disks around young stars supports this notion. Because circumstellar disks are larger than either stars or planets, and usually brighter at longer wavelengths due to the reprocessing of stellar light by dense dusty material, disks can be studied with current astronomical instruments and techniques. However, the challenges to observing circumstellar disks around young stars remain severe because, at typical distances to regions of star formation ($\gtrsim 140$ pc), the sizes of disks are beyond the angular resolution of most astronomical telescopes.

In this thesis, we describe high angular resolution observations of circumstellar disks that can resolve their spatial structure on scales relevant to both terrestrial and giant planet formation. By studying the ubiquity, evolutionary timescales, and structure of protoplanetary disks around young stars, we place crucial constraints on the formation and evolution of planetary systems. These observations help to place our own solar system in context, and provide insight into our place in the Universe.

1.1 Star and Planet Formation: The Role of Disks

1.1.1 Disk Formation

In the canonical theories of star formation, a giant molecular cloud initially supported by thermal and magnetic pressure begins to collapse under the influence of gravity, aided by ambipolar diffusion (e.g., Shu et al. 1987, 1993). As collapse continues, the density in some regions of the cloud increases (thus decreasing the Jeans Mass), and these high-density regions may fragment into molecular cloud cores. These cores continue to collapse, and since they typically contain at least a small amount of angular momentum, if only because of differential Galactic rotation, material in the outer regions cannot fall directly onto the star, but instead creates a rotating disk (e.g., Ulrich 1976; Cassen & Moosman 1981; Terebey et al. 1984).

Simple geometrical arguments can be used to estimate the size of the disk (e.g., Ulrich 1976; Cassen & Moosman 1981): conservation of angular momentum dictates that for a collapsing cloud with specific angular momentum j and central mass M_*, the angular velocity at the edge of the disk, R_c, is

$$\Omega^2 = \frac{j^2}{R_c^4} = \frac{GM_*}{R_c^3}. \tag{1.1}$$

Assuming $M_* = 0.5$ $M_\odot$ and $j = 6 \times 10^{20}$ cm^2 s^{-1} (Goodman et al. 1993), we obtain $R_c \approx 300$ AU. Thus, we expect that young stars will be surrounded by sizable disks of dust and gas.

1.1.2 Disk Evolution

Disks represent a stage in the process of star and planet formation that is probably intermediate to spherical collapsing clouds and fully assembled main-sequence stars surrounded by planets. Although disk evolution is a continuous process, discrete evolutionary classes have been defined that provide a useful framework in which to describe different stages of disk life-cycles. Disk evolution is typically divided into four observationally-determined evolutionary classes, Classes 0, I, II, and III (Figure 1.1). This classification scheme was originally defined based on infrared spectral index and the ratio of sub-millimeter to bolometric luminosity (Lada & Wilking 1984; Lada 1987; Adams et al. 1987; André et al. 1993), and it has subsequently been shown to be consistent with other observational indicators, including mid-IR spectral index (Myers et al. 1987) and bolometric temperature (Myers & Ladd 1993).

This evolutionary sequence is illustrated in Figure 1.1, and described below. Class 0 objects are thought to be true protostars, surrounded by roughly spherical collapsing envelopes from which forming young stars are still accreting substantial fractions of their final mass. Because of the very high columns of cold dust in these envelopes, these objects emit most of their radiation at sub-millimeter wavelengths. Class I objects are still deeply embedded and have high mass accretion rates, but have begun to clear away material from the polar regions because of strong outflows. These

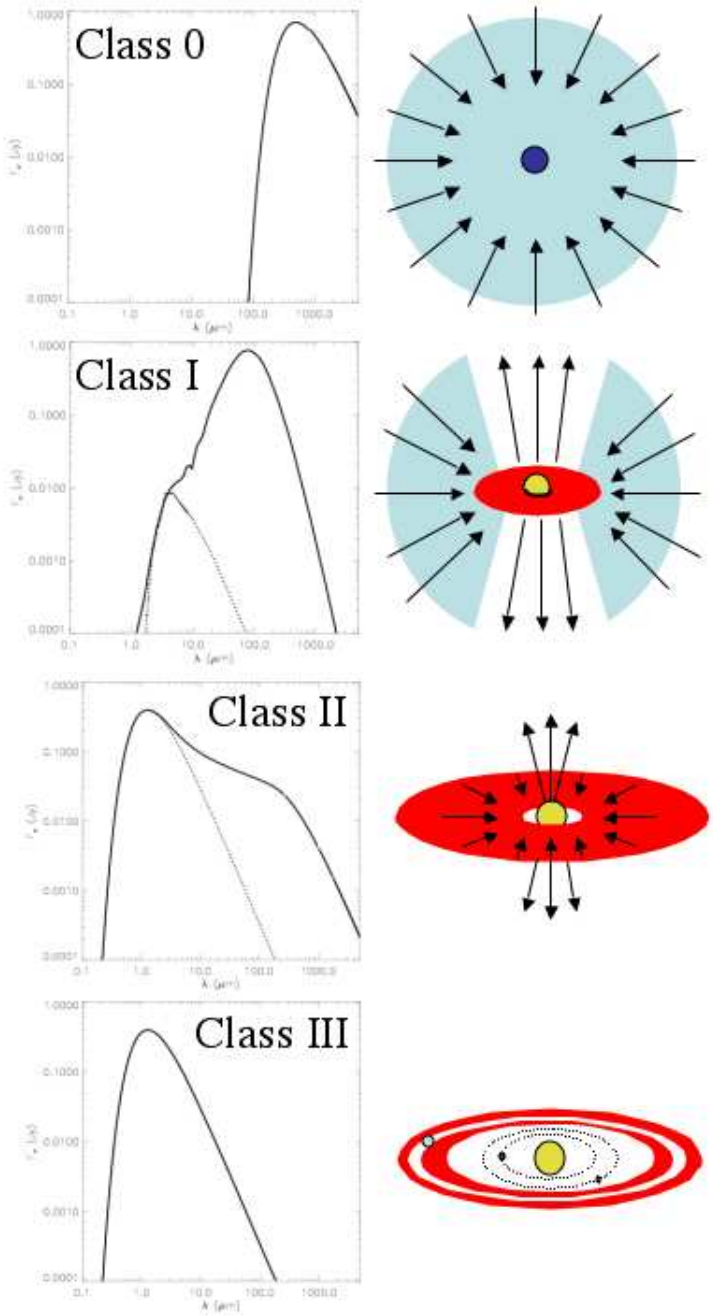

Figure 1.1 Observational classification of the star formation process. The left panels show the spectral energy distributions that typify members of the different evolutionary classes, and on the right we sketch the approximate geometry for each stage.

sources are still not directly visible, and emit most of their radiation at far-IR wavelengths due to reprocessing of the stellar radiation by warm dust. Class II sources are optically-visible young stars, which have probably already assembled almost all of their final mass, but which still show excess emission at infrared and millimeter wavelengths indicative of optically-thick circumstellar disks. Finally, Class III sources appear to be pre-main-sequence stars that have already depleted most or all of the material in their circumstellar disks, and therefore show little or no infrared emission in excess of that expected from the stellar photosphere.

1.1.3 Disk Accretion

During the various phases of disk evolution, material in the disk accretes inward onto the central star, losing angular momentum in the process (e.g., Shakura & Sunyaev 1973; Lynden-Bell & Pringle 1974). Various mechanisms have been proposed for angular momentum transfer, and different processes may be operative at different stages of disk evolution. Hydromagnetic outflows are one possible way to remove angular momentum from disk material (e.g., Blandford & Payne 1982; Shu et al. 1994). Since energetic, collimated outflows may only exist in the early stages of disk evolution (with substantially weaker or no outflows for Class II and III objects), and magnetic outflows may only couple with the hot, ionized inner disk regions, outflows cannot provide a complete explanation for how angular momentum is transported in disks. Angular momentum may also be transported by gravitational instabilities (e.g., Papaloizou & Savonije 1991; Laughlin & Bodenheimer 1994). Since this process occurs only in massive disks, gravitational instability is probably most important for less evolved objects like Class I sources, where massive envelopes provide a large reservoir of material still building up the disk. For lower mass disks, or systems that have already undergone gravitational instability and thereby depleted much of their mass (e.g., Class II objects), angular momentum must be transported by viscous processes, and the most prominent theory of viscosity in circumstellar disks is the "magneto-rotational instability" (MRI; Balbus & Hawley 1991). However, MRI requires an

ionized disk for magnetic coupling, and thus may not operate everywhere in disks (e.g., Gammie 1996).

Magnetic fields may also be important in regulating accretion from the innermost disk regions onto the central stars. The paradigm for accretion onto the central star (at least for low-mass stars, $M_* \lesssim 2$ M$_\odot$) is magnetospheric accretion (Hartmann 1998, and references therein). The stellar magnetic field threads the inner disk regions, and at some radius $R_{\rm mag}$, the ram pressure of accreting material is balanced by this magnetic pressure. Material is therefore no longer able to move inward through the disk midplane, but rather is funneled along magnetic field lines onto high-latitude regions of the star, where hot accretion shocks form. The alternative that may operate in more massive stars is boundary layer accretion, where material accretes through the disk midplane, forming a shock at the stellar equator (e.g., Lynden-Bell & Pringle 1974).

At some point, likely during the transition from Class II to Class III, accretion onto the central star ceases. This may occur when disks are completely depleted, due to a combination of viscous accretion, stellar winds, and photo-evaporation (e.g., Hollenbach et al. 2000), or when accretion rates become low enough (due to disk depletion) that the inward pressure of infalling material is balanced by outward pressure from a stellar wind. At this point, the stellar wind may cause dispersal of whatever material remains in the disk, both by blowing out small grains by radiation pressure and causing larger grains to spiral inward because of Poynting-Robertson (PR) drag. The gas is also probably depleted at this stage, although the dispersal mechanism is not known. This marks the end of the protoplanetary disk phase.

1.1.4 Planet Formation

The prevalent theory of both terrestrial and giant planet formation is core accretion, also referred to as sequential accretion, where small dust grains collide and stick with each other, forming progressively larger bodies (e.g., Safronov 1969; Kusaka et al. 1970; Cameron 1973). Small ($\sim$ 1 μm) dust grains in the disk may grow to ap-

proximately meter-sized bodies through slow collisions that result in the formation of van-der-Waals or molecular bonds. Once bodies grow to larger than kilometer-sized, self-gravity becomes the dominant mechanism for holding bodies together after (typically binary) collisions. While growing bodies from meter to kilometer-sized by collisions remains an unsolved problem, very recent work suggests that effects such as gas drag, high porosity, or turbulent vortices may enable growth to kilometer-sized planetesimals (e.g., Wurm et al. 2001; Klahr & Bodenheimer 2004). The core accretion process requires $\gtrsim 10^7$ years to form Jupiter-mass planets (e.g., Bodenheimer & Pollack 1986; Pollack et al. 1996), longer than inferred lifetimes for protoplanetary disks (§1.2). However, various effects including orbital migration, gas drag, or turbulence, may lead to shorter formation timescales (e.g., Papaloizou & Terquem 1999; Rafikov 2004; Klahr & Bodenheimer 2004).

An alternative to core accretion, which has the potential to form massive planets over very short timescales, is gravitational instability (e.g., Cameron 1978; Boss 1997). In this theory, a very massive disk becomes highly gravitationally unstable and a fragment of the disk begins to collapse. The density of a typical fragment must be high enough to overcome both pressure and centrifugal forces: for typical assumptions for protoplanetary disks, these requirements lead to fragment masses on the order of a Jupiter mass for disk radii $\gtrsim$ 100 AU, and larger masses at smaller radii (e.g., Rafikov 2005). The timescale for this mass to collapse is on the order of the disk dynamical timescale, which may be hundreds or thousands of years (e.g., Boss 1997). Thus, gravitational instability has the potential to form gas giant planets in very little time. One potential problem is that unless mass is being added to the disk very rapidly, marginally-unstable disks may re-adjust themselves through non-axisymmetric instabilities to stable configurations before fragmentation can occur (Laughlin & Bodenheimer 1994). Moreover, if fragmentation does occur, these fragments must be able to cool quickly (faster than disk dynamical timescales), or else they will be mixed back into the disk before a self-gravitating body can form (e.g., Rafikov 2005).

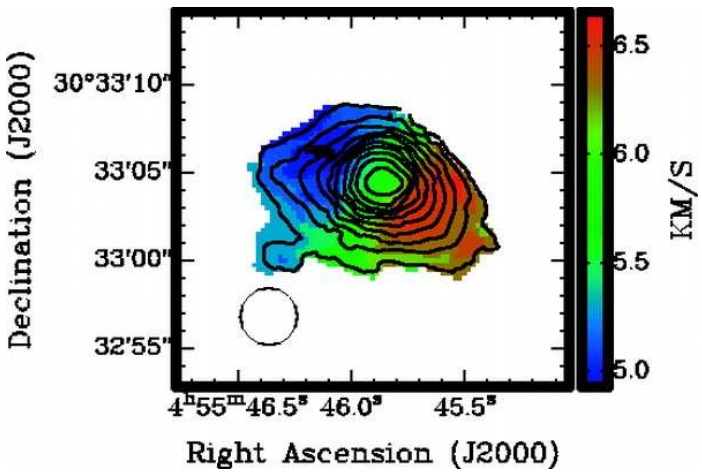

Figure 1.2 Velocity-weighted image of the young star AB Aur in millimeter emission from CO (Corder et al. 2005). The disk appears marginally asymmetric and displays a velocity gradient along the major axis, consistent with rotation. Detailed modeling shows these data to be consistent with a disk in Keplerian rotation.

1.2 Evidence for Disks around Young Stars

The existence of disks of dust and gas around young stars has now been demonstrated convincingly in a few cases. While the first image of a circumstellar disk was of light scattered by a dust disk around the nearby main-sequence star β Pictoris (Smith & Terrile 1984), images of protoplanetary disks around young pre-main-sequence stars have now been obtained as well. Spatially resolved images of millimeter emission from dust and gas, which show both flattened disk-like brightness distributions and velocity profiles characteristic of Keplerian rotation, provide the clearest evidence for rotating disks (e.g., Figure 1.2; Koerner & Sargent 1995; Dutrey et al. 1996; Corder et al. 2005). Disk-like brightness distributions have also been imaged directly at optical wavelengths with the *Hubble Space Telescope*: flattened distributions of dust and gas can be seen against the bright background in the Orion nebula, and faint emission is often seen toward the center of these dark structures (Figure 1.3; McCaughrean & O'Dell 1996; O'Dell & Wong 1996). More recently, flattened, disk-like structures have been observed at near-IR (e.g., Eisner et al. 2004) and mid-IR wavelengths (e.g., Liu et al. 2005) using cutting-edge interferometers.

In addition to direct images of flattened, rotating disks, scattered light has been

detected around several young stars, and observed morphologies are consistent with expectations for disk models: symmetric scattered light emission probably arises in the surface layers of flared disks. In some cases, flattened millimeter emission has been observed in the disk midplane and outflows are seen emerging from the expected disk rotation axis, confirming that these scattered light structures probably trace disks (e.g., Figure 1.4; Burrows et al. 1996; Padgett et al. 1999).

In addition to this direct evidence, the presence of disks around large samples of stars has also been deduced from indirect arguments. One of the earliest indications of circumstellar material around a young star came from observations of polarized scattered light, as expected for singly-scattered photons from a flattened dust distribution (Elsasser & Staude 1978). Modeling of forbidden optical emission line profiles, which showed predominantly blue-shifted emission, were also interpreted as indicating occultation by circumstellar disks (e.g., Appenzeller et al. 1984; Edwards et al. 1987). Furthermore, in a few cases, optical and infrared line emission profiles were shown to be consistent with disks in Keplerian rotation (e.g., Hartmann & Kenyon 1985, 1987; Carr et al. 1993; Najita et al. 1996).

Perhaps the strongest indirect evidence for both the existence and ubiquity of circumstellar disks is the presence of infrared emission in excess of that expected from a stellar photosphere (e.g., Strom et al. 1989). This infrared excess emission arises because hot stellar photons are absorbed by cooler circumstellar dust, and re-emitted at longer wavelengths. Most stars aged $\lesssim$ 1 Myr show near-IR excess

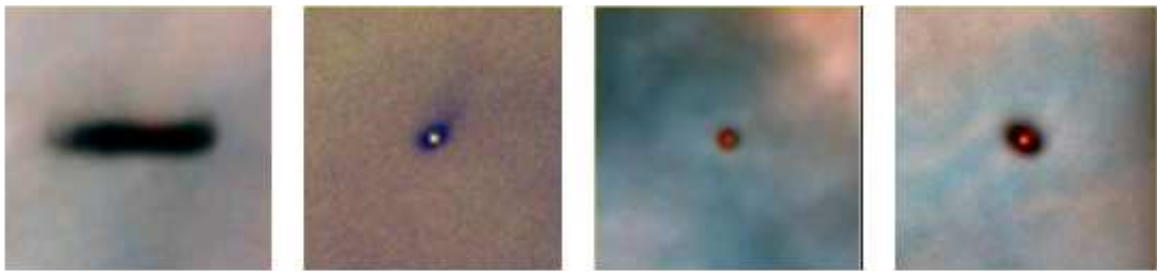

Figure 1.3 Images of disk-like distributions of gas and dust observed against the bright ionizing background in Orion (McCaughrean & O'Dell 1996). In some cases, red emission from the central star is visible toward the middle of the dark structures.

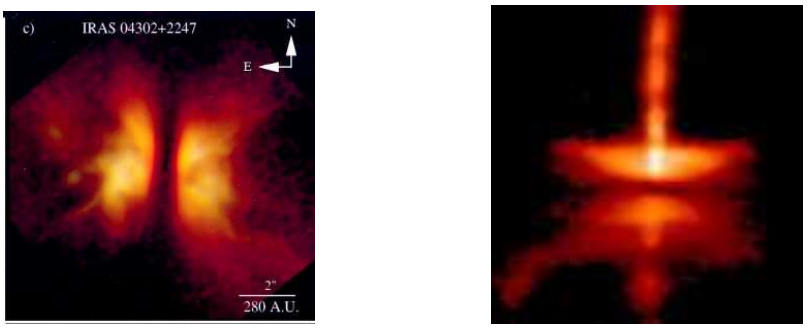

Figure 1.4 Scattered light images of IRAS 04302+2247 (left; Padgett et al. 1999) and HH 30 (right; Burrows et al. 1996), both obtained with the *Hubble Space Telescope*. In each image, a symmetric structure with a dark lane in the middle is observed, consistent with the scattering arising from the surface layers of flared disks. In HH 30, a narrowly-collimated jet is seen along the apparent rotation axis of the disk.

emission, while this emission has largely disappeared in stars older than about 6 Myr (Figure 1.5), perhaps indicating that the lifetime of circumstellar disks is on the order of 10 Myr. Observations of millimeter emission in excess of the stellar photosphere also provide evidence for circumstellar material, and imply large masses of material in small volumes around young stars. The fact that the central stars are not completely extincted by this material indicates flattened, disk-like distributions (e.g., Beckwith et al. 1990). Modeling of the excess emission spanning optical through millimeter wavelengths has shown that the spectral energy distributions (SEDs) of many young stellar objects are consistent with protoplanetary disk models (e.g., Adams et al. 1988; Bertout et al. 1988; Beckwith & Sargent 1993).

1.3 Open Questions

The observations described in §1.2 demonstrate the existence of circumstellar disks around several young stars, and suggest that at least small amounts of hot circumstellar material are ubiquitous among stars younger than ~ 1 Myr. However, several important questions about disks, relevant to processes of star and planet formation, remain unanswered. Here, we discuss several of these questions, focusing on those that will be addressed in this thesis.

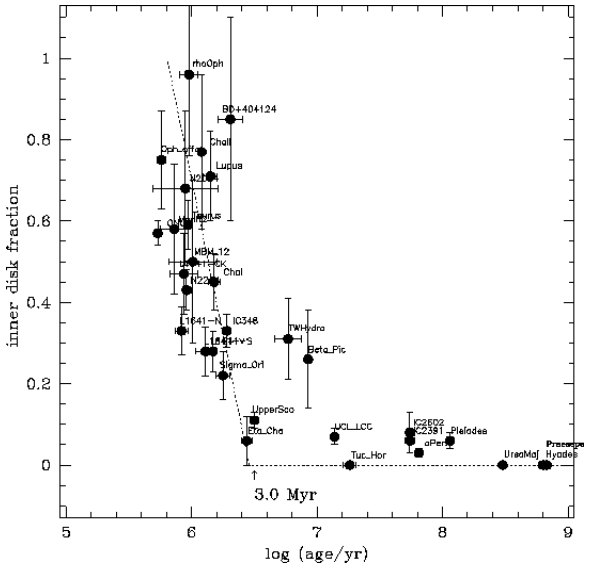

Figure 1.5 Fraction of stars exhibiting near-IR emission in excess of the stellar photosphere, as a function of stellar age. Figure courtesy of L. Hillenbrand.

1.3.1 Planet Formation

One of the main motivations for studying protoplanetary disks is to understand the origins of planets and planetary systems, and a critical open question therefore concerns the suitability of disks around young stars for both terrestrial and giant planet formation. While terrestrial planets likely form at radii smaller than a few AU, giant planets form in the more massive outer regions ($\gtrsim$ 5 AU), and thus observations at different wavelengths are necessary to understand both processes.

Terrestrial planets probably form at radii near 1 AU around solar-type stars (or larger radii for more luminous stars), which means that the inner disk density and temperature profiles have implications for the formation of Earth-like planets. The density structure is obviously important because dust is the basic building block of rocky planets, and thus a certain mass of material is necessary to build a terrestrial planet. Temperature is important as well, because at very high temperatures, dust is destroyed. Moreover, the presence of solid ices, including water and carbon monoxide, in the terrestrial region depends on the location of the "snowline" (Hayashi 1981), which depends sensitively on disk temperatures. Thus, the temperature structure of the inner disk may influence the chemical composition of planets forming in the

terrestrial region. In this thesis, I discuss near-IR interferometric observations that spatially resolve the inner disks on size scales $\lesssim 1$ AU, allowing *direct* constraints on inner disk structure.

Giant planet formation is also linked crucially with protoplanetary disk properties. Most importantly, disks must have sufficient masses of dust and gas to form large planets like Jupiter. For our own solar system, estimates of the minimum disk mass necessary to form all the planets is on the order of 0.01 $M_\odot$ (Weidenschilling 1977). Thus, an understanding of the disk mass is necessary to constrain whether disks around other stars are capable of producing planetary systems similar to our own. While observations of near-IR excess emission showed that hot inner disk material is ubiquitous around young stars, observations of optically-thin emission, including millimeter-wavelength emission, are necessary to constrain directly disk masses.

The process of giant planet formation is also dependent on the lifetimes of circumstellar disks. As discussed in §1.1.4, the time required to form a gas giant planet by core accretion may be $\gtrsim 10^7$ yr. In contrast, gravitational instability can be quite rapid, operating on timescales as short as 1000 yr. Thus, by determining the evolutionary timescales of massive circumstellar disks, one can constrain which of these mechanisms is more plausible for creating Jupiter-mass planets. While near-IR excess disappears within $\sim 10^7$ yr, the timescale for dissipation of the bulk of the disk mass remains poorly understood. Below, I discuss millimeter observations that constrain the disk mass distribution around large numbers of stars, and help to constrain the evolutionary timescales of this material.

1.3.2 Disk Accretion

As discussed in §1.1.3, several mechanisms have been proposed to allow accretion of dust and gas through disks, and eventually onto the central star. However, few observational data exist to constrain these processes. One important aspect of this question concerns how the star accretes the bulk of its mass during its early evolutionary stages. The other aspect I address is the process by which material is accreted

from the inner disk onto the mostly-assembled young star at later stages.

In the earlier stages of disk evolution (Class I), material falls onto the disk, and must somehow then move through the disk onto the central star. For sufficiently massive disks, gravitational instabilities like spiral arms provide a fast and efficient possibility for angular momentum transport outward, and thus for inward accretion of material. However, for lower-mass, gravitationally-stable disks, viscous processes must be invoked, in which case the theory must be able to produce sufficiently large viscosities to build stellar-mass objects within the evolutionary timescales. I attempt to address this issue below by modeling the circumstellar material around Class I objects, and inferring disk masses and accretion rates.

At later stages, accretion rates are much lower, and viscous processes are likely responsible for angular momentum transport. However, in the inner disk regions, material may be transported in other ways. As discussed in §1.1.3, the paradigm of inner disk accretion for low-mass stars is magnetospheric accretion, while in higher-mass stars, the alternative of boundary layer accretion may be operative. In this thesis, I test these possibilities by measuring directly the inner disk properties, which differ for the two theories.

1.3.3 Circumstellar Geometry

An issue related to both planet formation and disk accretion is the geometry of the circumstellar material. During the earlier stages of the star formation process, material may be spherically distributed, while at later stages the circumstellar matter has probably settled into a relatively thin disk. Thus, the geometry of dust and gas around young stars can provide insights into circumstellar evolution.

During the earliest evolutionary stages, most of the circumstellar material likely resides in roughly spherical envelopes. However, although early investigators attempted to model spatially-unresolved emission from Class I objects with spherically symmetric envelopes (e.g., Larson 1969), subsequent observations of asymmetric emission structures necessitated the inclusion of enhanced midplane densities and regions of

lower density in the polar regions. The exact distribution of material is still unclear, and in this dissertation, we argue based on additional spatially resolved imaging information that further refinements to the models are necessary. Specifically, it appears that both massive envelopes and embedded disks may comprise the circumstellar material around Class I objects, although the exact density distributions remain ambiguous.

For more evolved objects, where most of the circumstellar material lies in rotating disks, large-scale geometry is important for understanding dust grain growth, vertical transport processes, and the conditions of gravitational stability. Early investigators modeled the emission observed toward young stars in terms of geometrically thin disks powered by accretion (e.g., Lynden-Bell & Pringle 1974; Bertout et al. 1988). Subsequent models incorporating flared surfaces were shown to provide better fits to (spatially-unresolved) observations for some young stars (e.g., Kenyon & Hartmann 1987). Flared disks are expected from hydrostatic balance between the vertical component of the gravitational force exerted by the central star and the disk pressure (e.g., Chiang & Goldreich 1997). However, the degree of flaring may depend on processes of dust grain growth and vertical settling (e.g., Dullemond & Dominik 2004b), and observations of disk vertical structure can thus constrain these processes.

For the same reason that outer disk surfaces flare, the inner disk may deviate from a simple, geometrically-thin geometry. Spatially-unresolved SEDs have traditionally been interpreted in terms of geometrically thin disks truncated within several stellar radii of the central star (e.g., Beckwith et al. 1990; Hillenbrand et al. 1992). However, for a truncated inner disk, stellar radiation is incident at normal angles (instead of the glancing angles encountered for an un-truncated, thin disk), and thus the inner disk experiences additional heating. Hydrostatic balance then leads to a vertically "puffed-up" inner edge (Dullemond et al. 2001). In addition to absorbing more radiation, which leads to higher temperatures in the inner disk, a puffed-up inner disk edge may cast a shadow over the terrestrial region, with possible implications for the location of the snowline and thus terrestrial planet formation (§1.3.1). Near-infrared interferometric observations can spatially resolve the inner disk emission and test

whether the circumstellar material is indeed "puffed-up" as expected from hydrostatic equilibrium.

1.3.4 Environmental Effects

The process of star and planet formation and the picture of disk evolution outlined above assumed the simple case of a single cloud core forming a single star. In fact, most stars form in dense, clustered star forming regions (e.g., Lada & Lada 2003), which may affect the evolution of young star+disk systems. For example, the massive stars in these clusters produce large amounts of ionizing radiation, which may externally photo-evaporate the outer disks, leading to more rapid dispersal of material in the outer regions (e.g., Hollenbach et al. 2000). In addition, close encounters with other stars in these regions of high stellar density may lead to tidal truncation of disks at radii smaller than assumed for more isolated regions (e.g., Scally & Clarke 2001). Since rich clusters probably represent the typical sites of star and planet formation in our Galaxy, understanding disk properties and evolution in these regions is a key part of understanding star and planet formation in general. Below, I discuss observations of large numbers of stars in rich clusters, and compare the properties of disks in clusters with better known systems in more isolated star forming regions.

1.4 Outline of Thesis

In this thesis, I present observations of protoplanetary disks around young stars, probing the innermost ($\lesssim$ 1 AU) to the outermost regions ($\gtrsim$ 100 AU). Since the circumstellar gas and dust have different temperatures and densities at different disk radii (e.g., Chiang & Goldreich 1997), I obtained observations over a range of wavelengths. Near-IR observations probe thermal emission from hot ($\sim$ 1000 K) dust within $\sim$ 1 AU of the central star, and in some cases, scattered emission at larger radii. In contrast, millimeter observations probe cooler material ($\sim$ 20 K), which is predominantly located at larger disk radii. Broadband spectral energy distributions spanning optical through millimeter emission probe scales and temperatures in

between.

The main thrust of these observations is to obtain high angular resolution, and to thereby resolve the circumstellar disk emission. In Chapter 2, I describe the novel instruments and techniques we used to achieve this goal. The Palomar Testbed and Keck Interferometers enable spatial resolutions smaller than 1 AU at typical distances to nearby star-forming regions. At millimeter wavelengths, I used the Owens Valley Millimeter Array to reach spatial resolutions of $\lesssim$ 1000 AU. I also employed adaptive optics imaging, multi-wavelength photometry, high-dispersion spectroscopy, and imaging of scattered light at the Palomar and Keck observatories to produce a more complete picture of the young star+disk systems studied in this thesis.

In Chapter 3, I describe multi-wavelength observations and radiative transfer modeling of Class I protostars, which constrain the geometry, and thus the evolutionary stage of circumstellar material around these protostars. Since this work has implications for disk lifetimes, geometries, masses, and accretion rates, it bears directly on most of the open questions discussed in §1.3. I also include in Chapter 3 a discussion of several simple models for the circumstellar dust distributions, and I explore which properties can be constrained by different observational data.

Chapters 4 through 6 focus on (presumably older) Class II objects, and I zoom in on the innermost disk regions in order to constrain inner disk accretion and terrestrial planet formation. This work constrains inner disk properties directly, and therefore allows me to draw firm conclusions about inner disk accretion, terrestrial planet formation, and even the migration of giant planets. In Chapters 4 and 5, I present near-IR interferometric observations with the Palomar Testbed Interferometer of disk regions within 1 AU of Herbig Ae/Be stars. Supplementing these data with spectral energy distributions measured from optical to millimeter wavelengths (from the literature and new data), I constrain the geometrical and temperature structure of the inner disk. In Chapter 6, I present similar observations and analysis for a sample of solar-type T Tauri stars. These chapters have been published in the scientific literature as Eisner et al. (2003, 2004, 2005).

Finally, Chapters 7 and 8 detail a statistical study of large numbers of young

stars, including both Class I and II objects, in rich stellar clusters. In Chapter 7, millimeter continuum observations with the Owens Valley Millimeter Array are used to measure the flux distribution around ~ 150 young stars in the rich cluster NGC 2024, which provides an estimate of the disk mass distribution. I also obtained similar observations of > 300 young stars in the slightly older Orion Nebula Cluster, and these are described in Chapter 8. The distribution of disk masses has crucial implications for massive planet formation, since a certain amount of material is necessary to form Jupiter-mass planets. Moreover, the evolutionary timescales of massive disks in clusters may shed light on the mechanism by which giant planets form. Finally, comparison of disk properties in these clusters with properties of systems in the more isolated Taurus star forming region enables investigation of potential environmental effects. The observations and analysis of NGC 2024 have been published as Eisner & Carpenter (2003), while the observations of Orion presented in Chapter 8 are as yet un-published.

Chapter 2

Observational Techniques and Instruments

2.1 Motivation for Interferometry

To understand the structure of protoplanetary disks around other stars, and to eventually image and characterize extra-solar planets, high angular resolution observations are necessary. At typical distances to nearby stars, e.g., Taurus at 140 pc, the orbital radius of the earth (1 AU) would subtend an angle of 7 milliarcseconds (mas). The orbit of Jupiter corresponds to 35 mas, and our Kuiper belt would subtend about 700 mas.

The diffraction-limited angular resolution of a single-aperture telescope is,

$$\theta_{\rm res} = 1.22\frac{\lambda}{D}, \tag{2.1}$$

where λ is the observing wavelength and D is the telescope diameter. The pre-factor of 1.22 arises from the assumption that the aperture is circular, and may be different for other telescope geometries. Equation 2.1 implies that the *Hubble Space Telescope* can attain an angular resolution of $\sim 0\farcs1$ at optical/IR wavelengths, orders of magnitude too large to image the hot inner regions of protoplanetary disks (which emit most of their radiation at these wavelengths). While the diffraction-limited resolution of the largest ground based telescopes, the 10m Keck telescopes, is ~ 50 mas at near-IR wavelengths, this is still too large to spatially resolve terrestrial regions around

young stars. Furthermore, the blurring effect of the atmosphere typically limits the resolution of ground-based telescopes to about $0\farcs5$. At millimeter wavelengths, where emission traces cooler material at larger disk radii (tens to hundreds of AU), the atmosphere is less of a problem, but the angular resolution is poorer due to the longer wavelength. The largest single-aperture millimeter telescope can obtain $\theta_{\rm res} \approx 10''$, much larger than expected extents for young disks.

In the future, very large single-aperture telescopes may allow one to probe interesting size scales in protoplanetary disks. The Thirty Meter Telescope, using an adaptive optics system to compensate for the blurring effects of the atmosphere, may reach a diffraction-limited resolution of ~ 10 mas, approaching the expected angular sizes of the terrestrial regions of young disks. At the moment, however, sufficient angular resolution to probe protoplanetary disks eludes single-aperture telescopes.

Interferometry provides a way to attain very high angular resolution without building a very large-aperture telescope. Small apertures separated by a baseline B are used to "synthesize" a larger aperture and thus obtain an angular resolution given by λ/B. For the near-IR interferometers used in this thesis, baselines from 80–110 m provide an angular resolution of ~ 1 mas at near-IR wavelengths, more than sufficient to probe the innermost regions of protoplanetary disks around young stars. This high angular resolution is a unique capability of near-IR interferometry, and thus can provide new insights into the structure of disks in the terrestrial planet region.

At millimeter wavelengths, the angular resolution of current interferometers is approximately $1''$ (significantly larger than in the near-IR since resolution scales linearly with λ). However, this angular resolution is extremely useful for studying cooler material in protoplanetary disks. Since disks are centrally heated by a young star, outer regions are substantially cooler than the terrestrial region, and these cooler regions will emit most of their radiation at longer wavelengths. Moreover, outer disk regions are often optically-thin, and thus millimeter emission can provide a direct probe of circumstellar dust mass. Thus millimeter interferometry provides an excellent tool for probing the mass content in protoplanetary disks on scales of $\lesssim 100$ AU, which has important implications for giant planet formation.

2.2 Theory of Interferometry

Interferometry is a natural result of diffraction, and is elegantly illustrated by the classic "two-slit" experiment, where a light source is passed through two narrow slits. The two-slit experiment is illustrated in Figure 2.1. Since light behaves as a wave under certain circumstances, when a beam of light encounters the two slits, photons essentially pass through both slits at once, and the waves emerging from the two slits interfere with each other. This interference produces a sinusoidal fringe pattern of peaks and troughs, corresponding to locations where the waves from the two slits interfere constructively or destructively. We note that this result holds when the light source is far enough away from the slits so that the incoming waves are essentially plane-parallel; since this requirement is almost always met for astronomical light sources, the results derived here are applicable for astronomical interferometry.

A two-element interferometer is completely analogous to a pair of slits: light from a source encounters the two telescopes, which represent two slits through which the source is viewed, and the light is subsequently re-combined to produce interference fringes. It is thus useful to develop some of the basic concepts of interferometry using the two-slit framework, before moving on to consideration of actual astronomical interferometers.

We now compute quantitatively the intensity pattern that arises on a screen to the right of the two slits shown in Figure 2.1. In addition, for generality, we now allow the light source to be off-axis by an angle θ with respect to the normal of the separation vector between the two slits, $\vec{B}$ (Figure 2.2). The main effect of an off-axis light source is that an incoming wavefront encounters one slit before the other, due to the longer distance the light must travel to the second slit. This introduces a "geometric delay" to the wavefront observed at the second slit,

$$\tau_{\rm g} = (|\vec{B}|/c)\sin\theta, \tag{2.2}$$

which offsets the fringe pattern by $\Delta x = D\sin\theta$ on the screen. If we consider a

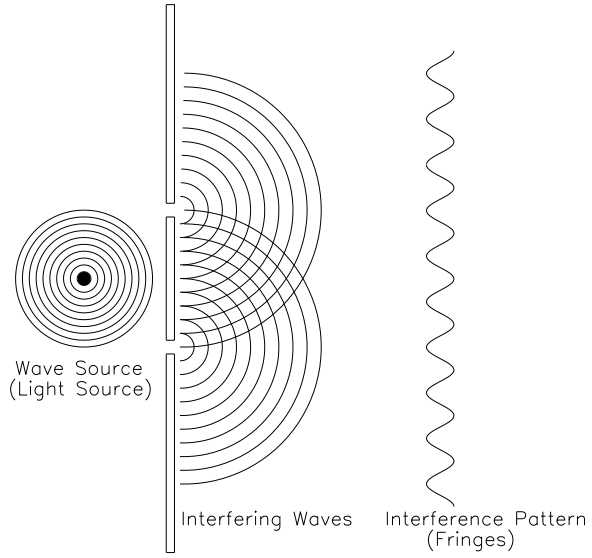

Figure 2.1 Diagram of the classic two-slit experiment. To understand this picture, imagine that the wave source produces simple water waves. When these waves pass through two small slits, two identical wavelets emerge and begin to propagate. When the peak of one wavelet runs into the peak of the other wavelet, an amplification occurs. Similarly, when one peak runs into another trough, the two wavelets cancel each other. If one views the resulting interference pattern, displaying the height of the interfering waves as a function of position, a sinusoidal pattern is observed. If instead of water waves, we now consider light, an amazing insight is gained into quantum mechanics. Although light has a particle nature (and is quantized into individual packets called photons), when a beam of light is shined onto two slits, interference fringes are observed, demonstrating the wave-like character of light.

point x on a screen placed D to the right of the two slits, the electromagnetic field contributions from the slits are,

$$\vec{E_1} = A_1 \exp\left(i\frac{2\pi}{\lambda}R_1(x)\right), \tag{2.3}$$

$$\vec{E_2} = A_2 \exp\left(i\frac{2\pi}{\lambda}[R_2(x) + |\vec{B}|\sin\theta]\right), \tag{2.4}$$

and the total observed field is $\vec{E} = \vec{E_1} + \vec{E_2}$. The observed intensity is therefore

$$I = \frac{< EE^* >}{2} \sim 1 + \cos\left(\frac{2\pi}{\lambda}\delta\right). \tag{2.5}$$

Here, δ is the total path length difference between the incoming light from the two

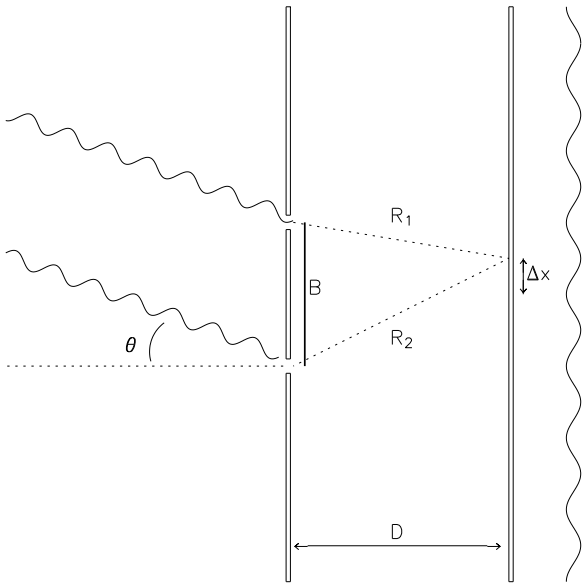

Figure 2.2 Illustration of the interference pattern observed for an off-axis source. For a source at angle θ away from the normal to the slit separation vector $\vec{B}$, the interference fringes observed at a distance D away from the slits will be shifted in position by Δx.

slits,

$$\delta = R_1 - R_2 - |\vec{B}| \sin\theta. \tag{2.6}$$

At a point x on the screen, assuming $D \gg B, x$,

$$R_1 - R_2 = \sqrt{(x + B/2)^2 + D^2} - \sqrt{(x - B/2)^2 + D^2} \approx \frac{xB}{\sqrt{x^2 + D^2}} \approx \frac{xB}{D}. \tag{2.7}$$

Thus, we can re-write Equation 2.6 as

$$\delta \approx \frac{xB}{D} - |\vec{B}| \sin\theta. \tag{2.8}$$

From this equation and Equation 2.5, we see that the frequency of the interference fringe depends on B, D, and λ, while the phase of the fringe, or in other words the position of the fringe on the screen, depends on θ.

Two sources separated on the sky by some angle θ' will produce overlapping fringe patterns of different phases. We define the angular resolution of an interferometer as that angle $\theta_{\rm res}$ for which the peak of one fringe falls on a null position of the other

fringe. As illustrated by Figure 2.3, this occurs when

$$\theta_{\rm res} = \frac{\lambda}{2B}. \tag{2.9}$$

As we discuss further below, structure smaller than $\theta_{\rm res}$ can actually be observed, since one does not need to observe a reduction of fringe amplitude all the way to zero. Smaller amplitude reductions, corresponding to smaller angular separations, can in fact be detected. Quantitatively, the degree to which a source is resolved is described by the fringe contrast, or visibility (e.g., Michelson 1920),

$$V = \frac{I_{\rm max} - I_{\rm min}}{I_{\rm max} + I_{\rm min}}. \tag{2.10}$$

For an unresolved point source, $V = 1$, while for an equal brightness binary source with $\Delta\theta = \theta_{\rm res}$, $V = 0$. Thus, the smallest angular scales we can probe with an interferometer are limited by the precision with which we can distinguish measured visibilities from unity.

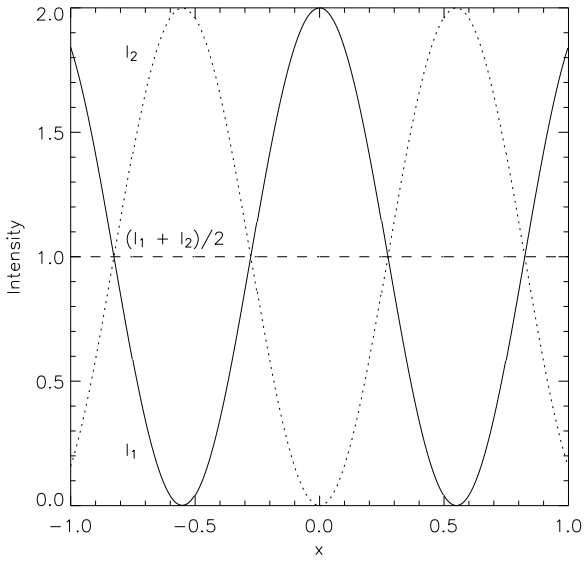

Figure 2.3 Illustration of the interference pattern observed for a binary source. For a source at angle θ away from the normal to the slit separation vector $\vec{B}$, the interference fringes observed at a distance D away from the slits will be shifted in position by $\Delta x = D \sin\theta$. For two sources separated by $\theta_{\rm res}$ (Equation 2.9), the two fringe patterns interfere destructively and no signal is observed.

Until now, we have been describing the fringes produced by monochromatic light. For radiation of a single wavelength, the interference pattern is an infinite sinusoid, and thus we can measure the fringes at any position on the screen. In practice, few light sources are exactly monochromatic, and in general we observe sources through some limited bandpass. In such cases, radiation with slightly different wavelengths will produce additional interference, which will affect the observed fringes. The main effect of polychromatic light is that although all wavelengths still produce constructive interference at $x = D \sin\theta$, at larger values of x, light of different colors tends to cancel out; thus the fringe pattern is modulated by an envelope centered at $x = D \sin\theta$ (Figure 2.4).

Quantitatively, this envelope is given by the Fourier transform of the spectral bandpass. For a square bandpass, the envelope is given by a sinc function, and the measured fringes are thus

$$I_{\text{polychromatic}} = I_\lambda \Delta\lambda \left(1 + \frac{\sin(\pi\delta/\Lambda_\text{c})}{\pi\delta/\Lambda_\text{c}} \cos(2\pi\delta/\lambda)\right). \tag{2.11}$$

Here, Λ_c is the "coherence length", which describes the largest value of $|x - D\sin\theta|$ for which fringes can be reasonably observed. The coherence length is related to the fractional spectral bandwidth:

$$\Lambda_\text{c} = \frac{\lambda_0^2}{\Delta\lambda}. \tag{2.12}$$

If we look at the screen far from the centerline, $|x - D\sin\theta| > \Lambda_\text{c}$, some signature of the fringe pattern may remain, but the amplitude will be suppressed by the envelope. Thus, one typically tries to observe fringes for values of $|x - D\sin\theta|$ smaller than the coherence length.

In addition to determining where on the screen one must look to observe fringes, the coherence length is also critical in determining the field of view of our two-slit experiment on the sky, i.e., the range of angles θ for which interference patterns may be observed. Similar to the beam pattern of a single-aperture telescope, the "delay beam" of an interferometer means that the amplitude of fringes observed off-axis will be reduced (e.g., Thompson et al. 1986). If we consider a source at angle θ_0 and a

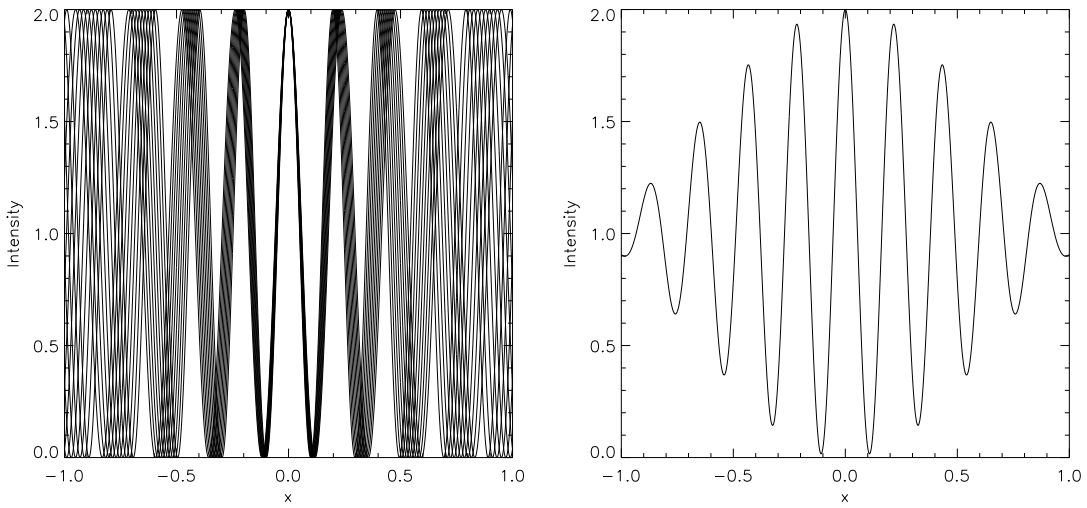

Figure 2.4 When polychromatic light is passed through a two-slit setup, the sinusoidal fringe patterns for light of different wavelengths tend to cancel each other out for $x \neq D \sin\theta$. This is illustrated in the left panel for an on-axis source ($\theta = 0$), where we have shown the fringe patterns for light spanning a fractional bandwidth of 20%. The resultant broadband fringes are modulated by an envelope, whose width is determined by the spectral bandwidth of the incident radiation (right).

secondary object at $\theta = \theta_0 + \Delta\theta$, the edge of the sinc function envelope defines the maximum value of $\Delta\theta$ for which fringes can be observed for the secondary:

$$\mathrm{sinc}(\pi\delta/\Lambda_\mathrm{c}) = 0, \tag{2.13}$$

which implies

$$\delta/\Lambda_\mathrm{c} = 1. \tag{2.14}$$

If we observe the position on the screen where the interference pattern for an on-axis source is maximal, $x = D\sin\theta_0$, the field of view is set by the condition

$$\frac{xB/D - |\vec{B}|\sin(\theta_0 + \Delta\theta)}{\Lambda_\mathrm{c}} = \frac{|\vec{B}|\sin\theta_0 - |\vec{B}|\sin\theta_0\cos\Delta\theta - |\vec{B}|\cos\theta_0\sin\Delta\theta}{\Lambda_\mathrm{c}} = 1. \tag{2.15}$$

Assuming $\Delta\theta$ is small (which implies $\sin\Delta\theta \approx \Delta\theta$ and $\cos\Delta\theta \approx 1$), this simplifies to

$$\Delta\theta = \frac{\Lambda_\mathrm{c}}{|\vec{B}|\cos\theta_0}. \tag{2.16}$$

The field of view of a Michelson interferometer thus depends on the fractional bandwidth and the projected separation of the slits. For a source at a large angle θ_0, the projected baseline is small and the field of view is large, while for small θ_0, the field of view is smaller.

2.3 Relation of Fringes to Source Properties

In §2.2, we discussed the signal measured by an interferometer for a point source, and we showed that at a certain separation, two point sources could produce fringe patterns that interfere destructively, eliminating any measured signal for a given baseline (Equation 2.9). Thus, by varying the baseline length until the interferometric signal goes to zero, one can measure the angular separation of binary sources. Here, we quantify how an arbitrary source geometry can be recovered from interferometric measurements.

The van Cittert-Zernike theorem, although originally developed to describe Fraunhoffer diffraction in optics, also provides a description of interferometric fringes because of the similarities between diffraction and interferometry. Full derivations of this theorem can be found elsewhere (e.g., Born & Wolf 1999), so we merely quote the result here. For a source subtending a solid angle Ω, at direction $\vec{s}$ on the sky, with two apertures at $\vec{r_1}, \vec{r_2}$ separated by $\vec{B} = \vec{r_1} - \vec{r_2}$, the mutual coherence of radiation from the two apertures is

$$V_\lambda(\vec{r_1}, \vec{r_2}) \sim \int I_\lambda(\vec{s}) e^{-\frac{i2\pi}{\lambda}\vec{B}\cdot\vec{s}} d\Omega. \tag{2.17}$$

Thus, the mutual coherence is the Fourier Transform of the source brightness distribution, $I_\lambda(\vec{s})$ (which quantifies why for a point source, the interference pattern is a sinusoid). V_λ is called the "complex visibility", and is the basic measured quantity in interferometry. In some cases, V_λ may be normalized, in which case the amplitude is equivalent to the fringe contrast defined in Equation 2.10.

Equation 2.17 indicates that the spatial scale probed by an interferometer depends

on the length and orientation of the baseline (since the argument of the exponential includes $\vec{B} \cdot \vec{s}$). In other words, the measured visibility depends on the components of the baseline in a 2-D plane on the sky. These components are generally described in a "uv" plane, where

$$u \equiv \frac{B\cos(\theta)}{\lambda};\ v \equiv \frac{B\sin(\theta)}{\lambda}, \tag{2.18}$$

where θ is the angle between the source and the normal of the baseline. Using these quantities, and expressing the source position on the sky using the coordinates α, β, we can re-write Equation 2.17 as

$$V(u,v) \sim \int\int I_\lambda(\alpha,\beta) e^{-i2\pi(\alpha u+\beta v)} d\alpha d\beta. \tag{2.19}$$

For astronomical interferometers, which have some finite aperture response, an additional term describing the aperture transmission pattern must be included in Equation 2.19.

In millimeter interferometry, both the amplitude and phase of the complex visibilities can be measured, and thus measured visibilities can be inverted using an Inverse Fourier Transform to recover the sky brightness distribution of the source, $I_\lambda(\alpha,\beta)$. However, in near-IR interferometry, the atmosphere corrupts the phase of incoming light on very short timescales, and only the amplitude of the fringe pattern is typically measured. While some phase information can be recovered using the "closure phase" measured for a triangle of three telescopes, for the instruments used in this thesis where only one baseline is used at a time, no phase information is available. Thus, in the near-IR we normally deal with only the amplitudes of the complex visibilities; in fact, we typically use squared visibility amplitudes, V^2, although we will often refer to these simply as visibilities in Chapters 4 through 6.

2.3.1 Modeling Visibilities

For near-IR interferometry data, where direct imaging via an Inverse Fourier Transform is not possible, we recover information about the source brightness distribution

by modeling the visibilities directly. Although direct imaging is generally viable for millimeter interferometry, in some cases we also model these data in the uv plane since the uncertainties for the measured visibilities are well understood. In Chapters 4-6, we derive the visibilities for several geometrical and simple physical models. Here, we discuss the simplest of these models, a uniform disk, in order to demonstrate some of the basics of visibility modeling.

A circularly-symmetric uniform disk (UD) is characterized entirely by the diameter, $\theta_{\rm UD}$:

$$I_{\rm UD} = \begin{cases} 1 & \text{if } \sqrt{\alpha^2 + \beta^2} \leq \theta_{\rm UD}/2 \\ 0 & \text{otherwise} \end{cases} . \tag{2.20}$$

The squared visibilities for this brightness distribution are,

$$V^2_{\rm UD} = \left[\frac{2J_1(\pi\theta_{\rm UD} r_{uv})}{\pi\theta_{\rm UD} r_{uv}} \right]^2 , \tag{2.21}$$

where J_1 is the first-order Bessel function and $r_{uv} = \sqrt{u^2 + v^2}$. Since the intensity distribution is circularly-symmetric, the Fourier Transform (i.e., the visibility distribution) is also symmetric, and depends only on the angular size $\theta_{\rm UD}$. The behavior of the predicted visibilities on $\theta_{\rm UD}$ is illustrated in Figure 2.5. By measuring how much the normalized V^2 values deviate from unity, the angular size of a circularly-symmetric source can be recovered.

In addition to angular size, interferometric observations can also determine whether a source is in fact circularly symmetric, and place constraints on the geometry of non-symmetric sources. This can be understood simply from Equation 2.19: since visibilities measure the Fourier Transform of the source brightness distribution, asymmetry on the sky translates into orthogonal asymmetry in the visibility distribution in the uv plane. We illustrate this in Figure 2.6, which shows the expected visibilities for both circularly symmetric and inclined uniform disks. By measuring V^2 over a range of position angles, we can recover the position angle and inclination of a source, in addition to its angular size.

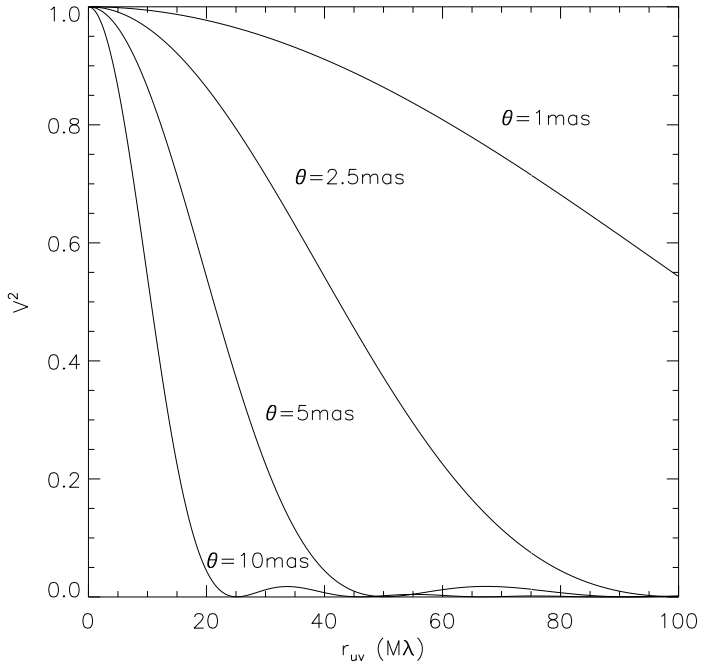

Figure 2.5 Visibilities calculated for uniform disk models with a range of angular sizes, θ. For larger sources, the V^2 values are smaller, as expected from the Fourier Transform relationship linking visibilities and sky brightness distributions (Equation 2.19). For smaller sources, one must probe larger values of r_{uv}, corresponding to longer projected baseline lengths, in order to resolve a source (i.e., easily observe V^2 values different from unity). Conversely, for large sources long baselines over-resolve the source, measuring V^2 values very close to zero, and thus short-baseline data is needed to constrain more extended structures.

2.4 Astronomical Interferometers

The two slit interferometer that we have been discussing until now is completely analogous to astronomical Michelson interferometers. The slits are replaced by telescopes, free-space propagation between the slits and the screen is replaced with a beam transport system, and the image plane is sampled with some kind of detector. In this section, we introduce the astronomical interferometers that are used in this thesis, and provide important properties for each instrument.

2.4.1 Palomar Testbed Interferometer

The Palomar Testbed Interferometer (PTI) is a long-baseline near-IR interferometer on Palomar Mountain near San Diego, CA. It was developed by the Jet Propulsion

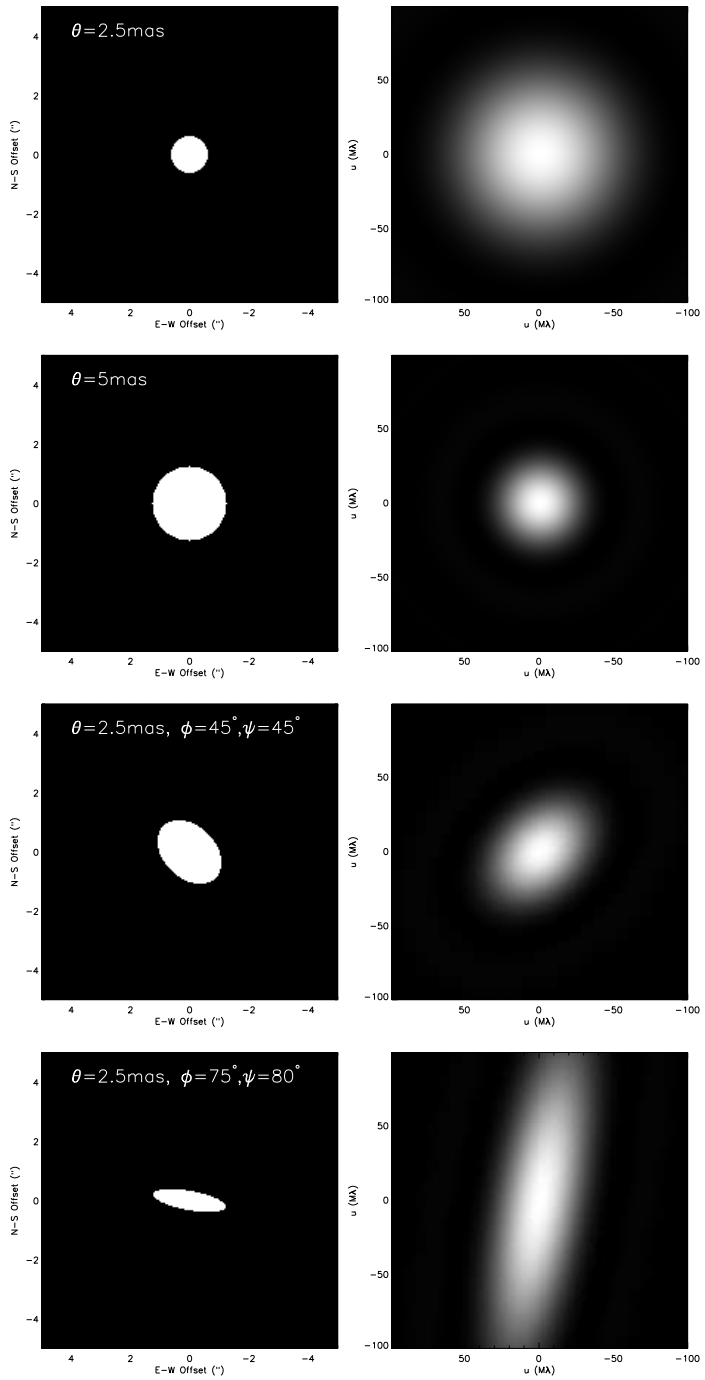

Figure 2.6 Brightness distributions (left panels) and visibilities (right panels) calculated for uniform disk models with a range of angular sizes, inclinations, and position angles. The Fourier Transform relationship linking V^2 with the source brightness distribution is illustrated: extended structures on the sky correspond with compact structures in the uv plane, and vice versa. By measuring V^2 over a range of uv coordinates, corresponding to different baseline lengths and orientations, we can recover the source geometry.

Figure 2.7 A photograph of the Palomar Testbed Interferometer (PTI), courtesy of NASA/JPL-Caltech. The three siderostats reside in small white huts. The North siderostat is in the top middle part of the image, West is on the left, and South is in the lower right corner. Vacuum pipes transport light from the siderostats to a central beam-combining building, which contains the delay lines, beam combiner, and detector.

Laboratory, California Institute of Technology for NASA as a testbed for future instruments including the Keck Interferometer and the Space Interferometry Mission. However, as we will demonstrate in this thesis, PTI has also produced a wealth of scientific results.

A photograph of PTI is shown in Figure 2.7. PTI consists of three siderostats ("North", "West", and "South"), any two of which can be combined at once (although the South-West baseline has been implemented fairly recently). Thus, PTI provides a 110 m North-South (NS) baseline, oriented 20° East of North, a 85 m North-West (NW) baseline 81° East of North, and a 87 m South-West (SW) baseline 211° East of North. The angular resolutions of these baselines (Equation 2.9) are $\sim 2 - 2.5$ mas.

Each siderostat feeds a 40 cm aperture telescope, which provides diffraction-limited resolution at near-IR wavelengths. For interferometry, we require that the wavefronts from the two telescopes comprising a baseline be as similar as possible, so that the wavefronts can be combined coherently. For the diffraction-limited apertures at PTI, the atmosphere does not introduce spatial variations within an aperture (although this is a problem for larger-aperture systems like the Keck Interferometer,

as discussed below). However, even for small apertures, different atmosphere above different apertures can cause relative "tip/tilt" errors. These effects are caused by the refraction that occurs in air: if one telescope looks through a somewhat different airmass than the other, additional refraction occurs, causing the wavefront to tip or tilt. If one examined the images observed at each telescope, the centroid of the image would move around, and these movements might differ for each aperture. To remove these tip/tilt errors, PTI employs an I-band angle tracker camera (consisting of a quad cell feeding four Avalanche Photo-Diodes) that measures the centroid of the image, and a fast ($\sim$ 100 Hz) servo loop that feeds back to the telescope and keeps the image centered.

The angle tracker also serves as the fine acquisition system at PTI. The first stage acquisition system consists of a CCD operating at R-band, which moves the star close to the field of view of the angle tracker. The angle tracker then executes a spiral search pattern until the source is acquired, and then keeps the source centered using the servo system described above.

From the telescopes, light is reflected down evacuated pipes and into a central building. Once inside the building, the light beams from each telescope are directed down separate delay lines, to compensate for the geometric delay (Equation 2.2) and maintain the fringe packet within the coherence length (Equation 2.12). For PTI, the coherence length is $\sim$ 10 μm, which means that the compensation introduced by the delay lines must be accurate to very fine scales. To this end, PTI employs a high-precision laser metrology system based on a single-mode laser, which maintains the path length to within 20 nm of the desired value.

Because sources move on the sky, the geometric delay changes with time, and thus the delay must be adjusted to maintain fringes within the coherence envelope. At PTI and other near-IR interferometers, variable delay is introduced using carts that travel on delay line rails. In addition to moving the cart along the rails, a voice-coil actuator and a piezo-driven mirror allow sequentially smaller variations in delay. These finer delay adjustments are used to compensate for small delays introduced by variable atmosphere over the individual siderostats. Specifically, the atmosphere

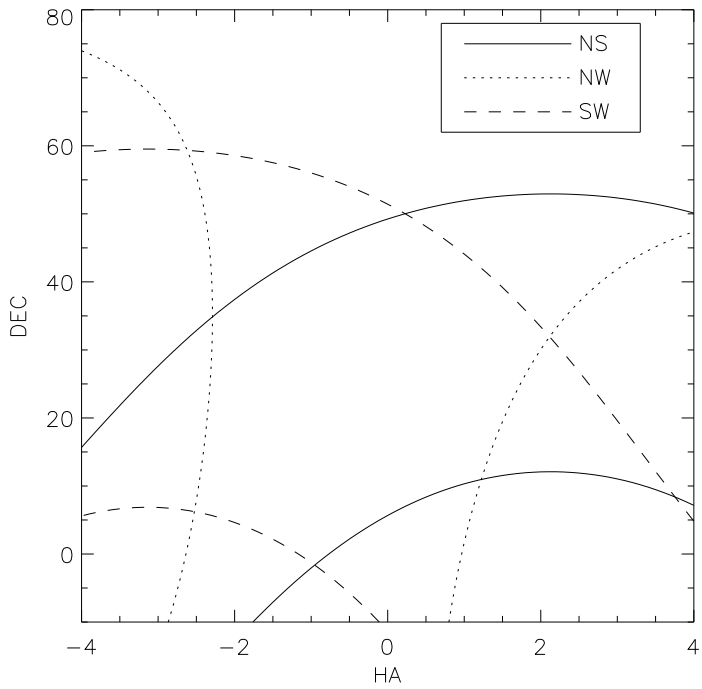

Figure 2.8 Sky coverage of the three PTI baselines, determined by finding the position on the sky for which the maximum possible delay allows observations of fringes within the coherence envelope (Equation 2.12). We see that sources above $\sim 50^\circ$ can be observed only with the NW baseline, while the other two baselines are best suited to sources between $\sim 10 - 50^\circ$.

can introduce an additional phase along one arm of the interferometer, which causes the fringe packet to move; since we want to measure the fringe near zero-delay where the intensity is maximal, a servo loop is used to compensate for these atmospheric effects. This servo loop is called "fringe tracking", and consists of determining the fringe phase over very short intervals ($\sim 10 - 50$ ms), and then adjusting the delay lines to keep the fringe phase close to zero (e.g., Colavita 1999).

The delay lines at PTI have finite lengths (19 m, for a total double-pass delay of 38 m), and the interferometer can therefore find fringes only in certain areas of the sky. The sky coverage for the PTI baselines is shown in Figure 2.8. We see that different baselines can view different parts of the sky; for example, high-declination and low-declination sources can only be easily viewed with the NW baseline, while both the NS and SW baselines are optimized for observing sources close to overhead.

Once the light has been path-compensated, the beams from each aperture are com-

bined at a beam combiner, producing two output beams. Each output now contains fringes. At PTI, one output is directed through a single-mode fiber, which rejects components of the wavefront that have been corrupted by the atmosphere. The result is that only uncorrupted light is passed through to the detector, resulting in an improved accuracy ($\sim 1\%$ vs $\sim 10\%$ for unfiltered light). This spatially-filtered beam is subsequently passed through a prism, which disperses the light onto five "spectral pixels" on the detector. The other output of the beam combiner is passed directly (unfiltered) onto a "white light pixel" on the detector. The detector, a PICNIC array camera, is read out every 10-50 ms.

2.4.2 Keck Interferometer

The Keck Interferometer (KI) combines light from the two 10 m Keck apertures on Mauna Kea, HI (Figure 2.9). The two apertures are separated by $B = 85$ m, providing an angular resolution of ~ 2.5 mas. The basic design of KI is similar to PTI, and we will therefore not discuss all of the components. However, one important difference is that the Keck apertures are bigger than the atmospheric coherence length, and thus the apertures are seeing-limited, rather than diffraction-limited. This presents a problem for interferometry, since it means that the wavefronts observed at the two apertures are corrupted by the atmosphere in different ways, and thus the combination of the two wavefronts will not necessarily be coherent. To compensate for this, adaptive optics (AO) is used to correct the atmospheric effects over each aperture, and provide nearly uniform wavefronts for interferometric combination.

We will not discuss AO in detail, but it is interesting to note that AO can be thought of as an extension of interferometry. If we think of a single aperture as a collection of baselines connecting small sub-apertures, we see that AO performs a function similar to the fringe-tracking delay lines employed at PTI and KI. The effect of non-uniform atmosphere over the aperture causes a relative phase offset between the wavefronts seen by two small sub-apertures, and the image formed by this baseline (also called a "speckle") will thus be slightly off-axis (see Equations 2.5-2.8). When

Figure 2.9 A photograph of the Keck Interferometer (KI), courtesy of NASA/JPL-Caltech. KI currently consists of the two 10 m Keck apertures, separated by an 85 m baseline. The basement of the building connecting the two telescopes contains the beam transport system, delay lines, beam combiner, and detector.

all of the sub-apertures are considered, speckles are formed that fill in the so-called seeing disk, whose radius is determined by the length scale over which the atmosphere is coherent. By adjusting the position of various sub-apertures, an AO system can compensate for these phase offsets and thus bring all of the speckles on-axis, resulting in a diffraction-limited image. Thus, an AO system corrects the phase distortions of the atmosphere and returns a nearly flat wavefront (in theory).

In practice, AO correction is not perfect, and KI therefore calibrates the effects of variable adaptive optics performance on measured fringes. This "ratio correction" (Colavita 1999) is accomplished by measuring the photometric counts down each arm of the interferometer, interspersed with the measurement of beam-combined fringes. Low visibilities due to poor AO performance on one telescope can thereby be accounted for.

Figure 2.10 A photograph of the Owens Valley Millimeter Array (OVRO). OVRO consists of six 10.4 m telescopes, located on the East side of the high Sierra Nevada.

2.4.3 Owens Valley Millimeter Array

The Owens Valley Millimeter Array (OVRO for short) is an array of six 10.4 m telescopes operating from 1-3 mm wavelengths, located near Big Pine, CA (Figure 2.10). Although the basic principles of interferometry discussed above in the context of near-IR interferometry still apply for mm-wave interferometry, there are some salient practical differences. The most important of these involves the way in which light is transported through the system and onto the detector. While the near-IR interferometers discussed above transport light using mirrors, mm-wave interferometers can use electronic components, thanks to the technique of heterodyne mixing.

OVRO has six antennas, which can be combined to provide 15 baselines. The antennas can be arranged in one of five array configurations, "compact", "low", "equatorial", "high", and "ultra-high", which provide baselines from 10 m to 480 m. At the 1-3 mm observing wavelengths, these array configurations yield angular resolutions from $\sim 1 - 10''$. 1 and 3 mm radiation incident on each of the OVRO antennas is detected using SIS junctions, and detected signals are mixed with LO signals providing bandpasses from 86-116 GHz and 210-270 GHz. With the advent of the new COBRA correlator, 4 GHz of bandwidth can now be correlated simultaneously. In addition, a

separate correlator allows high spectral resolution observations of line emission over a more limited bandwidth. Currently, OVRO is being combined with the BIMA array to create CARMA, which will correlate a much larger number of baselines.

2.4.4 Signal-to-Noise Considerations

For direct detection instruments such as PTI and KI, the noise is essentially determined by the Poisson photon noise, and thus the signal-to-noise ratio is proportional to $\sqrt{N_{\rm photons}}$. Following Thompson et al. (1986),

$$S/N_{\rm direct} = \sqrt{\frac{2\Omega_{\rm s}A}{\lambda^2}\frac{\Delta\nu\tau_{\rm a}}{e^{h\nu/kT}-1}}. \tag{2.22}$$

Here, $\Omega_{\rm s}$ is the solid angle subtended by the source, A is the collecting area of the instrument, λ is the observing wavelength (and $\nu = c/\lambda$), $\Delta\nu$ is the bandwidth, T is the blackbody temperature of the source, and $\tau_{\rm a}$ is the integration time.

For a heterodyne system like OVRO, the noise is determined mainly from the uncertainty principle: since the LO preserves the phase of the incoming radiation, there is resultant uncertainty in the total energy, and the noise power resulting from this uncertainty is $P = h\nu\sqrt{\Delta\nu}$ (e.g., Thompson et al. 1986). Although photon shot noise is still present for heterodyne detection, at long wavelengths where large numbers of photons are collected the Poisson photon noise is insignificant compared to the quantum noise. Neglecting the Poisson noise, and accounting for a signal loss of a factor of two due to the fact that heterodyne systems only couple with a single polarization state of incoming radiation, the signal-to-noise is

$$S/N_{\rm hetero} = \frac{\Omega_{\rm s}A}{\lambda^2}\frac{\sqrt{\Delta\nu\tau_{\rm a}}}{e^{h\nu/kT}-1}. \tag{2.23}$$

From Equations 2.22 and 2.23, we see that the noise for a heterodyne system differs from that of a direct detection instrument by a factor of $\sqrt{\Delta\nu/N_{\rm photons}}$:

$$\frac{S/N_{\rm hetero}}{S/N_{\rm direct}} = \sqrt{\frac{\Omega_{\rm s}A}{2\lambda^2}\frac{1}{e^{h\nu/kT}-1}\left(\frac{\Delta\nu_{\rm H}}{\Delta\nu_{\rm D}}\right)}, \tag{2.24}$$

where the factor in parentheses is the ratio of bandwidths for heterodyne and direct detection systems.

At near-IR wavelengths, we can use Equation 2.24 to illustrate why direct detection is preferable. Assuming a source with a diameter of 2 mas and a brightness temperature of 1500 K, using a 0.5 m telescope at 2.2 μm, and assuming $\Delta\nu_{\rm H}/\Delta\nu_{\rm D} = 10^{-3}$, the signal-to-noise for heterodyne detection is $\sim 10^{-5}$ that for direct detection. In contrast, for wavelengths longer than ~ 120 μm, this ratio may approach unity, implying that heterodyne detection is suitable at these wavelengths. Thus, it is not surprising that almost all millimeter and radio interferometers, including OVRO, employ heterodyne detection, while optical and near-infrared telescopes use direct detection.

Chapter 3

Constraining the Evolutionary Stage of Class I Protostars: Multi-wavelength Observations and Modeling[1]

We present new scattered light images at 0.9 μm and OVRO 1.3 mm continuum images of five Class I protostars in the Taurus star forming region. We analyze these data in conjunction with broadband spectral energy distributions and 8-13 μm spectra from the literature using a Monte Carlo radiative transfer code. By fitting models for the circumstellar dust distributions simultaneously to the scattered light and thermal continuum images, and the SEDs, we attempt to distinguish between flared disks, infalling envelopes with outflow cavities, and combinations of disks and envelopes. The best-fits, for which the residuals between the model and data are minimal, are obtained for models incorporating *both* massive envelopes and massive embedded disks. For our best-fit disk+envelope models, we determine mass accretion rates, centrifugal radii, outer radii, envelope and disk masses, and source inclinations. We discuss how these properties constrain the evolutionary stage of our sample, and compare our findings with previous work. In addition, we discuss how models may be improved to provide better fits to the observational data. Finally, we discuss how constraints on the circumstellar dust distributions around Class I sources can

[1]This chapter is based on a manuscript in preparation by J. Eisner, L. Hillenbrand, J. Carpenter, and S. Wolf.

be improved in the future with new observations that will become available with upcoming millimeter interferometers, the *Spitzer Space Telescope*, and other facilities.

3.1 Introduction

The canonical picture of low-mass star formation is that of a rotating, collapsing cloud of dust and gas that forms a protostar surrounded by a disk (e.g., Terebey et al. 1984; Shu et al. 1987, 1993). Protostellar objects have been grouped into evolutionary classes, 0-III, based on their infrared spectral index and the ratio of sub-millimeter to bolometric luminosity (Lada & Wilking 1984; Lada 1987; Adams et al. 1987; André et al. 1993). In this classification scheme, Class 0 and I sources are still in the main accretion phase, and emit most of their radiation at far-IR and submm wavelengths due to reprocessing of light from the central protostars by dust grains in the infalling envelope. In contrast, Class II and III sources exhibit directly revealed pre-main sequence stars in addition to emission from circumstellar disks. This classification scheme is an attempt to represent discretely a continuous evolutionary sequence, and there are transition objects that create some blur between classes. Moreover, this sequence is defined solely from spatially unresolved spectral energy distributions (SEDs), which contain only limited information about the circumstellar distributions.

A crucial test of this evolutionary picture is constraining the geometry of material around members of these different, SED-defined evolutionary classes. Direct imaging of Class II sources has shown that the bulk of the circumstellar material lies in disks (e.g., McCaughrean & O'Dell 1996; Koerner & Sargent 1995; Eisner et al. 2003, 2004), while there may be a small amount of material in tenuous envelopes (e.g., Grady et al. 1999; Semenov et al. 2004). Thus, Class II sources appear to be fully-assembled young stars surrounded by rotating disks from which they continue to accrete material. Direct images of the less evolved Class I sources are relatively rare, due to the large extinctions to these embedded objects. While one expects that these objects should be surrounded by massive envelopes which provide a reservoir of gas and dust for accretion, this expectation has not been verified directly.

Studies of the emergent spectral energy distributions at wavelengths $\gtrsim$ 10 μm have provided some important constraints on the circumstellar dust distributions for Class I objects (e.g., Adams et al. 1987; Kenyon et al. 1993a; Efstathiou & Rowan-Robinson 1991). Specifically, models incorporating infalling, rotating, envelopes with mass accretion rates on the order of 10^{-6} $M_{\odot}$ yr^{-1} are consistent with observed SEDs (Kenyon et al. 1993a). Similar models have also been shown to be consistent with scattered light images at near-IR wavelengths (e.g., Kenyon et al. 1993b; Whitney et al. 1997). Derived mass accretion rates are consistent with the statistically-inferred ages of Class I sources (Adams et al. 1987; Myers et al. 1987; Benson & Myers 1989; Kenyon et al. 1990), providing support for the hypothesis that Class I objects are still in the main accretion phase, where the bulk of the stellar mass is accumulated.

Model fits to SEDs or scattered light images alone are not unique, however, and can not necessarily distinguish between different dust distributions. For example, it has been suggested that for some objects whose SEDs can be explained by spherically-symmetric dust distributions, nearly edge-on flared disk models may also be able to reproduce the observed SEDs (Chiang & Goldreich 1999). Observations that spatially resolve the circumstellar emission at several wavelengths provide less ambiguous diagnostics of geometry. Because images at short wavelengths may trace scattered light from low-density surface layers while longer-wavelength images probe deeper, cooler layers at larger radii, multi-wavelength images can place tight constraints on circumstellar dust models.

For the Class I source L1551 IRS 5, spatially resolved observations at several wavelengths (e.g., Strom et al. 1976; Keene & Masson 1990; Butner et al. 1991; Lay et al. 1994; Ladd et al. 1995; Rodriguez et al. 1998; Chandler & Richer 2000; Motte & André 2001) and detailed spectroscopy (White et al. 2000) have been combined with SED modeling, providing important additional constraints on the models (Osorio et al. 2003). Moreover, the combination of low and high resolution millimeter observations facilitated distinction of compact disk emission and more extended envelope emission. Similar modeling of multi-wavelength observations for IRAS 04302+2247 provided firm constraints on the distribution of circumstellar material and the prop-

erties of the circumstellar dust grains (Wolf et al. 2003).

In order to further our understanding of the Class I population as a whole, we have obtained high spatial resolution observations of five additional Class I sources at multiple wavelengths which, when combined with SEDs, enable much tighter constraints on circumstellar dust models than available from any single dataset. We present images of scattered light at 0.9 μm and thermal emission from dust at 1.3 mm. In addition, we augment SEDs compiled from the literature with new photometry at 0.9 μm, 18 μm, 1.3 mm, and 3 mm wavelengths. Using the three dimensional radiative transfer code MC3D (Wolf & Henning 2000; Wolf 2003), we model our data in the context of three types of circumstellar dust distributions: 1) rotating infalling envelopes; 2) flared disks; and 3) combinations of envelopes+disks.

The best fits are obtained for models incorporating a collapsing envelope and an embedded disk, although we show that pure disks or envelopes can reproduce certain aspects of our data. For each source, we discuss the properties of the best-fit models, including the geometry of the dust distribution and implied mass accretion rates. We use these results to help place Class I sources in the proper evolutionary context. Finally, we discuss properties of these models relevant to future observations, which will become available with the *Spitzer Space Telescope* and other facilities.

3.2 Observations

3.2.1 The Sample

We selected a sample of five Class I sources in the Taurus star forming region, which are a subset of a larger sample of protostars studied by Kenyon et al. (1993a). This subset was selected based on three criteria: 1) sources must be detected at near-IR wavelengths ($F_{0.9\mu\mathrm{m}} \gtrsim 10^{-5}$ Jy), 2) this emission must appear resolved, and 3) sources must emit strongly at millimeter wavelengths ($F_{1\mathrm{mm}} \gtrsim 10^{-2}$ Jy). We initially observed the complete Kenyon et al. (1993a) sample at 0.9 μm with Keck/LRIS (see §3.2.3 and Appendix 3.7), and chose only objects that satisfy our selection criteria for

high angular resolution millimeter observations (§3.2.2) and detailed modeling. Our sample includes IRAS 04016+2610, IRAS 04108+2803B, IRAS 04239+2436, IRAS 04295+2251, and IRAS 04381+2540. General properties of our sample are discussed here, and information about individual objects is given below in §3.4.1.

The bolometric luminosities of our sample span 0.4 to 3.7 $L_\odot$, similar to the distribution of luminosities for the complete sample of Kenyon et al. (1993a), which has a median luminosity of 0.7 $L_\odot$. The SEDs for our sample objects are similar in shape, exhibiting high extinction of the central objects, small amounts of mid-IR absorption, and peaks near 100 μm. While these SED characteristics are common to most other sources in the Kenyon et al. (1993a) sample, several of the SEDs for their sample exhibit deep 10 μm absorption features. As discussed below, the depth of the 10 μm feature is correlated with source viewing angle; the dearth of objects with deep 10 μm absorption in our sample may therefore indicate selection against edge-on sources.

There are other clear selection effects for our sample, since we are biased toward sources exhibiting bright scattered light and millimeter continuum emission. For example, by selecting sources exhibiting bright scattered light nebulae, we are selecting against face-on sources where the directly visible, point-like protostar would dominate the short-wavelength emission, as well as objects with extremely high line-of-sight extinctions, such as one might expect for massive spherical envelopes. Since edge-on sources produce dimmer scattered nebulosity, these may also be under-represented in our sample. Finally, our selection criteria for bright millimeter emission favors objects with higher masses of dust concentrated in smaller volumes. Future observations of larger samples with more sensitive instruments are necessary to investigate these potential biases.

3.2.2 OVRO Observations

We imaged each source in our sample at both 1.3 mm and 3 mm wavelengths with the OVRO Millimeter Array between 2002 August and December. The 3 mm observations

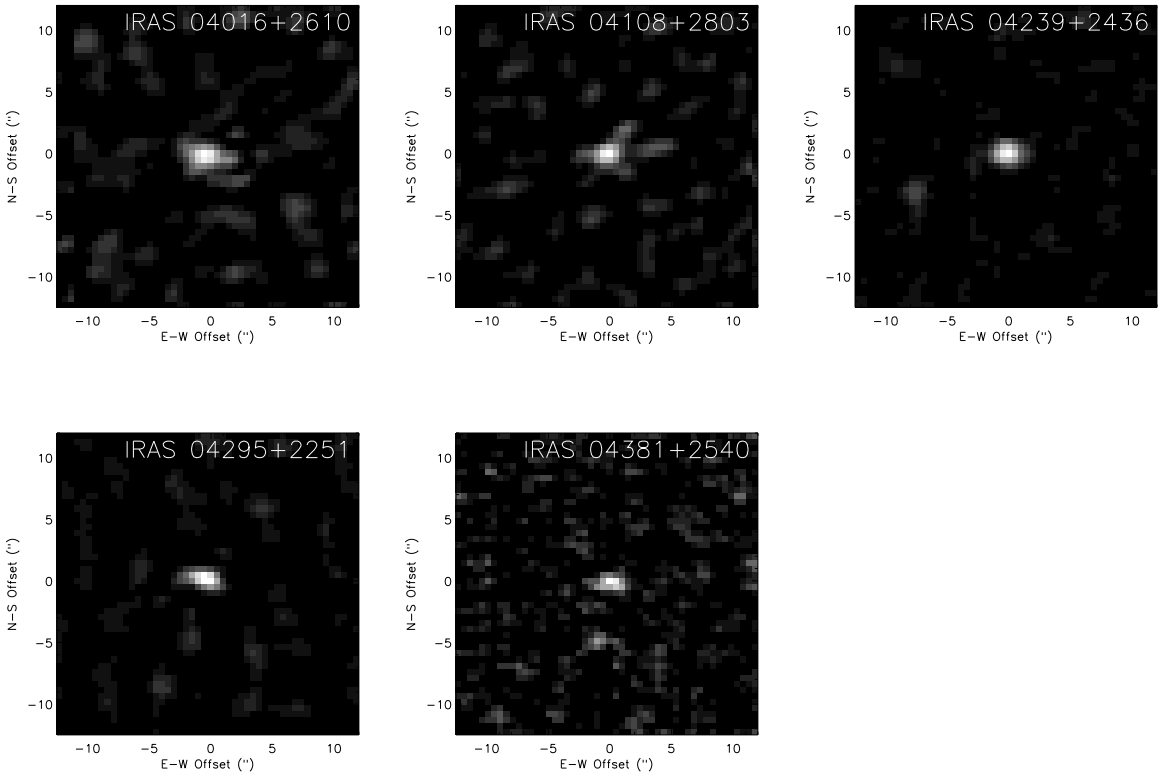

Figure 3.1 Images of our sample in thermal emission at 1.3 mm wavelength, obtained with OVRO. The origin of each image corresponds to the centroid of the millimeter emission. The J2000 coordinates at the origin of the images are ($04^{\rm h}04^{\rm m}43\overset{\rm s}{.}11$, $+26°18'56\overset{''}{.}5$) for IRAS 04016+2610, ($04^{\rm h}13^{\rm m}54\overset{\rm s}{.}72$, $+28°11'33\overset{''}{.}0$) for IRAS 04108+2803B, ($04^{\rm h}26^{\rm m}56\overset{\rm s}{.}29$, $+24°43'35\overset{''}{.}1$) for IRAS 04239+2436, ($04^{\rm h}32^{\rm m}32\overset{\rm s}{.}06$, $+22°57'26\overset{''}{.}3$) for IRAS 04295+2251, and ($04^{\rm h}41^{\rm m}12\overset{\rm s}{.}71$, $+25°46'35\overset{''}{.}3$) for IRAS 04381+2540.

were all conducted in the "compact" array configuration, which provides baselines between 20 and 55 m, while the 1.3 mm observations were obtained mostly with the "equatorial" configuration, providing baselines from 30 to 120 m. For IRAS 04295+2251 and IRAS 04381+2540, 1.3 mm data were also obtained with the "high" configuration, which provides baselines from 35 to 240 m. Continuum data were recorded in four 1-GHz channels. We calibrated the amplitudes and phases of the data using quasars near on the sky ($\lesssim 20°$) to our target sources. The flux of our target sources was calibrated using observations of Neptune and Uranus, which have known millimeter fluxes, to calibrate the response of the instrument. All data calibrations were performed using the OVRO software package MMA (Scoville et al. 1993). Using

the calibrated data for each source, we inverted the interferometric visibilities to create an image, and de-convolved and CLEANed the images using the MIRIAD package (Sault et al. 1995). We averaged the data using robust weighting (with a robustness parameter of 0.5) to obtain a good balance between sensitivity and angular resolution.

From our data, we measure photometric fluxes for our targets at both 3 mm and 1 mm wavelengths. The emission is much stronger at 1 mm, as expected for thermally-emitting dust, and thus the sources are more clearly detected at the shorter wavelengths. In addition, since the angular resolution is inversely proportional to the observing wavelength, and because we obtained longer-baseline data at 1 mm than at 3 mm, our 1 mm images have better angular resolution. Our 1 mm images, shown in Figure 3.1, have angular resolutions of $\sim 2''$, and rms sensitivities of $\sim 1.5 - 2.5$ mJy.

3.2.3 Keck/LRIS Observations at 0.9 μm wavelength

We obtained images of our sample at 0.9 μm (Cousins I-band) using the W.M. Keck II telescope and the Low Resolution Imaging Spectrograph (LRIS; Oke et al. 1995) in imaging mode. The observations were conducted on 1998 October 30-31 and 1999 December 13. The integration time was 300 seconds, the seeing was $0\farcs5 - 0\farcs6$, the field of view was $6' \times 8'$, and the plate scale was 0.21 arcseconds per pixel. Image processing included bias subtraction and flat fielding. The photometric fluxes of the target sources, integrated over a $6\farcs3$ diameter aperture, were calibrated using equatorial standards from Landolt (1992), assuming typical extinction coefficients for Mauna Kea (0.07 mag/airmass at I band; Bèland et al. 1988); all sources were observed at an airmass of less than 1.1.

All objects in our sample were detected at 0.9 μm, and show varying amounts of extended emission arising from scattered light from obscured sources. Our images are shown in Figure 3.2. We determined absolute astrometry for these images by finding reference sources in common to our images and the 2MASS survey, and computing a six coefficient fit for the image coordinates, plate scale, and distortion. The astrometry

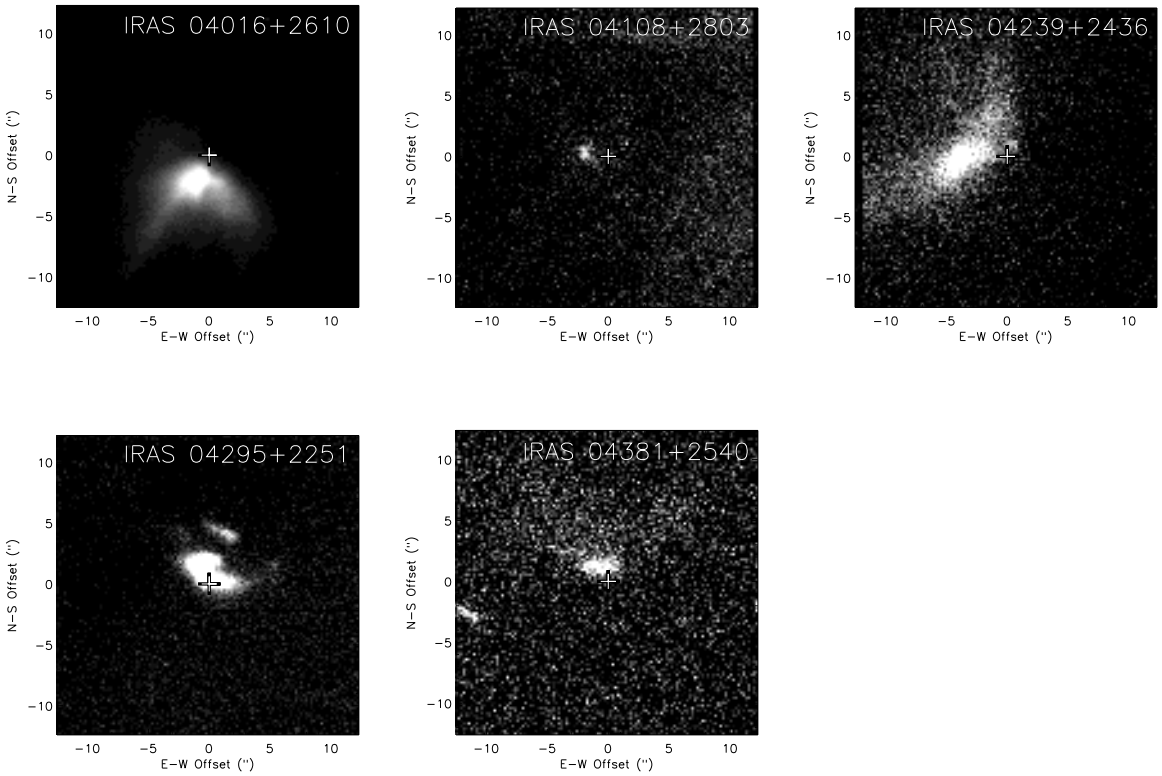

Figure 3.2 Images of our sample in scattered light emission at 0.9 μm wavelength, obtained with Keck/LRIS. The images are registered with respect to the centroid of the millimeter emission for each source (Figure 3.1), indicated by a cross.

is accurate to $\sim 0\farcs3$, including the uncertainty in our astrometric solution and the overall uncertainty from 2MASS.

Because we determine accurate positions for our I-band images, we can register the scattered light emission with the millimeter-wavelength emission observed with OVRO (§3.2.2). Since the longer wavelength radiation is optically thin, it traces dust mass and is therefore likely to be centered on the central source. In Figure 3.2, we have indicated the centroid of the millimeter continuum emission (and thus the likely position of the central protostar) with a cross. As we discuss below, the offset of the scattered light emission with respect to the central protostar provides valuable insights into source geometry and viewing angle.

3.2.4 Keck/LWS Observations

Our sources were also observed at 10.3 and 17.9 μm with Keck/LWS between 1999 August and 2000 December. LWS allows diffraction-limited (FWHM=0.″2) imaging over a 10″ field of view. With this angular resolution, none of our sample are angularly resolved at $10 - 18$ μm. Photometric fluxes were measured in a 0.″96 (12 pixels) aperture, with subtraction of the sky background measured in a annulus of radius 2.″0-3.″2 (25-40 pixels). Flat-fielding did not improve the data quality, and was therefore not applied before measuring photometry. Standard stars were observed each night to obtain atmospheric extinction curves, and curve-of-growth corrections were applied to each star to convert measured aperture photometry to infinite-aperture values. In addition, these Keck/LWS observations provided 8-13 μm spectra, which have been reduced and analyzed by Kessler-Silacci et al. (2005).

3.2.5 SEDs

SEDs were constructed using photometric fluxes from the literature and new measurements at 0.9 μm (§3.2.3), 18 μm (§3.2.4), 1.3 mm, and 3 mm (§3.2.2) wavelengths. Uncertainties are not available for much of the photometry from the literature, and we therefore do not include photometric uncertainties in the modeling described below. Since this tends to over-weight higher fluxes (which may have larger uncertainties), we typically consider the logarithms of the SEDs. The fluxes used in our analysis, converted into units of Jy, are listed in Table 3.1, and SEDs are plotted (logarithmically) along with best-fit models below in §3.4.

Table 3.1. Spectral energy distributions for our sample

λ (μm)	Source Fluxes, F_ν (Jy)					reference[a]
	04016+2610	04108+2803	04239+2436	04295+2251	04381+2540	
0.55	2.42e-05					Kenyon et al. (1993a)
0.63	6.17e-05					Kenyon et al. (1993a)
0.79	0.0001					Kenyon et al. (1993a)
0.89	0.0001	3.23e-06	3.89e-05	2.23e-05	8.13e-06	This work
1.10	0.0003					Padgett et al. (1999)
1.22	0.0055	0.0004	0.0010	0.0055	0.0005	Kenyon et al. (1993a)
1.22				0.0038		Whitney et al. (1997)
1.60	0.0095					Padgett et al. (1999)
1.63	0.0217	0.0050	0.0075	0.0360	0.0018	Kenyon et al. (1993a)
1.63	0.0233	0.0242	0.0076	0.0229	0.0029	Park & Kenyon (2002)
1.63	0.0263	0.0043	0.0066	0.0220		Whitney et al. (1997)
1.87	0.0214					Padgett et al. (1999)
2.05	0.0416					Padgett et al. (1999)
2.19	0.1160	0.0226	0.0421	0.0943	0.0101	Kenyon et al. (1993a)
2.19	0.1045	0.0420	0.0464	0.0690	0.0147	Park & Kenyon (2002)
2.19	0.1055	0.0148	0.0439	0.0671	0.0149	Whitney et al. (1997)
3.45	0.4593	0.0492	0.2302	0.1667	0.0470	Kenyon et al. (1993a)

Table 3.1 (cont'd)

λ (μm)	Source Fluxes, F_ν (Jy)					reference[a]
	04016+2610	04108+2803	04239+2436	04295+2251	04381+2540	
4.75	2.0465	0.1702				Kenyon et al. (1993a)
7.80	2.8000	0.3100				Myers et al. (1987)
8.69	2.0999	0.5000				Myers et al. (1987)
9.50	1.7000	0.4900				Myers et al. (1987)
10.3	2.5000	0.5699				Myers et al. (1987)
10.6	2.5682	0.6020		0.5883	0.2087	Kenyon et al. (1993a)
10.7	2.9700	0.7599	1.7100	0.7200	0.2300	Kessler-Silacci et al. (2005)
11.6	3.4000	0.4400				Myers et al. (1987)
12.0	3.8327	0.7647	1.7120	0.6215	0.4106	Kenyon et al. (1993a)
12.5	4.9000	1.3000				Myers et al. (1987)
17.9	4.5708			1.0665		This work
21.0	10.6303	2.6094	4.4314		0.1979	Kenyon et al. (1993a)
25.0	16.3030	3.6498	6.9545	1.8718	2.7686	Kenyon et al. (1993a)
60.0	48.1371	7.6292	15.2222	3.4872	10.5312	Kenyon et al. (1993a)
100	62.2772	10.8225	17.1525	8.2097	14.9392	Kenyon et al. (1993a)
100	55.5046					Kenyon et al. (1993a)
160	46.6067					Kenyon et al. (1993a)

Table 3.1 (cont'd)

λ (μm)	Source Fluxes, F_ν (Jy)					reference[a]
	04016+2610	04108+2803	04239+2436	04295+2251	04381+2540	
350	4.7686					Kenyon et al. (1993a)
450	3.2926	1.8094				Kenyon et al. (1993a)
450	2.8199				1.2000	Hogerheijde & Sandell (2000)
450	4.2300	1.1300	2.1400	2.6600	2.8199	Young et al. (2003)
800	0.5820	0.0850	0.3330	0.2410	0.2890	Moriarty-Schieven et al. (1994)
800	0.3143	0.8859	2.3303			Kenyon et al. (1993a)
850	0.5899	0.1700	0.4199	0.4199	0.5600	Young et al. (2003)
850	0.4300				0.2399	Hogerheijde & Sandell (2000)
1100	0.1800	<0.1000	0.1140	0.0939	0.1160	Moriarty-Schieven et al. (1994)
1100	0.5317	0.0882	0.0768			Kenyon et al. (1993a)
1300	0.1500	0.0390	0.1700	0.1150	0.3000	Motte & André (2001)
1300	0.0658	0.0271	0.0329	0.0484	0.0135	This work
2700	<0.0068				<0.0075	Hogerheijde et al. (1997)
3000	<0.0096	<0.0210	<0.0120	<0.0210		Ohashi et al. (1996)
3000		0.0058	0.0120	0.0087		This work
3369	<0.0043				<0.0050	Hogerheijde et al. (1997)
3440	<0.0180		<0.0240			Saito et al. (2001)

Table 3.1 (cont'd)

λ (μm)	Source Fluxes, F_ν (Jy)					reference[a]
	04016+2610	04108+2803	04239+2436	04295+2251	04381+2540	
20000	0.0005					Lucas et al. (2000)
35000	0.0003		0.0001			Lucas et al. (2000)
60000	<0.0002					Lucas et al. (2000)

References. — [a]–Kenyon et al. (1993a) compiled SEDs from new data and the literature, and this work contains references for much of this photometry.

Note. — Different observations were conducted with different angular resolutions, which explains some of the photometric variations. In addition, all of the sources in our sample except IRAS 04295+2251 are known to be variable at short wavelengths (e.g., Park & Kenyon 2002).

3.3 Modeling

We use the three dimensional Monte Carlo radiative transfer code MC3D (Wolf & Henning 2000; Wolf 2003) to model simultaneously the SEDs, near-IR scattered light images, and millimeter continuum images of our sample of Class I sources. The MC3D code solves the radiative transfer equation and determines the temperature distribution of circumstellar dust self-consistently. Moreover, the code takes into account absorption and multiple scattering events. The main inputs for this modeling are 1) parameters of the central star, 2) properties of dust grains, and 3) geometry of circumstellar dust. We now describe which of these properties are allowed to vary in our modeling, as well as our assumptions for the other parameters.

For the models described below, we assume that the central object resembles a typical, Class II T Tauri star. We therefore assume $T_* = 4000$ K, $R_* = 2$ $R_\odot$, and $M_* = 0.5$ $M_\odot$ (e.g., Gullbring et al. 1998). Although few direct constraints exist on these parameters, spectroscopy of IRAS 04016+2610 has yielded an estimated effective temperature between $\sim 3300 - 4200$ K and a radius of ~ 0.9 $R_\odot$ (White & Hillenbrand 2004; Ishii et al. 2004), reasonably consistent with our assumptions. The dynamically-estimated stellar mass of IRAS 04381+2540 is $\sim 0.2 - 0.4$ $M_\odot$ (Brown & Chandler 1999), also compatible with our assumptions.

Accretion onto the stellar surface may generate substantial luminosity in shocks near the stellar surface, which would supplement the stellar luminosity (Calvet & Gullbring 1998; Gullbring et al. 2000): $L_{\rm central} = L_* + L_{\rm acc}$. In our modeling, we initially assume that $L_{\rm central} = L_*$, but we include a scale factor to allow for additional accretion luminosity. As the last step in our modeling procedure, we find the value of $L_{\rm central}$ for which no scale factor is required. Although the spectral shape of emission from the accretion shock may differ from the stellar emission, we ignore this effect and assume that the temperature of all emission is 4000 K; the spectral shape is not critical given the extremely high optical depths in the inner regions of our models.

We assume that the dust grains are spherical with a power-law size distribution $n(a) \propto a^{-3.5}$ (Mathis et al. 1977), where $a_{\rm min} = 0.005$ μm and $a_{\rm max} = 1.0$ μm,

appropriate for ISM-like grains. We further assume that the dust is composed of a standard ISM mixture of 62.5% silicate and 25% ortho + 12.5% para graphite (e.g., Draine & Malhotra 1993; Weingartner & Draine 2001), with optical properties from Draine & Lee (1984). Previous authors have explored the effects of varying the chemical composition and particle size distribution of the circumstellar dust (e.g., D'Alessio et al. 1999, 2001). These parameters affect the overall SED, and 10 and 18 μm Silicate features, to some extent. To minimize complications, we keep the dust composition and particle size distribution fixed in our modeling.

The main remaining input for radiative transfer is the density distribution, for which we consider three classes of models: rotating infalling envelopes, flared disks, and envelopes+disks. Each of these models is defined from an inner radius, $R_{\rm in}$, to an outer radius, $R_{\rm out}$. The inner radius is assumed to be 0.1 AU (comparable to the dust sublimation radius), although this parameter is not crucial to the modeling given the high optical depths near to the central protostar. However, $R_{\rm out}$ may have substantial effects on models for the circumstellar material, and thus we allow this parameter to vary in our modeling.

For each of the density distributions described below, we generate small grids of models by varying several important parameters. Large grids are not possible due to the long run-time of Monte Carlo radiative transfer codes (typically several hours per model). For the pure envelope model (§3.3.1), we vary the mass infall rate, $\dot{M}$, the centrifugal radius, $R_{\rm c}$, the outer radius, $R_{\rm out}$, and the inclination, i. The values of $\dot{M}$ are chosen to provide total envelope masses[2] of $5 \times 10^{-3}, 10^{-2}$, and 5×10^{-2} M$_\odot$; since the envelope mass depends to some extent on parameters other than $\dot{M}$ (see Equation 3.2 and §3.3.1), the accretion rates explored include 27 discrete values between $\sim 10^{-7} - 10^{-4}$ M$_\odot$ yr^{-1}. Sampled values of the other parameters are $R_{\rm c} = 30, 100$, and 500 AU; $R_{\rm out} = 500, 1000$, and 2000 AU; and $i = 5 - 90^\circ$ in increments of 5°. For the pure disk model, we vary the disk mass, scale height, outer radius and inclination; $M_{\rm disk} = 10^{-3}, 5 \times 10^{-2}$, and 1.0 M$_\odot$, $h_0 = 5, 15$, and 25 AU, $R_{\rm out} = 500, 1000$, and 2000 AU, and $i = 5 - 90^\circ$ in increments of 5° . Finally, for the

[2]All envelope and disk masses assume a gas to dust ratio of 100.

envelope+disk model, we assume $h_0 = 15$ AU, but allow $M_{\rm disk}$ to vary, in addition to varying several important envelope parameters: $\dot{M}$, $R_{\rm c}$, $R_{\rm out}$, and i. The range of envelope parameters are the same as for the pure envelope model, and we sample $M_{\rm disk} = 10^{-3}, 10^{-2}$, and 1.0 $M_\odot$. All of the parameter values in these grids are chosen to bracket physically-plausible values.

We compute the SED from 0.1-5000 μm, the scattered light image at 0.9 μm, and the dust continuum image at 1.3 mm for each model. The best-fit models are determined by minimizing the residuals between model and data for the combined SED+imaging dataset. Since we do not have error bars for the SEDs or images, we perform a Least-Squares (X^2) minimization, rather than employing a χ^2 technique. The best-fit model weights each dataset equally, and is determined by minimizing the "normalized" residuals,

$$X^2_{\rm norm} = \frac{X^2_{\rm sed}}{\min(X^2_{\rm sed})} + \frac{X^2_{0.9\mu{\rm m}}}{\min(X^2_{0.9\mu{\rm m}})} + \frac{X^2_{1{\rm mm}}}{\min(X^2_{1{\rm mm}})}. \quad (3.1)$$

When fitting the SED, we minimize the difference between the logarithms of the model and data, to emphasize the shape of the SED over the peak value. In addition, we allow a scale factor between the model SED and the observed fluxes. When fitting 0.9 μm and 1 mm images, we first rotate the observed images to a position angle where the brightest scattered light is south of the millimeter emission, consistent with the position angle definition in our models.

Once the best-fit model out of these grids has been determined, we attempt to "zoom in" on the solution with more finely gridded values of inclination. During this zoom-in stage, we also vary $L_{\rm central}$ in order to produce the correct normalization between the modeled and observed SEDs (without a scale factor). Because the central luminosity is somewhat degenerate with the total optical depth of the system (e.g., Kenyon et al. 1993a), minor adjustments to $\dot{M}$ and/or $M_{\rm disk}$ may be required when $L_{\rm central}$ is varied. Thus, when zooming in on a solution, we vary i, $L_{\rm central}$, and $\dot{M}$ and/or $M_{\rm disk}$ simultaneously.

The effects of various parameters on the SEDs have already been explored by

previous investigators (e.g., Adams et al. 1987; Kenyon et al. 1993a; D'Alessio et al. 1999), and some work has studied the effects on scattered light images (e.g., Whitney & Hartmann 1992; Whitney et al. 1997). We attempt to improve on this previous work by exploring the effects of model parameters on our combined SED+imaging dataset, and discussing how degeneracies between fitted parameters can be broken.

3.3.1 Rotating, Infalling Envelope

The density distribution for a rotating, infalling envelope is given by (e.g., Ulrich 1976; Cassen & Moosman 1981; Terebey et al. 1984),

$$\rho_{\rm env}(r,\theta) = \frac{\dot{M}}{4\pi}(GM_* r^3)^{-1/2}\left(1+\frac{\mu}{\mu_0}\right)^{-1/2}\left(\frac{\mu}{\mu_0}+2\mu_0^2\frac{R_c}{r}\right)^{-1}. \qquad (3.2)$$

Here, r is the radial coordinate, M_* is the mass of the central star (assumed to be 0.5 $M_\odot$), $\dot{M}$ is the mass infall rate, R_c is the centrifugal radius, $\mu = \cos\theta$ defines the angle above the midplane, and μ_0 defines the initial streamline of the infalling material.

For each value of r, θ, there is a unique value of μ_0, since the streamlines of infalling particles do not cross. Before determining the density distribution using Equation 3.2, we analytically solve for μ_0 :

$$\frac{r}{R_c} = \frac{\cos\theta_0 \sin^2\theta_0}{\cos\theta_0 - \cos\theta} = \frac{1-\mu_0^2}{1-\mu/\mu_0}. \qquad (3.3)$$

This is a cubic equation with three solutions. The correct solution is the one for which $\sin\theta_0$ has the same sign as $\sin\theta$, and for which the solution is real. In other words, a particle that starts in the northern or southern hemisphere never leaves that hemisphere. The correct analytic solution is

$$\mu_0 = X - \frac{1}{3X}, \qquad (3.4)$$

where X is defined as

$$X \equiv \frac{\left(27\mu r R_c^2 + \sqrt{729\mu^2 r^2 R_c^4 + 108 R_c^3 (r - R_c)^3}\right)^{(1/3)}}{2^{(1/3)} 3 R_c}. \quad (3.5)$$

We include an outflow cavity in our envelope models by decreasing the density by some factor, $f_{\rm cav}$, in the polar regions of the circumstellar distributions. The cavity shape is defined by

$$\rho(r, z > z_0 + r^{\zeta}) = f_{\rm cav} \times \rho_{\rm env}(r, z). \quad (3.6)$$

Here, z is the height above the midplane, z_0 describes how close to the star the outflow cavity begins, and ζ describes the opening angle and shape of the outflow. We fix $z_0 = 1$ AU, since this parameter does not have major affects on the observed SEDs or scattered light images. We also assume that within the outflow cavity, the density decreases by a factor of $f_{\rm cav} = 4$ relative to the rest of the envelope; this value of $f_{\rm cav}$ produces the correct amount of extinction to match the observed short-wavelength SEDs. The cavity profile has some effect on the structure of modeled scattered light emission. However, these effects are small compared with the other envelope properties; thus, we fix the value of ζ at 1.1 in our analysis. Using other types of cavities (e.g., cones) may have small effects on the scattered light images, but will have negligible effects on SEDs (e.g., Whitney et al. 2003b).

We fit this envelope model to our data by varying $\dot{M}$, $R_{\rm c}$, the outer radius of the envelope, $R_{\rm out}$, and the viewing angle of the model, i. Some of these parameters produce degenerate effects on the models, which is why we generate grids where these parameters are varied simultaneously. However, we address the effects of each parameter below in order to shed light on how our different datasets constrain various envelope properties.

The accretion rate, $\dot{M}$, is one of the most important parameters in terms of its effects on the SED, since it is linked to the total envelope mass (Equation 3.2), and thus governs directly the optical depth of the dust surrounding the protostar (Figure 3.3). For higher mass accretion rates, the optical depth will increase, and less of the

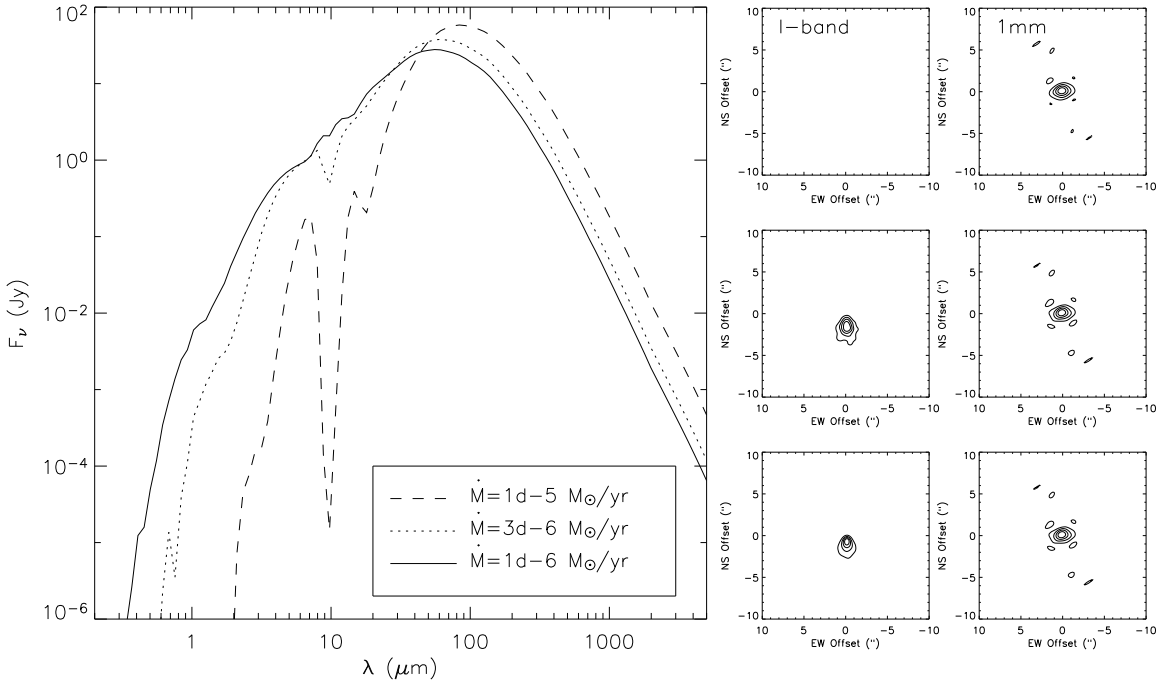

Figure 3.3 SEDs, scattered light images, and millimeter continuum images for a rotating, collapsing envelope with a range of mass accretion rates, spanning 10^{-6} to 10^{-5} $M_\odot$ yr^{-1} ($\dot{M}$ increases from the bottom to top panels). This model assumes $R_c = 30$ AU, $R_{out} = 1000$ AU, and $i = 45°$. The I-band images were generated by convolving our model images with a 1″ FWHM Gaussian, to simulate the seeing of our LRIS observations. Similarly, we convolved the 1 mm images with the actual beam that was used to observe IRAS 04016+2610. For both 0.9 μm and 1 mm images, the contours intervals are 20% of the peak flux, beginning at 20%. As $\dot{M}$ increases, the strength of near-IR scattered emission decreases, although the shape of the emission broadens (note that for $\dot{M} = 10^{-5}$ $M_\odot$ yr^{-1}, the scattered emission is undetected in our models). Higher mass accretion rates also produce larger mid-IR absorptions. While the appearance of millimeter images is relatively unaffected by changes in $\dot{M}$, the long-wavelength flux is enhanced for higher accretion rates.

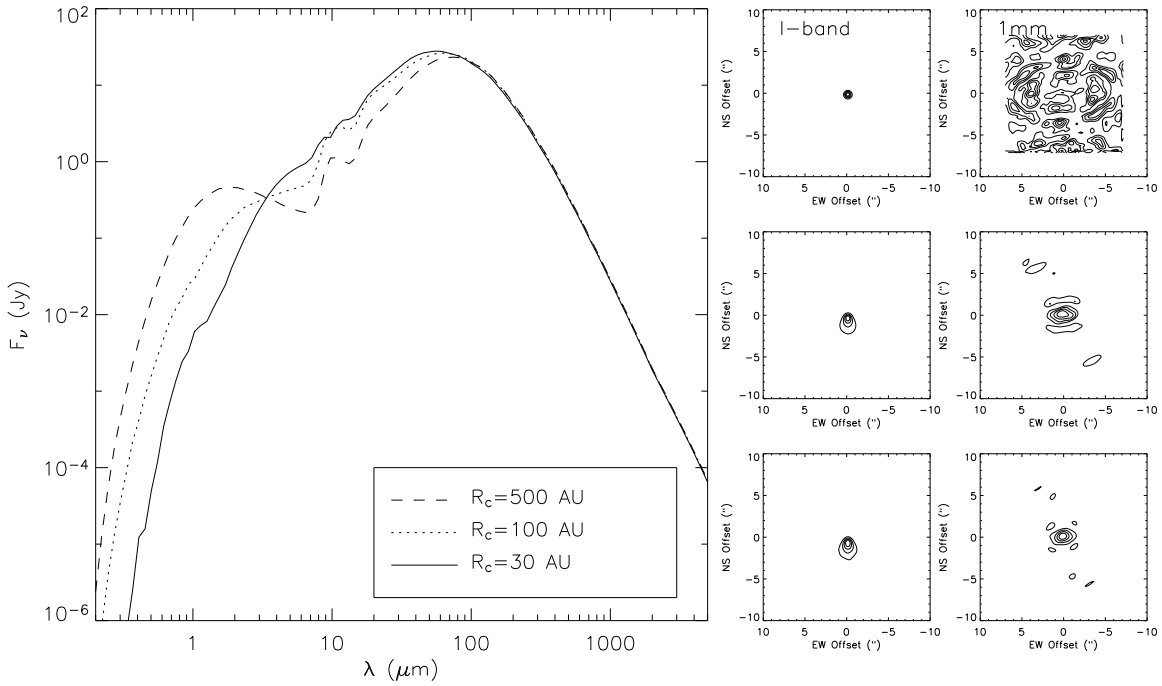

Figure 3.4 SEDs, scattered light images, and millimeter continuum images for a rotating, collapsing envelope with a range of centrifugal radii, spanning 30 to 500 AU. This model assumes $\dot{M} = 10^{-6}$ M$_\odot$ yr^{-1}, $R_{\rm out} = 1000$ AU, and $i = 45°$. Larger values of $R_{\rm c}$ lead to less spherically symmetric dust distributions, leading to increased absorption in the midplane, but less absorption out of the midplane. Thus, for large $R_{\rm c}$, the central star becomes visible directly. The centrifugal radius also represents a region of enhanced density, and thus larger $R_{\rm c}$ lead to significantly larger millimeter images. In fact for $R_{\rm c} = 500$ AU, the millimeter emission is almost completely over-resolved in our OVRO observations.

short-wavelength emission will escape (either directly or as scattered light). Moreover, the mid-IR absorption deepens, because of increased extinction of the stellar emission and absorption in the 10 and 18 μm Silicate features. The short-wavelength radiation is re-processed and emitted at longer wavelengths, leading to more emission at far-IR through millimeter wavelengths for higher values of $\dot{M}$. The higher optical depths associated with large mass accretion rates also push the visible scattering surfaces outward, leading to somewhat larger I-band images. However, for very large accretion rates, the near-IR emission may be quenched altogether (Figure 3.3).

The centrifugal radius, $R_{\rm c}$, defines the radius in the model where material falling in from outer regions joins rotationally-supported material in the inner region. Outside of $R_{\rm c}$, the envelope is essentially spherical (except for the outflow cavity), while the

density distribution is significantly flattened interior to the centrifugal radius. In addition, matter builds up at R_c, leading to a region of enhanced density. For smaller values of R_c, a larger fraction of the envelope material is spherically distributed, and the optical depth is larger for most sight-lines. Thus, models with small R_c show large near-IR extinctions and deep mid-IR absorption (largely degenerate with the effects of $\dot{M}$; Figures 3.3 and 3.4). In contrast, for larger R_c, more of the envelope's mass is relegated to the midplane, making it easier for emission to escape. Thus, scattered emission is stronger for larger values of R_c. This parameter also has a critical effect on the modeled millimeter images: since the density is higher for radii $\lesssim R_c$, the size of the millimeter emission will correlate with the centrifugal radius (Figure 3.4). Thus, the sizes of our millimeter images constrain R_c directly.

The outer radius also affects the model, mainly by changing the optical depth; larger values of R_{out} lead to more mass in the envelope, and thus more extinction of short wavelength light and more emission of long-wavelength radiation (Figure 3.5). Smaller values of R_{out} may require larger values of $\dot{M}$ and/or smaller values of R_c in order to correctly model the SED. R_{out} is constrained strongly from our scattered light and millimeter images, since larger outer radii produce larger images (Figure 3.5). For our sample, the observed sizes of scattered light constrain R_{out} to be $\gtrsim 1000$ AU, while the fact that the millimeter images are fairly compact rules out outer radii larger than $\sim 1500 - 2000$ AU.

Inclination is a crucial parameter for modeling both the SED and the scattered light images. As noted by previous authors (e.g., Kenyon et al. 1993a; Nakazato et al. 2003) and shown in Figure 3.6, the SED changes drastically depending on viewing angle. At larger inclinations, where the observer's line of sight passes through more of the dense midplane, the overall optical depth of the model increases, leading to enhanced extinction at short wavelengths and absorption at mid-IR wavelengths. In contrast, for smaller inclinations the optical depth is lower, and for face-on models, the line of sight may go directly down the outflow cavity to the central protostar. In addition to affecting the amount of scattering or direct stellar radiation, the inclination also affects the shape of the scattered emission: for edge-on distributions,

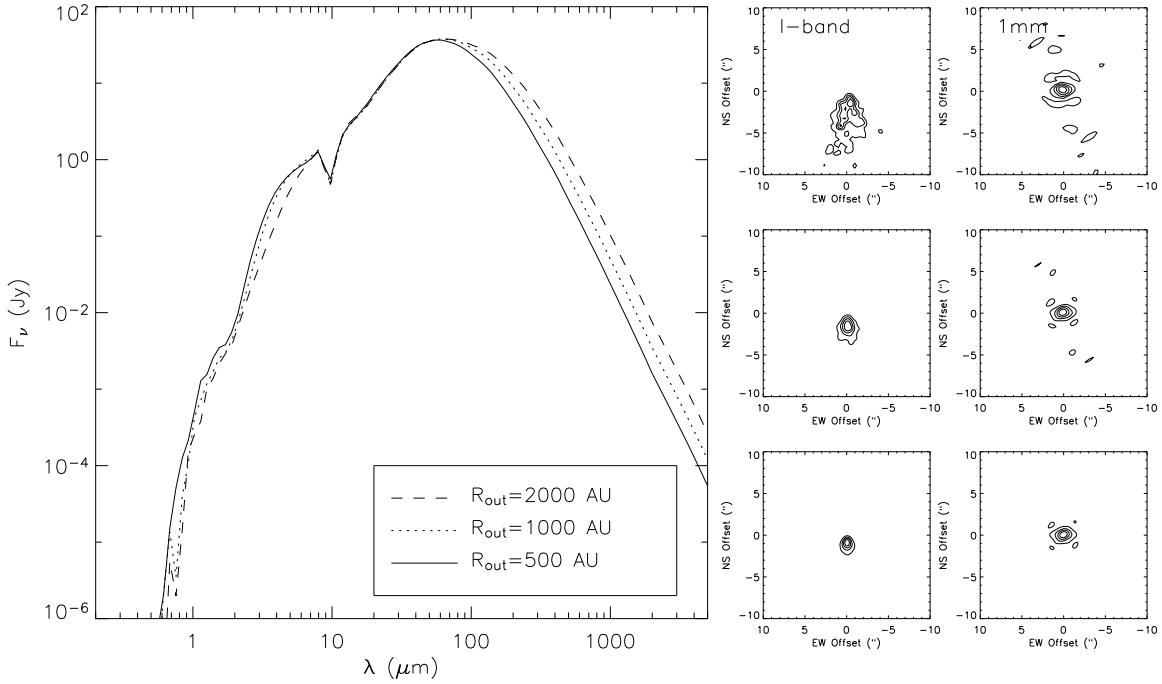

Figure 3.5 SEDs, scattered light images, and millimeter continuum images for a rotating, collapsing envelope with a range of outer radii, spanning 500 to 2000 AU. This model assumes $\dot{M} = 3 \times 10^{-6}$ M$_\odot$ yr^{-1}, $R_c = 30$ AU, and $i = 45°$. As R_{out} increases, the amount of material in the envelope is increased (for a fixed $\dot{M}$), increasing the optical depth and leading to slightly higher absorption at near-to-mid-IR wavelengths. Not surprisingly, the images at both 0.9 μm and 1 mm become larger as R_{out} is increased. For the 1 mm images, the increased extended emission is manifested primarily by stronger sidelobe features, which are artifacts of the limited sampling in our interferometric observations (the 1 mm images have been convolved with the OVRO beam obtained for IRAS 04016+2610).

the scattered light arises mainly from the edges of the outflow cavity, producing a symmetric structure with two lobes. As the inclination decreases, one lobe brightens with respect to the other, and moves closer to the central protostar as the line of sight pierces further into the cavity. Finally, for inclinations close to face-on, the protostar is visible directly, swamping any scattered emission that might be present. Since our millimeter images are only marginally spatially resolved, inclination is not important in modeling this emission. However, the offset between 1 mm and 0.9 μm emission *is* sensitive to inclination; the visible scattering surface moves farther from the mass-sensitive millimeter emission for larger inclinations (Figure 3.6).

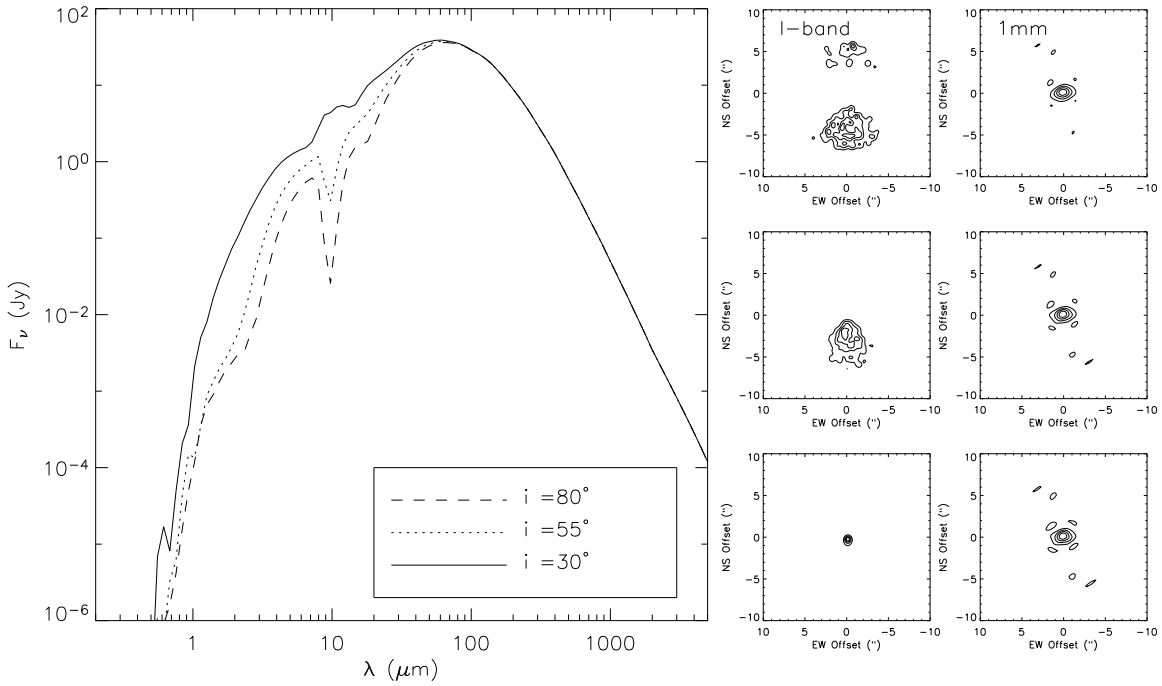

Figure 3.6 SEDs, scattered light images, and millimeter continuum images for a flared disk model at a range of viewing angles. The panels are labeled as in Figure 3.3. More edge-on models exhibit deeper absorption at mid-IR wavelengths, and higher extinction of the central star. For small inclinations ($i \lesssim 30°$), the central star is visible, and dominates the I-band emission. For moderate inclinations, an asymmetric scattered light structure is observed, while for nearly edge-on orientations, a symmetric, double-lobed structure is observed. The millimeter emission for this model is unresolved by our observations, and the model images are thus insensitive to inclination.

3.3.2 Flared Disk

The density distribution for a flared disk is given by (Shakura & Sunyaev 1973),

$$\rho_{\rm disk} = \rho_0 \left(\frac{R_*}{r}\right)^{\alpha} \exp\left\{-\frac{1}{2}\left[\frac{z}{h(r)}\right]^2\right\}, \tag{3.7}$$

where

$$h(r) = h_0 \left(\frac{r}{100\ {\rm AU}}\right)^{\beta}. \tag{3.8}$$

Here, r is the radial distance from the star in the disk mid-plane, z is the vertical distance from the mid-plane, R_* is the stellar radius, and h is the disk scale height. We assume fixed values for the exponents of radial and vertical density distributions,

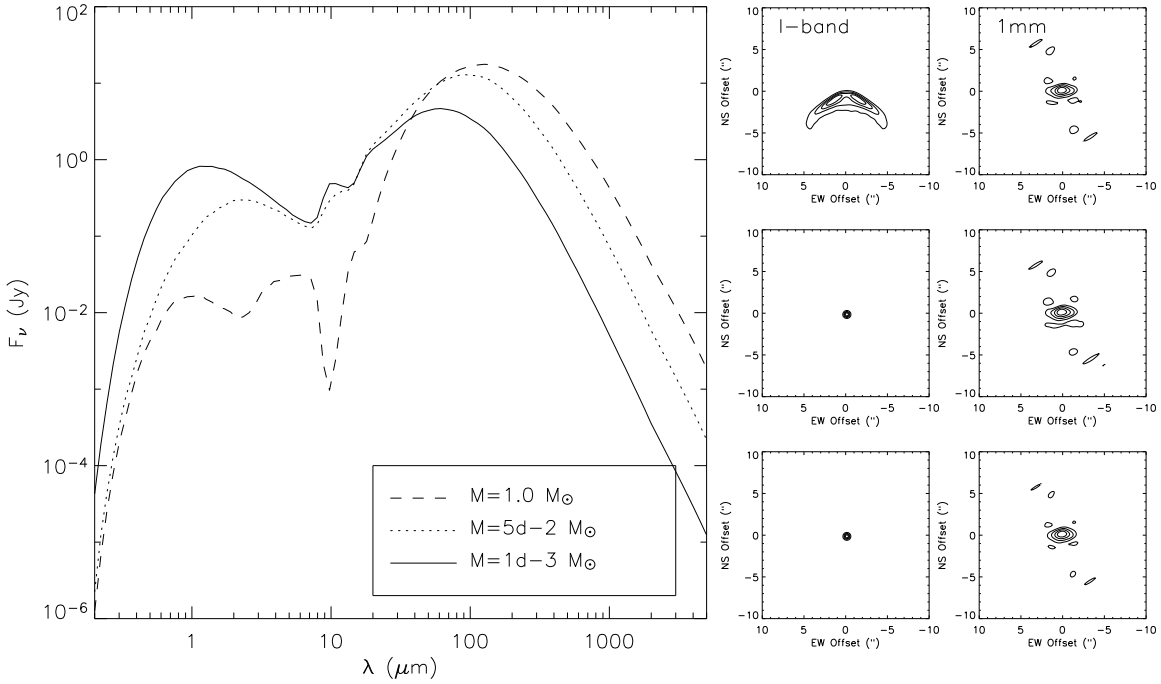

Figure 3.7 SEDs, scattered light images, and millimeter continuum images for a flared disk model with a range of disk masses. The panels are labeled as in Figure 3.3. For this model, $R_{\rm out} = 1000$ AU, $h_0 = 15$ AU, and $i = 60°$. Higher disk mass increases the optical depth of the model, leading to higher absorption at short wavelengths and enhanced emission at long wavelengths. In addition, if there is sufficient dust mass, the central star is obscured, and scattered light is visible at short wavelengths. The flux in millimeter continuum images is increased for higher disk mass, and the emission becomes slightly more extended.

α and β, respectively. For a flared disk in hydrostatic equilibrium, one expects $\beta = 58/45$ (Chiang & Goldreich 1997), and we adopt this value. Using the relation that results from viscous accretion theory, $\alpha = 3(\beta - 1/2)$ (Shakura & Sunyaev 1973), we obtain $\alpha = 2.37$. These values for α and β are similar to those used in previous modeling of circumstellar disks (e.g., D'Alessio et al. 1999; Wood et al. 2002; Wolf et al. 2003).

The disk mass affects our modeled SEDs, scattered light images, and millimeter images. Higher dust mass increases the optical depth, leading to higher absorption at short wavelengths and enhanced emission at long wavelengths. As illustrated by Figure 3.7, for smaller disk masses ($\lesssim 10^{-2}$ $M_\odot$) the central protostar is visible for inclination $\lesssim 70°$, and this stellar radiation swamps any scattered light. However,

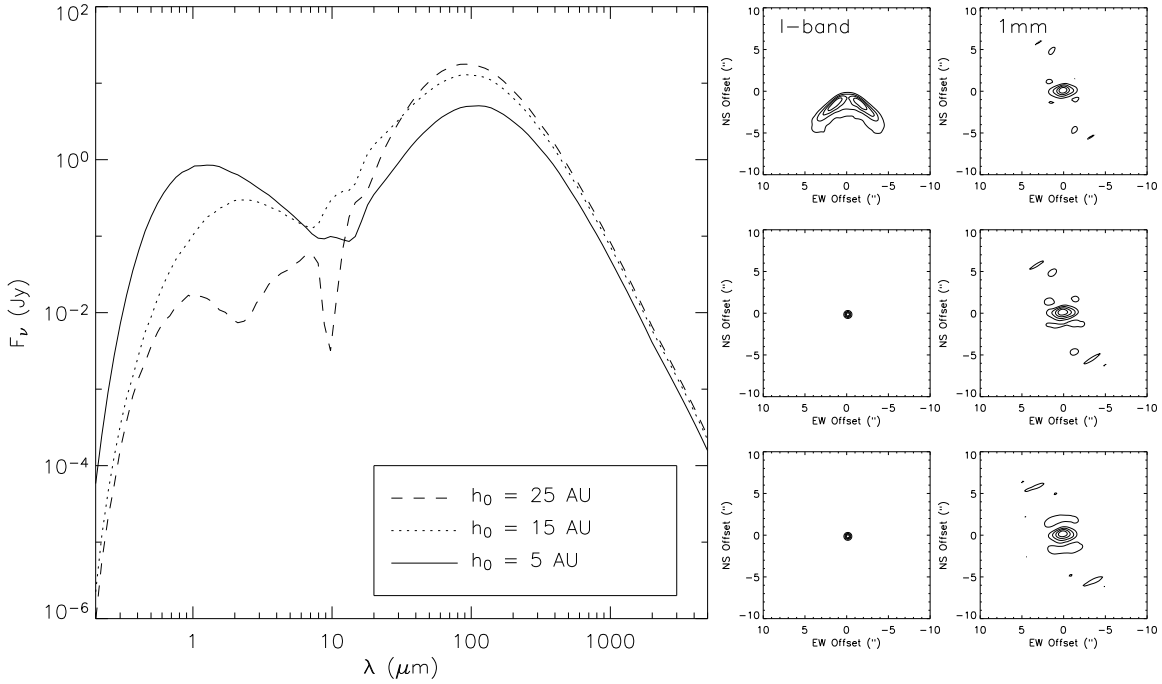

Figure 3.8 SEDs, scattered light images, and millimeter continuum images for a flared disk model with a range of disk scale heights. The panels are labeled as in Figure 3.3. This model assumes $M_{\rm disk} = 5{\times}10^{-2}$ M$_\odot$, $R_{\rm out} = 1000$ AU, and $i = 60°$. Larger values of h_0 produce similar effects on the short-wavelength SED and scattered light images as larger values of $M_{\rm disk}$ (Figure 3.7); higher absorption, and increased visibility of scattered light. However, the effects on the longer-wavelength emission differ; higher values of h_0 increase the far-IR flux, but have little effect on millimeter fluxes and lead to slightly more compact morphologies at millimeter wavelengths (corresponding to weaker sidelobe emission features).

for higher disk masses, the flared disk surface becomes sufficiently optically-thick to obscure the protostar, allowing scattered emission to be observed. The millimeter images are only slightly affected by disk mass: more massive disks have millimeter emission detectable out to larger radii, leading to slightly larger observed images.

The effects of h_0 are similar to the effects of $M_{\rm disk}$ in some respects; however, SED+imaging data allows us to disentangle the two. Larger values of h_0 produce more absorption at short wavelengths, and if the scale height becomes large enough to obscure the central protostar, scattered emission becomes visible (Figure 3.8). These effects are similar to those produced by higher values of disk mass. However, the effects on the longer-wavelength emission differ; higher values of h_0 increase the far-IR

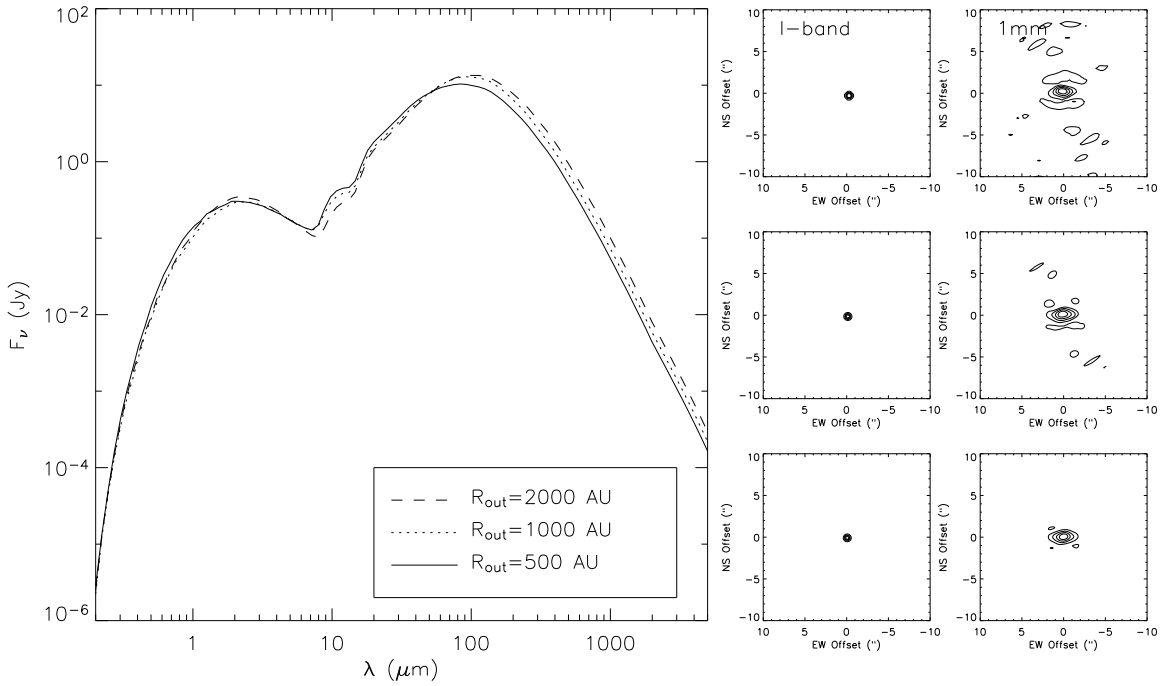

Figure 3.9 SEDs, scattered light images, and millimeter continuum images for a flared disk model with a range of outer radii. The panels are labeled as in Figure 3.3. This model assumes $M_{\rm disk} = 5 \times 10^{-2}$ M$_\odot$, $h_0 = 15$ AU, and $i = 60°$. Since we have fixed the disk mass, different values of $R_{\rm out}$ do not significantly affect the opacity of the model. However, a larger outer radius produces a larger surface area of cool dust, which leads to a slight enhancement of the long-wavelength flux. Moreover, larger $R_{\rm out}$ will produce larger images in both scattered light and millimeter emission (the short-wavelength images shown here are dominated by light from the central protostar, and thus no scattered emission is visible).

flux, but have little effect on fluxes or image morphologies at millimeter wavelengths.

Changing $R_{\rm out}$ does not significantly affect the SEDs, as long as the disk mass is held fixed (Figure 3.9). This is because the optical depth of the model is not affected substantially by $R_{\rm out}$. However, larger outer radii will produce larger images in both scattered light and millimeter emission, since disk material will be distributed to larger radii.

Disk viewing angle is a crucial property in modeling the SEDs and scattered light images (e.g., D'Alessio et al. 1999; Whitney & Hartmann 1992). More edge-on models exhibit deeper absorption at mid-IR wavelengths, and higher extinction of the central star (Figure 3.10). For moderate inclinations ($i \lesssim 55°$), the central star is visible,

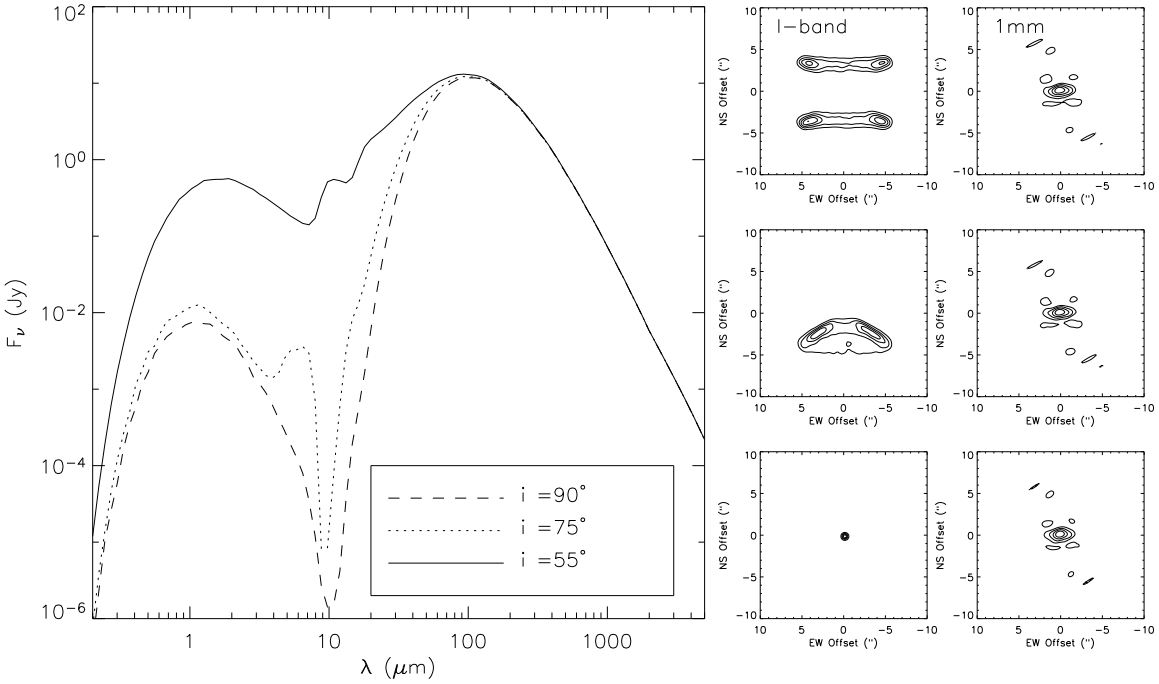

Figure 3.10 SEDs, scattered light images, and millimeter continuum images for a flared disk model at a range of viewing angles. The panels are labeled as in Figure 3.3. This model assumes $M_{\rm disk} = 5 \times 10^{-2}$ M$_\odot$, $h_0 = 15$ AU, and $R_{\rm out} = 1000$ AU. The effects of inclination on disk models are similar to those shown for envelope models in Figure 3.6. More edge-on models exhibit deeper absorption at mid-IR wavelengths, and higher extinction of the central star. For moderate inclinations ($i \lesssim 55°$), the central star is visible, and dominates the I-band emission. For large inclinations, an asymmetric scattered light structure is observed, while for nearly edge-on orientations, a symmetric, double-lobed structure is observed. The millimeter emission becomes more extended in appearance as inclination increases, although this is a minor effect.

and dominates the I-band emission, while for larger inclinations, the protostar is obscured and an asymmetric scattered light structure is observed. For nearly edge-on orientations, a symmetric, structure is observed, corresponding to the top and bottom surfaces of the flared disk.

3.3.3 Envelope+Disk

In addition to pure envelopes and pure disks, we consider a model incorporating both an envelope and an embedded disk. The main difference between this model and the pure envelope model is an enhanced density in the midplane, especially interior

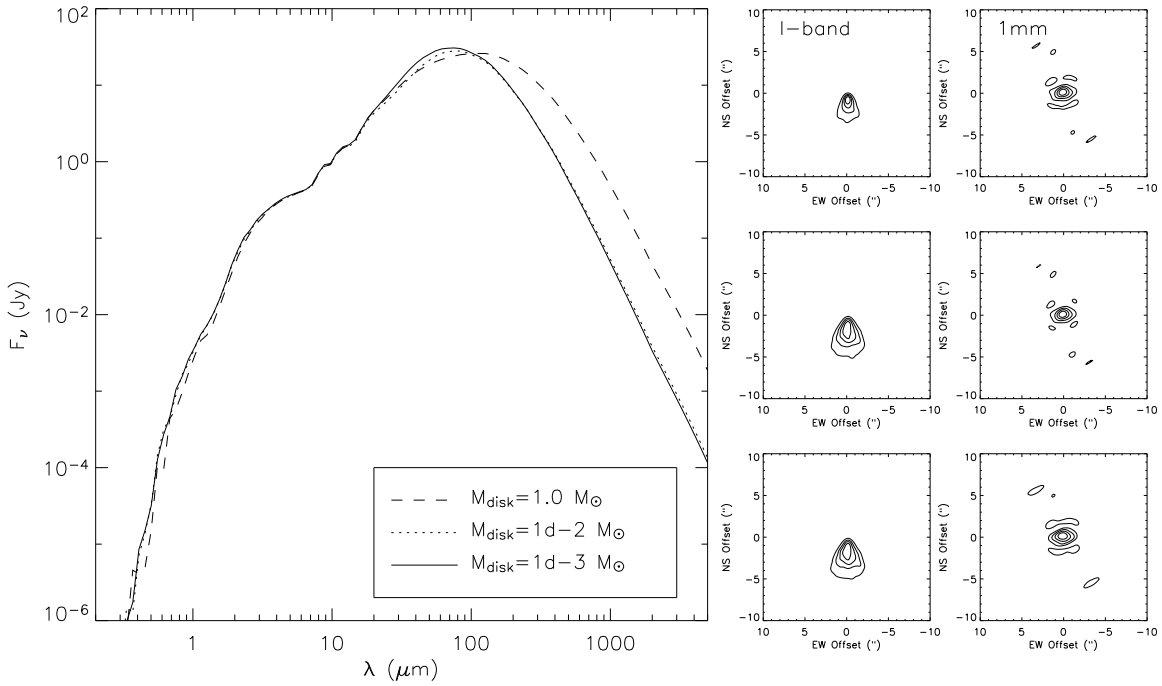

Figure 3.11 SEDs for envelope+disk models for a range of disk masses. The inclination of the models has been fixed at 45°. The envelope component of the model has the following properties: $\dot{M} = 3 \times 10^{-6}$ $M_\odot$ yr^{-1}, $M_* = 0.5$ $M_\odot$, $R_c = 100$ AU, and $R_{out} = 1000$ AU. The various models illustrate the effect of adding progressively more massive (plotted bottom to top) disks to the model: $M_{disk} = 10^{-3}$, 10^{-2}, and 1.0 $M_\odot$. The main effect of the disk is on the SED long-ward of 100 μm, where the dense, cool dust in the disk component adds substantial flux. The 0.9 μm and 1 mm images are also affected slightly, becoming more centrally concentrated for larger disk masses.

to the centrifugal radius. As a result of this enhanced midplane density, more long-wavelength emission is produced than for a pure envelope model. Since the amount of long-wavelength emission for a pure envelope model depends primarily on the mass infall rate, $\dot{M}$, additional long-wavelength emission from the disk component may allow good fits to the data with lower inferred values of $\dot{M}$. The effect of the disk component on the SED is illustrated in Figure 3.11.

In addition to larger fluxes, inclusion of a disk component also leads to more centrally concentrated modeled scattered light and millimeter images. With our marginally resolved millimeter images, we can not probe such density concentrations directly. However, as we discuss further below, comparison of our interferometrically measured fluxes, which trace compact emission, with lower-resolution measurements

(e.g., Motte & André 2001; Young et al. 2003) can provide some constraint on the relative amounts of compact and large-scale material, providing an additional test of how well these models fit the data.

The envelope+disk model is implemented by computing the density distributions for both a disk and an envelope, and then setting the density of the combined model to be the greater of the two individual densities for a given position, (r, θ). The temperature distribution, spectral energy distribution, and images are then calculated self-consistently for the combined model using MC3D. In our current implementation of the disk+envelope density distribution, the outer radius of the disk cannot be specified independently of the outer radius of the envelope. Thus, our models may not truly represent a physical disk+envelope model, where one might expect the disk component to end at R_c. These models thus should be regarded as only qualitative indicators that both disk and envelope components are needed to match the data.

3.3.4 Disk+Extinction Model

Finally, we consider a model incorporating a flared disk density distribution plus foreground extinction. We consider values of $A_{\rm V}$ ranging from 0 to 60 mag, which allows foreground extinctions much higher than expected from ambient material in the Taurus region (e.g., Kenyon & Hartmann 1995). Extinctions higher than $A_{\rm V} \sim 5$ probably arise in some sort of envelope material surrounding the sources. Sub-millimeter fluxes observed in large-beam SCUBA maps (Young et al. 2003) can be used to estimate column densities, and thus extinctions toward our sample of Class I objects: extinctions larger than ~ 5 mag are only possible if the material is distributed primarily on scales smaller than ~ 5000 AU, on the order of expected envelope sizes. The disk+extinction model thus provides an alternative, and more simplistic way to represent a density distribution including both a disk and a more extended envelope structure.

The main difference between this model and the disk+envelope model in §3.3.3 is that we assume the envelope material to be uniformly distributed, whereas the

disk+envelope model assumes a centrally-condensed envelope as described by Equation 3.2. In the disk+extinction model, the morphology of scattered light and millimeter continuum images are unaffected by the uniformly-distributed obscuring envelope material. This model thus provides a way to produce disk-like images at the same time as heavily reddened SEDs.

3.4 Results

For each of the density distributions described in §3.3, we determine the model providing the best-fit to our combined SED+imaging dataset. The properties of the best-fit models, as well as the residuals between models and data, are listed in Table 3.2, and the models are plotted in Figures 3.12–3.16. Our results clearly indicate that pure disk models are not applicable for Class I sources. Rather, the data suggest models incorporating a massive envelope with an outflow cavity, although most sources are fitted best by models including *both* envelopes *and* disks. In this section, we discuss general results of our SED and image fitting, then describe results for individual sources in detail in §3.4.1.

While the observed SEDs for our sample show fairly shallow absorption at mid-IR wavelengths (Figures 3.12–3.16), edge-on disk models produce deep mid-IR absorption (Figure 3.10; see also D'Alessio et al. 1999; Wood et al. 2002; Wolf et al. 2003), In addition, our asymmetric scattered light images rule out disk models close to edge-on, since such models would produce symmetric structures (Figure 3.10). However, the extended scattered light images indicate that disk models viewed close to face-on are not applicable either, since such models would be dominated by emission from the point-like central protostar. Since we observe spatially resolved, asymmetric scattered light toward our sample objects, we know that we are not directly observing the star, as would be the case for face-on or moderately inclined disk models.

While there may be a narrow range of inclinations for which pure disk models can fit both the SEDs and scattered light images of some of our sources, substantial foreground extinction ($\gtrsim$ 20 mag) is needed to make such a model consistent with the

small optical/near-IR fluxes for our sample. As indicated by Table 3.2 and Figures 3.12–3.16, disk+extinction models provide far superior fits than pure disk models with $A_V = 0$. However, the extinction values for the best-fit disk+extinction models are all much larger than expected from ambient material in the Taurus cloud (e.g., Kenyon & Hartmann 1995), indicating a large concentration of mass near these Class I sources. Thus, these models imply the existence of massive envelopes in addition to disk components. Moreover, we note that these disk+extinction models still do not provide good fits for all objects.

Pure envelope models also fail to fit the data well for most targets in our sample (Table 3.2). As illustrated in Figures 3.12–3.16, pure envelope models typically over-predict the peak flux in the SED. As discussed further below, pure envelopes also predict more extended millimeter emission than actually observed. Thus, pure envelope density distributions also do not seem suitable for explaining most features of the data for our sample.

For most, if not all, of the objects in our sample, the best fitting models (i.e., those for which the residuals between model and data are minimized) incorporate both an envelope and a disk (Table 3.2). However, while SEDs and 1 mm images are fitted best by disk+envelope models, the scattered light images for some sources seem to favor pure disk or pure envelope models. This may suggest that our disk+envelope model is too simplistic, and that a more complex implementation of a disk+envelope model would allow all of the data to be fitted simultaneously. One piece of evidence in support of this hypothesis is the fact that the best-fit pure disk or envelope models, which usually fit the scattered light images well, generally have larger values of $R_{\rm out}$ than the best-fit disk+envelope models (Table 3.2). This suggests a flattened distribution of small dust grains that extends beyond the outer radius of our best-fit disk+envelope models. We discuss this issue further in §3.5.1.

Table 3.2. Best-fit Models

Source	$X^2_{\rm all}$	$X^2_{\rm sed}$ ([log Jy]^2)	$X^2_{0.9\mu{\rm m}}$ (Jy^2)	$X^2_{1{\rm mm}}$ (Jy^2)	$\dot{M}$ (M$_\odot$ yr^{-1})	$R_{\rm c}$ (AU)	$M_{\rm env}$ (M$_\odot$)	$M_{\rm disk}$ (M$_\odot$)	h_0 (AU)	$R_{\rm out}$ (AU)	i (°)	$L_{\rm central}$ (L$_\odot$)
Rotating Infalling Envelope Models												
IRAS 04016+2610	103.5	7.09	29.05	67.43	8×10^{-6}	100	0.07	...	...	2000	36	3.8
IRAS 04108+2803B	149.6	7.03	99.62	42.98	6×10^{-6}	30	0.05	...	...	2000	26	0.7
IRAS 04239+2436	341.3	7.40	307.8	26.03	8×10^{-6}	100	0.07	...	...	2000	42	2.3
IRAS 04295+2251	59.40	12.37	6.19	40.84	9×10^{-6}	100	0.01	...	...	500	34	1.1
IRAS 04381+2540	269.4	4.19	186.8	78.46	1×10^{-5}	100	0.10	...	...	2000	30	0.6
Flared Disk Models												
IRAS 04016+2610	172.3	43.70	69.39	59.30	...	...	...	0.10	25	2000	51	2.8
IRAS 04108+2803B	180.5	27.22	111.7	41.56	...	...	...	1.00	25	500	44	1.0
IRAS 04239+2436	323.9	17.54	286.4	19.90	...	...	...	0.10	25	2000	57	2.6
IRAS 04295+2251	49.90	13.05	11.51	25.33	...	...	...	1.00	15	1000	55	0.9
IRAS 04381+2540	273.4	16.52	190.4	66.49	...	...	...	0.70	15	2000	56	0.4
Disk+Envelope Models												
IRAS 04016+2610	93.32	5.65	31.18	61.50	6×10^{-6}	100	0.05	0.03	15	2000	36	5.0
IRAS 04108+2803B	144.8	3.87	96.67	44.31	5×10^{-6}	30	5×10^{-3}	0.70	15	500	34	0.9
IRAS 04239+2436	468.5	3.12	443.5	21.80	3×10^{-6}	30	0.01	0.50	15	1000	36	2.1
IRAS 04295+2251	37.57	5.62	6.24	25.72	4×10^{-6}	100	5×10^{-3}	1.00	15	500	36	0.7

Table 3.2 (cont'd)

Source	$X^2_{\rm all}$	$X^2_{\rm sed}$ ([log Jy]^2)	$X^2_{0.9\mu{\rm m}}$ (Jy^2)	$X^2_{1{\rm mm}}$ (Jy^2)	$\dot{M}$ ($M_\odot$ yr^{-1})	$R_{\rm c}$ (AU)	$M_{\rm env}$ ($M_\odot$)	$M_{\rm disk}$ ($M_\odot$)	h_0 (AU)	$R_{\rm out}$ (AU)	i (°)	$L_{\rm central}$ ($L_\odot$)
IRAS 04381+2540	258.2	4.20	188.8	65.16	9×10^{-6}	100	0.01	1.00	15	500	38	0.7
Disk+Extinction Models												
IRAS 04016+2610	160.3	18.61	82.47	59.29	...	...	A_V=15	0.05	25	2000	59	20.9
IRAS 04108+2803B	150.1	3.06	105.1	41.98	...	...	A_V=20	1.00	15	500	55	2.2
IRAS 04239+2436	323.9	5.40	298.7	19.89	...	...	A_V=20	0.10	25	2000	55	12.7
IRAS 04295+2251	44.20	7.35	11.41	25.44	...	...	A_V=25	1.00	15	500	49	6.6
IRAS 04381+2540	266.0	2.40	198.7	64.99	...	...	A_V=20	1.00	15	500	57	2.2

Note. — Best-fit models for different density distributions considered in §3.3. X^2 is the sum of the squared (non-normalized) residuals between the data and model, and $X^2_{\rm all}$ is the sum of this quantity for the SEDs, scattered light images, and millimeter images. In the case of the disk+extinction models, entries in the $M_{\rm env}$ column correspond to foreground extinction. Although the disk masses listed in this Table are the results of our model-fitting, we believe that these are likely over-estimated (§3.5.2).

Table 3.3. Comparison of compact and large-scale millimeter emission

Source	$R_{\rm data}$	$R_{\rm disk}$	$R_{\rm env}$	$R_{\rm disk+env}$
IRAS 04016+2610	0.43	0.17	0.06	0.16
IRAS 04108+2803B	0.70	0.52	0.08	0.52
IRAS 04239+2436	0.19	0.18	0.06	0.26
IRAS 04295+2251	0.42	0.27	0.26	0.39
IRAS 04381+2540	0.05	0.12	0.05	0.33

References. — In this table, $R_{\rm data}$ is the ratio of emission observed in our compact OVRO beam to the emission observed in the larger-beam survey of Motte & André (2001). $R_{\rm disk}$, $R_{\rm env}$, and $R_{\rm disk+env}$ are the ratios one would measure for pure disk, pure envelope, and disk+envelope models. For disk+extinction models (§3.3.4), the distribution of large-scale material is unconstrained, and thus we do not calculate expected ratios for these models.

One way to test the relative contributions of disks and envelopes is to compare the compact millimeter emission observed in our OVRO observations with more extended emission seen in lower-resolution single-dish observations (Motte & André 2001). As illustrated in the case of IRAS 04016+2610 in Figure 3.17, pure disks, pure envelopes, and disks+envelopes produce varying amounts of compact and extended emission, and thus comparison of high- and low-resolution millimeter data can help to distinguish between models. As described in §3.4.1, our interferometric fluxes typically (with one exception) differ by $\sim 20-50\%$ from the single-dish measurements of Motte & André (2001) (Table 3.3), indicating that the sources we are observing produce most of their emission from compact inner regions.

3.4.1 Results for Individual Sources

3.4.1.1 IRAS 04016+2610

IRAS 04016+2610 is an IRAS source (Beichman et al. 1986) lying at the western edge of the L1489 dark cloud (Benson & Myers 1989), and driving a molecular outflow (Myers et al. 1988; Terebey et al. 1989; Moriarty-Schieven et al. 1992). Previous

modeling of this source in terms of an infalling envelope model has found $\dot{M} \sim 5 \times 10^{-6}$ $M_\odot$ yr^{-1}, $R_c \sim 50$ AU, $i \sim 45 - 65°$, and $L_* = 3.72$ $L_\odot$ (Kenyon et al. 1993a; Whitney et al. 1997). An independent estimate of the inclination ($i \sim 60°$) was obtained from observations of a compact molecular outflow (Hogerheijde et al. 1998). Previous observations of scattered light at near-IR wavelengths (Tamura et al. 1991; Whitney et al. 1997; Park & Kenyon 2002; Ishii et al. 2004) show a similar morphology to our I band observations. However, our observations enable for the first time accurate registration of the scattered light to the position of the central source, which allows better constraints on the circumstellar dust distribution than possible in previous analysis.

Our best-fit model for IRAS 04016+2610 incorporates both a rotating, infalling envelope and an embedded disk. This model fits all of our data well, including the 0.9 μm image, 1 mm image, and SED (Figure 3.12). The properties of this model are $\dot{M} = 6 \times 10^{-6}$ $M_\odot$ yr^{-1}, $R_c = 100$ AU, $R_{out} = 2000$ AU, and $M_{disk} = 0.03$ $M_\odot$. The properties of the envelope and disk components are consistent with previous analyses in the context of either model individually (Kenyon et al. 1993a; Whitney et al. 1997; Hogerheijde 2001).

In order to correctly fit the total luminosity of the system, we require a large central luminosity, $L_{central} \approx 5$ $L_\odot$. This is substantially larger than the stellar luminosity inferred from near-IR spectroscopy (Ishii et al. 2004), and suggests a large accretion luminosity. Since the total accretion rate determined from our fitting of disk+envelope models is not substantially higher than for other sources, we suggest that this additional luminosity may be generated in a more active accretion shock near the protostellar surface.

For IRAS 04016+2610, the flux measured in our $\sim 2''$ beam is approximately 40% of the value measured by Motte & André (2001) in an $11''$ beam. This is somewhat larger than the ratios predicted by our best-fit models, and may indicate that there is additional compact emission that we have not accounted for in the models. For example, if the disk is confined to radii smaller than R_c, as opposed to R_{out} as assumed in our models, more mass would be concentrated at smaller radii.

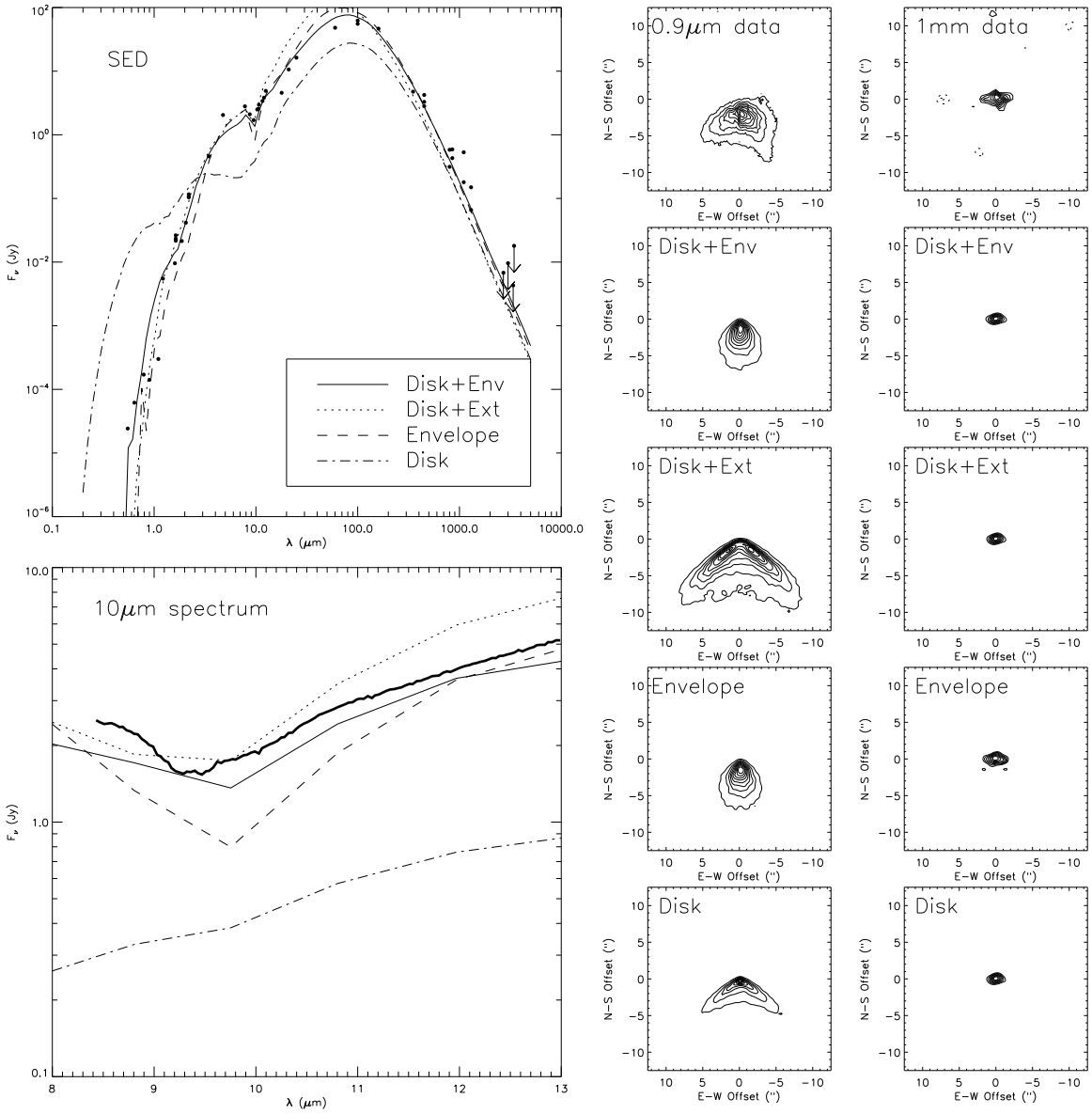

Figure 3.12 SED data (Table 3.1), 10 μm spectrum (Kessler-Silacci et al. 2005), 0.9 μm scattered light image, and 1.3 mm continuum image for IRAS 04016+2610, along with best-fit models for different assumed circumstellar geometries (Table 3.2). The observed images have been rotated on the sky by $-10°$ (east of north) so that they have the same position angle definition as the models. Images have contour levels of 10% of the peak flux, beginning at 10% for the 0.9 μm images and 30% for the 1 mm images. While pure disk models do not provide an adequate match to the data, extincted disks, pure envelopes, and disk+envelopes match reasonably well. The disk+envelope, which provides the smallest residuals between model and data, is preferred.

3.4.1.2 IRAS 04108+2803B

IRAS 04108+2803 is a binary system (e.g., Duchêne et al. 2004) in the L1495 region, and IRAS 04108+2803B is the component that appears less environmentally evolved based on its spectral energy distribution; it emits the vast majority of the far-IR emission from the system. IRAS 04108+2803B also shows large scatter in photometric observations, indicating that it may be a variable star (Kenyon et al. 1993a).

Previous modeling of this object in the context of infalling envelope models found $\dot{M} \sim 5 \times 10^{-6}$ $M_\odot$ yr^{-1}, $R_c \sim 70 - 100$ AU, $i \sim 30 - 60°$, and $L_* = 0.63$ $L_\odot$. (Kenyon et al. 1993a; Whitney et al. 1997). In contrast, Chiang & Goldreich (1999) showed that the SED of this object can be fit well by a flared disk model with $i = 65°$, $\beta = 1.2$, and $R_{out} = 270$ AU. The small fractional polarization (5.1%) relative to other Class I sources ($\sim$ 20%; Whitney et al. 1997) has been invoked as further evidence that the scattered emission from IRAS 04108+2803B arises in a disk rather than in the walls of an outflow cavity (Chiang & Goldreich 1999). Finally, IRAS 04108+2803B has been modeled as a T Tauri star in a disk that is dynamically warped by a hypothetical stellar companion (Terquem & Bertout 1996).

Our results show that the data for this object cannot be fitted by a pure disk model, although the best fit is obtained for a model incorporating a massive disk in addition to an infalling envelope (Table 3.2; Figure 3.13). The best-fit disk+envelope model for this source implies $\dot{M} = 5 \times 10^{-6}$ $M_\odot$ yr^{-1}, $R_c = 30$ AU, R_{out}=500 AU, and $i = 34°$. The central luminosity is close to what one would expect for a T Tauri star, $L_{central} \approx 0.9$ $L_\odot$. The disk mass of our best-fit model is 0.7 $M_\odot$ (Table 3.2); however, as discussed in §3.5.2, this is likely an over-estimate.

The ratio of compact to extended millimeter emission (0.7; Table 3.3) implies that a large fraction of the flux is generated by a compact disk component. Thus, this source appears to be extremely disk-dominated, supporting the hypothesis of Chiang & Goldreich (1999). On the other hand, a massive envelope component also appears necessary to fit the imaging+SED data, consistent with previous models (e.g., Kenyon et al. 1993a) and recent Spitzer observations which attribute 15.2 μm CO_2

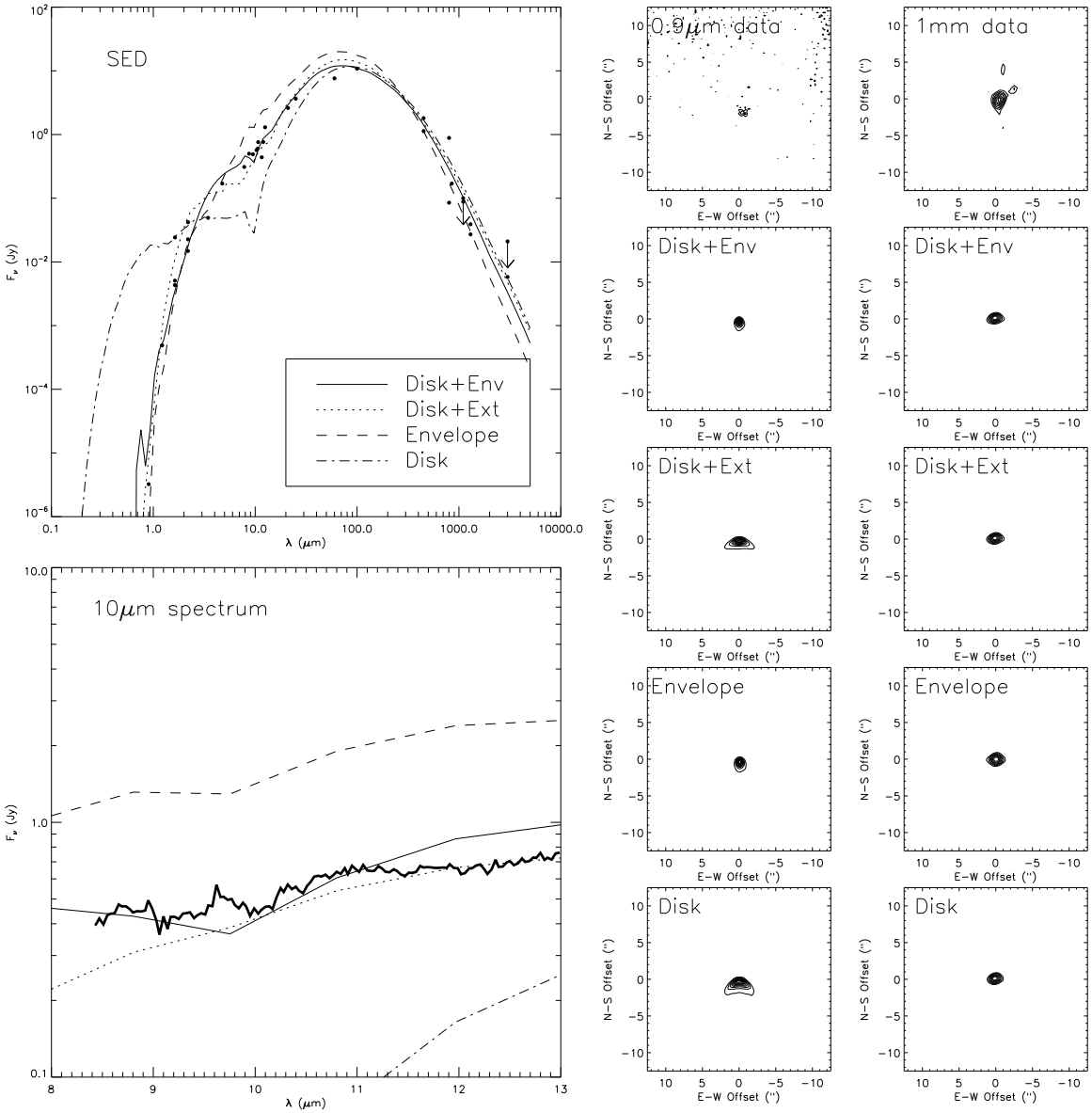

Figure 3.13 SED data (Table 3.1), 10 μm spectrum (Kessler-Silacci et al. 2005), 0.9 μm scattered light image, and 1.3 mm continuum image for IRAS 04108+2803B, along with best-fit models for different assumed circumstellar geometries (Table 3.2). The observed images have been rotated on the sky by $-90°$ (east of north) so that they have the same position angle definition as the models. Images have contour levels of 10% of the peak flux, beginning at 10% for the 0.9 μm images and 30% for the 1 mm images. The disk+envelope model provides the best match to the data for this source.

ice absorption to a cold envelope (Watson et al. 2004).

3.4.1.3 IRAS 04239+2436

IRAS 04239+2436 is an IRAS source (Beichman et al. 1986) with a bright scattered light nebula (Kenyon et al. 1993b), which has been tentatively associated with high-velocity molecular gas (Moriarty-Schieven et al. 1992). Previous modeling of SEDs and near-IR scattered light (separately) in the context of rotating, infalling envelopes, found $\dot{M} \sim 2 - 4 \times 10^{-6}$ $M_\odot$ yr^{-1}, $R_c \sim 10 - 70$ AU, $i = 30 - 55°$, and $L_* = 1.23$ $L_\odot$ (Kenyon et al. 1993a; Whitney et al. 1997).

Although the SED for this source is fit best by a disk+envelope model, the best-fit to our combined imaging+SED dataset is actually obtained for a disk+extinction model with $A_V = 20$ (Table 3.2; Figure 3.14). Thus, while there seem to be both disk and envelope components, the exact density profile of the source may not be matched exactly by either the disk+envelope or disk+extinction models. As we discuss further in §3.5.1, the fact that the disk+envelope model fails to represent accurately our 0.9 μm image may suggest that an additional flattened distribution of small dust grains extending out to $\sim$ 2000 AU (not currently included in the model) is necessary to fit all of the data simultaneously. Assuming that our best-fit disk+envelope model provides an accurate tracer of the mass, the properties of this source are $\dot{M} = 3 \times 10^{-6}$ $M_\odot$ yr^{-1}, $R_c \sim 30$ AU, $R_{out} = 1000$ AU, $M_{disk} = 0.5$ $M_\odot$, $L_{central} = 2.1$ $L_\odot$, and $i = 36°$. However, as discussed in §3.5.2, this value of M_{disk} may be substantially over-estimated.

In addition to our modeling, there are several arguments suggesting that IRAS 04239+2436 is surrounded by both a massive envelope and an embedded disk. The ratio of compact to extended millimeter emission (Table 3.3) shows that a pure envelope model cannot fit the data, and thus there must be a compact disk component. On the other hand, recent Spitzer observations find a deep 15.2 μm CO_2 ice absorption feature, which likely arises in a large, cold envelope (Watson et al. 2004). These arguments provide further support for a combined disk+envelope distribution of material around this source, and motivate future modeling that can fit all of the data

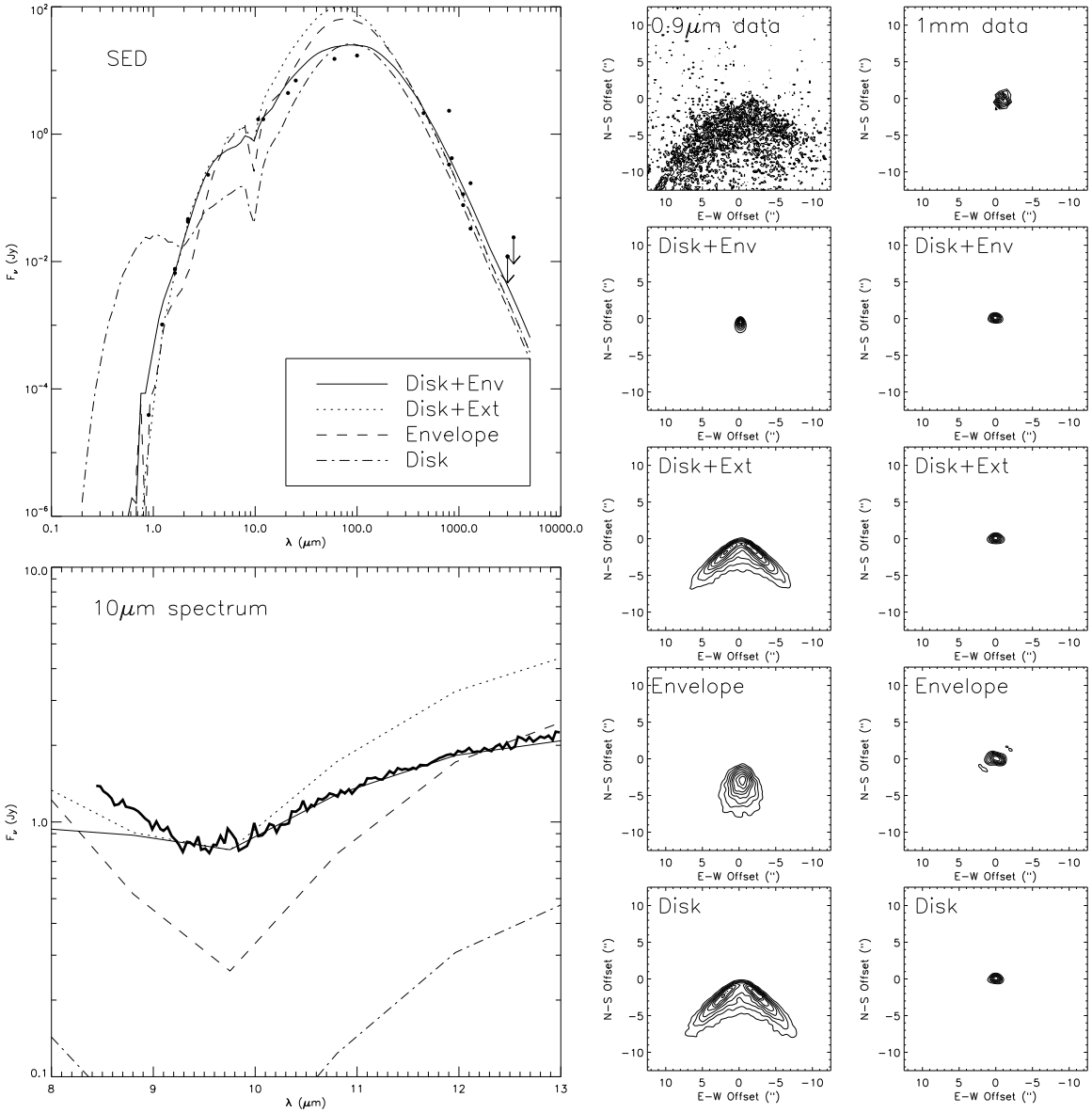

Figure 3.14 SED data (Table 3.1), 10 μm spectrum (Kessler-Silacci et al. 2005), 0.9 μm scattered light image, and 1.3 mm continuum image for IRAS 04239+2436, along with best-fit models for different assumed circumstellar geometries (Table 3.2). The observed images have been rotated on the sky by $-120°$ (east of north) so that they have the same position angle definition as the models. Images have contour levels of 10% of the peak flux, beginning at 20% for the 0.9 μm images and 30% for the 1 mm images. For this object, the best-fit to the complete data set is obtained for disk+extinction and pure disk models, although the SED and 10 μm spectra are fitted best by the disk+envelope model.

simultaneously.

3.4.1.4 IRAS 04295+2251

IRAS 04295+2251 has appeared point-like in previous near-IR imaging observations (e.g., Park & Kenyon 2002), and is tentatively associated with a molecular outflow (Moriarty-Schieven et al. 1992). Previous investigators have analyzed SEDs and scattered light images (separately) in the context of infalling envelope models, and found $\dot{M} = 1-5\times10^{-6}$ $M_\odot$ yr^{-1}, $R_c = 70-100$ AU, $i = 0-30°$, and $L_* = 0.44$ $L_\odot$ (Kenyon et al. 1993a; Whitney et al. 1997). It has also been suggested that a pure disk model may be able to fit the SED for this source (Chiang & Goldreich 1999).

Our modeling shows that the best-fit is obtained for a density distribution including both envelope and disk components (Table 3.2; Figure 3.15). The properties of the best-fit model are $\dot{M} = 4 \times 10^{-6}$ $M_\odot$ yr^{-1}, $R_c \sim 100$ AU, $R_{out} = 500$ AU, $M_{disk} = 1.0$ $M_\odot$, and $i = 30°$. As for other sources in our sample, this value of M_{disk} is probably too high (§3.5.2). The central luminosity in the model is 0.73 $L_\odot$. The ratio of compact to extended millimeter emission observed for IRAS 04295+2251 (0.42; Table 3.3) is consistent with that predicted for the best-fit disk+envelope model, and implies a relatively disk-dominated density distribution.

3.4.1.5 IRAS 04381+2540

IRAS 04381+2540 is in the B14 region, and is associated with high-velocity molecular gas (Terebey et al. 1989). In addition, extended near-IR emission has been observed toward this object (Tamura et al. 1991). Previous modeling in the context of a rotating, infalling envelope found $\dot{M} = 5 - 13 \times 10^{-6}$ $M_\odot$ yr^{-1}, $R_c = 50 - 300$ AU, $i = 30-75°$, and $L_* = 0.66$ $L_\odot$ (Kenyon et al. 1993a; Whitney et al. 1997). Moreover, the inclination was estimated independently from observations of a compact molecular outflow to be $\sim 40 - 70°$ (Chandler et al. 1996).

Our modeling shows that the best fit is obtained for a density distribution incorporating both an envelope and a disk (Table 3.2; Figure 3.16). The best-fit properties are $\dot{M} = 9\times10^{-6}$ $M_\odot$ yr^{-1}, $R_c = 100$ AU, $M_{disk} = 1.0$ $M_\odot$, $i = 30°$, and $L_{central} = 0.73$

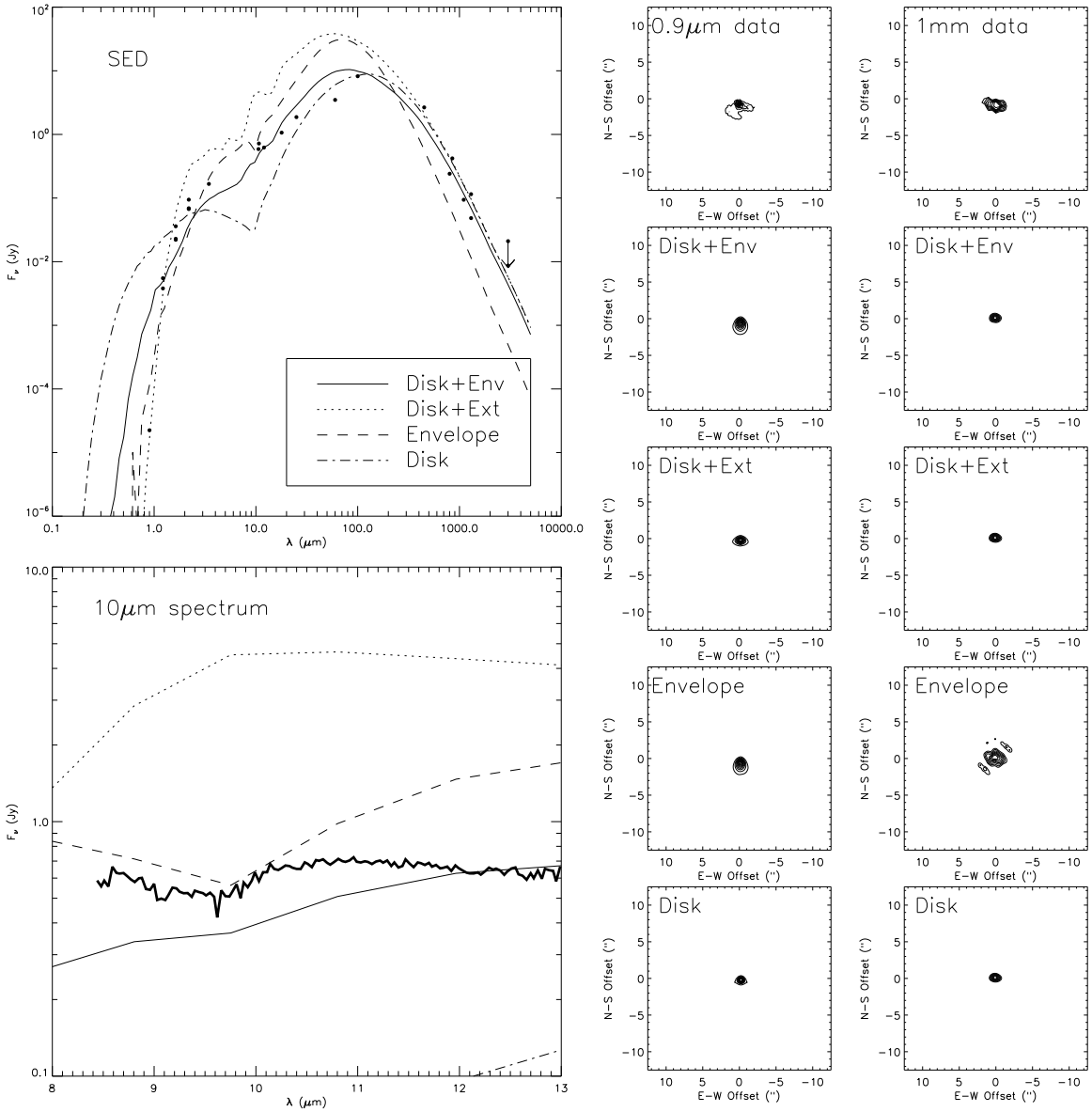

Figure 3.15 SED data (Table 3.1), 10 μm spectrum (Kessler-Silacci et al. 2005), 0.9 μm scattered light image, and 1.3 mm continuum image for IRAS 04295+2251, along with best-fit models for different assumed circumstellar geometries (Table 3.2). The observed images have been rotated on the sky by 155° (east of north) so that they have the same position angle definition as the models. Images have contour levels of 10% of the peak flux, beginning at 10% for the 0.9 μm images and 30% for the 1 mm images. Only the disk+envelope model provides a good match to the data for this source.

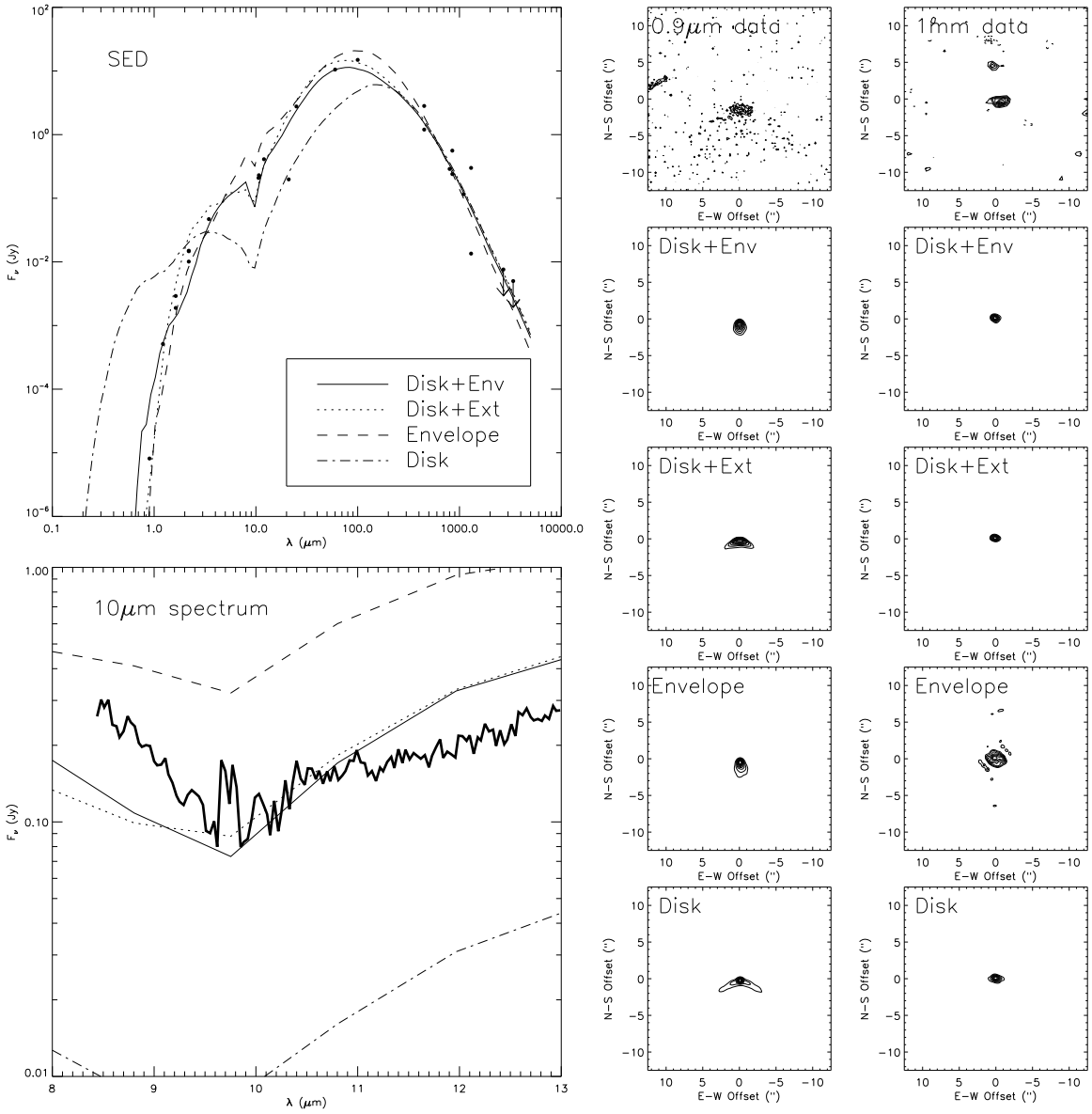

Figure 3.16 SED data (Table 3.1), 10 μm spectrum (Kessler-Silacci et al. 2005), 0.9 μm scattered light image, and 1.3 mm continuum image for IRAS 04381+2540, along with best-fit models for different assumed circumstellar geometries (Table 3.2). The observed images have been rotated on the sky by 180° (east of north) so that they have the same position angle definition as the models. Images have contour levels of 10% of the peak flux, beginning at 20% for the 0.9 μm images and 30% for the 1 mm images. While pure disk models and pure envelope models do not provide an adequate match to the data, extincted disks and disk+envelopes do. The disk+envelope model provides the smallest residuals between model and data (Table 3.2), although this figure demonstrates that the disk+extinction model also provides a good fit to the combined SED+imaging dataset for this object.

$L_\odot$. However, the disk+extinction model also provides a good fit, and may provide a more accurate representation of the 0.9 μm scattered light image. These results indicate that the circumstellar dust distribution around IRAS 04381+2540 is dominated by a disk, although a massive envelope is also required to fit the data. However, the values of $M_{\rm disk}$ in Table 3.2 are probably over-estimated (§3.5.2) and the disk mass may be closer to ~ 0.2 $M_\odot$ for this object.

A potential problem with the best-fit disk+envelope model is that it does not correctly reproduce the observed ratio of compact to extended millimeter flux (Table 3.3). Rather, this ratio indicates that the density distribution for this source is envelope-dominated. This may indicate that there is envelope material distributed uniformly over large spatial scales, leading to large amounts of extended flux being resolved out in our OVRO image. This is consistent with an extended structure extending to large radii from the central source ($\gtrsim$ 3000 AU) observed by Young et al. (2003), and may favor the disk+extinction model, which allows a large mass of dust to be distributed out to larger radii. Regardless of the exact density distribution, it seems that both disk and envelope components are necessary to fit the data for this source.

The high derived accretion rate for IRAS 04381+2540, as well as the strong indication from Table 3.3 that the source is envelope-dominated, suggest that this object may be evolutionarily younger than other sources in our sample. Moreover, the mass accretion rate may be underestimated for this source: the mass of this object has been estimated dynamically from millimeter spectral line observations to be $\sim 0.2-0.4$ $M_\odot$ (Brown & Chandler 1999), somewhat lower than our assumed value of 0.5 $M_\odot$, which implies that the value of $\dot{M}$ derived above may be underestimated by $\sim 10-30\%$ (Equation 3.2).

3.5 Discussion

In §3.4, we fit our combined imaging+SED data for a sample of Class I sources with several models for the circumstellar dust distribution: flared disks, collaps-

ing envelopes, and combinations of disks and envelopes. Of the models considered, disk+envelope density distributions generally provided the smallest residuals between model and data (Table 3.2). The properties of best-fit models are similar for the five sources in our sample, and for most parameters the spread in best-fit values is less than an order of magnitude. These tightly-clustered values are not surprising given the similarity of the observational data for our targets, and the selection criteria for our sample (§3.2.1; Figures 3.12-3.16). However, these similar parameter values may also be due in part to finite parameter sampling and limitations in our models.

In this section, we discuss potential modifications to our disk+envelope model that may be required to provide better fits to combined imaging+SED data, and examine the physical plausibility of derived model parameters. We also use our results to understand better the evolutionary stage of Class I sources, and to place them in context relative to the better-studied Class II objects. Finally, we discuss how new astronomical instruments will improve constraints on the circumstellar dust distributions for Class I objects.

3.5.1 Large-Scale Geometry

While previous investigations of Class I sources argued for either pure envelope or pure disk models (e.g., Kenyon et al. 1993a; Whitney et al. 1997; Chiang & Goldreich 1999), our results based on simultaneous modeling of scattered light images, thermal images, and SEDs (§3.4) indicate that the most suitable dust distributions likely incorporate massive envelopes *and* massive embedded disks. Given the large envelope centrifugal radii determined for our sample, the fact that massive disk components are also required is not surprising. In models of rotating infalling envelopes, the centrifugal radius demarcates the point at which infalling material piles up due to conservation of angular momentum (e.g., Terebey et al. 1984; Kenyon et al. 1993a). Because the centrifugal radius grows with time as the collapsing cloud rotates faster ($R_c \propto t^3$; e.g., Hartmann 1998), material should have previously piled up within the current value of R_c, creating a dense disk. Moreover, viscous spreading tends to

smear out the material piled up at R_c into a more disk-like distribution. Since this material is not accounted for in the envelope density distribution (Equation 3.2), it is not surprising that the addition of a disk component improves the agreement between model and data.

Although disk+envelope models generally yield the best fits to our combined SED+imaging dataset (Table 3.2), the scattered light images for some sources are fit better by pure disk models with large ($\sim$ 2000 AU) outer radii. Since scattered light traces tenuous material, potentially at large radii, our 0.9 μm images may contain contributions from different dust distributions than the disk+envelope components traced by SEDs or millimeter images. Thus, the fact that disk+envelope models provide the best-fits to the SEDs and 1 mm images may suggest that this model provides an accurate representation of most of the mass, while the scattered light images may trace a flattened distribution of tenuous material at larger radii. Since our model assigns a single value of R_{out} for both the envelope and disk components, we cannot test this possibility directly. Moreover, our model assumes that the dust grain properties are the same everywhere. If one takes into account the effects of dust settling (e.g., Goldreich & Ward 1973), then the grains in the disk surface layer and outer envelope may be smaller than those in the dense midplane, allowing more scattering for a given mass of dust (e.g., Wolf et al. 2003; Whitney et al. 2003a).

The large polarizations observed toward Class I sources in near-IR polarimetric imaging observations support the notion of extended distributions of small dust grains (Whitney et al. 1997; Lucas & Roche 1998). At the edges of near-IR scattered light nebulosity observed for our sample, where most of the light is single-scattered at approximately 90°, linear polarizations are 70-80% (Whitney et al. 1997). In contrast, the maximum polarizations predicted[3] by our disk+envelope I-band model images are $\sim$ 25%. Moreover, the integrated polarizations in our model images are substantially lower than the integrated near-IR polarizations measured by Whitney et al. (1997), re-enforcing our hypothesis that there may be a population of small grains at large

[3]The MC3D code has the capability of computing scattered light images in different Stokes parameters, allowing recovery of polarimetric information (Wolf 2003).

radii not included in our models.

Since our best-fit models indicate that Class I sources are surrounded by envelopes with outflow cavities (in addition to disks), we expect observed outflows from these objects to lie in the middle of these cavities. For IRAS 04016+2610, IRAS 04239+2436, and IRAS 04381+2540, outflows have been observed at position angles of 165°, $45 - 60°$, and 10°, respectively (Hogerheijde et al. 1998; Gomez et al. 1997; Saito et al. 2001). Comparison of these position angles with Figure 3.2 demonstrates that the outflows lie in the middle of the observed scattered light structures. For IRAS 04295+2251 and IRAS 04108+2803B, no geometrical information about molecular outflows is available. Thus, in all cases where outflow geometries can be derived, they are consistent with expectations from our modeling.

The range of inclinations for best-fit models is very small, typically $5 - 10°$ for a given model. This may be explained to some extent by selection effects: bright scattered light can only be observed if targets are inclined sufficiently to block the light from the central star. Moreover, scattered light is somewhat brighter for moderate than for edge-on inclinations, which may bias our sample against edge-on sources as well. Nevertheless, the extremely tight clustering of inclinations, especially for the disk+envelope models (Table 3.2), is probably due in some part to limitations of our models in accurately representing the true density distributions. For example, for the disk+envelope model the assumed disk density profile may favor small inclinations for which the observer's line of sight passes through the flared surface of the disk rather than the dense midplane, while inclinations $\gtrsim 30°$, for which the line of sight does not pierce directly down the outflow cavity, are required to reproduce the extended scattered light structures and heavily reddened SEDs. Observations of larger samples and refinements to the models are necessary to provide a more reliable estimate of the inclination distribution of Class I sources.

3.5.2 Disk and Envelope Masses

As seen in Table 3.2, the masses of best-fit disk models, and the masses of the disk components of disk+envelope models, span a range of values from $\sim$ 0.01 to 1.0 $M_\odot$. These high disk masses result naturally from the high optical depths of these models. For pure disk models, large masses are required to extinct the central star (thus allowing scattered light to be observed) and to produce the observed millimeter emission (Figure 3.7). Moreover, the high optical depths that result from large disk masses lead to large amounts of cold dust in the midplane, which emits most of its radiation at millimeter wavelengths. For disk+envelope models, large disk masses enable enhanced millimeter emission without substantially altering the peak flux at shorter wavelengths. Moreover, substantial disk components lead to more centrally-concentrated millimeter emission, consistent with observations (Figure 3.17; Table 3.3).

Disk masses larger than $\sim$ 0.1 $M_\odot$ may be unphysical, since they are gravitationally unstable (e.g., Laughlin & Bodenheimer 1994). Specifically, when the mass of a rotating disk is larger than approximately $M_* H/R$ (where H/R is the disk aspect ratio), the disk becomes gravitationally unstable and rapidly transfers angular momentum outward, resulting in rapid accretion of material onto the central protostar. This accretion process occurs on the order of the outer disk dynamical timescale ($\sim 10^3 - 10^4$ yr), and is thus very fast compared to the inferred infall rate and should rapidly bring the disk mass down to a stable level. For our best-fit disk models, $H/R \sim 1/10$, and for a 0.5 $M_\odot$ star the stability criterion requires $M_{\rm disk} \lesssim 0.05$ $M_\odot$. While numerical simulations suggest that disks may remain stable with slightly higher masses, $\sim 0.3 M_* \approx 0.15$ $M_\odot$ (e.g., Laughlin & Bodenheimer 1994; Yorke et al. 1995), our models still require disk masses far in excess of this value.

One implication of these un-physically-large disk masses is that rotating disk models seem untenable for modeling the imaging and SED data for Class I sources. Our massive, best-fit disk models may therefore resemble the magnetically-supported "pseudo-disks" proposed to occur during the early stages of protostellar collapse (Galli

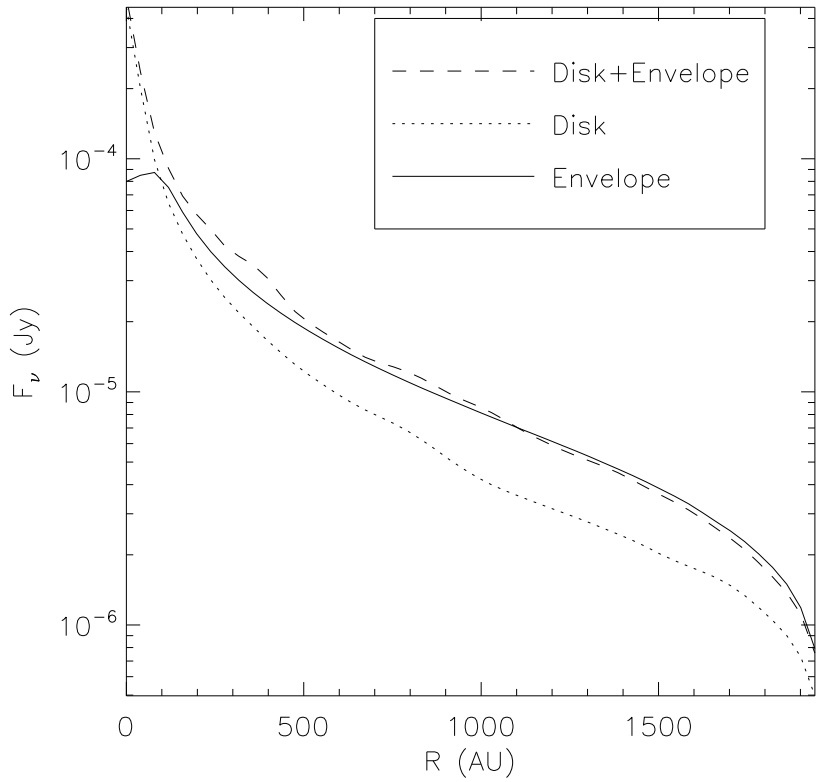

Figure 3.17 Azimuthally-averaged radial profile of millimeter emission of best-fit models for IRAS 04016+2610 (Table 3.2). The pure envelope model (solid line) produces most of its millimeter emission near the centrifugal radius, 100 AU in this case. The pure disk model (dotted line) is more centrally-peaked, producing the majority of the millimeter emission at small radii. The disk+envelope model resembles the pure disk at small radii and the pure envelope at large radii.

& Shu 1993a,b). However, our modeling shows that pure disk models (even with such high masses) cannot fit the data as well as models incorporating massive envelopes (§3.4; Table 3.2).

These large disk masses are also a concern for the best-fit disk+envelope models, where disk components are necessary to fit the SEDs well (Figures 3.12-3.16), and to provide the correct ratios of compact to extended millimeter emission (Table 3.3). As illustrated in Figure 3.17, the most important contribution of the disk component occurs within the envelope's centrifugal radius, while outside of R_c, the millimeter emission from a disk+envelope model has a similar profile to the emission from a pure envelope. If the disk component is truncated at R_c (as opposed to R_{out}, as implemented in our radiative transfer code), the disk mass can be decreased by a

factor of ~ 5, while the compact disk emission within R_c will still produce ratios of compact to extended millimeter emission consistent with observations. In order to produce the correct total millimeter flux, the envelope mass must be increased to compensate for the loss of emission from larger disk radii. As indicated by Figure 3.17, these outer disk regions contribute approximately 50% of the millimeter flux at radii $\gtrsim R_c$. By truncating the disk component of disk+envelope models at R_c, the disk masses listed in Table 3.2 may be decreased by a factor of ~ 5, while the envelope masses may increase by factors of ~ 2. Thus, true masses of the disk components for disk+envelope models may be $\lesssim 0.2$ $M_\odot$, close to the limit of gravitational stability and therefore more physically plausible than the values listed in Table 3.2.

Even for disks truncated at R_c, the disk masses are often larger than the masses of the envelope components of disk+envelope models. Envelope masses range from 5×10^{-3} to 0.05 $M_\odot$, and sources with smaller envelope masses tend to have relatively large disk masses, suggesting that different objects in our sample may be more or less disk-dominated. However, large-scale emission from extended material belies this trend to some extent: for example, while IRAS 04381+2540 appears to be the most disk-dominated source in our sample based on estimated disk and envelope masses, Table 3.3 indicates that there is probably a substantial extended dust component as well. Thus, it is hard to draw conclusions about the relative evolutionary stages of different objects in our sample based on inferred disk and envelope masses.

3.5.3 Evolutionary Stage

An issue closely related to the properties of circumstellar material in Class I sources is their evolutionary stage. While flared disk models are consistent with the SEDs of Class II objects (e.g., Kenyon & Hartmann 1987; Chiang & Goldreich 1999; Dullemond et al. 2001; Eisner et al. 2004; Leinert et al. 2004), we have shown that such models are not suitable for the Class I objects in our sample. Indeed, we have found that models incorporating both envelopes and disks provide a better match to the data. This finding would seem to support the standard assumption that Class I

sources are more embedded, still surrounded by massive envelopes, and potentially younger than Class II sources. On the other hand, spherically symmetric models (e.g., Larson 1969; Shu 1977) are not compatible with our data, indicating that Class I sources are at a stage intermediate to cloud cores and star+disk systems.

However, other investigators have suggested that Class I and II sources may actually be at similar evolutionary stages. One piece of evidence in support of this hypothesis is that the spectroscopically-determined stellar ages of Class I and II sources appear indistinguishable (White & Hillenbrand 2004). It has also been suggested that differences in observed circumstellar properties between the two classes are caused by different viewing angles, rather than different amounts or geometry of circumstellar material (Chiang & Goldreich 1999; White & Hillenbrand 2004). However, our results show that the five Class I objects in our sample are viewed at moderate inclinations ($\sim 30 - 50^{\circ}$), refuting earlier suggestions that optically-visible Class I objects are predominantly viewed edge-on, and arguing that the circumstellar material around Class Is is indeed less evolved than that around Class IIs.

Another argument supporting similar evolutionary states of Class I and II objects is that fact that measured accretion rates, pertaining to the transfer of material from the inner disk onto the central star, appear similar for the two classes (White & Hillenbrand 2004). In contrast, the new data and modeling presented in this paper confirm earlier estimates of mass infall rates from the envelope onto the disk orders of magnitude higher than the derived inner disk accretion rates. The fact that disk and envelope accretion rates are not the same suggests periodic "FU-Ori" episodes where the accretion rate temporarily increases by more than an order of magnitude, likely due to a gravitational instability in the accretion disk (e.g., Bell & Lin 1994; Hartmann & Kenyon 1996, and references therein).

As noted by White & Hillenbrand (2004), the episodic accretion scenario would imply more massive disks in Class I sources relative to Class II objects. While Class I objects appear to be surrounded by larger total masses of dust, the emission on scales smaller than $\sim 12''$ indicates similar masses in the compact disk components (André & Montmerle 1994; Motte & André 2001; White & Hillenbrand 2004). However, the

conversion of millimeter flux into mass depends on the optical depth, dust opacity and temperature; the higher optical depths and cooler dust temperatures in Class I sources may therefore lead to higher masses. Estimated disk masses for our best-fit disk+envelope models (§3.5.2) are larger than typically observed for Class II objects and are close to the values required for gravitational instability, providing support for the non-stationary accretion model.

3.5.4 Further Constraints on the Horizon

We have demonstrated the power of combining spatially-resolved images at multiple wavelengths with broadband spectral energy distributions when modeling the dust distributions around Class I sources. Scattered light images trace the low-density surface layers, mid-IR images trace the hot inner regions near 1-10 AU, and millimeter images trace deeper, cooler layers at larger radii. Because images at these various wavelengths probe different regions of the disk, and even different emission mechanisms, they place tight constraints on the range of circumstellar dust models consistent with the data.

Although our marginally-resolved millimeter images place important constraints on the centrifugal and outer radii (and viewing angle when combined with the position of near-IR scattered light), well-resolved images will provide useful additional information. Perhaps most importantly, well-resolved millimeter emission will allow a direct measurement of the radial intensity profile, and for extremely well-resolved images, the vertical intensity profile. Analyzing these profiles with self-consistent radiative transfer codes like MC3D will allow a determination of the radial and vertical density and temperature profiles, which are assumed quantities in the modeling presented here. Well-resolved millimeter images will also constrain directly the inclination of the system, facilitating constraints on other model properties. Maps of millimeter-wavelength spectral lines can determine kinematics of the circumstellar material and constrain the central mass, in addition to establishing the geometry of the gaseous component (e.g., Hogerheijde 2001). Moreover, analysis of multiple

spectral lines with different excitation conditions can probe directly the density and temperature structure. The enhanced angular resolutions and sensitivities of new and upcoming millimeter interferometers, including the SMA, CARMA, and ALMA, will enable detailed studies of Class I sources.

Spectroscopy from the *Spitzer Space Telescope* will add valuable constraints on dust mineralogy and particle size distribution (e.g., Watson et al. 2004). Moreover, as already illustrated here to some extent, the shape of spectral features can provide a sensitive probe of dust optical depth and source inclination. Since different molecules, ices, and dust species arise in different physical conditions, *Spitzer* observations will also provide powerful constrains on large-scale geometry.

Spitzer can also probe wavelengths of 24 μm, 70 μm, and 160 μm, encompassing the peak of the SEDs for Class I sources. We used the MC3D code to calculate images at these wavelengths for a representative disk+envelope model (see Table 3.2). These images are quite compact, since the emission traces predominantly the warm inner regions within 100 AU of the central protostar. The FWHM angular sizes of the images (at 140 pc) are $\sim 0\farcs3$ to $1\farcs2$, much smaller than the $\sim 6 - 40''$ angular resolution of *Spitzer* at these wavelengths. Even the 1% emission contours are ~ 4 times smaller than the available angular resolution. Thus, the images would likely appear unresolved. However, if the dust properties are substantially different than we have assumed, *Spitzer* may be able to resolve some emission. In recent observations of Vega, 24 μm imaging found the source to be much larger than anticipated based on earlier results, and suggest that there may be a large population of transiently-heated small dust grains at large radii responsible for the extended mid-IR emission (Su et al. 2005). As suggested in §3.5.1, Class I sources may also be surrounded by large-scale distributions of small dust grains; *Spitzer* observations can test this hypothesis.

Finally, important constraints on the circumstellar structure of Class I sources can be established from ground-based mid-IR interferometry. Since 10-20 μm emission is generated at small radii ($\lesssim$ 10 AU), it traces dense material close to the star. We generated 10 and 18 μm images for a typical disk+envelope model, and found that the FWHM of the emission is $\sim$ 30 and 40 mas at these wavelengths, respectively. The

1% contour is larger, 140 and 280 mas at 10 and 18 μm, but at low flux levels ($\lesssim 30$ mJy). Current sparse-aperture interferometry with the Keck telescope can achieve angular resolutions of ~ 100 mas for sources brighter than a few Jy (e.g., Monnier et al. 2004), while future instruments like LBTI should yield additional improvements in resolution and sensitivity. These sources are thus too small and/or faint for the current generation of 10 μm instruments, but may be accessible to future instruments. We also note that different density distributions (e.g., pure envelopes or pure disks) can produce less centrally-peaked emission, which would lead to larger and thus more easily resolved images at mid-IR wavelengths.

3.6 Conclusions

We have imaged a sample of five embedded Class I sources in the Taurus star forming region in 0.9 μm scattered light and thermal 1 mm continuum emission, and we analyzed these data together with spectral energy distributions and 10 μm spectra from the literature. Using the MC3D Monte Carlo radiative transfer code, we generated synthetic images and SEDs for four classes of models: 1) rotating infalling envelopes including outflow cavities; 2) flared disks; 3) disks+envelopes; and 4) disks+extinction. For each class of model, we generated small grids and determined the circumstellar dust distributions providing the best-fits to our data.

The imaging and SED data are generally inconsistent with either pure disk or pure envelope models, and we find that the best fits are usually obtained with models incorporating both massive envelopes and massive embedded disks. Given the large centrifugal radii derived for our sample ($R_{\rm c} = 30-100$ AU), the need for massive disks is not necessarily surprising. While not included in the rotating infalling envelope model, one expects a dense disk of material interior to $R_{\rm c}$ because of the growth of centrifugal radius with time: at earlier times, $R_{\rm c}$ was smaller, and thus material should have gradually piled up at successively larger radii out to the current value of $R_{\rm c}$. Thus, models incorporating both envelopes and disks may be the most accurate (of those considered) for representing physical infalling envelopes.

However, our results indicate that refinements to the models are necessary. For example, disk+envelope models including disk components truncated at R_c may yield disk masses closer to physically plausible values. In addition, our scattered light images point to the existence of extended, tenuous distributions of material, which must be included in the models in order to fit all of the data simultaneously. As more spatially-resolved data is collected, further refinements to the models will likely be warranted.

The overall geometry inferred for our sample of Class I objects in neither spherically-symmetric, as expected for the earliest stages of cloud collapse, nor completely flattened as seen in Class II sources. Thus, our models confirm the picture where Class I sources are at an evolutionary stage intermediate to collapsing cores and fully assembled stars surrounded by disks.

The mass infall rates derived for our sample are between $3 - 9 \times 10^{-6}$ $M_\odot$ yr^{-1}, consistent with previous results. However, these infall rates are more than an order of magnitude higher than accretion rates pertaining to the transfer of material from the disk onto the central star derived from high-resolution spectroscopy. This discrepancy argues for periodic "FU Ori" episodes of increased accretion: since infalling material is not accreted onto the star at the same rate, material piles up in the disk. Once the disk becomes unstable to gravitational instability, the accretion rate rises dramatically for a short period, depleting the disk mass and restoring stability. The "FU Ori" accretion hypothesis is also consistent with the high disk masses of disk+envelope models, which suggest disks near to the limit of gravitational stability.

We have demonstrated the power of modeling broadband SEDs in conjunction with images at multiple wavelengths. In addition, we showed that 10 μm spectra can provide valuable additional constraints on circumstellar geometry, since the depth and shape of spectral features depends on dust optical depth and source inclination. Future observations with upcoming millimeter interferometers, the *Spitzer Space Telescope*, and other instruments will provide additional spatially- and spectrally-resolved information, greatly enhancing constraints on the circumstellar dust around Class I objects.

Acknowledgments. The 0.9 μm images and 10-18 μm photometry presented in this paper were obtained at the W.M. Keck Observatory, which is operated as a scientific partnership among California Institute of Technology, the University of California, and NASA. The Observatory was made possible by the generous financial support of the W.M. Keck Foundation. The authors wish to recognize and acknowledge the cultural role and reverence that the summit of Mauna Kea has always had within the indigenous Hawaiian community. We are most fortunate to have the opportunity to conduct observations from this mountain. This publication makes use of data products from the Two Micron All Sky Survey, which is a joint project of the University of Massachusetts and the Infrared Processing and Analysis Center, funded by the National Aeronautics and Space Administration and the National Science Foundation. 2MASS science data and information services were provided by the Infrared Science Archive at IPAC. The authors wish to thank R. Sari and R. White for stimulating and constructive conversations about this work. J.A.E. acknowledges support from a Michelson Graduate Research Fellowship. J.M.C. acknowledges support from Long Term Space Astrophysics grant NAG5-8217 and the Owens Valley Radio Observatory, which is supported by the National Science Foundation through grant AST 99-81546. S.W. was supported by the German Research Foundation (DFG) through the Emmy Noether grant WO 857/2-1.

3.7 Appendix: LRIS Images of Larger Sample

As discussed in §3.2.1, we obtained 0.9 μm images using Keck/LRIS of the entire sample studied by Kenyon et al. (1993a). The details of these observations are described in §3.2.3. Although the analysis presented above concentrated on only those sources that satisfied our selection criteria (§3.2.1), we display the LRIS images for the larger sample in Figure 3.18 for completeness.

Several of these objects are detected strongly at 0.9 μm: IRAS 04181+2654A, IRAS 04248+2612, IRAS 04263+2436, IRAS 04264+2433AB, IRAS 04287+1802, IRAS 04303+2247, IRAS 04361+2547AB, IRAS 04368+2557, and IRAS 04489+3402.

Four other sources exhibit faint smudges that may correspond to actual emission: IRAS 04169+2702, IRAS 04181+2655, IRAS 04325+2402, and IRAS 04365+2635. The remaining sources were not detected, with a limiting I-band magnitude of ~ 24. Photometry for these objects, measured within a $6\farcs3$ diameter aperture, is listed in White & Hillenbrand (2004).

Because these images are not very deep ($\leq$ 300s), we can not comment on whether the pattern of detections and non-detections corresponds to variations in the underlying protostellar luminosities, different inclinations, or other factors. However, it is clear from Figure 3.18 that there are several sources exhibiting bright scattered light structures; these sources are ideal candidates for future work.

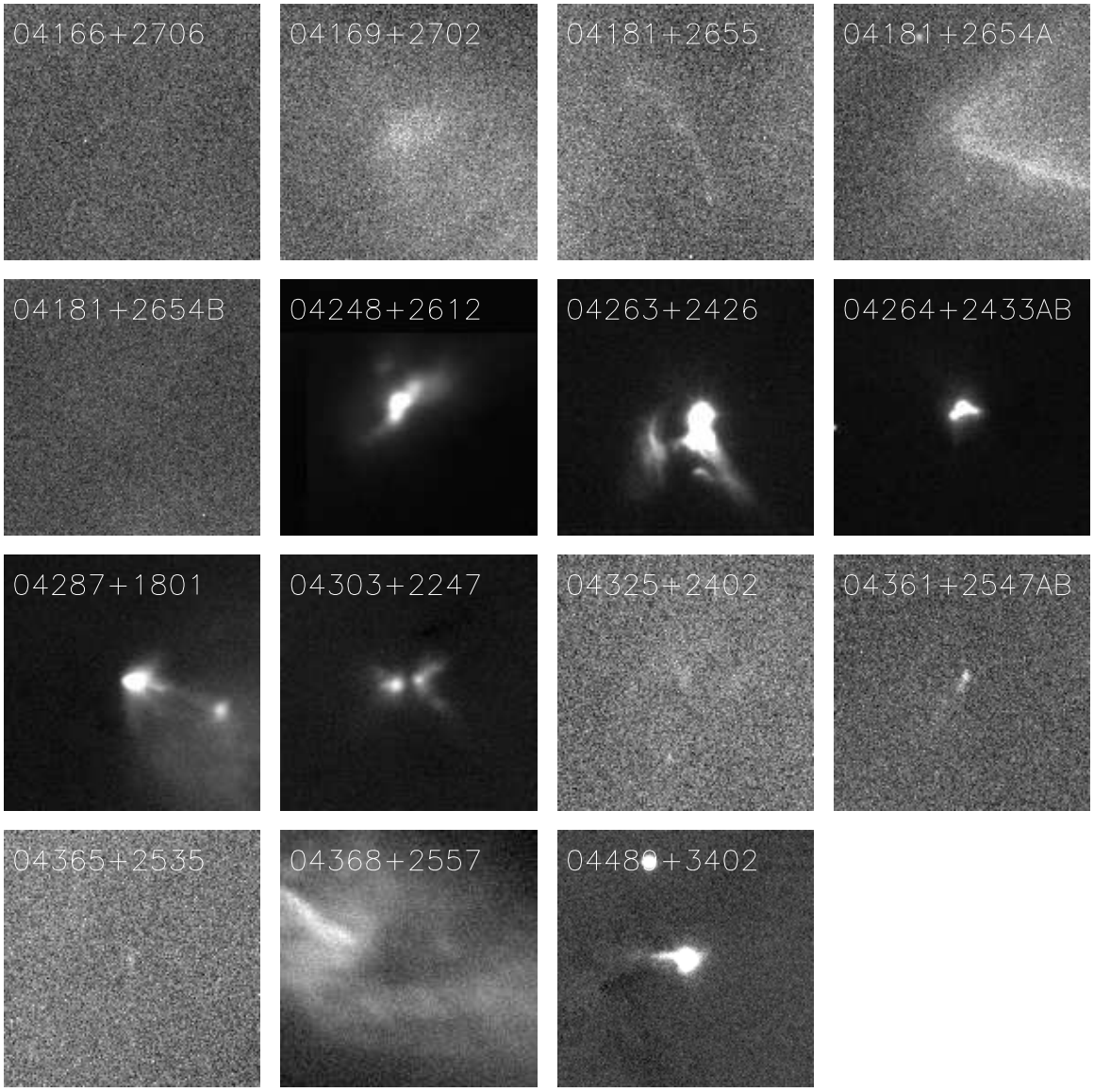

Figure 3.18 Keck/LRIS images of the Class I source sample defined by Kenyon et al. (1993a). Each panel shows a $30'' \times 30''$ area. The LRIS images of the five sources analyzed in this paper are given in Figure 3.2, and those sources we did not analyze are shown here. Some of these objects are not detected in our observations, which may indicate different source luminosities or circumstellar dust geometries.

Chapter 4

Near-Infrared Interferometric Measurements of Herbig AeBe Stars[1]

We have observed the Herbig Ae/Be sources AB Aur, VV Ser, V1685 Cyg (BD+40°4124), AS 442, and MWC 1080 with the Palomar Testbed Interferometer, obtaining the longest baseline near-IR interferometric observations of this class of objects. All of the sources are resolved at 2.2 μm with angular size scales generally $\lesssim 5$ mas, consistent with the only previous near-IR interferometric measurements of Herbig Ae/Be stars by Millan-Gabet and collaborators. We determine the angular size scales and orientations predicted by uniform disk, Gaussian, ring, and accretion disk models. Although it is difficult to distinguish different radial distributions, we are able to place firm constraints on the inclinations of these models, and our measurements are the first that show evidence for significantly inclined morphologies. In addition, the derived angular sizes for the early type Herbig Be stars in our sample, V1685 Cyg and MWC 1080, agree reasonably well with those predicted by the face-on accretion disk models used by Hillenbrand and collaborators to explain observed spectral energy distributions. In contrast, our data for the later-type sources AB Aur, VV Ser, and AS 442 are somewhat inconsistent with these models, and may be explained better through the puffed-up inner disk models of Dullemond and collaborators.

[1]This chapter has been published previously as Eisner et al. (2003).

4.1 Introduction

Herbig Ae/Be (HAEBE; Herbig 1960) stars are intermediate-mass (2–10 $M_\odot$) young stellar objects that show broad emission lines, rapid variability, and excess infrared and millimeter-wavelength emission. These properties are consistent with the presence of hot and cold circumstellar dust and gas. While there is still some debate about the morphology of this circumstellar material, most evidence supports the hypothesis that in many cases the dust and gas lies in a massive (~ 0.01 $M_\odot$) circumstellar disk (Natta, Grinin, & Mannings 2000; Hillenbrand et al. 1992, hereafter HSVK).

The strongest evidence for circumstellar disks around HAEBE stars comes from direct imaging with millimeter interferometry. Flattened structures around several sources have been resolved on $\sim$ 100 AU scales (Mannings & Sargent 1997, 2000; Piétu et al. 2003), and detailed kinematic modeling of one source, MWC 480, shows that the observations are fit well by a rotating Keplerian disk (Mannings et al. 1997). For a spherical distribution, these and other observations (e.g., Mannings 1994) imply extinctions at visible and infra-red wavelengths much higher than actually observed. In addition, in recent Hα spectropolarimetric observations of HAEBE sources (which trace dust on scales of tens of stellar radii), Vink et al. (2003) find signatures of flattened circumstellar structures around 83% of their sample, and evidence for rotation around 9 HAe stars. Furthermore, the forbidden emission lines that arise in winds and outflows around HAEBE sources typically show blue-shifted emission but lack redshifted emission, which suggests that the redshifted component of the outflow is occluded by a circumstellar disk. The broad linewidths of low-velocity features are consistent with this emission arising in rotating circumstellar disk winds (Corcoran & Ray 1997).

The distribution of circumstellar material around HAEBEs can also be inferred from modeling of spectral energy distributions (SEDs). Three distinct morphologies were identified in this way by HSVK, who classified observed HAEBE sources into three groups, I, II, and III. All sources in our observed sample fall into Group I, which has SEDs of the form $\lambda F_\lambda \propto \lambda^{4/3}$. These can be modeled well by flat, irradiated,

accretion disks with inner holes on the order of $\sim$ 10 stellar radii. Recent SED modeling of a sample of fourteen isolated HAEBE stars with the characteristics of Group I sources is consistent with emission from a passive reprocessing disk (Meeus et al. 2001). Moreover, Meeus et al. (2001) (and other investigators, e.g., Natta et al. 2001) attribute this emission to the outer part of a flared circumstellar disk (e.g., Chiang & Goldreich 1997), while previous authors attributed blackbody components observed in SEDs of HAEBE sources to tenuous envelopes (Hartmann et al. 1993; Miroshnichenko et al. 1999; Natta et al. 1993).

Size scales and orientations of disks around HAEBE stars can only be determined directly through high angular resolution imaging. The spatial and velocity structure of cooler outer HAEBE disks on $\sim$ 100 AU scales has been mapped with millimeter-wave interferometers (as discussed above). To probe the warmer inner regions of the disk ($\sim$ 1 AU scales), measurements with near-IR interferometers are necessary. The only near-IR interferometric observations of HAEBE sources to date, conducted with the IOTA interferometer (Millan-Gabet et al. 1999; Millan-Gabet, Schloerb, & Traub 2001, hereafter MST), led to sizes and orientations of sources largely inconsistent with values estimated using other techniques. A geometrically flat disk may be too simplistic to accommodate all the observations, and puffed up inner disk walls (Dullemond, Dominik, & Natta 2001; hereafter DDN) or flared outer disks (e.g., Chiang & Goldreich 1997) may need to be included in the models. However, the limited number of HAEBE sources observed with near-IR interferometers and the sparse $u-v$ coverage of these observations (Millan-Gabet et al. 2001) make it difficult to draw unambiguous conclusions about the structure of the circumstellar material.

We have begun a program with the Palomar Testbed Interferometer (PTI) to observe HAEBE stars. By increasing the sample size and improving $u - v$ coverage, we aim to understand better the structure of the circumstellar emission on $\sim$ 1 AU scales. In this paper, we present results for five sources, AB Aur, VV Ser, V1685 Cyg (BD+40°4124), AS 442, and MWC 1080. We note that neither our list of HAEBEs, nor that of MST, represents an unbiased sample, but rather, is limited to those stars that are bright enough ($K \lesssim 6.5$) to be successfully observed. We model the structure

of circumstellar dust around HAEBE stars using these PTI data, together with IOTA measurements where available. Specifically, we compare various models—Gaussians, uniform disks, uniform rings, and accretion disks with inner holes—to the visibility data to determine approximate size scales and orientations of the circumstellar emission.

In §5.2, we describe the PTI observations. In §5.4, we fit the observed data to several different models for the circumstellar dust distribution and derive angular sizes and orientations. Implications of the modeling and comparisons with previous observations are discussed in §4.4.

4.2 Observations and Calibration

The Palomar Testbed Interferometer (PTI) is a long-baseline near-IR Michelson interferometer located on Palomar Mountain near San Diego, CA (Colavita et al. 1999). PTI combines starlight from two 40-cm aperture telescopes using a Michelson beam combiner, and records the resulting fringe visibilities. These fringe visibilities are related to the source brightness distribution via the van Cittert-Zernike theorem, which states that the visibility distribution in $u - v$ space and the brightness distribution on the sky are Fourier transform pairs (Born & Wolf 1999).

We observed five HAEBE sources, AB Aur, VV Ser, V1685 Cyg (BD+40°4124), AS 442, and MWC 1080, with PTI between May and October of 2002. Properties of the sample are included in Table 4.1. We obtained K-band (2.2 μm) measurements on an 85-m North-West (NW) baseline for all five objects, and on a 110-m North-South (NS) baseline for three. The NW baseline is oriented 109° west of north and has a fringe spacing of ~ 5 mas, and the NS baseline is 160° west of north and has a fringe spacing of ~ 4 mas. A summary of the observations is given in Table 4.2.

PTI measures fringes in two channels, corresponding to the two outputs from the beam combiner. One output is spatially filtered with an optical fiber and dispersed onto five "spectral" pixels, while the other output is focused onto a single "white-light" pixel (without spatial filtering). The white-light pixel is used principally for fringe-

Table 4.1. Observed Sources

Source	Alt. Name	α (J2000)	δ (J2000)	d (pc)	Sp.Ty.	V	K	$F_*^\dagger$ (Jy)	$F_{\rm x}^\dagger$ (Jy)
AB Aur	HD 31293	$04^{\rm h}55^{\rm m}45.84^{\rm s}$	$+30°33'04.''3$	140	A0pe	7.07	4.27	1.92	10.59
VV Ser	HBC 282	$18^{\rm h}28^{\rm m}49.00^{\rm s}$	$+00°08'39.''0$	310	A0Vevp	11.90	6.44	0.20	1.85
V1685 Cyg	BD+40°4124	$20^{\rm h}20^{\rm m}28.25^{\rm s}$	$+41°21'51.''6$	1000	B2Ve	10.71	5.70	0.42	3.64
AS 442	V1977 Cyg	$20^{\rm h}47^{\rm m}37.47^{\rm s}$	$+43°47'24.''9$	600	B8Ve	10.89	6.75	0.20	1.21
MWC 1080	V628 Cas	$23^{\rm h}17^{\rm m}26.10^{\rm s}$	$+60°50'43.''0$	1000	B0eq	11.68	4.83	0.87	9.85

References. — Distances, spectral types and V magnitudes from Hillenbrand et al. (1992), Mora et al. (2001), Strom et al. (1972), de Lara et al. (1991), and Bigay & Garner (1970). For discussion of the adopted distances, see Appendix 4.6. K magnitudes from the present work. †: De-reddened fluxes.

Table 4.2. Summary of Observations

Source	Date (MJD)	Baseline	ha cov.†	Calibrators (HD)
AB Aur	52575	NW	[1.21,1.85]	29645, 32301
	52602	NW	[-1.95,1.51]	29645, 32301
VV Ser	52490	NW	[-0.72,0.54]	171834
	52491	NS	[-1.55,-0.74]	171834
	52493	NW	[-1.31,0.20]	171834
	52499	NW	[-0.96,0.84]	164259,171834
V1685 Cyg	52418	NW	[-1.10,-1.00]	192640,192985
	52475	NW	[-1.69,1.44]	192640,192985
	52476	NW	[-1.80,-0.48]	192640,192985
	52490	NW	[-0.97,1.70]	192640,192985
	52491	NS	[-1.27,2.38]	192640
	52492	NW	[-0.90,-0.90]	192640
	52545	NS	[-1.12,2.48]	192640,192985
AS 442	52475	NW	[0.21,1.33]	192640,192985
	52476	NW	[-0.21,-0.21]	192640,192985
	52490	NW	[-1.11,0.38]	192640
	52491	NS	[-0.69,2.54]	192640
	52492	NW	[-1.05,0.00]	192640
	52545	NS	[-0.87,1.58]	192640,192985
MWC 1080	52475	NW	[0.17,0.17]	219623
	52476	NW	[-1.99,0.52]	219623
	52490	NW	[-0.14,1.39]	219623

References. — †: Hour angle coverage of the observations.

tracking: the fringe phase is measured and then used to control the delay line system to track atmospheric fringe motion (and thus maintain zero optical path difference between the two interfering beams). The spectral pixels are generally used to make accurate measurements of the squared visibility amplitudes (V^2) of observed sources. We sample the data at either 20 or 50 milliseconds in order to make measurements on a timescale shorter than the atmospheric coherence time. A "scan", which is the unit of data we will use in the analysis below, consists of 130 seconds of data, divided into five equal time blocks. The V^2 is calculated for each of these blocks using an incoherent average of the constituent 20 or 50-ms measurements from a synthetic wide-band channel formed from the five spectral pixels (Colavita 1999). V^2 for the entire scan is given by the mean of these five estimates, and the statistical uncertainty is given by the standard deviation from the mean value.

We calibrate the measured V^2 for the observed HAEBE sources by comparing them to visibilities measured for calibrator sources of known angular sizes, for which we can easily calculate the expected V^2 for an ideal system. The visibilities are normalized such that $V^2 = 1$ for a point source observed with an ideal system. We calculate the expected V^2 by assuming that the calibrators are uniform stellar disks. Making use of the van Cittert-Zernike theorem, the squared visibilities for these sources are given by

$$V^2_{\rm calc} = \left(2 \frac{J_1(\pi \theta r_{\rm uv})}{\pi \theta r_{\rm uv}} \right)^2 . \tag{4.1}$$

Here, J_1 is the first-order Bessel function. θ is the angular diameter of the star, and $r_{\rm uv}$ is the "uv radius", defined by

$$r_{\rm uv} = \sqrt{u^2 + v^2} = \frac{\vec{B} \cdot \vec{s}}{\lambda}, \tag{4.2}$$

where $\vec{B}$ is the baseline vector, $\vec{s}$ is a unit vector pointing from the center of the baseline toward the source, and λ is the observing wavelength. (The qualitative explanation of Equation 4.1 is that while for unresolved sources the visibility is constant with increasing uv radius, for progressively larger sources the visibility decreases faster

Table 4.3. Properties of Calibrator Sources

Name	α (J2000)	δ (J2000)	Sp.Ty.	V	K	Cal. Size (mas)	$\Delta\alpha$ (°)
HD 29645	$04^h41^m50.26^s$	$+38°16'48.''7$	G0V	6.0	4.6	0.56 ± 0.09	8.2
HD 32301	$05^h03^m05.75^s$	$+21°35'23.''9$	A7V	4.6	4.1	0.47 ± 0.10	9.1
HD 164259	$18^h00^m29.01^s$	$-03°41'25.''0$	F2IV	4.6	3.7	0.77 ± 0.08	7.5
HD 171834	$18^h36^m39.08^s$	$+06°40'18.''5$	F3V	5.4	4.5	0.54 ± 0.07	6.8
HD 192640	$20^h14^m32.03^s$	$+36°48'22.''7$	A2V	4.9	4.9	0.46 ± 0.02	4.7^1,9.4^2
HD 192985	$20^h16^m00.62^s$	$+45°34'46.''3$	F5V	5.9	4.8	0.44 ± 0.04	4.3^1,5.9^2
HD 219623	$23^h16^m42.30^s$	$+53°12'48.''5$	F7V	5.6	4.3	0.54 ± 0.03	9.5

References. — 1,2: Offsets from V1685 Cyg, AS 442, respectively.

with increasing uv radius.) By comparing $V^2_{\rm calc}$ to the measured V^2 for a calibrator, we derive the "system visibility", which represents the point source response of the interferometer:

$$V^2_{\rm sys} = \frac{V^2_{\rm meas,calibrator}}{V^2_{\rm calc}}. \tag{4.3}$$

This system visibility, in turn, is used to calibrate the squared visibilities for the target source:

$$V^2_{\rm target} = \frac{V^2_{\rm meas,target}}{V^2_{\rm sys}}. \tag{4.4}$$

Specifically, we determine $V^2_{\rm sys}$ at the time of each target scan, using an average of $V^2_{\rm meas,calibrator}$ weighted by the proximity of the target and calibrator in both time and angle. For further discussion of the calibration procedure, see Boden et al. (1998).

Calibrators must be close to the target sources (on the sky an in time) so that the atmospheric effects will be the same for both. They should also be of small angular size, θ, so that $V^2 \to 1$ and $dV^2_{\rm sys}/d\theta \to 0$, and the calibration is thus less sensitive to uncertainties in the assumed calibrator diameter. The angular size of a calibrator can be estimated from the published stellar luminosity and distance, from a blackbody fit to published photometric data with the temperature constrained to that expected for the published spectral type, or from an unconstrained blackbody fit to the photometric data. We adopt the average of these three size estimates in

our analysis, and the uncertainty is given by the spread of these values. Relevant properties of the calibrators used in these observations are given in Table 4.3.

4.3 Results

We measured calibrated squared visibilities for AB Aur, VV Ser, V1685 Cyg, AS 442, and MWC 1080 (Table 4.2). All five sources are resolved by PTI (i.e., V^2 is significantly different from unity), implying angular sizes $\gtrsim$ 1 mas. The data are consistent with disk-like morphologies for all sources, and we can place good constraints on disk inclinations for most sources. MWC 1080, V1685 Cyg, and VV Ser show evidence for significantly non-zero inclinations, while a circularly symmetric distribution appears appropriate for AB Aur. The AS 442 data are insufficient to constrain the inclination.

Interferometric observations of AB Aur and MWC 1080 at 2.2 μm have also been obtained with the 21-m and 38-m baselines of the IOTA interferometer (Millan-Gabet et al. 1999, 2001). When combined with our longer baseline PTI data (85-m and 110-m), these help fill in the $u - v$ plane, and enable us to improve constraints on source models (see below; Figure 4.1). Based on discussion with R. Millan-Gabet, we assign an uncertainty to each IOTA visibility given by the standard deviation of all data obtained for a given source with a given baseline. We verify the registration of the IOTA and PTI data using calibrators observed by both interferometers. Since the IOTA data for AB Aur was calibrated using HD 32406, which is unresolved by both PTI and IOTA, we can be confident of the registration. We measured the diameter of HD 220074, the calibrator for MWC 1080, to be $\theta_{\rm UD} = 1.98 \pm 0.06$, while MST assumed a size of 2.10 ± 0.22. This difference in angular size translates into only a 0.7% effect, which is within the measurement errors (the effect is so small because the calibrator is essentially unresolved by IOTA).[2]

[2]In this chapter, the IOTA visibilities were interpreted incorrectly, leading to slightly erroneous results for those objects where PTI and IOTA data were analyzed simultaneously. This error is described in detail, and rectified in Chapter 5.

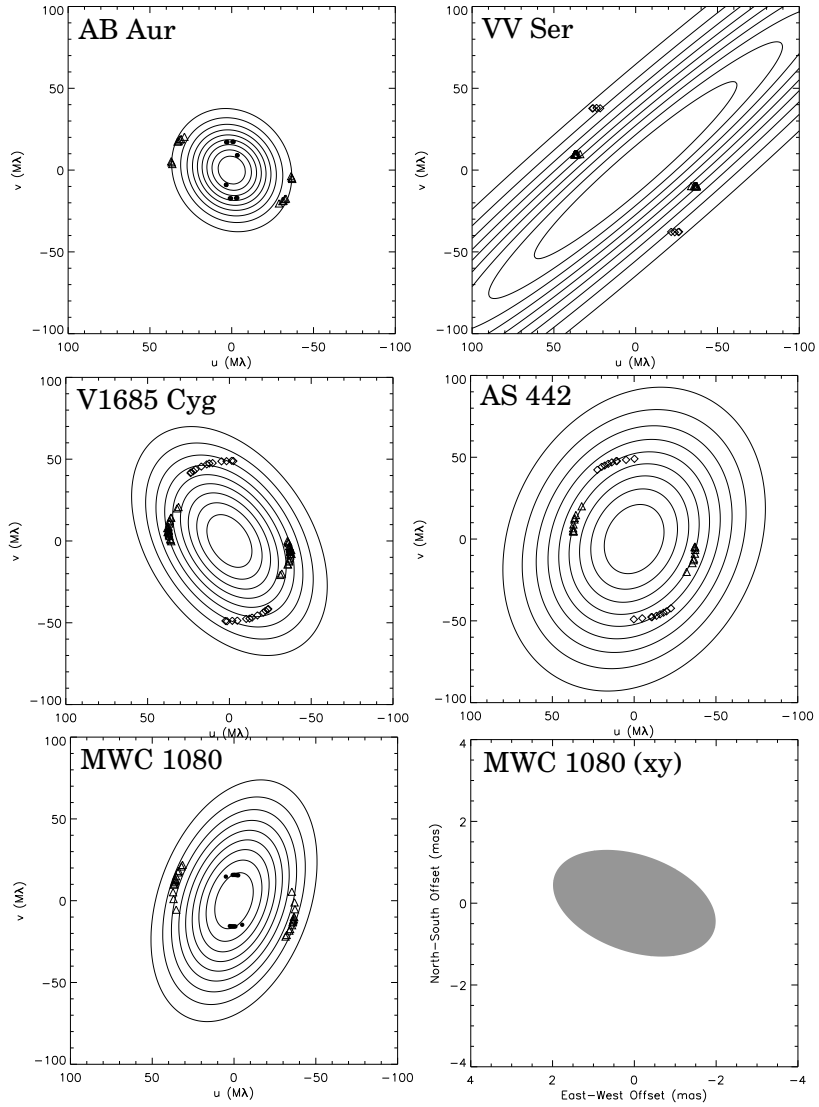

Figure 4.1 Contour plots of best-fit inclined uniform disk models for AB Aur, VV Ser, V1685 Cyg, AS 442, and MWC 1080, whose parameters are listed in Tables 4.4-4.8. The contour increment is 10% in V^2. We also plot the best-fit inclined disk model for MWC 1080 on the sky (bottom right panel, greyscale). We over-plot the uv points sampled for each source by the PTI NW baseline (open triangles), the PTI NS baseline (open diamonds), and by IOTA (filled dots). Since we know that the brightness distributions of the sources are real, the visibilities must be reflection symmetric (through the origin), and so we also plot these reflections of the sampled uv points.

4.3.1 Visibility Corrections

Nearby companions that lie outside the interferometric field of view, ~ 50 mas, but within the field of view of the detector, $\sim 1''$, will contribute incoherent light to the visibilities. For MWC 1080, which has a known nearby companion (Corporon 1998), we use the correction factor[3]

$$\frac{V^2_{\rm meas}}{V^2_{\rm true}} = \left(\frac{1}{1+10^{-\Delta K/2.5}}\right)^2, \tag{4.5}$$

where ΔK is the difference in K-band magnitudes between the two stars. For MWC 1080, we measured $\Delta K = 2.70$ (angular separation $= 0\farcs78$) using the Palomar Adaptive Optics system on the 200-inch telescope on November 18, 2002. V1685 Cyg is also known to have a faint companion ($\Delta K = 5.50$; Corporon 1998), but the effect of this companion on the visibilities is negligible. Adaptive optics images of the other sources in our sample show that none of these has any bright companions ($\Delta K < 5$) at distances between ~ 50 mas and $1''$.

Our measured visibilities contain information about emission from both the circumstellar material and the star itself. We can remove the effect of the central star on the visibilities by including it in the models:

$$V^2_{\rm tot} = \left(\frac{F_* V_* + F_{\rm x} V_{\rm x}}{F_* + F_{\rm x}}\right)^2 \approx \left(\frac{F_* + F_{\rm x} V_{\rm x}}{F_* + F_{\rm x}}\right)^2, \tag{4.6}$$

where F_* is the stellar flux, $F_{\rm x}$ is the excess flux (both measured at 2.2 μm), $V_* \approx 1$ is the visibility of the (unresolved) central star, and $V_{\rm x}$ is the visibility due to the circumstellar component. It is reasonable to assume that $V_* \approx 1$, since for typical stellar radii (~ 5 R$_\odot$) and distances (~ 500 pc), the angular diameters of the central stars will be ~ 0.5 mas. In the case of the binary model described below (§4.3.3.5), we do not perform any such correction, since the basic model already includes the stellar component.

Equation 4.6 assumes that the central star is a point source, and thus contributes

[3]An error in the previously published version of this equation has been corrected here.

coherently to the visibilities. It is also possible that the starlight is actually observable only as scattered light emission, and that it will have some incoherent contribution to the visibility ($V_* \neq 1$). For example, coronographic imaging with the Hubble Space Telescope has revealed scattered light on angular scales from $\sim 0\farcs1$–$9''$ around AB Aur (Grady et al. 1999). A proper treatment of the effects of this scattered light on the visibilities is beyond the scope of this work, but we mention it as a possible source of uncertainty. Since the near-IR excess from HAEBE sources typically dominates over the near-IR stellar emission (§4.3.2; Table 4.1), the effect should be insignificant.

4.3.2 Photometry

F_* and $F_{\rm x}$ affect the visibilities (Equation 4.6), and thus it is important to determine these quantities accurately. Since HAEBE objects are often highly variable at near-IR wavelengths (e.g., Skrutskie et al. 1996), we obtained photometric K-band measurements of the sources in our sample that are nearly contemporaneous with our PTI observations, using the Palomar 200-inch telescope between November 14 and 18, 2002. Calibration relied on observations of 2MASS sources close in angle to the target sources, and we estimate uncertainties of ~ 0.1 magnitudes. Our photometry is consistent with published measurements to within ~ 0.3 magnitudes for all objects (Hillenbrand et al. 1992; Eiroa et al. 2002).

Following HSVK and MST, we calculate F_* and $F_{\rm x}$ using our K-band photometry (Table 4.1) combined with BVRI photometry, visual extinctions, and stellar effective temperatures from the literature (Hillenbrand et al. 1992; Oudmaijer et al. 2001; Eiroa et al. 2002; Bigay & Garnier 1970). De-reddening uses the extinction law of Steenman & Thé (1991). Assuming that all of the short-wavelength flux is due to the central star, we fit a blackbody at the assumed effective temperature to the de-reddened BVRI data. The K-band stellar flux is derived from the value of this blackbody curve at 2.2 μm. The excess flux is then given by the difference between the de-reddened observed flux and the stellar flux. The derived fluxes are given in Table 4.1. We note that VV Ser and AS 442 are optically variable by $\Delta V \gtrsim 1$ magnitudes on timescales

of days to months (while the other sources in our sample show little or no optical variability; Herbst & Shevchenko 1999), and thus F_* is somewhat uncertain. However, since $F_{\rm x}/F_* \gg 1$ for these objects, this uncertainty is negligible when modeling the visibilities.

4.3.3 Models

For each source, we compare the observed visibilities to those derived from a uniform disk model, a Gaussian model, a ring model, and an accretion disk model with an inner disk hole (all models are 2-D). If we assume that the inclination of the circumstellar material is zero, then the one remaining free parameter in the models is the angular size scale, θ. When we include inclination effects, we fit for three parameters: size (θ), inclination angle (ϕ), and position angle (ψ). Inclination is defined such that a face-on disk has $\phi = 0$, and ψ is measured east of north. Following MST, we include ϕ and ψ in our models of the brightness distribution via a simple coordinate transformation[4]:

$$x' = x\sin\psi + y\cos\psi;\ y' = \frac{y\sin\psi - x\cos\psi}{\cos\phi}. \tag{4.7}$$

Here, (x, y) are the coordinates on the sky, and (x', y') are the transformed coordinates. The effect of this coordinate transformation on the visibilities will be to transform (u, v) to (u', v'):

$$u' = u\sin\psi + v\cos\psi;\ v' = \cos\phi(v\sin\psi - u\cos\psi). \tag{4.8}$$

Substitution of (x', y') for (x, y), and (u', v') for (u, v) in the expressions below yield models with inclination effects included.

In addition to these four models, we also examine whether the data are consistent with a wide binary model, which we approximate with two stationary point sources. For this model, the free parameters are the angular separation (θ), the position angle (ψ), and the brightness ratio of the two components (R).

[4]An error in the previously published version of this equation has been corrected here.

4.3.3.1 Gaussian Model

The brightness distribution for a normalized Gaussian model is given by

$$I_{\rm gauss}(x,y) = \exp\left(-\frac{4\ln 2\ \ (x^2+y^2)}{\theta^2}\right), \tag{4.9}$$

and the (normalized) visibilities expected for this observed brightness distribution are calculated via a Fourier transform to be,

$$V_{\rm gauss}(r_{\rm uv}) = \exp\left(-\frac{\pi^2\theta^2 r_{\rm uv}^2}{4\ln 2}\right). \tag{4.10}$$

Here, (x, y) are the angular offsets from the central star, θ is the angular FWHM of the brightness distribution, and $r_{\rm uv} = (u^2+v^2)^{1/2}$ is the "uv radius" (Equation 4.2). The model for the observed squared visibilities is obtained by using Equation 4.6 with $V_{\rm x} = V_{\rm gauss}$.

4.3.3.2 Uniform Disk Model

The brightness distribution for a uniform disk is simply given by a 2-D top-hat function. Thus, the normalized visibilities are given by

$$V_{\rm uniform}(r_{\rm uv}) = 2\frac{J_1(\pi\theta r_{\rm uv})}{\pi\theta r_{\rm uv}}, \tag{4.11}$$

where θ is the angular diameter of the uniform disk brightness distribution, and $r_{\rm uv} = (u^2+v^2)^{1/2}$ is the "uv radius" (Equation 4.2). The model for the observed squared visibilities is obtained by using Equation 4.6 with $V_{\rm x} = V_{\rm uniform}$.

4.3.3.3 Accretion Disk Model

We derive the brightness distribution and predicted visibilities for a geometrically thin irradiated accretion disk following the analysis of HSVK and MST. Assuming that the disk is heated by stellar radiation and accretion (Lynden-Bell & Pringle

1974), the temperature profile (in the regime where $R_*/R \ll 1$) is,

$$T_{\rm disk} = T_{\rm 1AU} \left(\frac{R}{\rm AU} \right)^{-3/4}, \tag{4.12}$$

where $T_{\rm 1AU}$ is defined as the temperature at 1 AU, given by

$$T_{\rm 1AU} = \left[2.52 \times 10^{-8} \left(\frac{R_*}{R_\odot} \right)^3 T_*^4 + 5.27 \times 10^{10} \left(\frac{M_*}{M_\odot} \right) \left(\frac{\dot{M}}{10^{-5}\ M_\odot\ {\rm yr}^{-1}} \right) \right]^{1/4}. \tag{4.13}$$

We assume that the disk is truncated at an inner radius $R_{\rm in}$, and an outer radius, $R_{\rm out}$. Guided by Figure 14 of HSVK, we choose $R_{\rm in}$ to be the radius where the temperature, $T_{\rm in}$, is 2000 K. Thus,

$$T_{\rm 1AU} = 2000 \left(\frac{R_{\rm in}}{\rm AU} \right)^{3/4}. \tag{4.14}$$

2000 K is a likely (upper limit) sublimation temperature for the dust grains that make up circumstellar disks, and thus it is reasonable that there would be little or no dust emission interior to $R_{\rm in}$ (although the model does not exclude the possibility of optically thin gas interior to $R_{\rm in}$). We choose $R_{\rm out}$ to be the lesser of 1000 AU or the radius at which $T = 3$ K ($R_{\rm out}$ is not crucial in this analysis, since most of the near-IR flux comes from the hotter inner regions of the disk).

The brightness distribution and visibilities for this disk are calculated by determining the contributions from a series of annuli from $R_{\rm in}$ to $R_{\rm out}$. The flux in an annulus specified by inner boundary $R_{\rm i}$ and outer boundary $R_{\rm f}$ is given by[5]

$$F_{\rm annulus} = \frac{\pi}{2d^2} [B_\nu(T_{\rm i}) + B_\nu(T_{\rm f})](R_{\rm f}^2 - R_{\rm i}^2) \cos(\phi), \tag{4.15}$$

and the visibilities for this annulus are (following Millan-Gabet et al. 2001),

$$V_{\rm annulus} = \frac{\pi}{d^2} [B_\nu(T_{\rm i}) + B_\nu(T_{\rm f})] \left[R_{\rm f}^2 \frac{J_1(\pi \theta_{\rm f} r_{\rm uv})}{\pi \theta_{\rm f} r_{\rm uv}} - R_{\rm i}^2 \frac{J_1(\pi \theta_{\rm i} r_{\rm uv})}{\pi \theta_{\rm i} r_{\rm uv}} \right]. \tag{4.16}$$

Here, d is the distance to the source, ν is the observed frequency, B_ν is the Planck

[5]An error in the previously published version of this equation has been corrected here.

function, T is the temperature, R is the physical radius, θ is the angular size, $r_{\rm uv}$ is the "uv radius" (Equation 4.2), and i, f indicate the inner and outer boundaries of the annulus. To obtain the visibilities for the entire disk, we sum the visibilities for each annulus, and normalize by the total flux:

$$V_{\rm disk} = \frac{\sum_{R_{in}}^{R_{out}} V_{\rm annulus}}{\sum_{R_{in}}^{R_{out}} F_{\rm annulus}}. \tag{4.17}$$

The resultant model visibilities are obtained by plugging this expression into Equation 4.6. We note that although we do not use the observed excess K-band flux to constrain the disk model, we do verify that the total flux in the model is consistent (to within a factor of 2) with the observations.

4.3.3.4 Ring Model

The brightness distribution for a uniform ring model is given by

$$I_{\rm ring}(x,y) = \begin{cases} \text{constant} & \text{if } \frac{\theta_{\rm in}}{2} < \sqrt{x^2+y^2} < \frac{\theta_{\rm out}}{2} \\ 0 & \text{otherwise} \end{cases} . \tag{4.18}$$

Here, (x, y) are the angular offsets from the central star. We define the width of the ring via the relation $f = W/R$, where R is the radius of the inner edge of the ring, and W is the width of the ring. Using this relation, we write the inner and outer angular radii of the ring as $\theta_{\rm in}$ and $\theta_{\rm out} = (1+f)\theta_{\rm in}$. The normalized visibility of the ring is given by

$$V_{\rm ring} = \frac{2}{\pi\theta_1(2f+f^2)} \left[(1+f)J_1([1+f]\pi\theta_{\rm in}r_{\rm uv}) - J_1(\pi\theta_{\rm in}r_{\rm uv})\right], \tag{4.19}$$

where $r_{\rm uv} = (u^2+v^2)^{1/2}$ is the "uv radius" (Equation 4.2). The model for the observed visibilities is obtained by using Equation 4.6 with $V_{\rm x} = V_{\rm ring}$.

In order to facilitate comparison of our data to puffed up inner disk models from the literature, we will use ring widths derived from radiative transfer modeling by DDN. Specifically, for stars earlier than spectral type B6, we assume $f = 0.27$, and for stars later than B6, we assume $f = 0.18$ (Table 1 from Dullemond et al. 2001).

4.3.3.5 Two-Component Model

This model simulates a wide binary, where visibilities are effectively due to two stationary point sources, with some flux ratio and angular separation vector. We explore flux ratios from 0.2 to 1, and angular separations from 1 to 100 mas. For flux ratios < 0.2, or angular separations < 1 mas, the effects of the companions on the visibilities will be negligible, and we can rule out angular separations $\gtrsim 100$ mas from adaptive optics imaging (§4.3.1). The squared visibility for the binary model is,

$$V^2_{\rm binary} = \frac{1 + R^2 + 2R\cos\left(\frac{2\pi}{\lambda}\vec{B}\cdot\vec{s}\right)}{(1+R)^2}, \tag{4.20}$$

where $(\vec{B}\cdot\vec{s})/\lambda = \theta[u\sin(\psi) + v\cos(\psi)]$, θ is the angular separation of the binary, ψ is the position angle, R is the ratio of the fluxes of the two components, and λ is the observed wavelength.

4.3.4 Modeling of Individual Sources

For each source, we fit the PTI and IOTA visibility data with the models described in §4.3.3 using grids of parameter values. The grid for face-on disk models was generated by varying θ from 0.01 to 10 mas in increments of 0.01 mas. For inclined disk models, in addition to varying θ, we varied ϕ from 0° to 90° and ψ from 0° to 180°, both in increments of 1°. As mentioned above, $\phi = 0$ corresponds to face-on, and ψ is measured east of north. Since inclined disk models are symmetric under reflections through the origin, we do not explore position angles between 180° and 360°. For the binary model, we varied θ from 1 to 100 mas in increments of 0.01 mas, ψ from 0° to 180° in increments of 1°, and $R = F_2/F_1$ from 0.2 to 1 in increments of 0.001.

For each point in the parameter grid, we generated a model for the observed $u-v$ coverage, and calculated the reduced chi squared (χ^2_r) to determine the "best-fit" model. 1-σ confidence limits were determined by finding the grid points where χ^2_r equals the minimum value plus one. For inclined disk or binary models, the confidence limits on each parameter were determined by projecting the 3-D $\chi^2_r = \min{+}1$ surface

onto the 1-D parameter spaces.[6]

Tables 4.4-4.8 list the best-fit angular size scales (θ) for face-on models, the sizes (θ), position angles (ψ), and inclinations (ϕ) for inclined disk models, and the angular separations (θ), position angles (ψ), and brightness ratios (R) for binary models. Values of χ^2_r are also included in the Tables. Figures 4.2, 4.4, 4.6, 4.8, and 4.10 show plots of observed V^2 versus $r_{\rm uv}$ for each source along with the curves predicted by various face-on models. Inclined models are not circularly symmetric, and the visibilities are a function of the observed position angle in addition to the projected baseline (Figure 4.1). We plot the observed and modeled V^2 for inclined models as a function of hour angle in Figures 4.3, 4.5, 4.7, 4.9, and 4.11.

The best-fit binary separations for all sources in our sample are $\gtrsim 2.5$ mas. For the distances and approximate masses of the sources in our sample, these separations correspond to orbital periods of many years. Thus, our assumption that the two point sources in the binary model are stationary is justified.

[6]The statistical error analysis presented in this paper is not rigorously correct, and thus the quoted confidence limits are not precise. A correct, rigorous error analysis is included in Chapter 5.

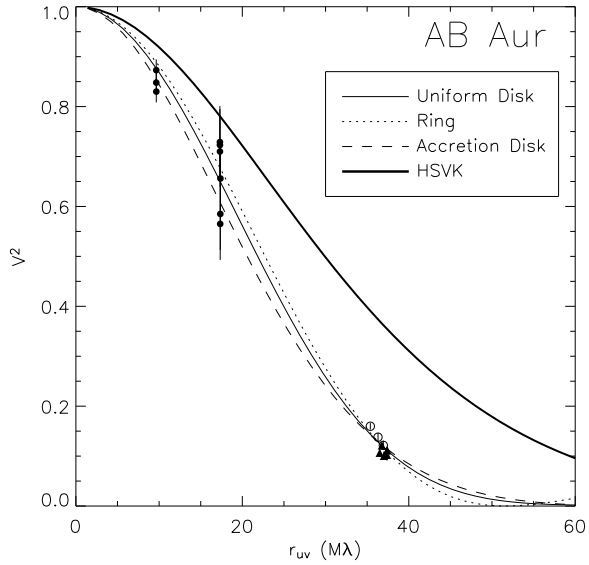

Figure 4.2 V^2 data from PTI (symbols) and IOTA (filled dots; MST) for AB Aur, as a function of $r_{\rm uv} = (u^2 + v^2)^{1/2}$. PTI data for individual nights are represented by different symbols. Face-on uniform disk (solid line), ring (dotted line), and accretion disk (dashed line) models are over-plotted. We also plot the visibilities calculated for an accretion disk model with $R_{\rm in} = 0.09$ AU and $T_{\rm in} = 2360$ K (HSVK; thick solid line).

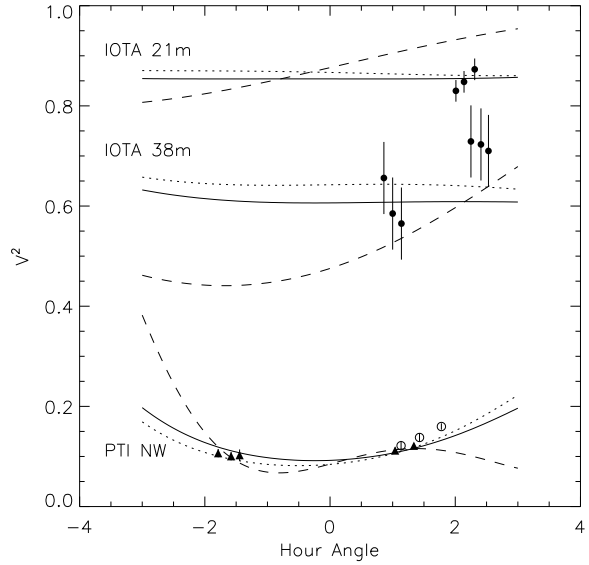

Figure 4.3 PTI and IOTA V^2 data for AB Aur (represented as in Figure 4.2), as a function of hour angle. Over-plotted are face-on and inclined accretion disk models (solid and dotted lines, respectively), as well as the best-fit binary model (dashed line).

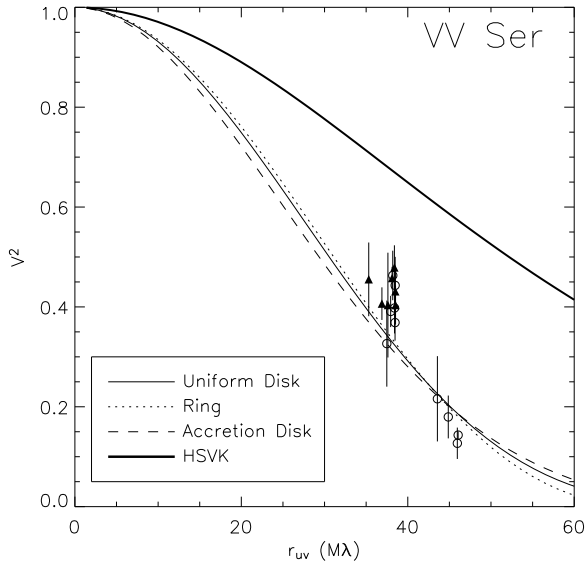

Figure 4.4 PTI V^2 data for VV Ser, as a function of $r_{\rm uv} = (u^2 + v^2)^{1/2}$. PTI data for individual nights are represented by different symbols. Face-on uniform disk (solid line), ring (dotted line), and accretion disk (dashed line) models are over-plotted. We also plot the visibilities calculated for an accretion disk model with $R_{\rm in} = 0.08$ AU and $T_{\rm in} = 2710$ K (HSVK; thick solid line).

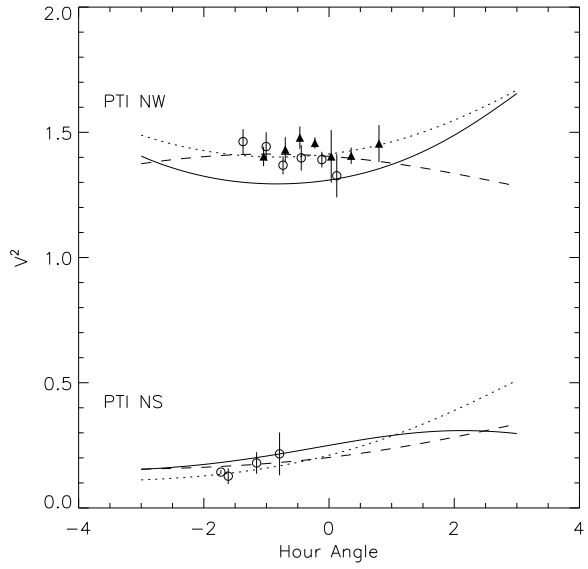

Figure 4.5 PTI V^2 data for VV Ser (represented as in Figure 4.4), as a function of hour angle. For clarity, we have plotted $V^2 + 1$ for the data taken with the NW baseline. Over-plotted are face-on and inclined accretion disk models (solid and dotted lines, respectively), as well as the best-fit binary model (dashed line).

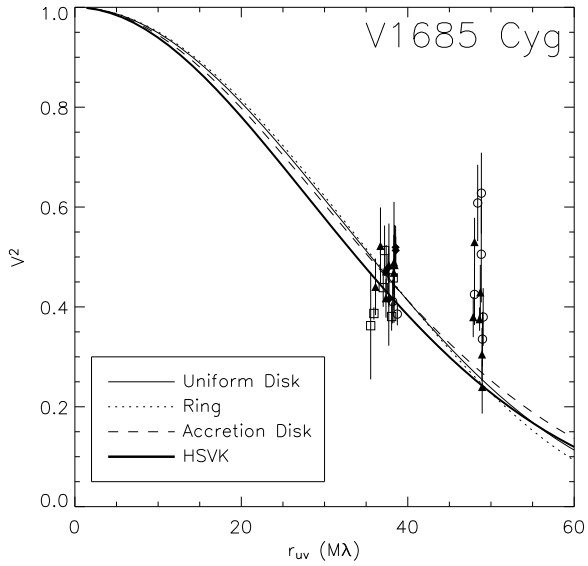

Figure 4.6 PTI V^2 data for V1685 Cyg, as a function of $r_{\rm uv} = (u^2 + v^2)^{1/2}$. PTI data for individual nights are represented by different symbols. Face-on uniform disk (solid line), ring (dotted line), and accretion disk (dashed line) models are over-plotted. We also plot the visibilities calculated for an accretion disk model with $R_{\rm in} = 0.63$ AU and $T_{\rm in} = 2060$ K (HSVK; thick solid line).

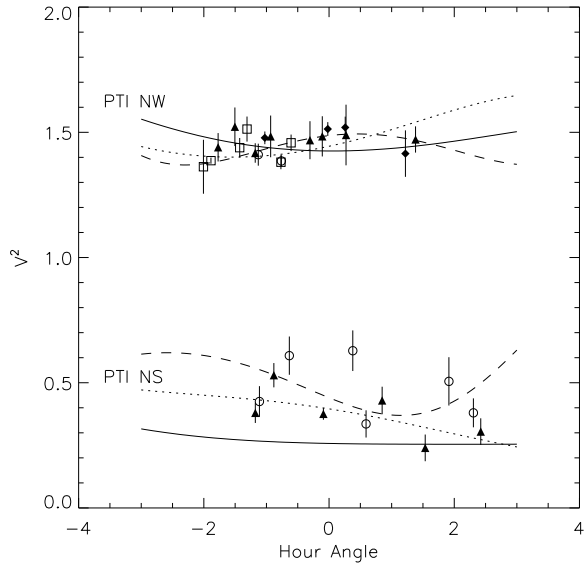

Figure 4.7 PTI V^2 data for V1685 Cyg (represented as in Figure 4.6), as a function of hour angle. For clarity, we have plotted $V^2 + 1$ for the data taken with the NW baseline. Over-plotted are face-on and inclined accretion disk models (solid and dotted lines, respectively), as well as the best-fit binary model (dashed line).

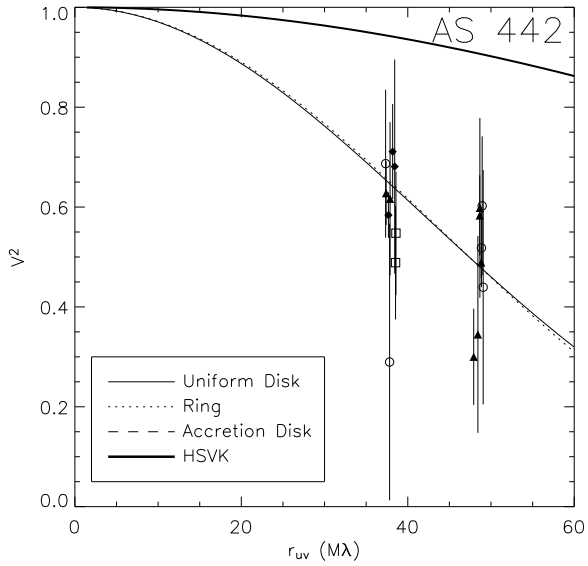

Figure 4.8 PTI V^2 data for AS 442, as a function of $r_{\rm uv} = (u^2 + v^2)^{1/2}$. PTI data for individual nights are represented by different symbols. Face-on uniform disk (solid line), ring (dotted line), and accretion disk (dashed line) models are over-plotted. We also plot the visibilities calculated for an accretion disk model with $R_{\rm in} = 0.10$ AU and $T_{\rm in} = 2000$ K (HSVK; thick solid line).

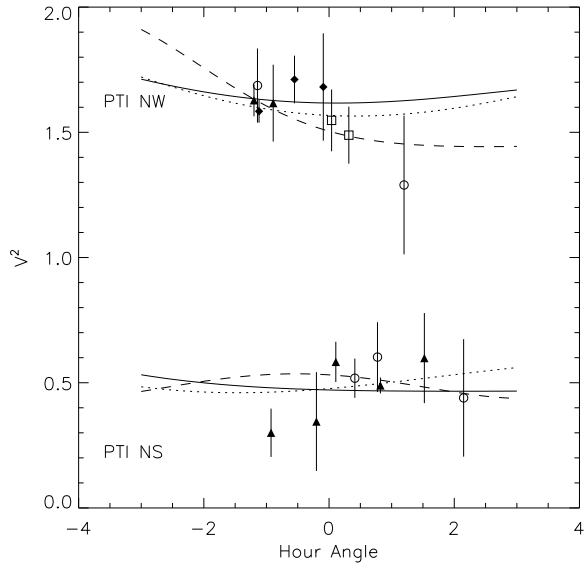

Figure 4.9 PTI V^2 data for AS 442 (represented as in Figure 4.8), as a function of hour angle. For clarity, we have plotted $V^2 + 1$ for the data taken with the NW baseline. Over-plotted are face-on and inclined accretion disk models (solid and dotted lines, respectively), as well as the best-fit binary model (dashed line).

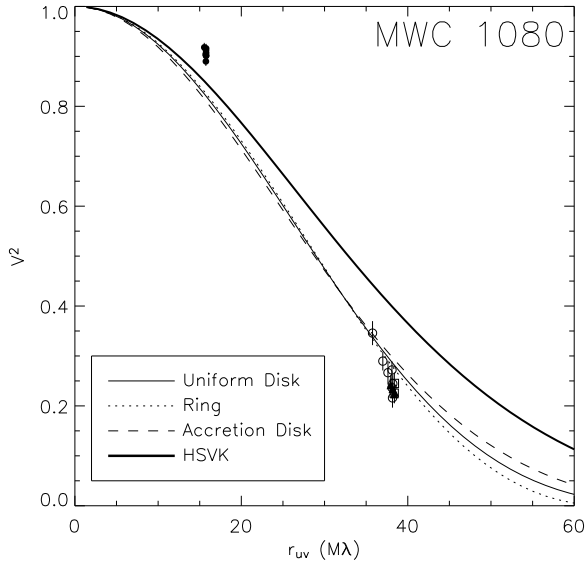

Figure 4.10 V^2 data from PTI (symbols) and IOTA (filled dots; MST) for MWC 1080, as a function of $r_{\rm uv} = (u^2 + v^2)^{1/2}$. PTI data for individual nights are represented by different symbols. Face-on uniform disk (solid line), ring (dotted line), and accretion disk (dashed line) models are over-plotted. We also plot the visibilities calculated for an accretion disk model with $R_{\rm in} = 0.59$ AU and $T_{\rm in} = 2490$ K (HSVK; thick solid line). While none of these face-on models fit the data well, good fits are obtained with inclined models (Figure 4.11).

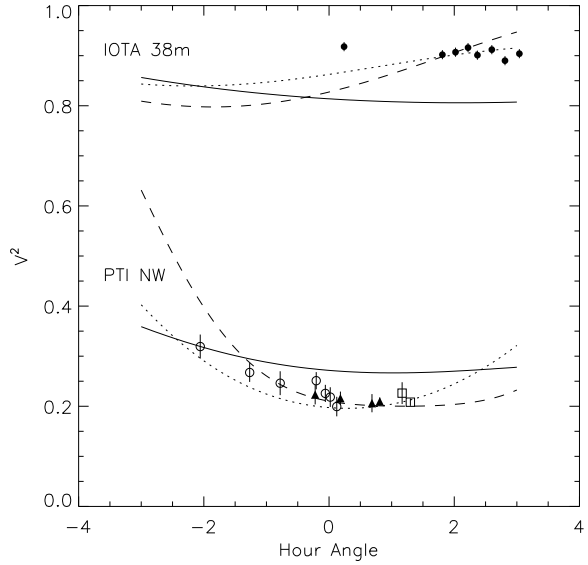

Figure 4.11 PTI and IOTA V^2 data for MWC 1080 (represented as in Figure 4.10), as a function of hour angle. Over-plotted are face-on and inclined accretion disk models (solid and dotted lines, respectively), as well as the best-fit binary model (dashed line). Note the significant improvement in the fit when inclination effects are included in the model.

Table 4.4. Results of Modeling for AB Aur

Model	$\chi^2_{\rm r}$	θ (mas)	ψ (°)	ϕ (°)†
Face-On Gaussian	2.42	$3.59^{+0.09}_{-0.08}$		
Face-On Uniform	1.78	$5.34^{+0.09}_{-0.09}$		
Face-On Accretion	1.93	$2.18^{+0.03}_{-0.02}$		
Face-On Ring	1.92	$3.26^{+0.02}_{-0.03}$		
Inclined Gaussian	0.96	$3.88^{+0.38}_{-0.27}$	103^{+23}_{-25}	35^{+12}_{-18}
Inclined Uniform	0.89	$5.80^{+0.65}_{-0.45}$	128^{+30}_{-45}	26^{+10}_{-19}
Inclined Accretion	0.88	$2.30^{+0.23}_{-0.11}$	105^{+34}_{-20}	27^{+13}_{-17}
Inclined Ring	0.88	$3.66^{+0.42}_{-0.38}$	144^{+17}_{-51}	28^{+10}_{-18}
Binary Model	8.96	$3.41^{+0.13}_{-0.28}$	38^{+7}_{-3}	$0.58^{+0.04}_{-0.03}$

References. — †: For the binary model, ϕ represents the brightness ratio, $R = F_2/F_1$.

4.3.4.1 AB Aur

The visibilities for AB Aur are consistent with a disk-like circumstellar distribution that is inclined by $\lesssim 30°$ (Figures 4.2–4.3). From Table 4.4, the best-fit models indicate size scales[7] between 2.2 and 5.8 mas, and an inclination angle between 27° and 35°. The values of χ^2_r are significantly lower for inclined models than for face-on models ($\chi^2_r \sim 1$ and 2, respectively; Table 4.4), and the data cannot be fit well by a binary model ($\chi^2_r \sim 8$).

4.3.4.2 VV Ser

The angular size scales for best-fit disk models range from 1.5 to 3.9, and the disk inclinations are between 80° and 90° (Table 4.5). An inclined disk model clearly fits the VV Ser data better than a face-on model (Figures 4.4 and 4.5). Inclined model fits

[7]As outlined in §4.3.3.1–4.3.3.4, characteristic size scales for different models measure different parts of the brightness distributions: Gaussian models measure full widths at half maxima, uniform disk models measure outer diameters, accretion disk models measure inner disk diameters, and ring models measure inner ring diameters. The spread in quoted angular sizes for a source is mainly due to these differences.

Table 4.5. Results of Modeling for VV Ser

Model	$\chi^2_{\rm r}$	θ (mas)	ψ (°)	ϕ (°)†
Face-On Gaussian	9.13	$2.33^{+0.09}_{-0.09}$		
Face-On Uniform	6.91	$3.68^{+0.12}_{-0.12}$		
Face-On Accretion	8.33	$1.49^{+0.05}_{-0.05}$		
Face-On Ring	5.86	$2.30^{+0.07}_{-0.07}$		
Inclined Gaussian	0.85	$2.56^{+1.66}_{-0.13}$	37^{+6}_{-55}	89^{+1}_{-50}
Inclined Uniform	0.85	$3.94^{+2.35}_{-0.17}$	41^{+2}_{-53}	82^{+8}_{-43}
Inclined Accretion	0.85	$1.62^{+1.58}_{-0.98}$	38^{+5}_{-70}	83^{+7}_{-45}
Inclined Ring	0.85	$2.44^{+1.92}_{-0.11}$	43^{+5}_{-78}	81^{+9}_{-51}
Binary Model	0.85	$8.80^{+1.02}_{-0.95}$	176^{+9}_{-3}	$0.45^{+0.38}_{-0.04}$

References. — †: For the binary model, ϕ represents the brightness ratio, $R = F_2/F_1$.

give $\chi^2_r < 1$, while face-on model fits have $\chi^2_r > 5$ (Table 4.5). However, as indicated in Figure 4.1, the $u-v$ coverage for this object is rather sparse, and precludes placing stringent constraints on the value of ϕ. Moreover, with such sparse $u-v$ coverage a binary model cannot be ruled out (Figure 4.5).

4.3.4.3 V1685 Cyg

The size scales for V1685 Cyg under the assumptions of various disk models range from 1.3 to 3.9 mas, and the inclinations are between 49° and 51° (Table 4.6). The visibility data are not fit very well by any model, although of those considered, inclined disks fit best (Figures 4.6–4.7). While we cannot rule out a binary model, we note that $\chi^2_r \sim 3$ for the binary model, compared to $\chi^2_r \sim 2$ for inclined disk models (Table 4.6). Better coverage of the $u-v$ plane should help to improve our understanding of this source (Figure 4.1).

Table 4.6. Results of Modeling for V1685 Cyg

Model	$\chi^2_{\rm r}$	θ (mas)	ψ (°)	ϕ (°)†
Face-On Gaussian	6.51	$1.96^{+0.11}_{-0.11}$		
Face-On Uniform	7.52	$3.17^{+0.16}_{-0.15}$		
Face-On Accretion	6.75	$1.27^{+0.06}_{-0.06}$		
Face-On Ring	8.10	$1.92^{+0.09}_{-0.09}$		
Inclined Gaussian	2.32	$2.43^{+0.44}_{-0.37}$	125^{+9}_{-28}	51^{+12}_{-16}
Inclined Uniform	2.36	$3.91^{+0.60}_{-0.55}$	124^{+9}_{-24}	50^{+11}_{-14}
Inclined Accretion	2.33	$1.57^{+0.27}_{-0.22}$	124^{+9}_{-22}	50^{+12}_{-14}
Inclined Ring	2.38	$2.33^{+0.37}_{-0.29}$	122^{+10}_{-24}	49^{+11}_{-13}
Binary Model	3.33	$3.41^{+0.37}_{-0.56}$	62^{+6}_{-11}	$0.24^{+0.08}_{-0.04}$

References. — †: For the binary model, ϕ represents the brightness ratio, $R = F_2/F_1$.

4.3.4.4 AS 442

The PTI data for AS 442 generally have low signal-to-noise, and it is difficult to distinguish between different models. Nevertheless, we can make an approximate determination of the size scale, although we cannot distinguish between inclined disk, face-on disk, or binary models (Figures 4.8 and 4.9). The size scales for various disk models range from 0.9 to 2.7 mas (Table 4.7).

4.3.4.5 MWC 1080

The PTI and IOTA observations for MWC 1080 are completely incompatible with face-on models ($\chi^2_r > 40$), and significantly non-zero inclinations are required to fit the data well (Figures 4.10 and 4.11). The best-fit inclination angles for various disk models range from 51° to 56°, and the angular size scales are between 1.5 and 4.1 mas (Table 4.8). For this source, we can rule out a binary model with a relatively high degree of confidence: $\chi^2_r \sim 10$ for the binary model, compared to $\chi^2_r \sim 2$ for inclined disk models.

Table 4.7. Results of Modeling for AS 442

Model	$\chi^2_{\rm r}$	θ (mas)	ψ (°)	ϕ (°)†
Face-On Gaussian	0.99	$1.49^{+0.19}_{-0.19}$		
Face-On Uniform	1.04	$2.44^{+0.29}_{-0.28}$		
Face-On Accretion	0.99	$0.95^{+0.13}_{-0.12}$		
Face-On Ring	1.07	$1.55^{+0.17}_{-0.17}$		
Inclined Gaussian	0.94	$1.63^{+0.82}_{-0.29}$	60^{+120}_{-60}	41^{+49}_{-41}
Inclined Uniform	0.94	$2.67^{+1.29}_{-0.34}$	63^{+117}_{-63}	39^{+51}_{-39}
Inclined Accretion	0.94	$1.03^{+0.57}_{-0.18}$	63^{+117}_{-63}	36^{+54}_{-36}
Inclined Ring	0.95	$1.70^{+0.80}_{-0.28}$	65^{+115}_{-65}	38^{+52}_{-38}
Binary Model	0.95	$2.69^{+0.69}_{-1.50}$	30^{+32}_{-19}	$0.21^{+0.79}_{-0.01}$

References. — †: For the binary model, ϕ represents the brightness ratio, $R = F_2/F_1$.

Table 4.8. Results of Modeling for MWC 1080

Model	$\chi^2_{\rm r}$	θ (mas)	ψ (°)	ϕ (°)†
Face-On Gaussian	56.33	$2.34^{+0.05}_{-0.05}$		
Face-On Uniform	42.04	$3.84^{+0.07}_{-0.07}$		
Face-On Accretion	54.24	$1.54^{+0.03}_{-0.03}$		
Face-On Ring	36.00	$2.33^{+0.04}_{-0.05}$		
Inclined Gaussian	3.21	$2.61^{+0.11}_{-0.08}$	71^{+11}_{-9}	56^{+6}_{-5}
Inclined Uniform	2.54	$4.13^{+0.12}_{-0.10}$	70^{+10}_{-8}	53^{+7}_{-5}
Inclined Accretion	3.07	$1.69^{+0.07}_{-0.05}$	71^{+10}_{-9}	55^{+5}_{-3}
Inclined Ring	2.28	$2.47^{+0.06}_{-0.06}$	69^{+10}_{-9}	51^{+6}_{-6}
Binary Model	9.32	$2.57^{+0.22}_{-0.18}$	56^{+4}_{-3}	$0.36^{+0.02}_{-0.02}$

References. — †: For the binary model, ϕ represents the brightness ratio, $R = F_2/F_1$.

4.4 Discussion

As discussed in §4.1, there is currently a wide variety of evidence that supports the existence of circumstellar disks around many HAEBE stars. Our new PTI results strengthen this contention. Resolved, small-scale ($\sim$ 1 AU) distributions of dust are found in all observed sources, and the non-symmetric intensity distributions of best-fit models for most objects provide support for inclined disk geometries.

We suggest that the material around VV Ser, V1685 Cyg, and MWC 1080 is significantly inclined, and we cannot rule out a high inclination angle for AS 442. This hypothesis is compatible with observed optical variability in VV Ser and AS 442 ($\Delta V_{\rm VVSer} \sim 2$, $\Delta V_{\rm AS442} \sim 1$; Herbst & Shevchenko 1999), which has been attributed to variable obscuration from clumps of dust orbiting in inclined circumstellar disks. The AB Aur data, in contrast, are consistent with a circumstellar distribution that is within 35° of face-on. This agrees well with MST and is compatible with modeling of scattered light observed with the Hubble Space Telescope, which suggests an inclination angle $\lesssim 45°$ (Grady et al. 1999). The small amplitude of variability in AB Aur ($\Delta V \sim 0.25$; Herbst & Shevchenko 1999) is also consistent with this low inclination angle (under the assumption that variability is caused by time-dependent circumstellar obscuration). The low inclination angle does *not*, however, agree with mm-wave imaging in the ^{13}CO(1-0) line, which yields an estimated inclination of 76° for the AB Aur disk (Mannings & Sargent 1997).

The angular sizes determined from our observations are generally in good agreement with the non-inclined ($\phi = 0$) flat accretion disk models of HSVK for early-type Herbig Be stars, V1685 Cyg and MWC 1080, but not for the later-type stars, AB Aur, VV Ser, and AS 442 (the spectral type for VV Ser, A0, is uncertain by $\pm$5 spectral subclasses; Mora et al. 2001). In contrast, the sizes of sources derived from the earlier IOTA observations (MST) were often an order of magnitude larger than those predicted by the HSVK models, and on this basis MST ruled these models out.

HSVK determined the best-fit models for the SEDs of HAEBE sources by assuming a face-on disk geometry, adjusting the accretion rate to match the mid-IR flux,

Table 4.9. Comparison with Hillenbrand et al. (1992) Models

Source	$R^*_{\rm face-on}$ (AU)	$R^*_{\rm inclined}$ (AU)	$R_{\dot{M}=0}$ (AU)	$R_{\dot{M}\neq 0}$ (AU)
AB Aur	0.15 ± 0.01	0.16 ± 0.01	0.07	0.12
VV Ser	0.23 ± 0.01	0.25 ± 0.19	0.03	0.13
V1685 Cyg	0.64 ± 0.03	0.79 ± 0.13	0.44	0.71
AS 442	0.29 ± 0.04	0.31 ± 0.12	0.10	
MWC 1080	0.77 ± 0.02	0.85 ± 0.03	0.79	0.79

References. — $*$: Error bars based on 1-σ uncertainties of best-fit face-on and inclined accretion disk models.

and then adjusting the size of the inner hole to match the near-IR flux. We compare our results with theirs in a qualitative way by plotting the visibilities predicted by the HSVK models along with the observed PTI and IOTA visibilities in Figures 4.2, 4.4, 4.6, 4.8, and 4.10. For a more quantitative comparison, we use published luminosities, effective temperatures, and accretion rates (Hillenbrand et al. 1992) to calculate the inner radii predicted by flat accretion disk models with $T_{\rm in} = 2000$ K (Equations 4.13 and 4.14), and compare these estimates to our interferometric results (which were also derived assuming $T_{\rm in} = 2000$ K; §4.3.3.3). In Table 4.9, $R_{\rm face-on}$ and $R_{\rm inclined}$ are the inner radii determined by fitting the interferometric data to face-on and inclined accretion disk models, respectively (§4.3.3.3), and $R_{\dot{M}=0}$, $R_{\dot{M}\neq 0}$ are the radii calculated using the HSVK flat disk models without accretion, and with accretion effects included, respectively. No estimate of $\dot{M}$ is available for AS 442.

Our data for the later-type stars AB Aur, VV Ser, and AS 442 are fairly consistent with the puffed up inner disk models of DDN, assuming inner disk temperatures $\gtrsim 2000$ K. In contrast, puffed up inner disk models are completely incompatible with the PTI results for the very early-type stars in our sample, V1685 Cyg and MWC

Table 4.10. Comparison with Dullemond et al. (2001) Models

Source	$R^*_{\rm face-on}$ (AU)	$R^*_{\rm inclined}$ (AU)	R_{2000} (AU)	R_{1500} (AU)
AB Aur	0.23 ± 0.01	0.26 ± 0.03	0.32	0.57
VV Ser	0.36 ± 0.01	0.38 ± 0.14	0.24	0.42
V1685 Cyg	0.96 ± 0.05	1.17 ± 0.16	3.71	6.59
AS 442	0.47 ± 0.05	0.56 ± 0.13	0.52	0.93
MWC 1080	1.17 ± 0.02	1.24 ± 0.03	8.69	15.45

References. — $*$: Error bars based on 1-σ uncertainties of best-fit face-on and inclined ring models.

1080. The radius of the inner wall, $R_{\rm in}$, predicted by DDN is,

$$R_{\rm in} = \sqrt{\frac{L_*}{4\pi T_{\rm in}^4 \sigma}(1+f)}, \tag{4.21}$$

where, L_* is the (published) stellar luminosity, $T_{\rm in}$ is the temperature of the inner wall, and f is the ratio of the width of the inner wall to its radius. Based on DDN, we assume $f = 0.27$ for stars earlier than spectral type B6, and $f = 0.18$ for later-type stars. We calculate $R_{\rm in}$ for $T_{\rm in} = 1500, 2000$ K (likely sublimation temperatures for silicate and graphite dust grains, respectively), and compare these to the ring diameters derived from fitting to near-IR interferometric visibilities. In Table 4.10, $R_{\rm face-on}$ and $R_{\rm inclined}$ represent the inner radii determined for face-on and inclined ring models, respectively (§4.3.3.4), and R_{2000}, R_{1500} are the inner radii predicted by the DDN puffed-up inner disk models, assuming sublimation temperatures of 2000 and 1500 K, respectively.

We note that although the distances to the sources in our sample are fairly uncertain (see Appendix 4.6), the comparisons of our interferometric results to physical models should be insensitive to this uncertainty (as long as the physical models and interferometric data both use the same adopted distance). The inner radius is

$\propto L^{1/2} \propto d$, in both the DDN and HSVK models. Similarly, the linear sizes determined from our interferometric results (converted from modeled angular sizes) are $\propto d$.

Flat accretion disk models Hillenbrand et al. (1992) are generally in good agreement with the observed visibility data for early-type B-stars, while puffed up inner disk models (DDN) seem more consistent for later-type stars. We speculate that this could be due to different accretion mechanisms in earlier and later-type stars. A similar idea has been put forward based on the results of Hα spectropolarimetry, where differences in the observations for early-type HBe stars and later-type HAe stars have been attributed to a transition from disk accretion in higher-mass stars to magnetic accretion in lower-mass stars (Vink et al. 2003).

There is always the possibility that the visibilities for some of the observed HAEBE sources may be (partially) due to close companions. For AB Aur and MWC 1080, we can rule out binary models (with separations $\gtrsim 1$ mas) with a high degree of confidence. However, MWC 1080 is an eclipsing binary with a period of $P \approx 2.9$ days (Shevchenko et al. 1994; Corporon & Lagrange 1999). The separation is much too small to be detected by PTI, and the observed visibilities for this source are thus probably due to an inclined circum-*binary* disk. Observations over a time-span of ~ 100 days (Table 4.2), with visibilities that are fairly constant in time (Figures 4.6 and 4.7) provide some evidence against V1685 Cyg being a binary. As yet, the binarity status of AS 442 and VV Ser remain uncertain based on our visibility data, although radial velocity variations of spectral lines in AS 442 have been attributed to a binary with $P \approx 64$ days and $e \approx 0.2$ (Corporon & Lagrange 1999).

4.5 Summary

We observed the HAEBE sources AB Aur, VV Ser, V1685 Cyg (BD+40°4124), AS 442, and MWC 1080 at 2.2 μm with the Palomar Testbed Interferometer. These are only the second published near-IR interferometric observations of HAEBE stars. From these high angular resolution data, we determined the angular size scales and

orientations predicted by uniform disk, Gaussian, ring, and accretion disk models, and we examined whether the data were consistent with binary models. AB Aur appears to be surrounded by a disk that is inclined by $\lesssim 30°$, while VV Ser, V1685 Cyg, and MWC 1080 are associated with more highly inclined circumstellar disks. With the available data, we cannot distinguish between different radial distributions, such as Gaussians, uniform disks, rings, or accretion disks.

While the angular size scales determined in this work are generally consistent with the only other near-IR interferometric measurements of HAEBE stars by MST, our measurements are the first that show evidence for significantly inclined morphologies. Moreover, the derived angular sizes for early type Herbig Be stars in our sample, V1685 Cyg and MWC 1080, agree fairly well with those predicted by face-on accretion disk models used by HSVK to explain observed spectral energy distributions. The observations of AB Aur, VV Ser, and AS 442 are, however, not entirely compatible with these models, and may be better explained through the puffed-up inner disk models of DDN.

Acknowledgments. The new data presented in this paper were obtained at the Palomar Observatory using the Palomar Testbed Interferometer, which is supported by NASA contracts to the Jet Propulsion Laboratory. Science operations with PTI are possible through the efforts of the PTI Collaboration (`http://huey.jpl.nasa.gov/palomar/ptimembers.html`) and Kevin Rykoski. This research made use of software produced by the Michelson Science Center at the California Institute of Technology. We thank R. Millan-Gabet for providing us with the IOTA data, and for useful discussion. We are also grateful to S. Metchev and M. Konacki for obtaining the adaptive optics images and photometric data, and to C. Koresko, B. Thompson, and G. van Belle for useful comments on the manuscript. J.A.E. and B.F.L. are supported by Michelson Graduate Research Fellowships.

4.6 Appendix: Distance Estimates

AB Aur is associated with the Taurus-Auriga molecular cloud, and thus the estimated distance to this source ($d = 140$ pc) is accurate to $\sim 10\%$. Photometric studies of VV Ser and other stars in Serpens estimated distances of $d \approx 250$ pc (Chavarria-K. et al. 1988) and $d \approx 310$ pc (de Lara et al. 1991), while an earlier study based on photometry of a single source estimated $d = 440$ pc (Strom et al. 1974). Based on these estimates, we adopt a distance of 310 pc. Distance estimates to V1685 Cyg range from 980 pc (based on an extinction-distance diagram for 132 stars within 3.5°; Shevchenko et al. 1991) to 1000 pc (based on locating V1685 Cyg on the main sequence; Strom et al. 1972), to 2200 pc (based on photometry of stars in a large scale region around V1685 Cyg; Hiltner & Johnson 1956). We adopt a distance of $d = 1000$ pc to V1685 Cyg, since the 2200 pc estimate would imply a luminosity higher than expected for the published spectral type. AS 442 is associated with the North American Nebula, and thus the adopted distance of 600 pc is probably accurate to $\sim 10\%$. The distance to MWC 1080 has been determined by fitting photometric observations to the main sequence ($d = 1000$ pc; Hillenbrand et al. 1992), and using the Galactic rotation curve ($d = 2500$ pc; Canto et al. 1984). We adopt a distance of 1000 pc to MWC 1080, since the 2500 pc estimate based on the Galactic rotation curve would imply a luminosity much higher than expected for the published spectral type. Moreover, the 2500 pc estimate is uncertain by $\sim 50\%$, while the 1000 pc estimate is accurate to $\sim 20\%$.

Chapter 5

Resolved Inner Disks around Herbig Ae/Be Stars[1]

We have observed 14 Herbig Ae/Be sources with the long-baseline near-IR Palomar Testbed Interferometer. All except two sources are resolved at 2.2 μm, with angular sizes generally $\lesssim$ 5 mas. We determine the size scales and orientations of the 2.2 μm emission using various models: uniform disks, Gaussians, uniform rings, flat accretion disks with inner holes, and flared disks with puffed-up inner rims. Although it is difficult to distinguish different radial distributions, we are able to place firm constraints on the inclinations of most sources; 7 objects display significantly inclined morphologies. The inner disk inclinations derived from our near-IR data are generally compatible with the outer disk geometries inferred from millimeter interferometric observations, implying that HAEBE disks are not significantly warped. Using the derived inner disk sizes and inclinations, we compute the spectral energy distributions for two simple physical disk models, and compare these with observed SEDs compiled from the literature and new near-IR photometry. While geometrically flat accretion disk models are consistent with the data for the earliest spectral types in our sample (MWC 297, V1685 Cyg, and MWC 1080), the later-type sources are explained better through models incorporating puffed-up inner disk walls. The different inner disk geometries may indicate different accretion mechanisms for early and late-type Herbig Ae/Be stars.

[1]This chapter has been published previously as Eisner et al. (2004).

5.1 Introduction

Herbig Ae/Be (HAEBE; Herbig 1960) stars are intermediate-mass (2–10 $M_\odot$) young stellar objects that show broad emission lines, rapid variability, and excess infrared and millimeter-wavelength emission. These properties are consistent with the presence of hot and cold circumstellar dust and gas. While there is still some debate about the morphology of this circumstellar material, most evidence supports the hypothesis that in many cases the dust and gas lie in massive (~ 0.01 $M_\odot$) circumstellar disks (Natta et al. 2000; Hillenbrand et al. 1992).

The strongest evidence for circumstellar disks around HAEBE stars comes from near-IR and millimeter interferometry. Flattened structures around several sources have been resolved on $\lesssim 1$ AU scales in the near-IR (Eisner et al. 2003, hereafter, ELAHS) and on ~ 100 AU scales at millimeter wavelengths (Mannings & Sargent 1997, 2000; Piétu et al. 2003), and detailed kinematic modeling of one source, MWC 480, is consistent with rotation in a Keplerian disk (Mannings et al. 1997; Simon et al. 2000). Hα spectropolarimetric observations, which trace dust on scales of tens of stellar radii (Vink et al. 2002), and modeling of forbidden emission lines that arise in winds and outflows around HAEBE stars (Corcoran & Ray 1997) provide further evidence for disks. Finally, disk-like distributions of material around HAEBEs are suggested by modeling of spectral energy distributions (SEDs). Various models, including geometrically flat accretion disks (e.g., Hillenbrand et al. 1992), flared outer disks (e.g., Chiang & Goldreich 1997), and puffed-up inner disk rims (Dullemond, Dominik, & Natta 2001; hereafter DDN), have been used to fit the data (although the SEDs for some sources can also be explained by more spherically distributed dust; e.g., Hartmann et al. 1993).

Previous near-IR interferometric observations probed the inner disks around several HAEBE sources (Akeson et al. 2000; Millan-Gabet, Schloerb, & Traub 2001, hereafter MST; ELAHS; Wilkin & Akeson 2003; see also aperture masking results, Danchi, Tuthill, & Monnier 2001; Tuthill et al. 2002). Here, we expand the sample and obtain superior $u - v$ coverage, enabling measurements of size scales and orien-

tations of the inner disks around 14 HAEBEs. We present results for AB Aur, MWC 480, MWC 758, CQ Tau, T Ori, MWC 120, HD 141569, HD 158352, VV Ser, MWC 297, V1295 Aql, V1685 Cyg (BD+40°4124), AS 442, and MWC 1080. Two sources, HD 141569 and HD 158352, show no evidence of near-IR circumstellar emission and appear unresolved in our interferometric observations. The other 12 sources in our sample show resolved circumstellar emission, consistent with disks.

We model the structure of circumstellar dust within $\sim$ 0.1-1 AU of these HAEBE stars, fitting three simple geometrical models (Gaussians, uniform disks, and uniform rings), and two basic physical models (flat accretion disks with inner holes and flared passive disks with puffed-up inner walls). For each model, we determine approximate size scales, position angles, and inclinations of the near-IR circumstellar emission. Where possible, we compare our 2.2 μm interferometry results with previously published 1.6 μm and 2.2 μm interferometric data from the IOTA interferometer (Millan-Gabet et al. 2001). In addition, we compare our results with SEDs compiled from the literature and new data, and millimeter interferometric results (where available), in order to further constrain simple physical models of HAEBE disks.

5.2 Observations and Calibration

The Palomar Testbed Interferometer (PTI) is a fringe-tracking long-baseline near-IR Michelson interferometer located on Palomar Mountain near San Diego, CA (Colavita et al. 1999). PTI combines starlight from two 40-cm aperture telescopes using a Michelson beam combiner, and the resulting fringe visibilities provide a measure of the brightness distribution on the sky (via the van Cittert-Zernike theorem). PTI measures normalized squared visibilities, V^2, which provide unbiased estimates of the visibility amplitudes (Colavita 1999); V^2 is unity for point sources and smaller for resolved sources.

We observed 14 HAEBE sources with PTI between May, 2002 and January, 2004. Properties of the sample are included in Table 5.1. We obtained K-band (λ_0 = 2.2 μm, $\Delta\lambda$ = 0.4 μm) measurements on an 85-m North-West (NW) baseline for all 14

Table 5.1. Observed Sources

Source	Alt. Name	α (J2000)	δ (J2000)	d (pc)	Sp.Ty.	V	J	H	K	$F^{\dagger}_{\mathrm{K},*}$ (Jy)	$F^{\dagger}_{\mathrm{K,x}}$ (Jy)
AB Aur	HD 31293	$04^{\mathrm{h}}55^{\mathrm{m}}45.84^{\mathrm{s}}$	$+30°33'04.''3$	140	A0pe	7.1	6.4	5.3	4.5	1.65	9.11
MWC 480	HD 31648	$04^{\mathrm{h}}58^{\mathrm{m}}46.27^{\mathrm{s}}$	$+29°50'37.''0$	140	A2/3ep+sh	7.7	7.1	6.4	5.7	0.81	2.45
MWC 758	HD 36112	$05^{\mathrm{h}}30^{\mathrm{m}}27.53^{\mathrm{s}}$	$+25°19'57.''1$	150	A3e	8.3	7.4	6.5	5.8	0.53	2.54
CQ Tau	HD 36910	$05^{\mathrm{h}}35^{\mathrm{m}}58.47^{\mathrm{s}}$	$+24°44'54.''1$	150	A8V/F2IVea	10.3	8.2	7.4	6.5	0.35	1.38
T Ori	MWC 763	$05^{\mathrm{h}}35^{\mathrm{m}}50.40^{\mathrm{s}}$	$-05°28'35.''0$	450	A3/5ea	10.6	8.2	7.4	6.5	0.20	1.58
MWC 120	HD 37806	$05^{\mathrm{h}}41^{\mathrm{m}}02.29^{\mathrm{s}}$	$-02°43'00.''7$	500	B9Ve+sh	7.9	7.0	6.1	5.4	0.53	3.92
HD 141569	SAO 140789	$15^{\mathrm{h}}49^{\mathrm{m}}57.75^{\mathrm{s}}$	$-03°55'16.''4$	99	B9/A0V	7.1	6.8	6.8	6.7	1.29	0.02
HD 158352	SAO 122418	$17^{\mathrm{h}}28^{\mathrm{m}}49.65^{\mathrm{s}}$	$+00°19'50.''3$	63	A8V	5.4	5.1	4.9	4.9	8.36	-0.98
MWC 297	NZ Ser	$18^{\mathrm{h}}27^{\mathrm{m}}39.60^{\mathrm{s}}$	$-03°49'52.''0$	400	O9/B1Ve	12.3	6.0	4.5	3.3	11.65	44.44
VV Ser	HBC 282	$18^{\mathrm{h}}28^{\mathrm{m}}47.90^{\mathrm{s}}$	$+00°08'40.''0$	310	A0Vevp	11.9	8.6	7.5	6.3	0.21	2.16
V1295 Aql	HD 190073	$20^{\mathrm{h}}03^{\mathrm{m}}02.51^{\mathrm{s}}$	$+05°44'16.''7$	290	B9/A0Vp+sh	7.7	7.1	6.6	5.9	0.85	2.09
V1685 Cyg	BD+40°4124	$20^{\mathrm{h}}20^{\mathrm{m}}28.25^{\mathrm{s}}$	$+41°21'51.''6$	1000	B2Ve	10.7	7.9	6.8	5.9	0.49	2.91
AS 442	V1977 Cyg	$20^{\mathrm{h}}47^{\mathrm{m}}37.47^{\mathrm{s}}$	$+43°47'24.''9$	600	B8Ve	11.0	8.2	7.1	6.5	0.30	1.73
MWC 1080	V628 Cas	$23^{\mathrm{h}}17^{\mathrm{m}}26.10^{\mathrm{s}}$	$+60°50'43.''0$	1000	B0eq	11.7	7.4	6.0	4.8	0.87	9.85

References. — Distances, spectral types and V magnitudes from Hillenbrand et al. (1992), Thé et al. (1994), Mora et al. (2001), Strom et al. (1972), de Lara et al. (1991), Warren & Hesser (1978), and Bigay & Garner (1970). JHK magnitudes from the present work (§5.2.1). †: De-reddened fluxes at K-band.

Table 5.2. Summary of Observations

Source	Date (MJD)	Baseline	HA†	Calibrators (HD)
AB Aur	52575	NW	[1.21,1.85]	29645
	52601	NW	[-1.80,1.24]	29645,32301
	52602	NW	[-1.95,1.51]	29645,32301
	52925	NW	[-2.10,1.23]	29645,32301
	52926	SW	[-2.86,0.83]	29645,32301
MWC 480	52575	NW	[-1.61,0.34]	29645
	52601	NW	[-1.05,0.78]	29645,32301
	52602	NW	[-0.65,0.63]	29645,32301
	52925	NW	[-1.91,1.41]	29645,32301
	52926	SW	[-3.16,1.66]	29645,32301
MWC 758	52575	NW	[-0.54,0.34]	29645
	52601	NW	[-2.07,1.37]	29645,32301
	52602	NW	[-1.61,-1.61]	29645,32301
	52925	NW	[-1.39,1.09]	29645,32301
	52926	SW	[-3.28,0.51]	29645,32301
	52977	NW	[-1.40,-1.40]	29645,32301
	53018	NS	[-0.52,-0.52]	29645,32301
	53019	NS	[-1.94,1.11]	29645,32301
CQ Tau	52926	SW	[-1.19,0.66]	29645,32301
	52934	SW	[-1.87,-0.5]	29645,32301
	52977	NW	[-1.69,0.83]	29645,32301
	53017	NW	[-2.13,-1.32]	29645,32301
	53018	NS	[-0.34,-0.34]	29645,32301
	53019	NS	[-1.79,1.16]	29645,32301
T Ori	52977	NW	[-0.20,0.09]	33608,38858
	53017	NW	[-1.06,-0.82]	33608,38858
MWC 120	52977	NW	[0.21,0.21]	33608,38858
	53017	NW	[-0.70,-0.21]	33608,38858
HD 141569	52780	NW	[-0.31,0.46]	139137, 147449
	52781	NW	[-1.01,-1.01]	139137, 147449
	52787	NW	[-1.22,0.01]	139137, 147449
HD 158352	52775	NS	[-2.07,-1.38]	164259,161868
	52781	NW	[0.33,0.33]	164259,161868
	52788	NW	[-1.37,0.27]	164259,161868
MWC 297	52798	NW	[-1.91,-0.86]	164259,171834
	52826	NW	[-1.17,-0.03]	164259,171834
VV Ser	52490	NW	[-0.72,0.54]	171834

objects, on an 86-m South-West (SW) baseline for 8, and on a 110-m North-South (NS) baseline for 6. The NW baseline is oriented 109° west of north and has a fringe spacing of $\sim$ 5 mas, the SW baseline is 211° west of north with a $\sim$ 5 mas fringe spacing, and the NS baseline is 160° west of north and has a fringe spacing of $\sim$ 4 mas. A summary of the observations is given in Table 5.2.

Table 5.2 (cont'd)

Source	Date (MJD)	Baseline	HA†	Calibrators (HD)
	52491	NS	[-1.55,-0.74]	171834
	52493	NW	[-1.31,0.20]	171834
	52499	NW	[-0.96,0.84]	164259,171834
	52869	SW	[-0.25,-0.25]	164259,171834
V1295 Aql	52799	NW	[-1.28,-0.66]	187293
	52827	NW	[-0.81,-0.42]	187293,193556
	52828	NW	[-1.55,-0.03]	187293,193556
	52925	NW	[0.42,0.85]	187293,193556
	52926	SW	[0.19,0.88]	187293,193556
V1685 Cyg	52418	NW	[-1.10,-1.00]	192640,192985
	52475	NW	[-1.69,1.44]	192640,192985
	52476	NW	[-1.80,-0.48]	192640,192985
	52490	NW	[-0.97,1.70]	192640
	52491	NS	[-1.27,2.38]	192640
	52492	NW	[-0.90,-0.90]	192640
	52545	NS	[-1.12,2.48]	192640,192985
	52869	SW	[-1.24,0.71]	192640,192985
	52878	SW	[-0.76,1.08]	192640,192985
	52879	SW	[-0.49,0.23]	192640,192985
	52925	NW	[1.14,1.97]	192640,192985
	52926	SW	[0.94,1.19]	192640
AS 442	52475	NW	[0.21,1.33]	192640,192985
	52476	NW	[-0.21,-0.21]	192640,192985
	52490	NW	[-1.11,0.38]	192640
	52491	NS	[-0.69,2.54]	192640
	52492	NW	[-1.05,0.00]	192640
	52545	NS	[-0.87,1.58]	192640,192985
	52878	SW	[-0.99,0.86]	192640,192985
MWC 1080	52475	NW	[0.17,0.17]	219623
	52475	NW	[-1.99,0.52]	219623
	52490	NW	[-0.14,1.39]	219623

References. — †: Hour angle coverage of the observations.

For the sample, V^2 were measured from a synthetic wide-band channel formed from five spatially-filtered spectral pixels covering the K-band (Colavita 1999). Since PTI tracks the central ("white light") fringe, and the fringe spacings for PTI baselines are much smaller than the interferometric field of view ($\sim$ 50 mas; set by baseline lengths and spectral bandpass), the effects of spectral smearing on the K-band visibilities are negligible.

The visibilities were calibrated by observing sources of known angular size. Our adopted angular size for a calibrator is the average of three estimates based on 1) published stellar luminosity and distance, 2) a blackbody fit to published photometric data with the temperature constrained to that expected for the published spectral type, and 3) an unconstrained blackbody fit to the photometric data. We propagate

Table 5.3. Properties of Calibrator Sources

Name	α (J2000)	δ (J2000)	Sp.Ty.	V	K	Cal. Size (mas)	$\Delta\alpha$ (°)
HD 29645	$04^h41^m50.26^s$	$+38°16'48.''7$	G0V	6.0	4.6	0.56 ± 0.04	8.2^a,9.1^b,16.5^c,17.7^d
HD 32301	$05^h03^m05.75^s$	$+21°35'23.''9$	A7V	4.6	4.1	0.47 ± 0.11	9.1^a,8.3^b,7.3^c,8.2^d
HD 33608	$05^h11^m19.18^s$	$-02°29'26.''8$	F5V	5.9	4.8	0.47 ± 0.05	6.5^e,7.4^f
HD 38858	$05^h48^m34.94^s$	$-04°05'40.''7$	G4V	6.0	4.4	0.56 ± 0.01	3.2^e,2.3^f
HD 139137	$15^h36^m33.71^s$	$-00°33'41.''5$	G8III	6.5	4.3	0.57 ± 0.08	4.7^g
HD 147449	$16^h22^m04.35^s$	$+01°01'44.''5$	F0V	4.8	4.1	0.65 ± 0.04	9.4^g
HD 161868	$17^h47^m53.56^s$	$+02°42'26.''2$	A0V	3.8	3.8	0.62 ± 0.12	5.3^h
HD 164259	$18^h00^m29.01^s$	$-03°41'25.''0$	F2IV	4.6	3.7	0.77 ± 0.04	8.9^h,7.0^i,7.5^j
HD 171834	$18^h36^m39.08^s$	$+06°40'18.''5$	F3V	5.4	4.5	0.54 ± 0.06	9.1^i,6.8^j
HD 187293	$19^h52^m03.44^s$	$+11°37'42.''0$	G0V	6.2	4.8	0.49 ± 0.05	6.5^k
HD 193556	$20^h20^m20.52^s$	$+14°34'09.''3$	G8III	6.2	4.0	0.82 ± 0.05	9.8^k
HD 192640	$20^h14^m32.03^s$	$+36°48'22.''7$	A2V	4.9	4.9	0.46 ± 0.01	4.7^l,9.4^m
HD 192985	$20^h16^m00.62^s$	$+45°34'46.''3$	F5V	5.9	4.8	0.44 ± 0.03	4.3^l,5.9^m
HD 219623	$23^h16^m42.30^s$	$+53°12'48.''5$	F7V	5.6	4.3	0.54 ± 0.02	9.5^n

References. — $\Delta\alpha$ is the offset on the sky between target and calibrator. a: Offset from AB Aur. b: Offset from MWC 480. c: Offset from MWC 758. d: Offset from CQ Tau. e: Offset from T Ori. f: Offset from MWC 120. g: Offset from HD 141569. h: Offset from HD 158352. i: Offset from MWC 297. j: Offset from VV Ser. k: Offset from V1295 Aql. l: Offset from V1685 Cyg. m: Offset from AS 442. n: Offset from MWC 1080.

the errors on individual estimates to determine the uncertainty of the average size. Relevant properties of the calibrators used in these observations are given in Table 5.3. For a more thorough discussion of the data measurement and calibration procedures, see ELAHS.

5.2.1 PALAO Observations

In addition to the PTI data, we obtained adaptive optics images of the sources in our sample. As we discuss in §5.3.1, the adaptive optics data help distinguish between components of the PTI visibilities, including circumstellar emission, the central stars, and nearby companions.

Using the Palomar 200-inch adaptive optics system (PALAO; Troy et al. 2000) with the PHARO camera (Hayward et al. 2001) on November 17-18, 2002, January 13-14, 2003, and July 14-15, 2003, we imaged our sources in the JHK bands with a 25 mas plate scale and a 25″ field of view. We used 1% or 0.1% neutral density filters and short integration times to prevent saturation of the camera. After bias correction, flat-fielding, and background subtraction, the reduced images enabled searches for

any companions $\gtrsim 0\farcs05$ away from the target sources. Source counts were obtained from aperture photometry with sky subtraction, and photometric calibration was achieved using nearby sources with measured 2MASS photometry. The determined JHK magnitudes of our target sources are listed in Table 5.1. While the single-night uncertainty of the photometry is typically < 0.05 mags, night-to-night variations (due to variable seeing and small instrumental changes) limit the photometric accuracy to ~ 0.15 mags. Since AS 442 appears to be variable with a short timescale (probably days), Table 5.1 quotes the average of two measurements. For all objects, our photometry is consistent with previously published measurements to within ~ 0.3 magnitudes (2MASS; Hillenbrand et al. 1992; Malfait et al. 1998; de Winter et al. 2001; Eiroa et al. 2001).

5.3 Modeling

From the PTI data, we measured calibrated squared visibilities for all sources listed in Table 5.1. For each source, we constrain the angular size and geometry of the emission by fitting the visibility data with several simple models: Gaussians, uniform disks, uniform rings, flat accretion disks with inner holes, and flared passive disks with puffed-up inner walls. In this section, we describe the models, as well as corrections to the visibilities required to separate the circumstellar component from contributions by the central stars or nearby companions.

5.3.1 Visibility Corrections

5.3.1.1 Nearby Companions

Nearby companions that lie outside the interferometric field of view, ~ 50 mas, but within the field of view of the detector, $\sim 1''$, will contribute incoherent light to the visibilities, leading to measured visibilities smaller than the true values:

$$\frac{V^2_{\rm meas}}{V^2_{\rm true}} = \left(\frac{1}{1+10^{-\Delta K/2.5}}\right)^2, \tag{5.1}$$

where ΔK is the difference in K-band magnitudes between the two stars. Our PALAO Adaptive optics images of the sources in our sample (§5.2.1) show that most of these have no bright companions ($\Delta K < 5$) at distances between $\sim$ 50 mas and 1″, and thus no companion corrections are required ($V^2_{\rm true}/V^2_{\rm meas} > 0.98$). For MWC 1080, we measured $\Delta K = 2.70$ for a companion at 0.″78 separation (consistent with previous measurements by Corporon 1998) and Equation 5.1 yields a correction factor of 0.85. V1685 Cyg is also known to have a faint companion ($\Delta K = 5.50$; Corporon 1998), but its effects on the visibilities are negligible.

5.3.1.2 Stellar Emission

We account for the effect of the central star on the visibilities by including it in the models:

$$V^2_{\rm tot} = \left(\frac{F_* V_* + F_{\rm x} V_{\rm x}}{F_* + F_{\rm x}}\right)^2 \approx \left(\frac{F_* + F_{\rm x} V_{\rm x}}{F_* + F_{\rm x}}\right)^2, \tag{5.2}$$

where F_* is the stellar flux, $F_{\rm x}$ is the excess flux (both measured at 2.2 μm), $V_* \approx 1$ is the visibility of the (unresolved) central star, and $V_{\rm x}$ is the visibility due to the circumstellar component. It is reasonable to assume that $V_* \approx 1$, since for the stellar radii ($\sim$ 2–9 $R_\odot$) and distances ($\sim$ 140–1000 pc) for our sample, the angular diameters of the central stars will be < 0.2 mas. In the case of the binary model described below (§5.3.2.4), we do not perform any such correction, since the basic model already includes the stellar component.

Since HAEBE objects are often variable at near-IR wavelengths (e.g., Skrutskie et al. 1996), we obtained nearly contemporaneous photometric K-band measurements for our sample, as described in §5.2.1. As in ELAHS, we calculate F_* and $F_{\rm x}$ using our K-band photometry (Table 5.1) combined with BVRI photometry, visual extinctions, stellar radii, and effective temperatures from the literature (Herbst & Shevchenko 1999; Hillenbrand et al. 1992; Oudmaijer et al. 2001; de Winter et al. 2001; Eiroa et al. 2002; Vieira et al. 2003; Bigay & Garnier 1970). For several sources where literature values were not available, we computed the stellar parameters using the published spectral types and photometry. The spectral type gives the effective tem-

perature and expected color, from which we determine the extinction. We determine the stellar luminosity (using the adopted distance from Table 5.1) from a bolometric correction applied to the optical photometry, and stellar radius is given by the Stephan-Boltzmann equation. Assuming that all of the short-wavelength flux is due to the central star, we fit a blackbody at the assumed effective temperature to the de-reddened BVRI data. De-reddening uses the extinction law of Steenman & Thé (1991). The K-band stellar flux, F_*, is derived from the value of this blackbody curve at 2.2 μm, and the excess flux, $F_{\rm x}$, is given by the difference between the de-reddened observed flux and the stellar flux. The derived fluxes are given in Table 5.1.

The uncertainties in our K-band photometric measurements ($\sim$ 0.15 mags) and the uncertainties in the optical photometry used to determine the stellar contributions to the K-band fluxes lead to some uncertainties in the sizes inferred from the interferometric data. This uncertainty decreases for larger $F_{\rm x}/F_*$ ratios, and is typically $\lesssim$ 0.1 mas for the sources discussed here. CQ Tau, VV Ser, V1685 Cyg, and AS 442 are optically variable by $\Delta V \gtrsim 1$ magnitudes on timescales of days to months (while the other sources in our sample show little or no optical variability; Herbst & Shevchenko 1999), and thus F_* is somewhat uncertain. However, since $F_{\rm x}/F_* \gg 1$ for these objects, this uncertainty is relatively unimportant when modeling the visibilities.

Uncertainties in the calculation of stellar and circumstellar fluxes can also have a small effect on the measured inclinations. However, since the fluxes for our sample are dominated by the excess component, only large errors ($> 100\%$) in the flux estimation will produce measurable effects on the determined inclinations. Since our photometric errors are generally $\lesssim 10\%$, the effect on measured inclinations is negligible.

5.3.1.3 Extended Emission

Equation 5.2 assumes that the point-like central star and compact circumstellar emission contribute coherently to the visibilities. There may also be an incoherent component due to extended emission (either thermal or scattered) from tenuous dust. The excess flux, $F_{\rm x}$, would then be the sum of the compact circumstellar emission,

$F_{\rm comp}$, and the extended emission, $F_{\rm ext}$. Including the incoherent contribution in the visibilities would modify Equation 5.2 to:

$$V_{\rm tot}^2 = \left(\frac{F_* + F_{\rm comp} V_{\rm comp}}{F_* + F_{\rm comp} + F_{\rm ext}} \right)^2 = \left(\frac{F_* + [F_{\rm x} - F_{\rm ext}] V_{\rm x}}{F_* + F_{\rm x}} \right)^2, \qquad (5.3)$$

causing a reduction in the measured visibilities.

The existence of dust on large angular scales around some Herbig Ae/Be stars is illustrated by optical light scattered from dust grains far from the star (e.g., Grady et al. 1999). Furthermore, SED models that include large-scale optically thin dust, in addition to disks, usually fit the data well for HAEBE sources (Vinković et al. 2003, and references therein). Nevertheless, these observations do not measure the exact contribution of extended K-band emission, and our adaptive optics observations (§5.2.1) do not have sufficient sensitivity to detect faint emission above the halo of the point spread function within 1″ (the PTI field of view) of the central stars. Thus, we do not include the effect of incoherent emission when modeling the visibilities; i.e., we use Equation 5.2 in the analysis below.

Because our measured visibilities are found to depend on projected baseline (see §5.4.1), contrary to the baseline-independent visibilities expected for incoherent emission, the incoherent contribution is probably insignificant compared to the compact circumstellar component. Although small incoherent contributions may lead to estimated size scales slightly larger than true values, we show below in §5.4.2 that the effect is likely to be quite small, perhaps as high as a few percent in the worst case.

5.3.2 Compact Circumstellar Emission

For each source, we compare the observed visibilities to those derived from a uniform disk model, a Gaussian model, a ring model, a geometrically flat accretion disk model with an inner hole, and a flared passive disk with a puffed-up inner wall; all models are 2-D. The uniform disk, Gaussian, ring, and flat accretion disk models were discussed in ELAHS, and the basic equations are merely recalled here. In addition, we develop and implement a flared disk model with a puffed-up inner wall, which is a more

physically plausible model than any of those considered in ELAHS.

As in ELAHS, we consider both face-on and inclined models. If we assume that the inclination of the circumstellar material is zero, then the one remaining free parameter in the models is the angular size scale, θ. When we include inclination effects, we fit for three parameters: size (θ), inclination angle (ϕ), and position angle (ψ). Inclination is defined such that a face-on disk has $\phi = 0$, and position angle, ψ, is measured east of north. Inclination effects are included in the models via a simple coordinate transformation:

$$x' = x \sin\psi + y \cos\psi;\ y' = \frac{y \sin\psi - x \cos\psi}{\cos\phi}, \tag{5.4}$$

$$u' = u \sin\psi + v \cos\psi;\ v' = \cos\phi(v \sin\psi - u \cos\psi). \tag{5.5}$$

Here, (x, y),(u, v) are the original sky and $u - v$ plane coordinates, and (x', y'),(u', v') are the transformed coordinates.

In addition to these five models, we also examine whether the data are consistent with a wide binary model, which we approximate as two stationary point sources. For this model, the free parameters are the angular separation (θ), the position angle (ψ), and the brightness ratio of the two components (R).

We fit these models to the PTI data for each source by searching grids of parameters for the minimum χ^2_r value. The grid for face-on disk models was generated by varying θ from 0.01 to 10 mas in increments of 0.01 mas. For sources with adequate $u - v$ coverage (Figure 5.1), we also fit inclined disk models, where in addition to varying θ, we vary ϕ from 0° to 90° and ψ from 0° to 180°, both in increments of 1°. Since inclined disk models are symmetric under reflections through the origin, we do not explore position angles between 180° and 360°. For the binary model, we vary θ from 1 to 100 mas in increments of 0.01 mas, ψ from 0° to 180° in increments of 1°, and $R = F_2/F_1$ from 0.2 to 1 in increments of 0.001 (for flux ratios < 0.2 or angular separations < 1 mas, the effects of the companions on the visibilities will be negligible, and we can rule out angular separations $\gtrsim 100$ mas from adaptive optics imaging). Although binary models are not symmetric under reflections through the

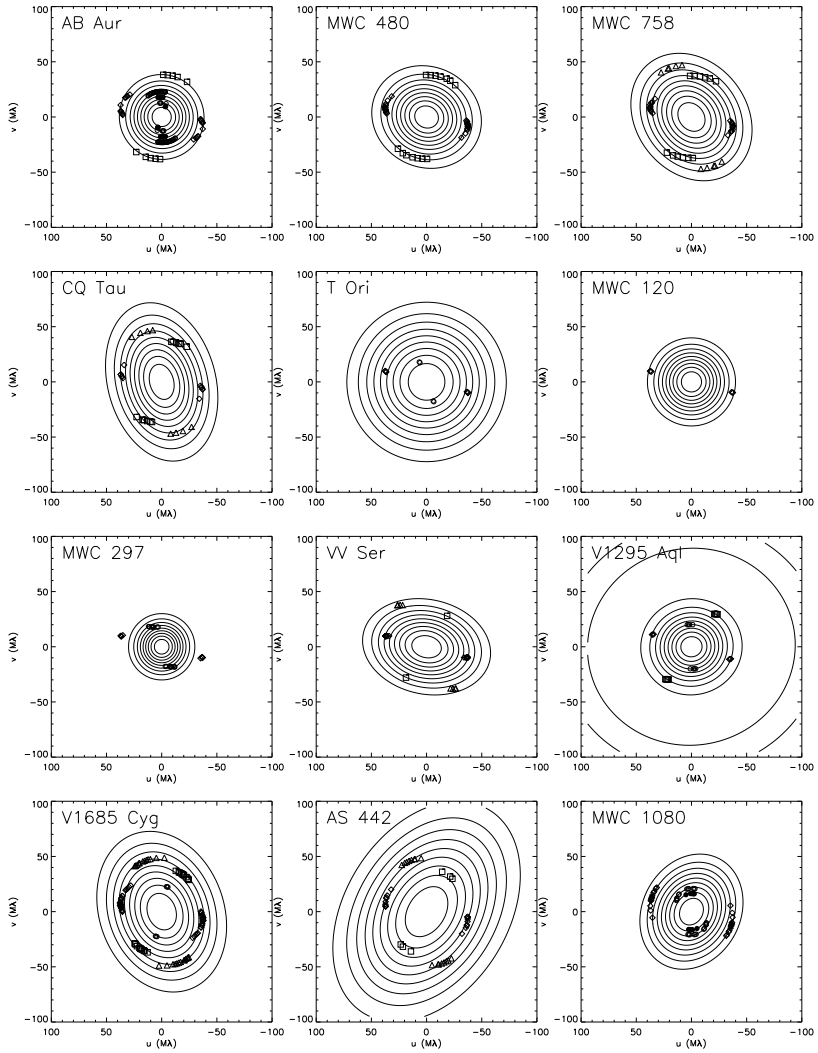

Figure 5.1 Contour plots of best-fit uniform disk models for AB Aur, MWC 480, MWC 758, CQ Tau, T Ori, MWC 120, MWC 297, VV Ser, V1295 Aql, V1685 Cyg, AS 442, and MWC 1080, whose parameters are listed in Table 5.4. We plot the best-fit inclined models except for T Ori, MWC 120, and MWC 297, where no inclination estimates are available, in which case we use the best-fit face-on models. For MWC 297, we have used the model determined from a combined fit to PTI+IOTA data (§5.4.2; Table 5.10), since the PTI visibilities only provide limits. The contour increment is 10% in V^2. We also plot the $u - v$ points sampled for each source by the PTI NW baseline (open diamonds), the PTI SW baseline (open squares), the PTI NS baseline (open triangles), and by IOTA (MST; H and K-band data, represented by open and filled circles, respectively).

origin, PTI does not measure phase and cannot distinguish 180°-rotated models; thus, we only consider position angles from 0° to 180°.

For each point in the parameter grid, we generate a model for the observed $u-v$ coverage, and calculate the reduced chi squared, χ^2_r, to determine the "best-fit" model. Standard 1-σ confidence limits for face-on models are determined by finding the grid points where the non-reduced χ^2 equals the minimum value plus 1. For inclined disk or binary models, the errors on each parameter correspond to an increment of 3.5 of the minimum χ^2 surface. The quoted uncertainties are not scaled by χ^2_r.

5.3.2.1 Simple Geometrical Disk Models

The normalized visibilities for a Gaussian, uniform disk, and uniform ring brightness distribution are,

$$V_{\rm gauss}(r_{\rm uv}) = \exp\left(-\frac{\pi^2\theta^2 r_{\rm uv}^2}{4\ln 2}\right), \tag{5.6}$$

$$V_{\rm uniform}(r_{\rm uv}) = 2\frac{J_1(\pi\theta r_{\rm uv})}{\pi\theta r_{\rm uv}}, \tag{5.7}$$

$$V_{\rm ring} = \frac{2}{\pi\theta r_{\rm uv}(2f+f^2)}\left[(1+f)J_1([1+f]\pi\theta r_{\rm uv}) - J_1(\pi\theta r_{\rm uv})\right]. \tag{5.8}$$

Here, (x, y) are the angular offsets from the central star, θ is the angular size scale (FWHM, diameter, and inner diameter for the Gaussian, uniform disk, and ring models, respectively), and $r_{\rm uv}$ is the "uv radius":

$$r_{\rm uv} = (u^2+v^2)^{1/2}. \tag{5.9}$$

For the ring model, $f = W/R$, where R is the radius of the inner edge of the ring, and W is the width of the ring. In order to facilitate comparison of this model to the more physical puffed up inner disk models (§5.3.2.3), we use ring widths derived from radiative transfer modeling by DDN (Table 1); for stars earlier than spectral type B6, we assume $f = 0.27$, and for stars later than B6, we assume $f = 0.18$. The models for the observed squared visibilities are obtained by substituting Equations 5.6, 5.7, or 5.8 for $V_{\rm x}$ in Equation 5.2.

5.3.2.2 Geometrically Flat Accretion Disk Model

We derive the brightness distribution and predicted visibilities for a geometrically thin irradiated accretion disk by determining the temperature and spectral energy distributions for a series of annuli extending from some inner radius, $R_{\rm in}$, to some outer radius, $R_{\rm out}$. We then weight the visibilities for each annulus (which are given by the ring visibilities described by Equation 5.8) by their SEDs to determine the visibilities expected for the entire disk.

For a disk heated by stellar radiation and accretion (Lynden-Bell & Pringle 1974), the temperature profile, $T_{\rm R}$, in the regime where $R_*/R \ll 1$, is given by $T_{\rm 1AU}\,(R/{\rm AU})^{-3/4}$. Here, $T_{\rm 1AU} = T_{\rm in}\,(R_{\rm in}/{\rm AU})^{3/4}$, where $T_{\rm in}$ is the temperature at the inner radius. We consider two values of $T_{\rm in}$: 1500 K and 2000 K. These are likely (upper limit) sublimation temperatures for silicate and graphite grains, respectively (e.g., Salpeter 1977; Pollack et al. 1994), and it is reasonable to assume that there is little or no dust emission interior to $R_{\rm in}$ (although the model does not exclude the possibility of optically thin gas interior to $R_{\rm in}$). We choose $R_{\rm out}$ to be the lesser of 100 AU or the radius at which $T_{\rm R} = 10$ K ($R_{\rm out}$ is not important in this analysis, since virtually all of the near-IR flux comes from the hotter inner regions of the disk).

The flux in an annulus specified by inner boundary $R_{\rm i}$ and outer boundary $R_{\rm f}$ is given by

$$F_{\rm annulus} = \frac{\pi}{d^2}[B_\nu(T_{\rm i}) + B_\nu(T_{\rm f})]R_{\rm i}(R_{\rm f} - R_{\rm i})\cos(\phi), \tag{5.10}$$

and the normalized visibilities for this annulus are (following Equation 5.8):

$$V_{\rm annulus} = \frac{2}{\pi r_{\rm uv}(\theta_{\rm f}^2 - \theta_{\rm i}^2)}\left[\theta_{\rm f} J_1(\pi\theta_{\rm f} r_{\rm uv}) - \theta_{\rm i} J_1(\pi\theta_{\rm i} r_{\rm uv})\right]. \tag{5.11}$$

Here, d is the distance to the source, ν is the observed frequency, B_ν is the Planck function, T is the temperature, R is the physical radius, θ is the angular size, ϕ is the inclination, $r_{\rm uv}$ is the "uv radius" (Equation 5.9), and i, f indicate the inner and outer boundaries of the annulus. To obtain the visibilities for the entire disk, we sum

the flux-weighted visibilities for each annulus and normalize by the total flux:

$$V_{\rm disk} = \frac{\sum_{R_{in}}^{R_{out}} F_{\rm annulus} V_{\rm annulus}}{\sum_{R_{in}}^{R_{out}} F_{\rm annulus}}. \quad (5.12)$$

The resultant model visibilities are obtained by substituting this expression for $V_{\rm x}$ into Equation 5.2.

As mentioned above, we compute the visibilities for models using $T_{\rm in} = 1500, 2000$ K. The main effect of $T_{\rm in}$ is that for lower temperatures, the flux difference between the inner several annuli is significantly larger (since we are on the Wien tail of the blackbody curve), leading to a smaller flux-weighted emitting region probed by the 2.2 μm visibilities. This smaller effective area for lower $T_{\rm in}$ leads to a slightly larger inner disk diameter (Equation 5.8). In practice, $T_{\rm in}$ is not a critical parameter since most of the 2.2 μm radiation in the disk comes from the innermost annulus.

5.3.2.3 Puffed-Up Inner Disk Model

We consider a two-layer flared disk model (Chiang & Goldreich 1997) with a puffed-up inner disk wall (Dullemond et al. 2001). The primary difference between this model and the geometrically flat model discussed above is the angle at which starlight is incident on the disk. While starlight tends to hit a flat disk at grazing angles, for this model the starlight is incident at larger angles and causes more heating of the disk at a given radius. This additional heating causes the disk to expand in the vertical direction (in order to maintain hydrostatic equilibrium), which leads to a puffed-up inner wall as well as flaring in the outer disk. Since stellar radiation is incident on the inner wall normally, most of the 2.2 μm flux is generated in this region.

As in the case of a geometrically flat disk (§5.3.2.2) we first calculate the radial temperature and SED distributions. The temperature distribution for this model has been discussed in detail by Chiang & Goldreich (1997) and DDN, but we present a brief outline of the equations here. For the flared two-layer disk we assume a radial dust surface density profile $\Sigma(R) = 10^5 (R/1{\rm AU})^{-1.5}$ g cm^{-2} and a flaring angle, α,

which defines the angle at which starlight impacts the disk:

$$\alpha = 0.4\left(\frac{R_*}{R}\right) + \frac{8}{7}\left(\frac{T_*}{T_{\rm c}}\right)^{4/7}\left(\frac{R}{R_*}\right)^{2/7}. \tag{5.13}$$

Here, R is the radial coordinate in the disk, $T_{\rm c} = GM_*\mu m_{\rm p}/kR_*$, M_* is the mass of the star, μ is the mean molecular weight, R_* is the stellar radius, and T_* is the stellar temperature. We define a flaring index, ξ, which corresponds to the exponent on the scale height as a function of radius minus one ($\gamma - 1$ in DDN). Following a simple hydrostatic equilibrium calculation from Chiang & Goldreich (1997), we have adopted a value for ξ of 2/7.

Assuming that the opacity in the disk is due to silicate dust (Draine & Lee 1984), we parameterize the opacity of the surface and interior layers using $\psi_{\rm surf}$ and $\psi_{\rm int}$:

$$\psi_{\rm surf} = \frac{\sum_{\nu=0}^{\infty} B_\nu(T_{\rm surf})\kappa_\nu\left(1 - \exp[-\Sigma(R)\kappa_\nu]\right)}{\sum_{\nu=0}^{\infty} B_\nu(T_{\rm surf})\kappa_\nu}, \tag{5.14}$$

$$\psi_{\rm int} = \frac{\sum_{\nu=0}^{\infty} B_\nu(T_{\rm int})\left(1 - \exp[-\Sigma(R)\kappa_\nu]\right)}{\sum_{\nu=0}^{\infty} B_\nu(T_{\rm int})}. \tag{5.15}$$

The temperature of the surface layer is determined from

$$T_{\rm surf} = \epsilon_{\rm s}^{-0.25}\left(\frac{R_*}{2R}\right)^{0.5} T_*. \tag{5.16}$$

Here, $\epsilon_{\rm s} = \kappa_p(T_{\rm surf})/\kappa_p(T_*)$, where κ_p is the Planck mean opacity. The interior temperature is then given by

$$T_{\rm int} = \left(\frac{\alpha\psi_{\rm surf}}{2\psi_{\rm int}}\right)^{0.25}\left(\frac{R_*}{R}\right)^{0.5} T_*. \tag{5.17}$$

Equations 5.14–5.17 are solved iteratively. The SED of an annulus is given by summing the contributions from the surface and the interior. We denote the surface temperatures at the inner and outer radii of the annulus by $T_{\rm si}, T_{\rm sf}$, and the interior

temperatures by $T_{\rm ii}, T_{\rm if}$. The surface component of the SED is given by

$$F_{\rm surf} = \frac{\pi}{d^2}[B_\nu(T_{\rm si}) + B_\nu(T_{\rm sf})]R_{\rm i}(R_{\rm f} - R_{\rm i})\left(1 + \exp[-\Sigma(R_{\rm i})\kappa_\nu/\cos(\phi)]\right)\kappa_\nu\Delta\Sigma, \quad (5.18)$$

where

$$\Delta\Sigma = \frac{\psi_{\rm int}}{\psi_{\rm surf}}\left(\frac{T_{\rm ii}}{T_{\rm si}}\right)^4\frac{1}{2\kappa_p}. \quad (5.19)$$

For the interior,

$$F_{\rm int} = \frac{\pi}{d^2}[B_\nu(T_{\rm ii}) + B_\nu(T_{\rm if})]R_{\rm i}(R_{\rm f} - R_{\rm i})\left(1 - \exp[-\Sigma(R_{\rm i})\kappa_\nu/\cos(\phi)]\right)\cos(\phi). \quad (5.20)$$

In addition to the surface and interior layers of the disk, a puffed-up inner disk wall is included in the model. We choose the radius of this inner rim, $R_{\rm in}$, to be the radius where $T = T_{\rm in}$ ($R_{\rm in}$ also defines the inner radius of the flared disk component). We consider $T_{\rm in} = 1500, 2000$ K, likely sublimation temperatures of graphite and silicate grains, respectively. Because the wall is directly exposed to stellar radiation (instead of the glancing angles encountered in a geometrically thin disk model), the inner rim puffs up, attaining a height given by

$$H_{\rm rim} = \chi_{\rm rim}\sqrt{\frac{kT_{\rm in}R_{\rm in}^3}{\mu m_{\rm p}GM_*}}. \quad (5.21)$$

$\chi_{\rm rim}$ is a dimensionless quantity that describes how the disk height depends on the stellar luminosity. For the stars in our sample, we adopt typical values of $\chi_{\rm rim} = 5.3$ for stars later than spectral type B6, and $\chi_{\rm rim} = 4.5$ for earlier spectral types (Dullemond et al. 2001). The emergent flux from the rim contributes only to the innermost annulus:

$$F_{\rm rim}(R_{\rm in}) = \frac{4R_{\rm in}H_{\rm rim}}{d^2}B_\nu(T_{\rm in}). \quad (5.22)$$

While DDN included the effects of inclination, for simplicity we ignore those here. In effect, this corresponds to assuming a different shape for the inner disk wall; DDN assumed a thin cylindrical annulus, and we adopt a more toroidal shape.

The total flux for each annulus is given by

$$F_{\rm annulus} = F_{\rm int} + F_{\rm surf} + F_{\rm rim}, \tag{5.23}$$

where $F_{\rm rim}$ is zero everywhere but the innermost annulus. To determine the visibilities for the entire disk, we sum the flux-weighted visibilities for each annulus, and normalize by the total flux (Equation 5.12). When calculating the visibilities for each annulus, we retain the approximation of a geometrically flat inner disk[2] and use Equation 5.11. Thus, the normalized squared visibilities for this model are computed using Equations 5.23, 5.11, 5.12, and 5.2.

As discussed in §5.3.2.2, the fitted inner disk sizes are not particularly sensitive to the choice of $T_{\rm in}$. However, for the puffed-up inner disk model, fitted sizes will be slightly *smaller* for lower values of $T_{\rm in}$. The puffed-up inner rim is much hotter than the flared disk component and, as the rim temperature decreases, the difference in flux between the rim and inner disk annuli decreases. This leads to a larger flux-weighted effective area, which, in turn, leads to smaller fitted sizes (Equation 5.8). While we have ignored the effect of the shadow cast by the inner rim onto the disk (Dullemond et al. 2001), this will not significantly alter the results since the fitted sizes are relatively insensitive to the temperature difference between the rim and the disk. We also note that of the two values of $T_{\rm in}$ considered, models with $T_{\rm in} = 2000$ K have a larger temperature difference between the puffed-up rim and the inner disk annuli, and thus more closely approximate the effects of shadowing.

[2]This approximation is valid for the inner disk (where the K-band emission arises) because flaring is negligible in the inner regions. Moreover, the vertical puffing of the inner rim will cause little deviation between the true and approximate visibilities. Even in the edge-on case, the approximation will not be far-off since the minor axis is essentially unresolved in either the true or approximate model.

5.3.2.4 Binary Model

This model simulates a wide binary, where visibilities are effectively due to two stationary point sources. The squared visibilities for the binary model are,

$$V^2_{\rm binary} = \frac{1 + R^2 + 2R\cos\left(\frac{2\pi}{\lambda}\vec{B}\cdot\vec{s}\right)}{(1+R)^2}, \tag{5.24}$$

where $(\vec{B}\cdot\vec{s})/\lambda = \theta[u\sin(\psi) + v\cos(\psi)]$, θ is the angular separation of the binary, ψ is the position angle, R is the ratio of the fluxes of the two components, and λ is the observed wavelength.

5.4 Results and Analysis

5.4.1 PTI Results

Disk models fit the PTI data reasonably well for most sources in our sample. All sources except HD 141569 and HD 158352 are resolved, with uniform disk diameters between $\sim$ 2.5 and 5.8 mas, and most sources show evidence for non-symmetric circumstellar distributions. While a nearly circularly symmetric distribution appears appropriate for AB Aur, the data for MWC 480, MWC 758, CQ Tau, VV Ser, V1685 Cyg, AS 442, and MWC 1080 show evidence for significantly non-zero inclinations. A high inclination cannot be ruled out for V1295 Aql, and the data for T Ori, MWC 120, and MWC 297 are insufficient to constrain the inclinations.

Tables 5.4–5.8 list the fitted parameters and χ^2_r values for various disk models. Columns 2 and 3 list the χ^2_r values and best-fit angular size scales (θ) for face-on models, and columns 4-7 list the χ^2_r, sizes (θ), position angles (ψ), and inclinations (ϕ) for inclined models. The $u-v$ coverage for T Ori, MWC 120, and MWC 297 is insufficient to fit inclined disk models, and for these sources we constrain only the angular size scales of face-on disk models. Table 5.8, which lists the fitted parameters for flared disk models with puffed-up inner walls, does not include MWC 297, V1685 Cyg, and MWC 1080, the sources with the earliest spectral types in our sample. For

Table 5.4. Uniform Disk Models

Source	Face-On Models χ^2_r	Face-On Models θ (mas)	Inclined Models χ^2_r	Inclined Models θ (mas)	Inclined Models ψ (°)	Inclined Models ϕ (°)
AB Aur	2.008	$5.31^{+0.01}_{-0.01}$	2.112	$5.34^{+0.06}_{-0.05}$	130^{+50}_{-130}	9^{+6}_{-9}
MWC 480	5.196	$4.85^{+0.01}_{-0.02}$	1.543	$4.99^{+0.07}_{-0.05}$	154^{+16}_{-13}	26^{+4}_{-2}
MWC 758	4.695	$3.69^{+0.02}_{-0.02}$	0.789	$4.15^{+0.10}_{-0.10}$	128^{+3}_{-4}	36^{+2}_{-3}
CQ Tau	5.567	$3.68^{+0.05}_{-0.05}$	0.975	$4.38^{+0.18}_{-0.19}$	105^{+5}_{-5}	48^{+3}_{-5}
T Ori	1.001	$2.71^{+0.11}_{-0.11}$				
MWC 120	2.736	$4.94^{+0.04}_{-0.03}$				
MWC 297		> 5.02				
VV Ser	6.077	$3.68^{+0.03}_{-0.03}$	0.816	$4.49^{+0.87}_{-0.46}$	168^{+22}_{-12}	43^{+10}_{-5}
V1295 Aql	0.623	$5.57^{+0.04}_{-0.04}$	0.716	$5.77^{+0.62}_{-0.27}$	10^{+170}_{-10}	19^{+41}_{-19}
V1685 Cyg	6.805	$3.25^{+0.01}_{-0.02}$	3.905	$3.59^{+0.07}_{-0.06}$	110^{+3}_{-4}	41^{+3}_{-2}
AS 442	1.039	$2.44^{+0.06}_{-0.06}$	0.872	$2.74^{+0.26}_{-0.29}$	58^{+59}_{-11}	47^{+28}_{-33}
MWC 1080	1.251	$4.09^{+0.01}_{-0.02}$	0.466	$4.13^{+0.24}_{-0.05}$	55^{+12}_{-45}	34^{+23}_{-15}

References. — Columns 2-3 contain the reduced chi squared and angular size values for best-fit face-on disk models. Columns 4-7 list χ^2_r, angular size, position angle, and inclination for best-fit inclined disk models. For T Ori, MWC 120, and MWC 297, we fit only face-on models, and the quoted angular size for MWC 297 is a lower limit.

these objects, the puffed-up inner wall model cannot fit the visibility data ($\chi^2_r \gg 100$), since the early-type central stars lead to hot inner disks at radii much larger than allowed by the PTI data.

Table 5.5. Gaussian Models

Source	Face-On Models χ^2_r	Face-On Models θ (mas)	Inclined Models χ^2_r	Inclined Models θ (mas)	Inclined Models ψ (°)	Inclined Models ϕ (°)
AB Aur	4.365	$3.60^{+0.01}_{-0.01}$	3.279	$3.69^{+0.04}_{-0.04}$	157^{+33}_{-157}	16^{+3}_{-3}
MWC 480	5.860	$3.21^{+0.02}_{-0.01}$	1.330	$3.36^{+0.07}_{-0.05}$	149^{+17}_{-9}	32^{+4}_{-4}
MWC 758	2.715	$2.34^{+0.01}_{-0.01}$	0.598	$2.57^{+0.08}_{-0.07}$	130^{+6}_{-5}	33^{+4}_{-4}
CQ Tau	4.470	$2.32^{+0.03}_{-0.04}$	0.871	$2.75^{+0.13}_{-0.13}$	104^{+6}_{-6}	48^{+4}_{-5}
T Ori	1.006	$1.64^{+0.07}_{-0.07}$				
MWC 120	3.576	$3.29^{+0.04}_{-0.03}$				
MWC 297		> 3.35				
VV Ser	7.963	$2.33^{+0.02}_{-0.01}$	0.802	$2.92^{+0.63}_{-0.29}$	173^{+20}_{-16}	47^{+9}_{-4}
V1295 Aql	0.697	$3.85^{+0.04}_{-0.05}$	0.666	$4.29^{+1.20}_{-0.50}$	110^{+70}_{-110}	50^{+30}_{-50}
V1685 Cyg	6.145	$2.00^{+0.02}_{-0.01}$	3.895	$2.21^{+0.05}_{-0.04}$	110^{+4}_{-4}	41^{+3}_{-3}
AS 442	1.000	$1.49^{+0.04}_{-0.04}$	0.868	$1.66^{+0.17}_{-0.18}$	57^{+62}_{-12}	47^{+30}_{-36}
MWC 1080	1.462	$2.59^{+0.01}_{-0.01}$	0.460	$2.62^{+0.16}_{-0.03}$	56^{+10}_{-41}	40^{+25}_{-17}

References. — Columns defined as in Table 5.4.

Table 5.6. Ring Models

Source	Face-On Models χ^2_r	Face-On Models θ (mas)	Inclined Models χ^2_r	Inclined Models θ (mas)	Inclined Models ψ (°)	Inclined Models ϕ (°)
AB Aur	2.263	$3.23^{+0.01}_{-0.01}$	2.016	$3.25^{+0.03}_{-0.02}$	105^{+75}_{-105}	9^{+5}_{-9}
MWC 480	4.879	$2.97^{+0.01}_{-0.01}$	1.390	$3.05^{+0.03}_{-0.03}$	155^{+17}_{-14}	24^{+3}_{-2}
MWC 758	6.149	$2.31^{+0.01}_{-0.01}$	0.938	$2.62^{+0.05}_{-0.05}$	127^{+3}_{-4}	37^{+2}_{-2}
CQ Tau	6.254	$2.30^{+0.03}_{-0.02}$	1.033	$2.75^{+0.10}_{-0.11}$	106^{+4}_{-5}	48^{+3}_{-4}
T Ori	1.000	$1.73^{+0.06}_{-0.06}$				
MWC 120	2.339	$3.03^{+0.02}_{-0.02}$				
MWC 297		> 2.95				
VV Ser	5.194	$2.30^{+0.01}_{-0.01}$	0.822	$2.80^{+0.50}_{-0.31}$	165^{+13}_{-10}	42^{+10}_{-7}
V1295 Aql	0.647	$3.37^{+0.02}_{-0.01}$	0.748	$3.76^{+0.23}_{-0.42}$	16^{+164}_{-0}	33^{+23}_{-33}
V1685 Cyg	7.198	$1.96^{+0.01}_{-0.01}$	3.914	$2.18^{+0.04}_{-0.04}$	110^{+3}_{-4}	41^{+3}_{-2}
AS 442	1.062	$1.55^{+0.04}_{-0.04}$	0.874	$1.74^{+0.17}_{-0.17}$	59^{+57}_{-9}	46^{+28}_{-30}
MWC 1080	0.706	$2.55^{+0.01}_{-0.01}$	0.344	$2.57^{+0.24}_{-0.02}$	56^{+123}_{-56}	28^{+21}_{-18}

References. — Columns defined as in Table 5.4.

Table 5.7. Geometrically Flat Accretion Disk Models

Source	Face-On Models χ^2_r	Face-On Models θ (mas)	Inclined Models χ^2_r	Inclined Models θ (mas)	Inclined Models ψ (°)	Inclined Models ϕ (°)
$T_{\rm in} = 2000$ K						
AB Aur	2.549	$2.24^{+0.01}_{-0.01}$	2.465	$2.26^{+0.03}_{-0.01}$	148^{+32}_{-148}	10^{+6}_{-4}
MWC 480	5.479	$2.03^{+0.01}_{-0.01}$	1.333	$2.10^{+0.03}_{-0.02}$	153^{+15}_{-12}	28^{+5}_{-2}
MWC 758	3.395	$1.51^{+0.01}_{-0.01}$	0.660	$1.69^{+0.03}_{-0.05}$	129^{+5}_{-4}	35^{+3}_{-4}
CQ Tau	4.846	$1.50^{+0.02}_{-0.02}$	0.898	$1.78^{+0.08}_{-0.08}$	105^{+5}_{-6}	48^{+4}_{-5}
T Ori	1.007	$1.08^{+0.04}_{-0.04}$				
MWC 120	3.057	$2.09^{+0.02}_{-0.02}$				
MWC 297		> 2.12				
VV Ser	7.195	$1.52^{+0.01}_{-0.01}$	0.804	$1.86^{+0.40}_{-0.18}$	172^{+20}_{-15}	45^{+10}_{-4}
V1295 Aql	0.631	$2.37^{+0.02}_{-0.01}$	0.694	$2.39^{+0.30}_{-0.05}$	135^{+45}_{-135}	12^{+22}_{-12}
V1685 Cyg	6.330	$1.32^{+0.01}_{-0.01}$	3.896	$1.46^{+0.03}_{-0.03}$	110^{+4}_{-4}	41^{+3}_{-2}
AS 442	1.004	$0.98^{+0.02}_{-0.03}$	0.869	$1.10^{+0.11}_{-0.12}$	57^{+62}_{-12}	48^{+29}_{-35}
MWC 1080	1.372	$1.69^{+0.01}_{-0.01}$	0.461	$1.71^{+0.10}_{-0.02}$	56^{+9}_{-42}	38^{+24}_{-17}
$T_{\rm in} = 1500$ K						
AB Aur	2.071	$2.49^{+0.01}_{-0.01}$	2.205	$2.50^{+0.03}_{-0.01}$	136^{+44}_{-136}	8^{+7}_{-8}
MWC 480	5.262	$2.27^{+0.01}_{-0.01}$	1.342	$2.34^{+0.03}_{-0.02}$	152^{+18}_{-11}	27^{+4}_{-3}
MWC 758	4.233	$1.71^{+0.01}_{-0.01}$	0.738	$1.93^{+0.04}_{-0.05}$	128^{+4}_{-4}	36^{+2}_{-4}
CQ Tau	5.309	$1.71^{+0.02}_{-0.03}$	0.944	$2.03^{+0.09}_{-0.08}$	105^{+5}_{-5}	48^{+4}_{-5}
T Ori	1.003	$1.25^{+0.05}_{-0.05}$				
MWC 120	2.795	$2.33^{+0.01}_{-0.02}$				
MWC 297		> 2.36				
VV Ser	6.434	$1.72^{+0.01}_{-0.01}$	0.810	$2.11^{+0.42}_{-0.22}$	169^{+22}_{-9}	44^{+10}_{-5}
V1295 Aql	0.623	$2.62^{+0.02}_{-0.01}$	0.712	$2.67^{+0.32}_{-0.08}$	3^{+177}_{-3}	14^{+25}_{-14}
V1685 Cyg	6.631	$1.51^{+0.01}_{-0.01}$	3.903	$1.67^{+0.04}_{-0.02}$	110^{+3}_{-4}	41^{+3}_{-2}

Table 5.7 (cont'd)

Source	Face-On Models χ^2_r	θ (mas)	Inclined Models χ^2_r	θ (mas)	ψ (°)	ϕ (°)
AS 442	1.024	$1.13^{+0.03}_{-0.03}$	0.871	$1.26^{+0.13}_{-0.13}$	58^{+60}_{-8}	46^{+18}_{-33}
MWC 1080	1.300	$1.92^{+0.01}_{-0.01}$	0.471	$1.94^{+0.0.}_{-0.02}$	54^{+13}_{-43}	35^{+19}_{-16}

References. — Columns defined as in Table 5.4.

In Table 5.9, we present the angular separations (θ), position angles (ψ), and brightness ratios (R) for binary models. The $u-v$ coverage for T Ori, MWC 120, and MWC 297 is insufficient to fit binary models, and these sources are therefore absent from Table 5.9. The best-fit binary separations for all sources in our sample are $\gtrsim 2.5$ mas. For the distances and approximate masses of the sources in our sample, these separations correspond to orbital periods of $\gtrsim 2$ years. For most objects, observations span several months, and our assumption that the two point sources in the binary model are stationary is reasonable. This assumption may break down for short-period binaries in sources with observations spanning more than 1 year (see Table 5.2). However, short-period orbits would produce visibilities that vary with time, and no time-variation is detected.

Figures 5.2–5.12 show plots of observed V^2 for each source along with the curves predicted by various models. Inclined disk and binary models are not circularly symmetric, and the visibilities are a function of the observed position angle in addition to the projected baseline (Figure 5.1). Thus, for sources with sufficient data to constrain the inclination, we have plotted V^2 as a function of both $r_{\rm uv}$ and hour angle. Since we were only able to derive lower limits on the angular size scales for MWC 297, we do not plot the models for this source here.

AB Aur, VV Ser, V1685 Cyg, AS 442, and MWC 1080 were discussed in ELAHS. Here, we have obtained additional data on additional baselines for all except MWC 1080, and the greatly enhanced $u-v$ coverage, shown in Figure 5.1, enables firmer constraints on the models. We include MWC 1080 in the present discussion largely

Table 5.8. Flared Disk Models with Puffed-Up Inner Walls

Source	Face-On Models χ^2_r	Face-On Models θ (mas)	Inclined Models χ^2_r	Inclined Models θ (mas)	Inclined Models ψ (°)	Inclined Models ϕ (°)
			$T_{\rm in} = 2000$ K			
AB Aur	1.994	$3.35^{+0.01}_{-0.01}$	2.163	$3.37^{+0.05}_{-0.03}$	130^{+50}_{-130}	8^{+7}_{-8}
MWC 480	4.919	$3.22^{+0.01}_{-0.01}$	1.387	$3.31^{+0.03}_{-0.03}$	156^{+16}_{-15}	24^{+4}_{-2}
MWC 758	5.858	$2.49^{+0.01}_{-0.01}$	0.921	$2.85^{+0.06}_{-0.05}$	127^{+3}_{-4}	37^{+2}_{-2}
CQ Tau	6.254	$2.51^{+0.04}_{-0.03}$	1.034	$3.01^{+0.10}_{-0.13}$	106^{+4}_{-5}	48^{+3}_{-4}
T Ori	1.006	$1.78^{+0.09}_{-0.10}$				
MWC 120	2.340	$3.31^{+0.02}_{-0.02}$				
VV Ser	5.287	$2.50^{+0.01}_{-0.02}$	0.820	$3.05^{+0.31}_{-0.21}$	165^{+15}_{-5}	42^{+6}_{-2}
V1295 Aql	0.646	$3.67^{+0.02}_{-0.02}$	0.765	$3.84^{+0.47}_{-0.20}$	14^{+166}_{-14}	21^{+19}_{-21}
AS 442	0.990	$1.57^{+0.06}_{-0.07}$	0.871	$1.83^{+0.19}_{-0.27}$	57^{+59}_{-11}	48^{+24}_{-38}
			$T_{\rm in} = 1500$ K			
AB Aur	4.320	$3.13^{+0.01}_{-0.01}$	3.404	$3.15^{+0.06}_{-0.01}$	155^{+25}_{-155}	16^{+3}_{-3}
MWC 480	5.052	$3.16^{+0.01}_{-0.02}$	1.474	$3.27^{+0.03}_{-0.02}$	145^{+9}_{-6}	28^{+2}_{-1}
MWC 758	5.033	$2.42^{+0.01}_{-0.02}$	0.867	$2.78^{+0.08}_{-0.06}$	127^{+4}_{-3}	36^{+3}_{-2}
CQ Tau	6.211	$2.50^{+0.04}_{-0.03}$	1.032	$3.00^{+0.11}_{-0.12}$	106^{+4}_{-5}	48^{+3}_{-4}
T Ori	2.246	$1.41^{+0.23}_{-0.07}$				
MWC 120	2.348	$3.30^{+0.02}_{-0.02}$				
VV Ser	5.585	$2.47^{+0.01}_{-0.02}$	0.818	$3.02^{+0.32}_{-0.24}$	166^{+17}_{-6}	42^{+6}_{-2}
V1295 Aql	0.643	$3.65^{+0.02}_{-0.02}$	0.751	$3.85^{+0.38}_{-0.24}$	14^{+166}_{-14}	23^{+15}_{-23}
AS 442	1.628	$1.36^{+0.02}_{-0.05}$	0.863	$1.49^{+0.32}_{-0.31}$	53^{+58}_{-11}	58^{+16}_{-40}

References. — Columns defined as in Table 5.4. MWC 297, V1685 Cyg, and MWC 1080 are excluded from this table because the puffed-up inner disk wall model cannot fit the data for these sources.

Table 5.9. Binary Models

Source	χ^2_r	θ (mas)	ψ ($^\circ$)	R
AB Aur	117.08	$4.06^{+0.01}_{-0.01}$	28^{+1}_{-1}	$0.71^{+0.01}_{-0.01}$
MWC 480	13.46	$3.24^{+0.03}_{-0.03}$	127^{+1}_{-1}	$0.43^{+0.01}_{-0.01}$
MWC 758	14.50	$2.69^{+0.02}_{-0.03}$	26^{+1}_{-1}	$0.48^{+0.01}_{-0.02}$
CQ Tau	4.408	$2.95^{+0.05}_{-0.06}$	32^{+1}_{-1}	$0.48^{+0.03}_{-0.04}$
VV Ser	0.750	$9.27^{+3.44}_{-2.74}$	175^{+1}_{-172}	$0.55^{+0.16}_{-0.03}$
V1295 Aql	0.692	$3.09^{+2.52}_{-0.20}$	109^{+25}_{-102}	$0.43^{+0.33}_{-0.02}$
V1685 Cyg	14.90	$3.61^{+0.04}_{-0.05}$	135^{+1}_{-1}	$0.28^{+0.01}_{-0.01}$
AS 442	0.864	$2.69^{+0.21}_{-0.69}$	30^{+19}_{-8}	$0.20^{+0.07}_{-0.01}$
MWC 1080	0.774	$2.55^{+0.11}_{-0.31}$	63^{+5}_{-5}	$0.38^{+0.05}_{-0.01}$

References. — Columns 2-5 list the reduced chi squared values, angular separations, position angles, and brightness ratios of best-fit binary models. T Ori, MWC 120, and MWC 297 are excluded from this table because the limited $u-v$ coverage for these sources is insufficient to constrain the parameters of the model.

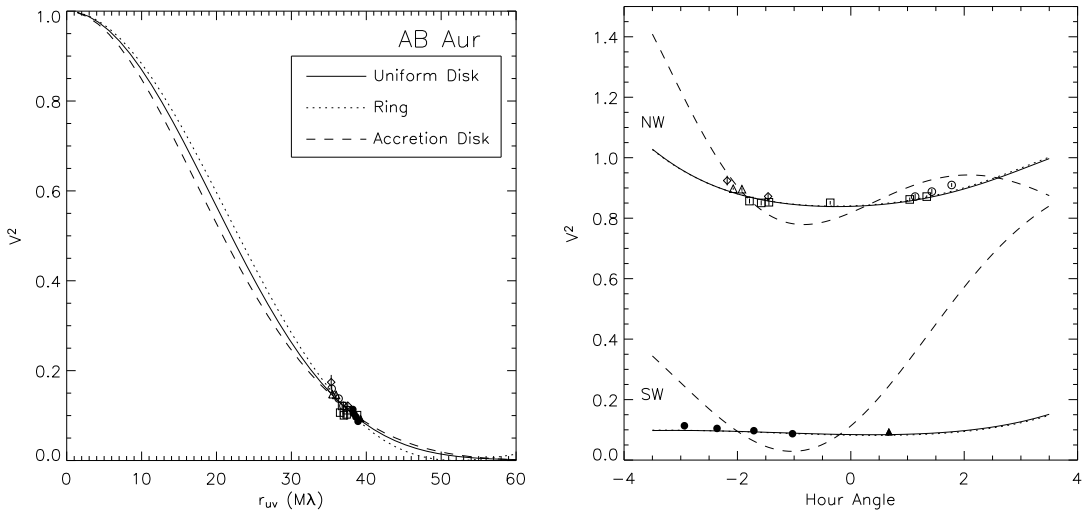

Figure 5.2 V^2 PTI data for AB Aur, as a function of $r_{\rm uv} = (u^2 + v^2)^{1/2}$ (left panel). Data for individual nights are represented by different symbols, where NW data are plotted with open symbols, and SW data use filled symbols. Face-on uniform disk (solid line), ring (dotted line), and geometrically flat accretion disk (dashed line) models are over-plotted. We also plot the data as a function of hour angle (right panel). For clarity, we have plotted $V^2 + 0.75$ for the NW data. The best-fit face-on uniform disk is plotted as a solid line, the best-fit inclined uniform disk model is represented with a dotted line, and the best-fit binary model is shown with a dashed line. We note that the different linestyles correspond to different models in the left and right panels. For this source, we see that a face-on model provides the best fit to the data.

for completeness, since we perform some additional analysis steps that were absent in the first paper.

5.4.1.1 AB Aur

The PTI visibilities for AB Aur are consistent with a disk-like circumstellar distribution that is nearly face-on (Figure 5.2). From Tables 5.4-5.8, the best-fit models indicate size scales[3] between 2.2 and 5.3 mas, and an inclination angle between 8° and 16°, consistent with the values found by ELAHS. We have, however, reduced the uncertainties using additional data on a second baseline. The data cannot be fit well

[3]As outlined in §5.3.2.1–5.3.2.3, characteristic size scales for different models measure different parts of the brightness distributions: Gaussian models measure full widths at half maxima, uniform disk models measure outer diameters, ring models measure inner ring diameters, and accretion disk models (flat or flared) measure inner disk diameters. The spread in quoted angular sizes for a source is mainly due to these differences.

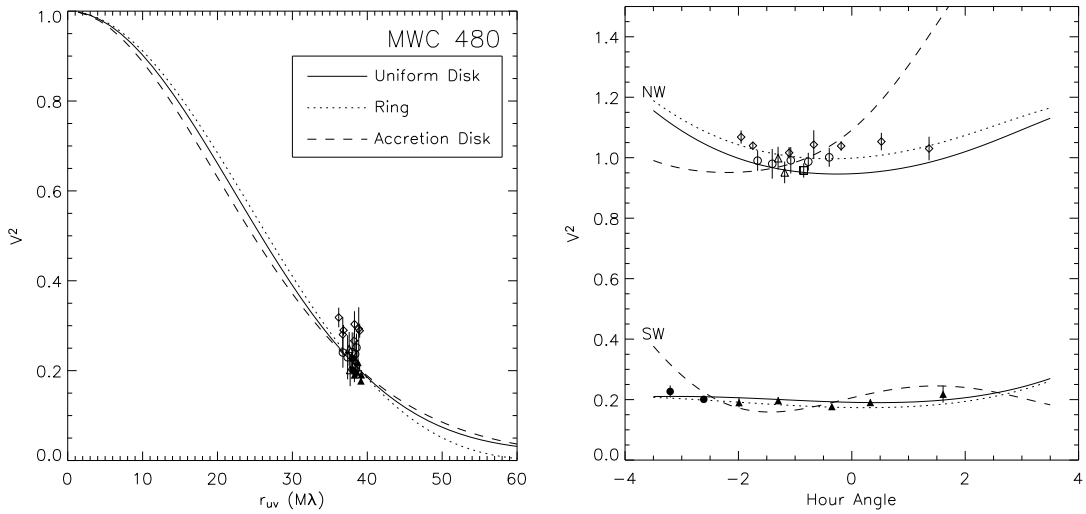

Figure 5.3 V^2 PTI data for MWC 480, as a function of $r_{\rm uv}$ (left panel) and hour angle (right panel). Symbols and models are plotted as in Figure 5.2. For this source, we see that an inclined disk model provides the best fit to the data.

by a binary model ($\chi^2_r \sim 117$; Table 5.9).

5.4.1.2 MWC 480

The PTI visibilities for MWC 480 are consistent with a disk inclined by $\sim 30°$, at a position angle of $\sim 150°$ (Figure 5.3). Specifically, best-fit angular size scales range from 2.0 to 5.0 mas, inclinations range from 24° to 32°, and position angles are between 127° and 155° (Tables 5.4–5.8). Inclined fits give $\chi^2_r \sim 1.4$, significantly lower then the $\chi^2_r \sim 5.0$ values for face-on models. A binary model can be ruled out with a high degree of confidence ($\chi^2_r = 13.5$).

5.4.1.3 MWC 758

The angular size scales for best-fit disk models range from 1.5 to 4.2 mas. Disk inclinations are between 33° and 37°, and position angles vary from 127° to 130° (Tables 5.4–5.8). For this source, all parameters are firmly constrained because we obtained data on three baselines. An inclined disk model clearly fits the data better than a face-on model (Figure 5.4; $\chi^2_r < 1$ for inclined models, compared to $\chi^2_r > 3$ for face-on models). A binary model provides a poor fit to the data, with $\chi^2_r = 5.9$.

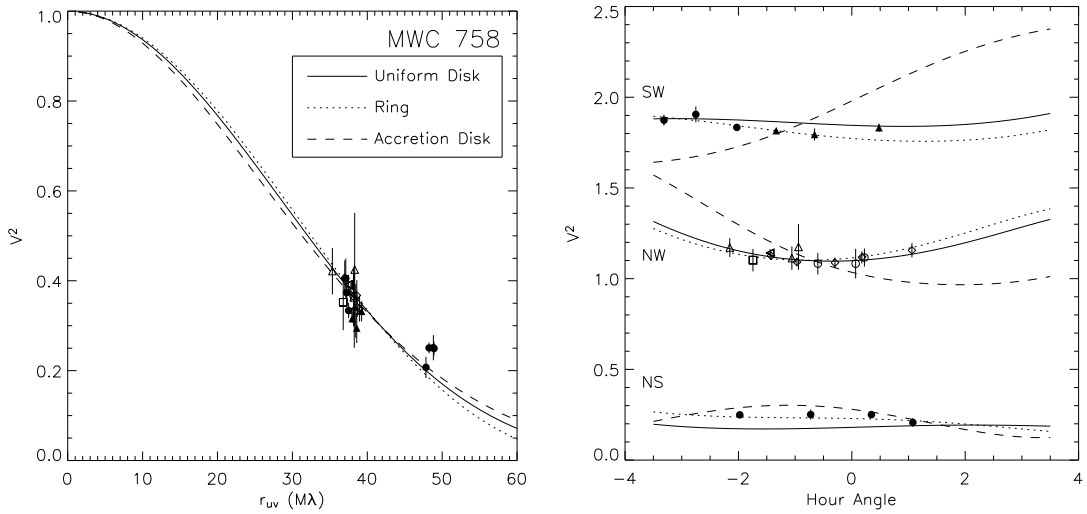

Figure 5.4 V^2 PTI data for MWC 758, as a function of $r_{\rm uv}$ (left panel) and hour angle (right panel). Symbols and models are plotted as in Figure 5.2, except that here, we have three baselines. NW data are plotted with open symbols, and NS and SW data use filled symbols. In the right panel, we have plotted $V^2 + 0.75$ for the NW data and $V^2 + 1.5$ for the SW data. An inclined disk model provides the best fit to the data.

5.4.1.4 CQ Tau

The best-fit angular size scales for CQ Tau are between 1.5 and 4.4 mas. The best-fit inclination is 48°, and position angles range from 104° to 106° (Tables 5.4–5.8). All parameters are firmly constrained because we obtained data on three baselines. Inclined model fits give $\chi^2_r < 1$, while face-on fits have much higher χ^2_r values, $\gtrsim 5$. A binary model seems unlikely, with $\chi^2_r = 4.4$.

5.4.1.5 T Ori and MWC 120

Since we obtained data on only one baseline for T Ori and MWC 120, we are unable to constrain inclinations or position angles. The best-fit angular size scales for T Ori range from 1.1 to 2.7 mas, and the values for MWC 120 are between 2.1 and 4.9 mas (Tables 5.4–5.8). The limited uv coverage for these sources does not allow us to rule out (or constrain the parameters of) binary models.

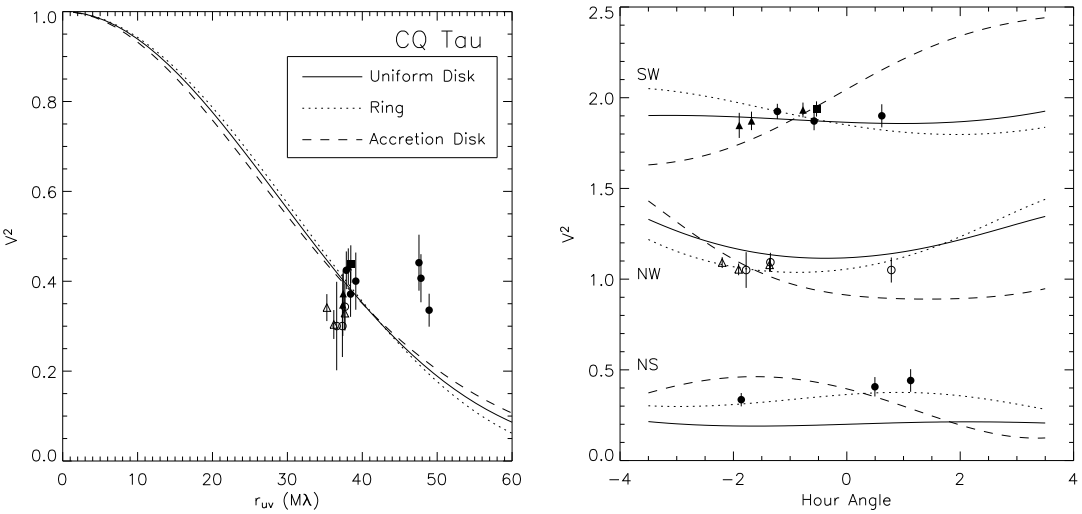

Figure 5.5 V^2 PTI data for CQ Tau, as a function of $r_{\rm uv}$ (left panel) and hour angle (right panel). Symbols and models are plotted as in Figure 5.4. For this source, an inclined disk model provides the best fit to the data.

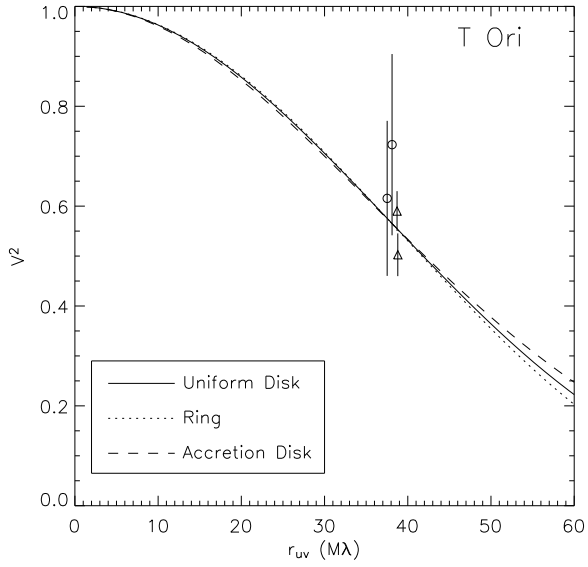

Figure 5.6 V^2 PTI data for T Ori, as a function of $r_{\rm uv}$. Symbols and models are plotted as in Figure 5.2. For this source, the limited $u-v$ coverage does not allow an estimate of inclination, so we plot only face-on models.

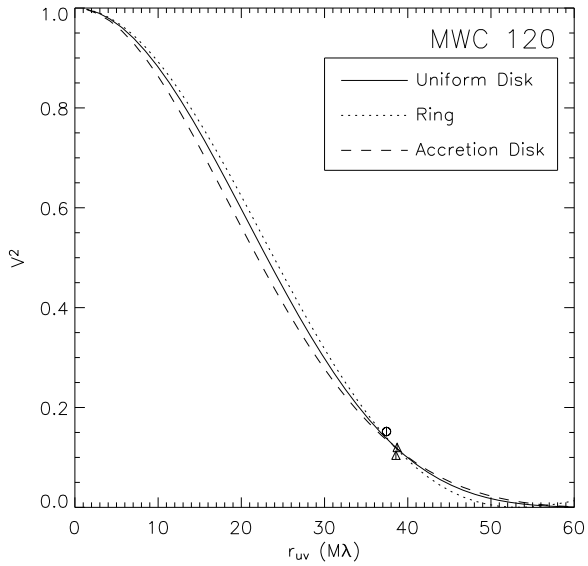

Figure 5.7 V^2 PTI data for MWC 120, as a function of $r_{\rm uv}$. Symbols and models are plotted as in Figure 5.2. For this source, the limited $u-v$ coverage does not allow an estimate of inclination, so we plot only face-on models.

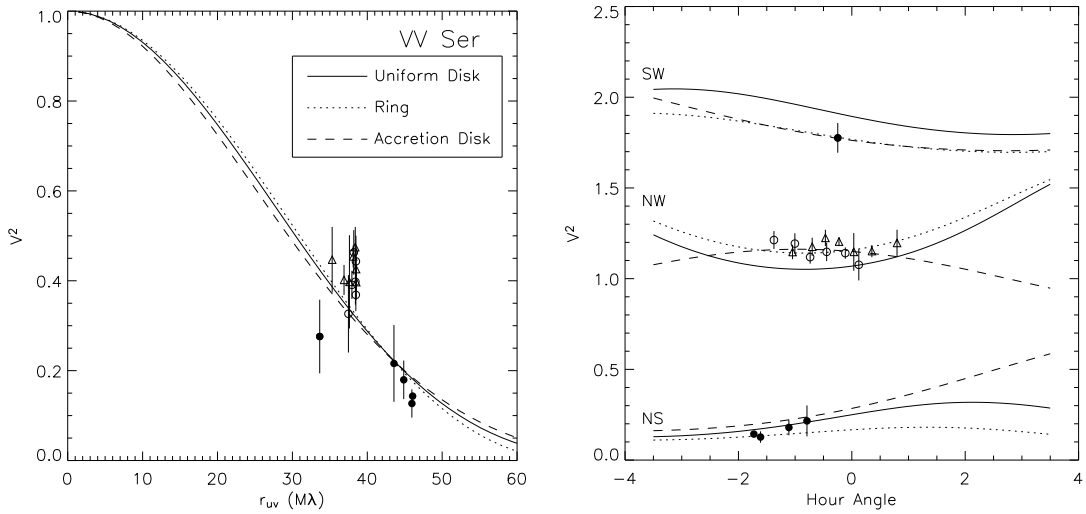

Figure 5.8 V^2 PTI data for VV Ser, as a function of $r_{\rm uv}$ (left panel) and hour angle (right panel). Symbols and models are plotted as in Figure 5.4. Inclined disk or binary models provide the best fit to the data for this source.

5.4.1.6 MWC 297

This source is extremely resolved, and we are only able to place lower limits on the angular size scales (corresponding to upper limits on the visibilities). We can neither constrain the exact geometry of the emission, nor rule out a binary model. For the face-on disk models discussed above, we find lower-limits on angular size scales of 2.1 to 5.0 mas. As we discuss below, this source has also been resolved by the IOTA interferometer (MST; §5.4.2), allowing more accurate constraints on angular size. The puffed-up inner disk model does not fit the visibility data for this source, since the flared disk is quite hot even at large radii due to the hotter central star, which leads to an inner disk radius much larger than allowed by the visibility data.

5.4.1.7 VV Ser

The angular size scales for best-fit disk models range from 1.5 to 4.5 mas, disk inclinations are between 42° and 47°, and position angles range from 165° to 173° (Tables 5.4–5.8). An inclined disk model clearly fits the VV Ser data better than a face-on model (Figure 5.8). Inclined model fits give $\chi^2_r < 1$, while face-on model fits have $\chi^2_r > 5$ (Table 5.4–5.8). However, as indicated in Figure 5.1, the $u - v$ coverage for

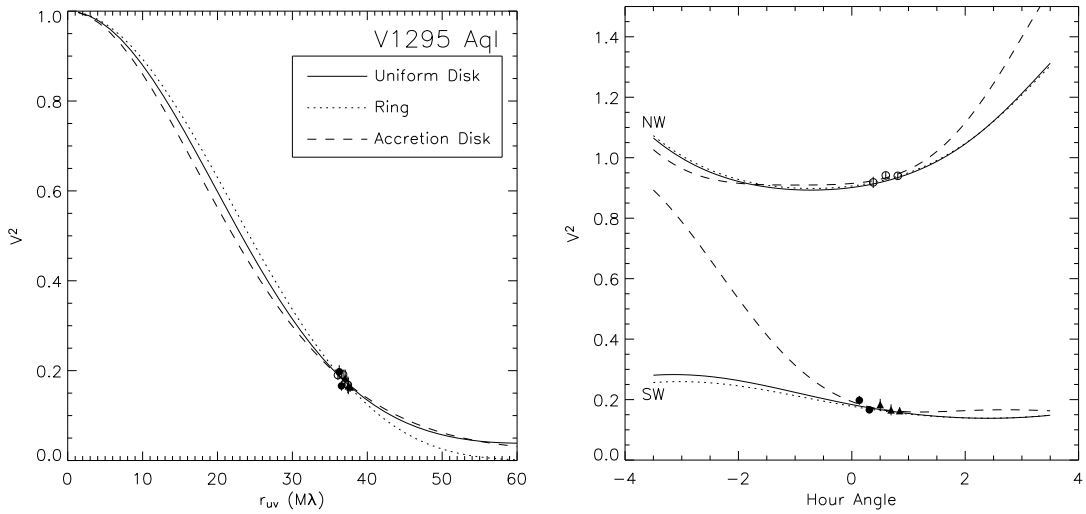

Figure 5.9 V^2 PTI data for V1295 Aql, as a function of $r_{\rm uv}$ (left panel) and hour angle (right panel). Symbols and models are plotted as in Figure 5.2. For this source, it appears that a face-on disk or a binary model provides the best fit to the data.

this object is somewhat sparse, and a binary model cannot be ruled out ($\chi^2_r \sim 0.75$; Figure 5.8).

While the fitted parameters are consistent (within the uncertainties) with those listed in ELAHS, the inclination determined here is significantly lower as a result of new data on an additional baseline. However, we note that we only have one data point on the SW baseline, which makes it difficult to estimate a true error bar, and thus the uncertainties on the fitted parameters may be larger than the statistical uncertainties quoted in Tables 5.4–5.8. We emphasize that if the SW data point is excluded from the fit, the inclination is closer to edge-on ($80^\circ - 89^\circ$; ELAHS).

5.4.1.8 V1295 Aql

The visibilities for V1295 Aql appear consistent with a disk that is close to face-on, although we do not rule out a significantly non-zero inclination. The angular size scales of best-fit models are between 2.4 and 5.6 mas, and inclinations range from 12° to 50°. While there is no discernible difference in the χ^2_r values for face-on and edge-on disks, the $u-v$ coverage for this source is sparse (Figure 5.1), and we cannot obtain an accurate estimate of the inclination. We also cannot rule out a binary

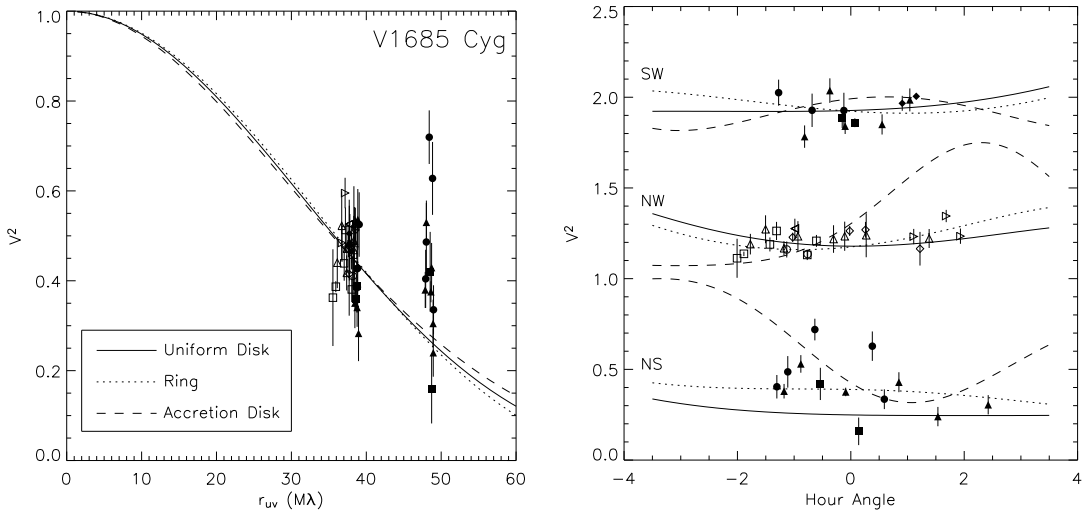

Figure 5.10 V^2 PTI data for V1685 Cyg, as a function of $r_{\rm uv}$ (left panel) and hour angle (right panel). Symbols and models are plotted as in Figure 5.4. For this source, we see that an inclined disk model provides the best fit to the data, although no models fit all of the data particularly well.

model (Figure 5.9).

5.4.1.9 V1685 Cyg

The size scales for V1685 Cyg under the assumptions of various disk models range from 1.3 to 3.6 mas, the best-fit inclination is 41°, and the best-fit position angle is 110° (Tables 5.4–5.8). These parameters are consistent with those found in ELAHS, and we have improved the uncertainties using additional data from a third baseline. The visibility data are not fit very well by any model, although of those considered, inclined disks fit best ($\chi^2_r \sim 3.9$; Figure 5.10). $\chi^2_r = 15$ for a binary model, making this an unlikely choice. The flared disk model with a puffed-up inner wall also does not fit the visibility data for this source, since the flared disk is quite hot even at large radii due to the hotter central star, which leads to an inner disk radius much larger than allowed by the visibility data.

Since none of the models provide very good fits to the data, we attempted to fit several more complex models, including an inclined disk+point source, binary face-on uniform disks, and a model consisting of three point sources. These models reduce the χ^2_r (to approximately 2.5), but still do not appear to accurately fit all of the

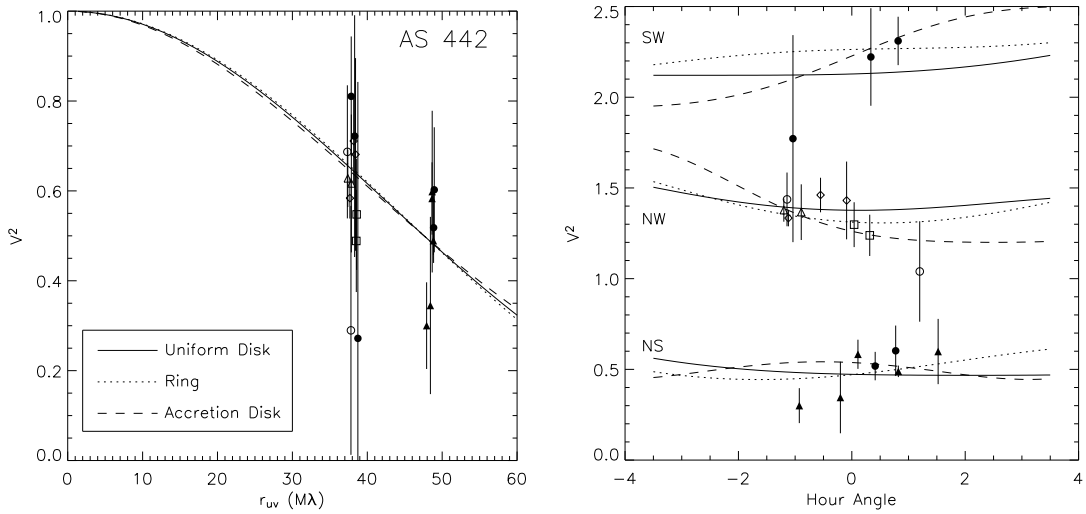

Figure 5.11 V^2 PTI data for AS 442, as a function of $r_{\rm uv}$ (left panel) and hour angle (right panel). Symbols and models are plotted as in Figure 5.4. Inclined disk or binary models provide the best fit to the data.

visibility data. We speculate that a more complex circumstellar distribution, such as as a highly non-uniform disk with multiple hot-spots, may be necessary to explain the observations. Complete understanding of this source may have to wait until multi-baseline interferometers like *IOTA-3T*, *CHARA*, *VLTI*, or *Keck Interferometer* allow synthesis imaging.

5.4.1.10 AS 442

The PTI data for AS 442 generally have low signal-to-noise, and it is difficult to distinguish between different models. We have added a third baseline to the dataset used in ELAHS, which allows us to make estimates of size scales and inclinations (albeit with large uncertainties). The size scales for various disk models range from 1.0 to 2.7 mas, the inclination ranges from 46° to 48°, and the position angles are between 57° and 59° (Tables 5.4–5.8). While we cannot rule out a face-on disk model, the χ^2_r values are somewhat lower for the inclined disk models: ~ 0.9 versus ~ 1.0 for face-on models. We cannot rule out a binary model with these data, and in fact, the binary model has the lowest χ^2_r value of all models considered.

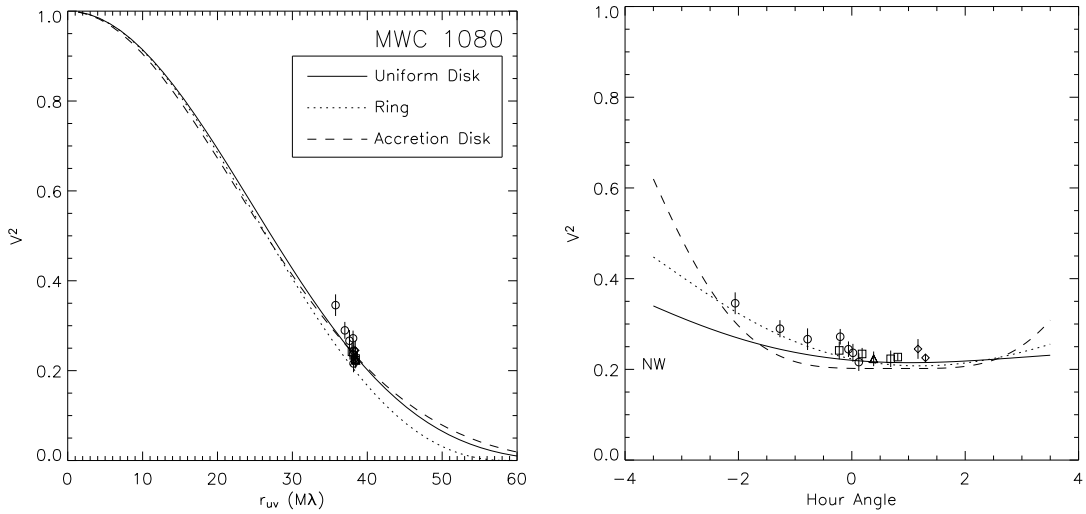

Figure 5.12 V^2 PTI data for MWC 1080, as a function of $r_{\rm uv}$ (left panel) and hour angle (right panel). Symbols and models are plotted as in Figure 5.2, except that no offset has been applied to the visibilities in the right panel. An inclined disk model provides the best fit to the data.

5.4.1.11 MWC 1080

The PTI visibilities for MWC 1080 are consistent with a disk inclined by $\sim 30°$ (Figure 5.12). The best-fit angular size scales are between 1.7 and 4.1 mas, inclination angles range from 28° to 40°, and position angles are between 54° and 56°. The χ^2_r values for inclined models are significantly lower than for face-on disk or binary models. While the uncertainties on position angle and inclination quoted in Tables 5.4–5.8 are somewhat large, we show below that when IOTA data is included, the uncertainties are reduced considerably (§5.4.2). The flared disk model with a puffed-up inner wall does not fit the visibility data for this source since the flared disk is quite hot even at large radii due to the hotter central star, which leads to an inner disk radius much larger than allowed by the visibility data.

5.4.2 Comparison with K and H-band IOTA Visibilities

Interferometric observations of AB Aur and MWC 1080 at 2.2 μm have also been obtained with the 21-m and 38-m baselines of the IOTA interferometer (Millan-Gabet et al. 1999, 2001). In ELAHS, we combined this 2.2 μm IOTA data with PTI data.

Table 5.10. Accretion Disk Models for PTI+IOTA Visibilities

Source	Face-On Models χ^2_r	Face-On Models θ (mas)	Inclined Models χ^2_r	Inclined Models θ (mas)	Inclined Models ψ (°)	Inclined Models ϕ (°)
			$T_{\rm in} = 2000$ K			
AB Aur	2.495	$2.26^{+0.01}_{-0.01}$	2.889	$2.27^{+0.02}_{-0.01}$	170^{+0}_{-170}	11^{+4}_{-3}
T Ori	0.834	$1.08^{+0.04}_{-0.05}$				
MWC 297	0.040	$3.38^{+0.24}_{-0.22}$				
V1295 Aql	0.604	$2.38^{+0.02}_{-0.02}$	0.343	$2.68^{+0.11}_{-0.33}$	15^{+165}_{-15}	35^{+4}_{-35}
V1685 Cyg	6.141	$1.32^{+0.01}_{-0.01}$	2.021	$1.46^{+0.03}_{-0.02}$	111^{+3}_{-4}	41^{+3}_{-3}
MWC 1080	9.355	$1.69^{+0.01}_{-0.01}$	6.408	$1.76^{+0.03}_{-0.03}$	43^{+6}_{-4}	37^{+5}_{-5}

References. — Columns defined as in Table 5.4.

However, we misinterpreted the IOTA data in that analysis (confusing V for V^2) such that the plotted IOTA visibilities appeared closer to unity than they actually are. We have rectified that error here. MST also obtained 1.6 μm H-band visibilities for AB Aur, T Ori, MWC 297, V1295 Aql, V1685 Cyg, and MWC 1080. Based on discussion with R. Millan-Gabet, we assign an uncertainty to each IOTA visibility given by the standard deviation of all data obtained for a given source with a given baseline.

We compare the visibilities measured by PTI and IOTA for each source by fitting a flat accretion disk model (§5.3.2.2) to the combined H+K-band dataset[4]. The best-fit face-on flat accretion disk models are plotted in Figure 5.13, and the fitted parameters for face-on and inclined disk models are listed in Table 5.10. Examination of Figure 5.13 and comparison of Tables 5.7 and 5.10 show that the PTI and IOTA data are consistent, and that the combined dataset gives results compatible with those derived from the PTI data alone.

For some sources, there may be a slight trend in the IOTA data toward lower visibilities than the PTI data: this difference is most pronounced for AB Aur, where

[4]Since we are interested primarily in the comparison between PTI and IOTA data, the choice of model is not important; we choose the flat accretion disk model because it is computationally simple compared to the puffed-up inner disk model.

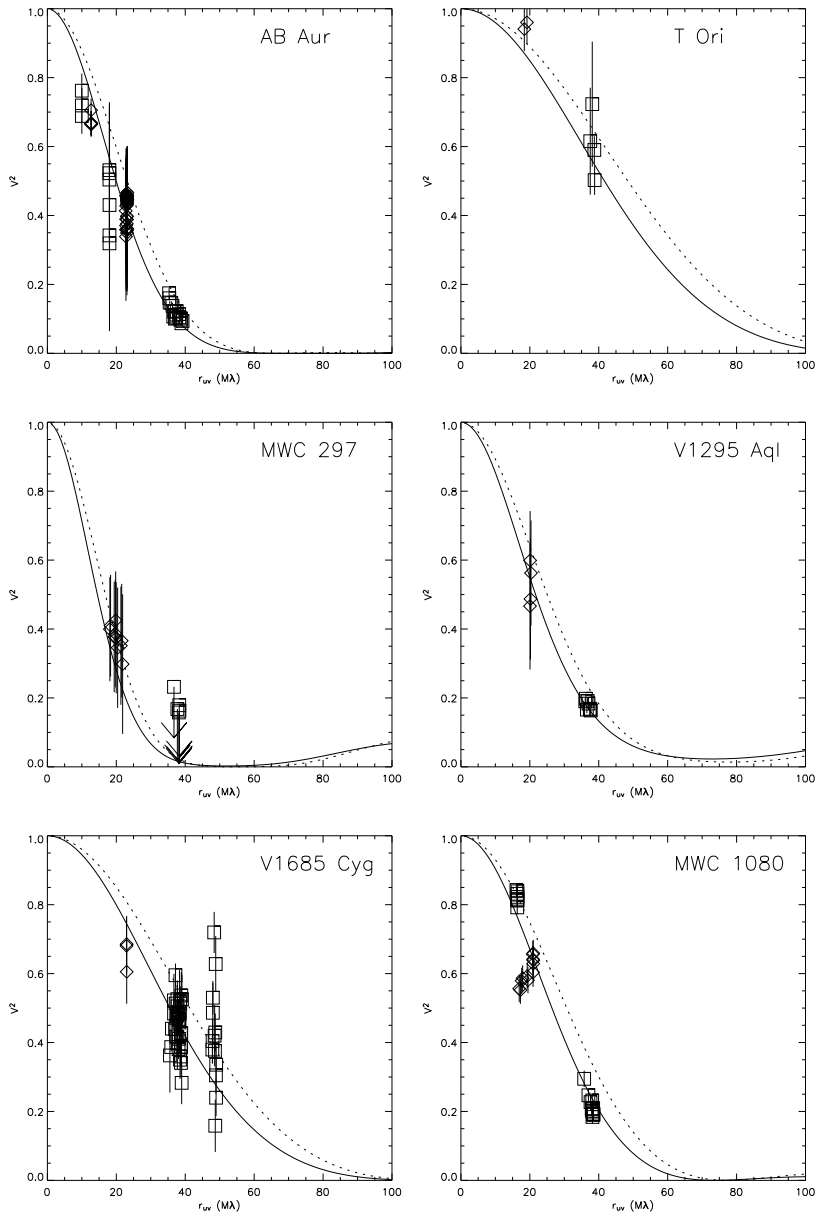

Figure 5.13 PTI and IOTA data for AB Aur, T Ori, MWC 297, V1295 Aql, V1685 Cyg, and MWC 1080, as a function of $r_{\rm uv} = (u^2 + v^2)^{1/2}$. PTI data have $r_{\rm uv} > 30$ Mλ, and IOTA data have $r_{\rm uv} < 30$ Mλ. K-band data are represented by squares, and H-band data are plotted with diamonds. The best fit of a face-on flat accretion disk model to the combined dataset is also plotted, where the predicted K-band visibilities are indicated by a solid line and the predicted H-band visibilities are indicated by a dotted line.

both the PTI and IOTA data sets are consistent with a nearly face-on disk model, but the IOTA data imply a size that is $\sim 20\%$ larger. We speculate that this discrepancy may be due to the $3''$ field of view of the IOTA interferometer, which is significantly larger than the $1''$ field of view of PTI. Scattered or thermal emission from dust on large scales ($\gtrsim 1''$) might contribute incoherent emission to the IOTA visibilities that is not present in the PTI data, leading to a larger measured size (see §5.3.1.3). Including a spatially uniform incoherent component via Equation 5.3, an incoherent flux of $0.6F_* = 1$ Jy leads to a measured size in the IOTA data equal to that measured by PTI. Near-IR and optical imaging have revealed scattered light structures up to $4'' - 9''$ away from AB Aur (Fukagawa et al. 2004; Grady et al. 1999), providing some evidence for (possibly K-band emitting) dust at large radii.

The sizes determined when uniform, incoherent emission is included in the model are $\lesssim 20\%$ larger than the values determined from the IOTA data when incoherent emission is ignored. For the PTI data, this discrepancy is $< 1\%$. Thus, while there may be some uncertainty in the disk sizes determined from the IOTA data, the smaller field of view of PTI should lead to uncertainties of less than a few percent. However, the exact brightness profile of the extended emission is unknown, and thus we cannot quantify precisely the magnitude of the uncertainty for the PTI data. Future measurements with interferometers possessing even smaller fields of view (e.g., *Keck Interferometer* with a 50 mas field of view), when combined with the data discussed here, will constrain further the effects of extended emission on the measured visibilities.

For MWC 1080, while the K-band visibilities from IOTA and PTI are compatible (the fit to the combined dataset gives very similar parameters to those determined in §5.4), the H-band data appears to be inconsistent with a disk model. This discrepancy was noted by MST, who speculated that the cause might be a resolved calibrator used in the IOTA observations, or possibly increased scattering at shorter wavelengths. Since the K-band data are consistent with a disk model while the H-band data are not, we favor the latter interpretation.

The H-band IOTA visibilities for MWC 297 lead to a size of 3.38 mas. Since our

PTI data presented in §5.4 yielded only an upper limit for the size of this source, we will adopt the size measured by IOTA in the further analysis presented below.

5.4.3 Binaries

There is always the possibility that the visibilities for some of the observed HAEBE sources may be (partially) due to close companions. For AB Aur, MWC 480, MWC 758, CQ Tau, V1685 Cyg, and MWC 1080, we can rule out binary models (with separations $\gtrsim 1$ mas) with a high degree of confidence based on the near-IR visibility data (Table 5.9). The stability of the visibilities over a long time baseline (> 1 year) for AB Aur and V1685 Cyg supports this conclusion. However, MWC 1080 is known to be an eclipsing binary with a period of $P \approx 2.9$ days (Shevchenko et al. 1994; Herbst & Shevchenko 1999), and T Ori is an eclipsing spectroscopic binary with a period of approximately 14 days (Shevchenko & Vitrichenko 1994). These orbital separations are much too small to be detected by PTI, and the observed visibilities for these sources are thus probably due to circum-*binary* disks. As yet, the binarity status of MWC 120, MWC 297, V1295 Aql, AS 442, and VV Ser remains uncertain based on our visibility data. Radial velocity variations of spectral lines in AS 442 have been attributed to a binary with $P \approx 64$ days and $e \approx 0.2$, while a lack of spectral line variation in V1295 Aql suggests a single source (Corporon & Lagrange 1999).

5.4.4 Spectral Energy Distributions

The inner disk sizes and inclinations determined from our near-IR interferometry data directly constrain common models of the spectral energy distributions (SEDs) for HAEBEs. The derived inner radii constrain the structure of the inner disks, while the inclination estimates provide constraints on the structure of the entire disks (assuming the disks are not significantly warped; see §5.5.3). For the geometrically flat accretion disk model discussed in §5.3.2.2 and the flared disk model with a puffed-up inner wall discussed in §5.3.2.3, we compute the SEDs for our best-fit inner disk

parameters (Tables 5.7 and 5.8; Table 5.10 for MWC 297). For T Ori, MWC 120, and MWC 297, which do not have inclination estimates, we assume an inclination of zero. The model SEDs are plotted in Figures 5.14 and 5.15.

We compare these predicted SEDs to actual measurements compiled from new data (§5.2.1) and the literature (Herbst & Shevchenko 1999; Hillenbrand et al. 1992; de Winter et al. 2001; Malfait et al. 1998; Oudmaijer et al. 1992; Vieira et al. 2003). Although photometry from the literature often lacks error bars, typical uncertainties are $\sim$ 0.05–0.1 mag for wavelengths $<$ 10 μm and $\sim$ 10% at longer wavelengths. Source variability may lead to additional errors since photometric observations (at different wavelengths) often span several years. Since we cannot quantify the uncertainties, we do not include them in our analysis of the SEDs.

For the geometrically flat disk model, the most important parameter beside $R_{\rm in}$ and inclination is $T_{\rm in}$ (Equation 5.10). As discussed in §5.3.2.2, the fitted inner radius depends very slightly on $T_{\rm in}$. However, as illustrated by Figure 5.14, which shows the SEDs predicted for different values of $T_{\rm in}$, this parameter has a significant effect on the SED. The other free parameter in the flat disk model is $R_{\rm out}$, which is relatively unimportant since most of the flux at wavelengths $<$ 1 mm is generated in the inner regions of the disk ($<$ 50 AU). We vary $T_{\rm in}$ between 1000 K and 2500 K (in increments of 10 K) and use a least squares technique to determine the value that provides the best fit to the measured SED (considering only the SED long-ward of 1 μm, since we are interested in the circumstellar emission). The best-fit $R_{\rm in}$ and $T_{\rm in}$ values for this model are listed in Table 5.11.

For the flared disk model with a puffed-up inner wall, several parameters may affect the predicted SED: $T_{\rm in}$, $R_{\rm out}$, $\Sigma(R)$, $\kappa(\nu)$, and the flaring index, ξ (Equations 5.18, 5.20, and 5.22). For simplicity, we will retain our initial assumptions about Σ and κ, and attempt to find the values of $T_{\rm in}$, ξ, and $R_{\rm out}$ that give the best fit of the model to the observed SEDs (again, considering the SED only long-ward of 1 μm). Specifically, we use a least squares fitting method, varying $T_{\rm in}$ from 1000 to 2500 K in 10 K increments, ξ from 0.10 to 0.28 in increments of 0.02, and $R_{\rm out}$ from 30 to 400 AU in 10 AU increments. We note that varying ξ qualitatively corresponds to

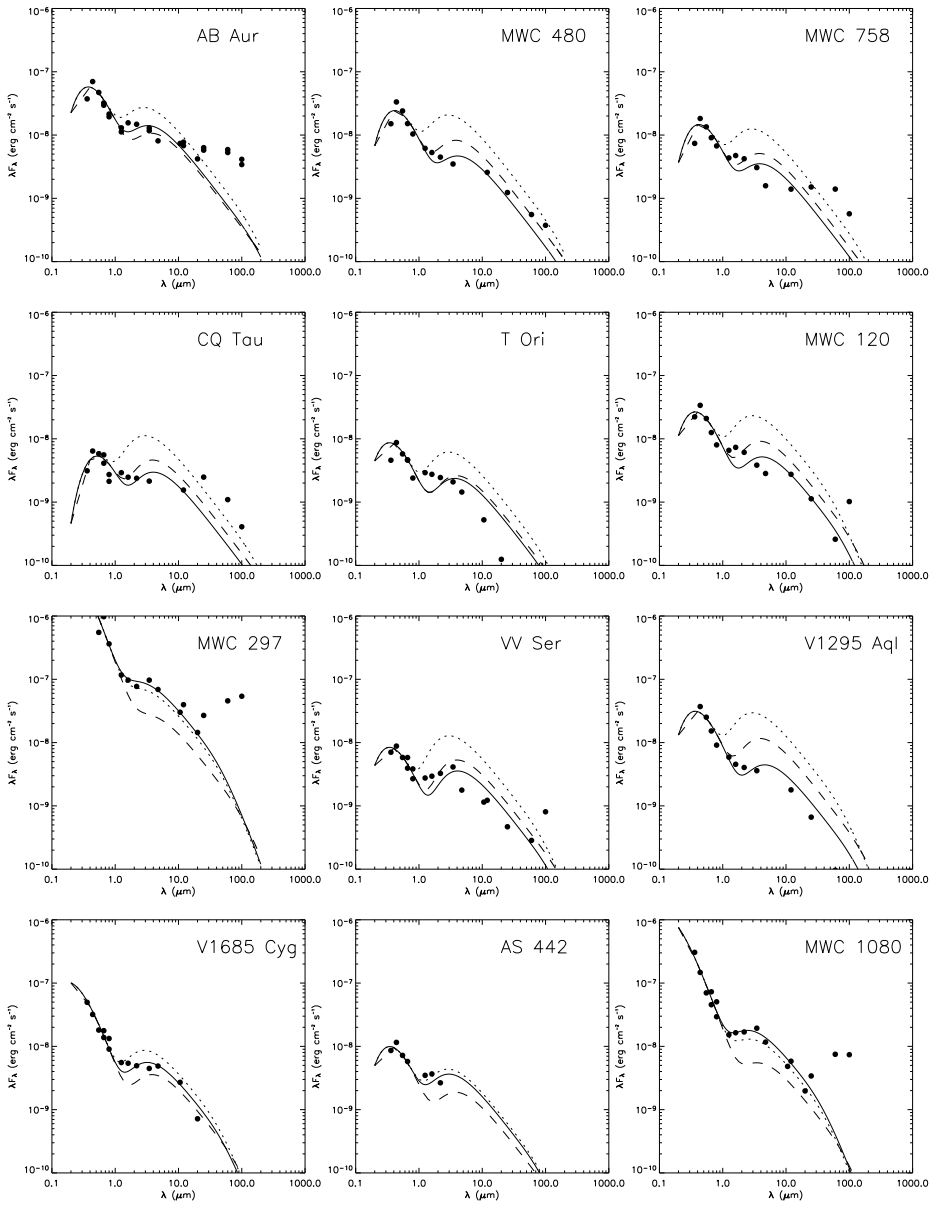

Figure 5.14 Measured SEDs for our sample compiled from the literature and new data (points) and predicted SEDs for geometrically flat accretion disk models (§5.3.2.2). For each source, we plot the predicted SED for $T_{\rm in} = 1500$ K (dashed lines), 2000 K (dotted lines), and a value we determined that gives the best fit to the near-IR data (solid lines). The best-fit $T_{\rm in}$ values are listed in Table 5.11. These models successfully reproduce the SEDs of early-type sources (MWC 297, V1685 Cyg, and MWC 1080), while they are less successful than the flared disk models with puffed-up inner walls (Figure 5.15) for later-type sources.

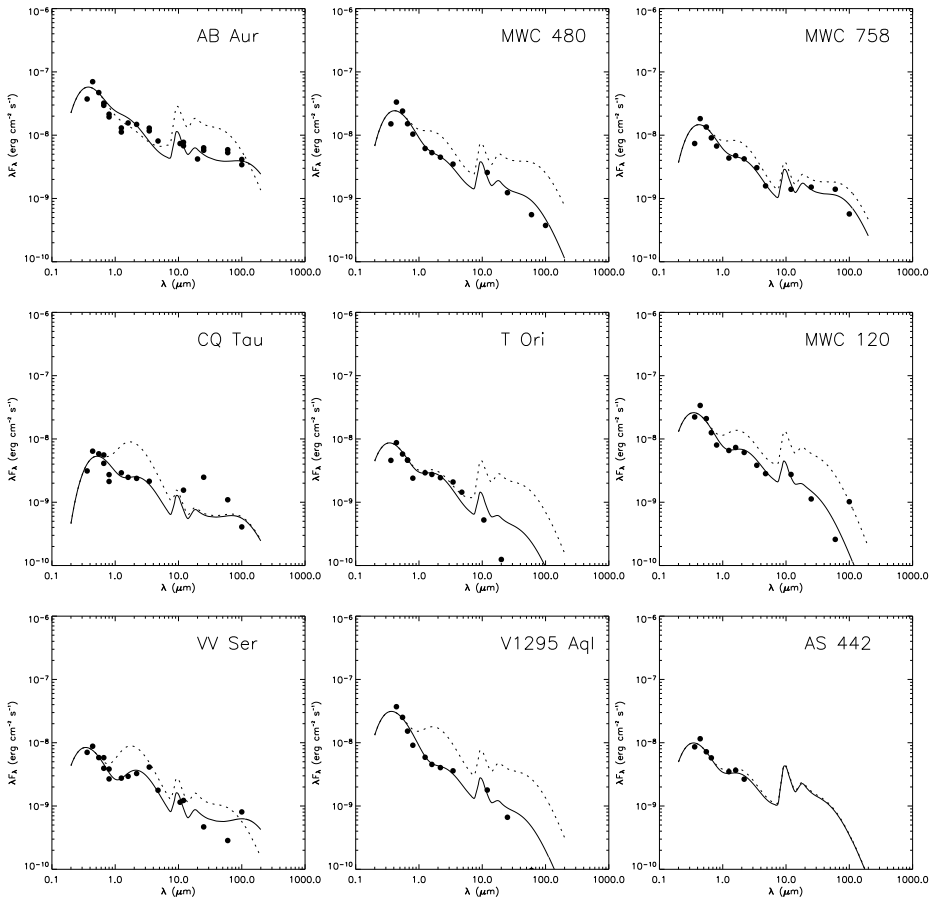

Figure 5.15 Measured SEDs for our sample compiled from the literature and new data (points) and predicted SEDs for flared disk models with puffed-up inner walls (§5.3.2.3). For each source, we plot the predicted SED for the fiducial model ($T_{\rm in}$ = 2000 K, $\xi = 0.28$, $R_{\rm out} = 100$ AU; dotted lines) and for a model where the values of $T_{\rm in}$, ξ, and $R_{\rm out}$ are chosen to give the best fits to the data (solid lines). The best-fit parameter values are listed in Table 5.11.

Table 5.11. Disk Parameters from Near-IR Interferometry and SEDs

Source	Flat Disks		Flared, Puffed-Up Inner Disks			
	$R_{\rm in}$ (AU)	$T_{\rm in}$ (K)	$R_{\rm in}$ (AU)	$T_{\rm in}$ (K)	ξ	$R_{\rm out}$ (AU)
AB Aur	0.17	1690	0.25	2230	0.12	360
MWC 480	0.16	1370	0.23	1580	0.16	30
MWC 758	0.14	1450	0.21	1700	0.24	70
CQ Tau	0.15	1430	0.23	1470	0.28	100
T Ori	0.28	1570	0.40	1950	0.10	30
MWC 120	0.58	1370	0.83	1690	0.14	30
MWC 297	0.68	2140				
VV Ser	0.33	1450	0.47	1630	0.20	400
V1295 Aql	0.39	1240	0.55	1390	0.12	30
V1685 Cyg	0.73	1790				
AS 442	0.33	1910	0.55	1910	0.28	100
MWC 1080	0.86	2170				

References. — Columns 2-3 list the inner disk radii and temperatures for geometrically flat disk models (§5.3.2.2) determined from near-IR interferometry and SEDs. Inner radii are computed from inner disk angular sizes (Table 5.7, and Table 5.10 for MWC 297), using the distances assumed in Table 5.1. Columns 4-7 list the inner radii, inner disk temperatures, flaring indexes, and outer radii determined for flared disk models with puffed-up inner walls (§5.3.2.3). The inner radii are computed from angular sizes in Table 5.8 and distances listed in Table 5.1. Puffed-up inner disk wall models are ruled out for MWC 297, V1685 Cyg, and MWC 1080, and thus no parameter values are listed.

changing the overall flaring of the disk, and while slight modifications to Equation 5.13 may be necessary when ξ is changed, we ignore those here. Since we can rule out the flared, puffed-up inner disk model for MWC 297, V1685 Cyg, and MWC 1080 on the basis of the near-IR visibility data alone (§5.4.1), we do not attempt to fit the SEDs for these sources. The best-fit $R_{\rm in}$, $T_{\rm in}$, ξ, and $R_{\rm out}$ values for the remaining sources are listed in Table 5.11.

From Figure 5.14, we see that with the parameters derived from the near-IR interferometry (inner radius and inclination), geometrically flat accretion disk models can fit the SEDs reasonably well for some sources. The best fits are achieved for MWC 297, V1685 Cyg, and MWC 1080, the sources with the earliest spectral types in our sample. The far-IR photometry for these objects appears somewhat inconsistent with the models, perhaps due to tenuous dust halos, or possibly due to source confusion in the large IRAS beams (not unlikely given that these higher-mass stars are found in small stellar clusters). For these early-type sources, we also find that the near-IR visibility data is completely inconsistent with the predictions of flared disk models with puffed-up inner walls.

For the other nine sources in our sample, which all have spectral types later than B9, the SEDs are generally fit well by flared disk models with puffed-up inner walls (Figure 5.15). However, while the puffed-up inner disk wall generally fits the near-IR data well, for CQ Tau and T Ori the model does not fit the long-wavelength data. Although this disagreement may be lessened for T Ori using a non-zero inclination (we assumed a face-on disk since no inclination estimate is available from our near-IR interferometry), the outer disk structure of CQ Tau is inconsistent with the model. Moreover, many of the sources in our sample require flaring angles smaller than those predicted by standard flared-disk models (i.e., $\xi < 2/7$), which could support the contention of DDN that shadowing by the inner rim plays a prominent role in the outer disk structure of HAEBEs.

Motivated by Monnier & Millan-Gabet (2002), we explore the apparently different disk structure for early and late-type HAEBEs from a different perspective in Figure 5.16, where we plot the ratio of predicted to measured inner disk size as a function of

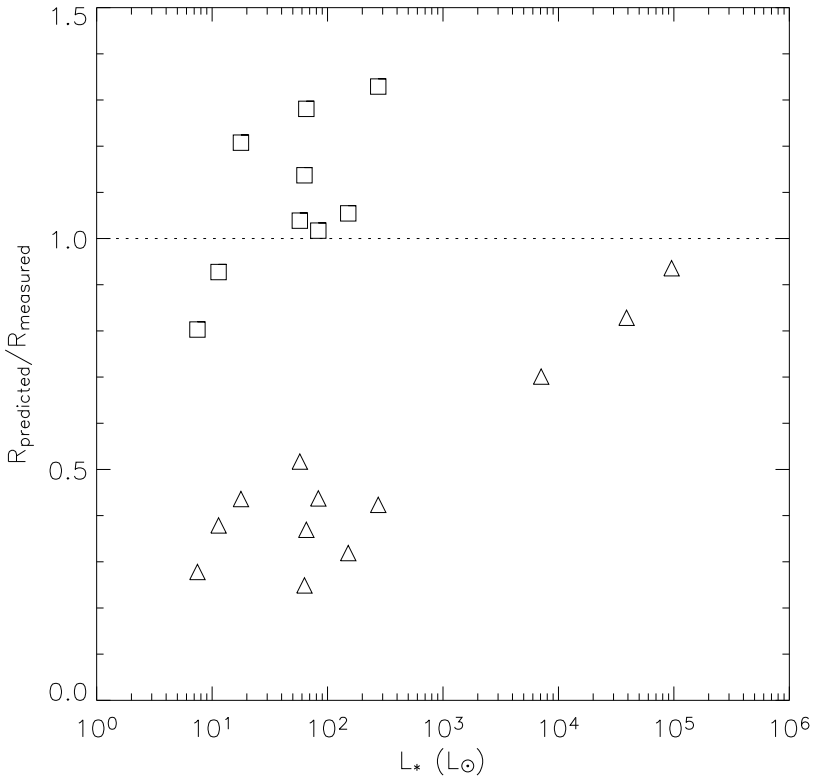

Figure 5.16 The ratio of measured to predicted inner disk sizes, as a function of stellar luminosity. The measured sizes are determined from near-IR interferometry for the geometrically-flat disk model (triangles; §5.3.2.2) and the puffed-up inner rim model (squares; §5.3.2.3), and the predicted sizes for each model are computed using the derived stellar parameters to determine the location in the disk where $T = T_{\rm in}$. The ratio of measured to predicted size is independent of distance (see ELAHS). This figure illustrates that for later-type sources ($L_* < 10^3\ L_\odot$), the puffed-up inner disk models predict inner disk sizes within a few tens of percent of the measured sizes, while the flat disk models predict sizes that are off by a factor of ~ 2. In contrast, the puffed-up inner disk models predict sizes much larger than measured for the early-type objects (not plotted here, since the disagreement is off the scale of the plot), while the flat disk model predicts sizes within $\sim 30\%$ of the measured values.

stellar luminosity for the two different disk models. The predicted inner disk size is computed by assuming the disk is heated only by stellar radiation (i.e., no accretion), and using the structure equations for flat or puffed-up inner disks (see ELAHS) to determine the radius where $T = T_{\rm in}$. For each source, $T_{\rm in}$ is the value determined from the SED (Table 5.11). The measured size is calculated from the angular size determined for either a flat inner disk model (§5.3.2.2) or a puffed-up inner disk wall model (§5.3.2.3) and the distance assumed in Table 5.1. Since the predicted and measured sizes are both directly proportional to distance (ELAHS), the ratio is independent of the assumed distance. Thus, Figure 5.16 is effectively testing whether the inner disk sizes determined from the near-IR interferometric data are consistent with the disk temperatures implied by the stellar parameters. While stellar variability may complicate the interpretation of this diagram, the general trends should be unaffected.

Figure 5.16 shows that for later-type sources, the predicted inner disk sizes are within a few tens of percent of the measured values for puffed-up inner disk models, while flat disk models are off by a factor of approximately 2. In contrast, the predictions of flat models are reasonably close to measured values for early-type sources, while the puffed-up inner disk models predict inner disk sizes much larger (factors $\gtrsim 5$) than allowed by the data. Including accretion luminosity in flat disk models will lead to warmer inner disk temperatures and thus larger predicted inner radii, in better agreement with the measurements. While this argues for flat disk models with accretion in early-type Herbig Be stars, the SEDs demonstrate that puffed-up inner disk models still provide superior fits for the later-type sources.

5.5 Discussion

Our new PTI results strengthen the arguments supporting the existence of circumstellar disks around HAEBE stars presented in §5.1. Resolved, small-scale (~ 1 AU) distributions of dust are found in all observed sources except HD 141569 and HD 158352, and the non-symmetric intensity distributions of best-fit models for most

objects provide support for inclined disk geometries.

5.5.1 Unresolved Sources

HD 141569 and HD 158352 show no evidence of near-IR emission in excess of that expected for the stellar photospheres, and thus it is not surprising that we did not resolve any circumstellar emission with PTI. Rather, our PTI observations imply uniform disk radii $\lesssim 10$ $R_{\odot}$, consistent with the near-IR emission arising in the stellar photospheres for these sources. Although HD 141569 is surrounded by a circumstellar disk, it appears to have a central gap extending out to $\sim 17 - 30$ AU (Brittain et al. 2003; Marsh et al. 2002; Weinberger et al. 1999; Augereau et al. 1999; Sylvester & Skinner 1996), which explains the lack of near-IR excess emission. Moreover, millimeter observations imply a very low dust mass, suggesting that this system is more evolved than other members of the HAEBE class (Sylvester et al. 2001). Although HD 158352 was listed as a candidate HAEBE by Thé, de Winter, & Pérez. (1994), recent observations suggest that it may in fact be a more evolved source, such as a shell star or Vega-like object (Grady et al. 1996; Eritsyan et al. 2002). Thus, it appears that HD 141569 and HD 158352 are probably more evolved than most HAEBE sources (including the remainder of our sample), which may explain the lack of near-IR circumstellar emission for these objects.

5.5.2 Disk Inclinations

The inclination estimates determined from near-IR interferometric data are generally compatible with inclinations inferred from other observations. Our interferometric measurements show that the resolved circumstellar material around MWC 480, MWC 758, CQ Tau, VV Ser, V1685 Cyg, AS 442, and MWC 1080 is significantly inclined. Large-amplitude flux and color variability in CQ Tau ($\Delta V \sim 2$ mag), VV Ser ($\Delta V \sim 2$ mag), V1685 Cyg ($\Delta V \sim 1$ mag), and AS 442 ($\Delta V \sim 1$ mag), which has been attributed to variable obscuration from clumps of dust orbiting in inclined circumstellar disks (Herbst & Shevchenko 1999), provides support for this high in-

clination distribution. Furthermore, high inclinations are suggested by resolved mm emission for MWC 480, MWC 758, and CQ Tau (§5.5.3), by optical polarization measurements for CQ Tau (Natta & Whitney 2000), and by ro-vibrational CO emission for MWC 480, MWC 758, and VV Ser (Blake & Boogert 2004). However, the broad, double-peaked line profile of ro-vibrational CO emission from VV Ser suggests an inner disk inclination higher than the $\sim 45^\circ$ estimate presented here. As described in §5.4.1.7, the lower inclination estimate depends on a single data point, and if this point is excluded, we obtain an inclination of $\sim 85^\circ$, consistent with the CO observations.

The PTI data for AB Aur are consistent with a circumstellar distribution that is within 20° of face-on. Other data for AB Aur support this contention, including near-IR interferometric results (Millan-Gabet et al. 2001, §5.4.2), ro-vibrational CO emission (Blake & Boogert 2004), resolved millimeter emission (§5.5.3), scattered optical and near-IR light (Grady et al. 1999; Fukagawa et al. 2004), and small amplitude optical variability ($\Delta V \sim 0.25$; Herbst & Shevchenko 1999). We also note that the inner disk size for AB Aur determined above is consistent with recent observations of ro-vibrational emission from hot CO gas, which show that the CO lies near to, but somewhat behind the inner disk boundary. Moreover, the CO emission is found only in the lowest vibrational state, suggesting that the hot gas is shielded from stellar UV radiation, perhaps by a puffed-up inner disk wall (Brittain et al. 2003; Blake & Boogert 2004).

While the V1295 Aql data seems consistent with a nearly face-on circumstellar distribution, we cannot rule out a high inclination value for this source based on the PTI data alone. The data for T Ori, MWC 120, and MWC 297 are insufficient to constrain the inclinations.

5.5.3 Inner versus Outer Disk Structure

Our PTI results probe dust in the inner (< 1 AU) disk, while millimeter interferometric observations probe dust and gas in the outer ($\gtrsim 100$ AU) disks of HAEBE

stars. Comparison of these observations enables constraints on disk warping. Of our sample, inclinations are available from millimeter CO observations for AB Aur, CQ Tau, MWC 480, and MWC 758 (Mannings & Sargent 1997; Mannings et al. 1997; Mannings & Sargent 2000; Simon et al. 2000; Testi et al. 2003; Corder et al. 2005).

As discussed in earlier papers (MST; ELAHS), the inclination for AB Aur estimated from the aspect ratio of resolved millimeter CO emission, $i = 76°$ (Mannings & Sargent 1997), is inconsistent with the lower inclinations from near-IR interferometry ($i \lesssim 20°$; ELAHS) and modeling of scattered light emission ($i < 30° - 45°$; Fukagawa et al. 2004; Grady et al. 1999). This suggests that the disk around AB Aur may be significantly warped, which is difficult to explain theoretically. However, more detailed kinematic modeling of millimeter observations with higher angular resolution and sensitivity find an outer disk around AB Aur inclined by $\lesssim 30°$ (Corder et al. 2005; Natta et al. 2001), compatible with our near-IR results.

For CQ Tau, the aspect ratio estimated from VLA data at 7mm implies an inclination angle ($\sim 70°$; Testi et al. 2003) somewhat larger than that determined from near-IR interferometry ($\sim 48°$; §5.4.1.4). Kinematic modeling of more sensitive millimeter observations shows that the outer disk is actually inclined by $\sim 45°$ (Corder et al. 2005), consistent with our PTI results.

For MWC 480, there is some variation in the outer disk geometry based on different observations. A Keplerian model fit to one set of millimeter CO observations yields an inclination and position angle of $\sim 30°$ and $157° \pm 4°$, respectively (Mannings et al. 1997), while another gives $38° \pm 1°$ and $148° \pm 1°$ (Simon et al. 2000). The millimeter continuum, which traces cool dust, gives yet another estimate of geometry; $i = 26° \pm 7°$, pa $= 170° \pm 11°$ (Simon et al. 2000). We compare these with estimates of the inner disk geometry from our PTI results: $i = 24° - 32°$, pa $= 149° - 156°$. Since the outer disk geometry estimates vary considerably, it is difficult to estimate the true uncertainty in inclination. However, it seems reasonable to say that the various observations are consistent with no offset at all, and that there is at most a difference of 15° between the inner and outer disk. While there is an intriguing hint that the dust may be somewhat less inclined than the gas, we cannot verify this possibility

with the current data.

Finally, for MWC 758, the aspect ratio of millimeter CO emission implies a disk inclined by 46° at a position angle of 116° (Mannings & Sargent 1997). For comparison, the PTI measurements imply an inclination of $33° - 37°$ and a position angle of $127° - 130°$. There is some spread between these estimates, but again, it seems that there is a difference of $\lesssim 10°$ between the inner and outer disk inclinations.

For the 4 sources in our sample that have inner and outer disk geometry measurements, there is little evidence for inner and outer disk mis-alignments of more than a few degrees. Thus, the inner disk geometries derived from our PTI data likely describe the structure of the entire disks. While we do not rule out small warps (up to ~ 10 degrees), such as those expected from resonant interactions with giant planets or magnetic warping (e.g., Mouillet et al. 1997; Lai 1999), our results argue against significant perturbation due to massive companions (e.g., Bate et al. 2000), consistent with the lack of binaries in our visibility and adaptive optics data.

5.5.4 Vertical Disk Structure

Figures 5.14 and 5.15 demonstrate that flared, puffed-up inner disk models tend to fit the SEDs better than geometrically flat accretion disk models for later-type HAEBE sources, while flat disk models fit the visibility and SED data well for early-type Herbig Be sources. Moreover, Figure 5.16 clearly demonstrates that puffed-up inner disk models more accurately predict the inner radii of late-type HAEBEs, while geometrically flat disk models are far more accurate for early-type sources.

We have already suggested (ELAHS, see also Vink et al. 2002) that the apparent difference between inner disk geometries for early and late-type HAEBEs may be due do a transition from disk accretion (Lynden-Bell & Pringle 1974) in early-type stars to magneto-spheric accretion (Königl 1991) in later-type stars. There is abundant evidence for magneto-spheric accretion in T Tauri stars (Hartmann 1998, and references therein), and it is plausible that the same accretion mechanism would apply to the more massive Herbig Ae stars. Magneto-spheric accretion provides a mechanism

for truncating the disks around HAEBE stars, which is necessary to obtain puffed-up inner disk walls (disk truncation allows direct irradiation of the inner disk regions, leading to higher temperatures and thus larger scale heights). In contrast, for earlier spectral types, such as the Herbig Be stars, higher accretion rates and/or weaker stellar magnetic fields may allow the accretion flow to overwhelm the magnetic field, leading to disk accretion down to the stellar surface.

5.6 Summary

Our new 2.2 μm observations of 14 HAEBE sources have the best $u-v$ coverage of any near-IR interferometric observations of young stellar objects to date. As a result, we accurately constrain the sizes and basic geometries of the material around HAEBEs, providing strong evidence for inner circumstellar disks.

We determine the angular size scales and orientations predicted by uniform disk models, Gaussian models, uniform ring models, geometrically flat accretion disk models with inner holes, and flared passive disk models with puffed-up inner rims. All except two sources are resolved, with angular sizes ranging from $\sim 1.0-5.8$ mas. AB Aur appears to be surrounded by a disk inclined by $\lesssim 20^{\circ}$, while MWC 480, MWC 758, CQ Tau, VV Ser, V1685 Cyg, AS 442, and MWC 1080 are associated with more highly inclined circumstellar disks ($\sim 30-50^{\circ}$). We cannot rule out a high inclination for V1295 Aql, although the data can be explained by a face-on disk model. For T Ori, MWC 120, and MWC 297, the $u-v$ coverage is too sparse to enable constraints on the inclination of the circumstellar material. There is little supporting evidence that our data result from binaries, although we cannot rule out binary models for T Ori, MWC 120, MWC 297, V1295 Aql, AS 442, or VV Ser.

Comparison of our 2.2 μm PTI visibilities with 1.6 μm and 2.2 μm visibilities from the IOTA interferometer (MST) shows that the two datasets are consistent, and allows firmer constraints on circumstellar geometry. Since IOTA has a field of view three times larger than PTI, we are also able to constrain the degree to which incoherent emission from extended dust may bias the measured sizes toward larger

values. The smaller field of view of PTI leads to very small biases, and the resulting uncertainties in the measured sizes are likely less than a few percent.

We constrain warping of HAEBE disks by comparing our near-IR measurements of the inner disks with resolved millimeter interferometric measurements of the outer disk geometries (where available). Our results for 4 sources indicate that the inner and outer disks of HAEBEs are not significantly mis-aligned. While this argues against significant perturbations to the disks, we do not rule out small warps such as those due to interactions between disks and slightly non-coplanar giant planets.

Our measurements also enable constraints on the vertical structure of HAEBE disks. Using the derived inner disk parameters, we compute the SEDs for flat accretion disk models with inner holes and flared passive disk models with puffed-up inner walls, and compare these with measured SEDs for our sample. Geometrically flat disk models fit the data well for the early-type Herbig Be stars in our sample, MWC 297, V1685 Cyg and MWC 1080, while the flared, puffed-up inner disk models cannot fit the data for these objects. In contrast, flared disk models with puffed-up inner rims provide superior fits to the data for the later-type stars in our sample. The different inner disk geometries may imply a transition from magneto-spheric accretion in late-type HAEBEs to disk accretion in early-type sources.

Acknowledgments. The new near-IR interferometry data presented in this paper were obtained at the Palomar Observatory using the Palomar Testbed Interferometer, which is supported by NASA contracts to the Jet Propulsion Laboratory. Science operations with PTI are possible through the efforts of the PTI Collaboration (`http://pti.jpl.nasa.gov/ptimembers.html`) and Kevin Rykoski. This research made use of software produced by the Michelson Science Center at the California Institute of Technology. This publication makes use of data products from the Two Micron All Sky Survey, which is a joint project of the University of Massachusetts and the Infrared Processing and Analysis Center, funded by the National Aeronautics and Space Administration and the National Science Foundation. 2MASS science data and information services were provided by the Infrared Science Archive (IRSA) at IPAC.

We thank R. Millan-Gabet for providing us with the IOTA data, for useful discussion, and for a critical review of the manuscript. We are also grateful to S. Metchev for his assistance with the adaptive optics observing and data reduction. J.A.E. is supported by a Michelson Graduate Research Fellowship, and B.F.L. acknowledges support from a Pappalardo Fellowship in Physics.

Chapter 6

Observations of T Tauri Disks at Sub-AU Radii: Implications for Magnetospheric Accretion and Planet Formation[1]

We determine inner disk sizes and temperatures for four solar-type (1-2 $M_\odot$) classical T Tauri stars (AS 207A, V2508 Oph, AS 205A, and PX Vul) using 2.2 μm observations from the Keck Interferometer. Nearly contemporaneous near-IR adaptive optics imaging photometry, optical photometry, and high-dispersion optical spectroscopy are used to distinguish contributions from the inner disks and central stars in the interferometric observations. In addition, the spectroscopic and photometric data provide estimates of stellar properties, mass accretion rates, and disk co-rotation radii. We model our interferometric and photometric data in the context of geometrically flat accretion disk models with inner holes, and flared disks with puffed-up inner walls. Models incorporating puffed-up inner disk walls generally provide better fits to the data, similar to previous results for higher-mass Herbig Ae stars. Our measured inner disk sizes are larger than disk truncation radii predicted by magnetospheric accretion models, with larger discrepancies for sources with higher mass accretion rates. We suggest that our measured sizes correspond to dust sublimation radii, and that optically-thin gaseous material may extend further inward to the magnetospheric truncation radii. Finally, our inner disk measurements constrain the location of ter-

[1]This chapter has been published previously as Eisner et al. (2005).

restrial planet formation as well as potential mechanisms for halting giant planet migration.

6.1 Introduction

T Tauri stars are low-mass ($\lesssim 2$ $M_\odot$) pre-main sequence objects, thought to be early analogs of stars like our own Sun. A wealth of evidence, including direct imaging at millimeter and optical wavelengths (e.g., Koerner & Sargent 1995; Dutrey et al. 1996; McCaughrean & O'Dell 1996), and modeling of spectral energy distributions (SEDs; e.g., Adams et al. 1988; Bertout et al. 1988; Beckwith et al. 1990), has confirmed the long-espoused hypothesis that T Tauri stars are surrounded by massive disks of dust and gas. Moreover, observed line profiles and UV continuum excesses indicate that T Tauri stars are actively accreting material from their circumstellar disks (e.g., Walker 1972; Edwards et al. 1994; Gullbring et al. 1998).

The structure of the innermost disk regions may reveal the mechanism by which material is accreted through the disk onto the star. In the current paradigm, T Tauri disks are truncated by the stellar magnetosphere within the co-rotation radius, with material accreting along magnetic field lines onto high-latitude regions of the star (e.g., Königl 1991; Shu et al. 1994). For typical T Tauri star masses, radii, magnetic field strengths, and accretion rates, predicted truncation radii range from $\sim 0.02-0.2$ AU. Observational measurements of these truncation radii are an obviously important test of the theory of magnetospheric accretion.

The spatial and temperature structures of inner circumstellar disks are also important for understanding the properties of dust and gas in the terrestrial planet region, and ultimately for understanding the formation of planets. For example, a puffed-up inner disk wall, due to the normal angle of incidence of stellar radiation on the truncated inner edge (e.g., Dullemond et al. 2001), may lead to shadowing, and thus cooler temperatures in the inner disk compared to standard flat or flared disk temperature profiles (e.g., Chiang & Goldreich 1997). This, in turn, would have profound implications as to how and where terrestrial planets form (e.g., Hayashi

1981; Sasselov & Lecar 2000). Furthermore, inner disk structure is important for understanding how the close-in extra-solar planets discovered by radial velocity surveys (e.g., Marcy & Butler 2000) either formed at, or migrated to their observed orbital radii (e.g., Lin et al. 1996).

Currently, only near-IR interferometric observations have sufficient spatial resolution to probe directly the geometry and temperature of hot ($\sim 1000 - 2000$ K) disk regions within ~ 1 AU of young stars. Observations of the inner disks of a few of the brightest T Tauri stars (Akeson et al. 2000; Colavita et al. 2003) and of their more massive counterparts, Herbig Ae stars (Millan-Gabet et al. 1999, 2001; Eisner et al. 2003, 2004), demonstrated that inner disks around lower-mass stars ($\lesssim 5$ $M_\odot$) are larger than inferred by fitting geometrically thin accretion disk models to SEDs (e.g., Beckwith et al. 1990). Inclusion of puffed-up inner walls in the models leads to consistent fits to both interferometric and SED data for these objects (Eisner et al. 2004; Muzerolle et al. 2003). On the other hand, higher-mass Herbig Be stars (Eisner et al. 2004) and the extreme accretor FU Ori (Malbet et al. 1998, 2005) are fitted well with simple flat disk models, suggesting that inner disk structure may depend on accretion rates or stellar properties. A larger sample of resolved inner disks, including lower-mass T Tauri stars, is necessary to explore such trends.

Here, we present 2.2 μm Keck Interferometer observations of the inner disks around four solar-type (1-2 $M_\odot$) T Tauri stars, potential analogs to our own young Sun. In order to model the stellar and circumstellar emission accurately, we combine our spatially resolved interferometry data with optical/near-IR SEDs and high-resolution echelle spectra. The photometric and spectroscopic data are essential for decomposition of the observed 2.2 μm flux into stellar and excess components. Since T Tauri stars are variable at near-IR wavelengths on timescales of several days to months (e.g., Skrutskie et al. 1996), our spectroscopic, photometric, and interferometric data were obtained within several days of one another. The photometry and spectra also enable determination of various properties of these systems, including stellar masses, ages, temperatures, radii, $v \sin i$, binarity, mass accretion rates, magnetospheric truncation radii, and co-rotation radii.

From the 2.2 μm interferometry data, we establish inner disk radii and temperatures, and distinguish between flat and puffed-up inner disk models. In addition, we compare these measured sizes with inferred magnetospheric and co-rotation radii. Although our sample is small, the range of stellar and accretion properties allows us to explore how inner disk structure depends on these parameters.

6.2 Observations and Data Reduction

6.2.1 Sample

Our sample consists of four classical T Tauri stars: AS 207A, V2508 Oph, AS 205A, and PX Vul. AS 207A, the optically-brightest T Tauri star in ρ Oph, was identified as a young star based on its Hα emission (Struve & Rudkjøbing 1949), and also as one component of a $0\farcs6$ binary system (Ghez et al. 1993). The T Tauri star V2508 Oph (Walter 1986) is located near the L162 dark cloud. AS 205A is a well-known young star near the ν Sco dark nebula (e.g., Merrill & Burwell 1950), identified as the brightest component of a $1\farcs3$ binary system by Ghez et al. (1993). We assume that AS 207A, V2508 Oph, and AS 205A are all at the approximate distance of the ρ Oph cloud, 160 pc (Chini 1981). Finally, PX Vul is a T Tauri star in the Vul R2 region, at a distance of 420 pc (e.g., Herbig & Kameswara Rao 1972; Herbst et al. 1982). Properties of our sample, including celestial coordinates, distances, and spectral types, are included in Table 6.1.

6.2.2 2.2 μm Interferometry

We observed AS 207A, V2508 Oph, AS 205A, and PX Vul with the Keck Interferometer (KI) on June 2, 2004. KI is a fringe-tracking long baseline near-IR Michelson interferometer combining light from the two 10m Keck apertures (Colavita & Wizinowich 2003; Colavita et al. 2003). The fringe-tracker detects a source in a 5ms integration, setting a limiting K-band magnitude of $m_K \sim 9$. In addition, sources

Table 6.1. Observed Properties of Sample

Source	Alt. Name	α (J2000)	δ (J2000)	d (pc)	SpTy	r_R	r_I	$v \sin i$ (km s^{-1})	$v_{\rm helio}$ (km s^{-1})	Hα EW	Hα 10% width
AS 207A	SR 9	16 27 40.28	-24 22 04.0	160[a]	K5±1	0.04 ± 0.07	-0.07 ± 0.15	15.2 ± 0.9	-7.17 ± 0.25	-16.4	342
V2508 Oph	Oph 6	16 48 45.62	-14 16 35.9	160[a]	K6±1	0.27 ± 0.07	0.09 ± 0.10	22.9 ± 1.0	-8.26 ± 0.56	-32.5	278
AS 205A	V866 Sco	16 11 31.40	-18 38 24.5	160[a]	K5±1	2.94 ± 0.32	1.95 ± 0.20	14.9 ± 1.8	-11.60 ± 0.87	-99.6	388
PX Vul	LkHα 483-41	19 26 40.30	+23 53 49.0	420[b]	F3±2[c,d]	0.82 ± 0.39	0.62 ± 0.45	78 ± 11	-7.0 ± 2.5	-9.4	512

References. — Spectral types, veilings (ratios of excess to stellar flux) at R and I bands, $v \sin i$ values, heliocentric radial velocities, Hα equivalent widths, and Hα widths at 10% of the peak, are determined from high-resolution optical spectroscopy (§6.2.5). *a*–Chini (1981); *b*–Herbst et al. (1982); *c*– Mora et al. (2001); *d*–Hernández et al. (2004). Distance estimates are likely uncertain by 10-20%.

must be optically bright enough for the adaptive optics (AO) systems on each Keck aperture. Superb seeing ($\lesssim 0\farcs5$) allowed excellent AO performance for our sample.

For each target, we measured squared visibilities (V^2) at K-band ($\lambda_0 = 2.2$ μm, $\Delta\lambda = 0.4$ μm). The system visibility (i.e., the point source response of the interferometer), was measured using observations of unresolved calibrators, weighted by the internal scatter in the calibrator and the temporal and angular proximity to the target source (Boden et al. 1998). Source and calibrator data were corrected for detection biases as described by Colavita (1999) and averaged into 5s blocks. The calibrated V^2 for the target sources are the average of the 5s blocks in each integration, with uncertainties given by the quadrature addition of the internal scatter and the uncertainty in the system visibility. Typical uncertainties are $\sim 5\%$.

All calibrators were chosen to be compact (angular diameters $\lesssim 0.2$ mas) and close to the target sources (within $\sim 10^\circ$). In addition, our calibrators have K-band magnitudes similar to those of our targets, to minimize potential biases. At optical wavelengths, the calibrators are brighter than the targets, which may lead to enhanced AO performance; by measuring the photon counts along both interferometer arms and applying a standard "ratio correction" (e.g., Colavita 1999), we calibrate out the effects of AO performance on the visibilities. The data for AS 207A, V2508 Oph, and AS 205A were calibrated using HD 142943 and HD 148968, and data for PX Vul were calibrated using HD 181383 and HD 182919.

6.2.3 JHK Adaptive Optics Imaging

We obtained dithered imaging observations of our sources at J,H, and K on June 4, 2004, using the Palomar 200-inch adaptive optics system (Troy et al. 2000) with the PHARO camera (Hayward et al. 2001). After bias correction, background subtraction, and flat-fielding of the images, photometric fluxes were measured with respect to the same calibrators used in our KI observations. Calibrator magnitudes are known from the 2MASS catalog, assuming they are non-variable. The photometric errors are given by the quadrature addition of the RMS variations in brightness between source

integrations and the uncertainties in the calibrator magnitudes. Since the sources and calibrators were observed at similar airmasses, we apply no atmospheric extinction corrections. The measured fluxes for these sources are listed in Table 6.2.

With the high angular resolution afforded by adaptive optics imaging ($\sim 0\farcs1$ at K-band) we were able to resolve AS 207 and AS 205 into binaries, finding parameters (see Table 6.3) consistent with previous measurements (Ghez et al. 1993; Reipurth & Zinnecker 1993; Koresko 2002; Barsony et al. 2003). For these systems, we measured photometric fluxes for both the primaries and secondaries; JHK magnitudes for the primaries are listed in Table 6.2, and ΔJHK values are given in Table 6.3. Since the projected binary separations are much larger than the field of view of KI (50 mas), we obtained interferometric data only for the primaries. No spatially resolved companions brighter than $\Delta K = 5$ were detected near V2508 Oph or PX Vul, and we consider these to be single stars hereafter.

6.2.4 $UBVRI$ Photometry

We observed our sample through Johnson U,B,V, and Kron R and I filters on June 8, 2004 using the robotic Palomar 60-inch telescope. Photometric fluxes were measured from bias-corrected, flat-fielded images using well-studied photometric standards (Landolt 1992). We determined extinction corrections and magnitude zero-points using observations of five Landolt standards obtained throughout the night. Photometric errors for our target sources are the sum of various uncertainties in quadrature: the RMS variation between integrations (where multiple integrations of a source are available), the uncertainties in zero-points and extinction coefficients, and uncertainties in magnitudes of our calibrators. Photometric uncertainties are typically $\lesssim 10\%$, except at U-band, where substantial uncertainties in the extinction coefficients lead to large error bars for the measured fluxes.

The seeing-limited resolution of these observations was $\sim 1\farcs7$, and the close binaries in our sample, AS 207 and AS 205, are unresolved. Optical photometry for these sources, listed in Table 6.2, therefore includes contributions from both the primaries

Table 6.2. Photometry of Observed Sources

Source	U	B	V	R	I	J	H	K
AS 207A[a]	13.52 ± 0.53	13.00 ± 0.07	11.78 ± 0.09	10.95 ± 0.13	9.80 ± 0.09	8.69 ± 0.05	7.96 ± 0.06	7.31 ± 0.06
V2508 Oph	15.74 ± 1.35	15.04 ± 0.06	13.45 ± 0.03	12.29 ± 0.04	10.74 ± 0.08	8.75 ± 0.04	7.73 ± 0.07	7.04 ± 0.08
AS 205A[a]	13.69 ± 0.47	13.74 ± 0.06	12.76 ± 0.03	11.82 ± 0.04	10.52 ± 0.08	8.63 ± 0.13	7.41 ± 0.07	6.36 ± 0.08
PX Vul	12.42 ± 0.38	12.35 ± 0.05	11.55 ± 0.02	11.01 ± 0.09	10.32 ± 0.06	9.33 ± 0.14	8.59 ± 0.09	7.74 ± 0.10

References. — *a*–For AS 207A and AS 205A, which have known companions, the $UBVRI$ photometry contains contributions from both components, while the JHK photometry reflects only the emission from the primaries.

Table 6.3. Binaries

Source	*Sep* (″)	*P.A.* (°)	ΔJ (mag)	ΔH (mag)	ΔK (mag)
AS 207B	0.63	354	1.59 ± 0.07	1.79 ± 0.09	2.19 ± 0.09
AS 205B[a]	1.31	213	1.10 ± 0.21	0.94 ± 0.10	0.91 ± 0.12

References. — *a*–AS 205B is a spectroscopic binary. See Appendix 6.7 for details.

and the secondaries.

6.2.5 High Resolution Optical Spectroscopy

High dispersion optical spectra of the sample were obtained on 2004 June 11 using the HIRES spectrograph (Vogt et al. 1994) on Keck I. HIRES was used with the red collimator, an RG-610 filter, and the D1 decker (1.″15 x 14.″0), yielding R≈ 34,000 spectra over 6330-8750 Å, with gaps between orders. An internal Quartz lamp and a ThAr lamp were observed with the same setup for flat fielding and dispersion correction. Several dwarf spectral type standards with known radial velocities were also observed to assist in the spectroscopic analysis. The binary AS 205 was observed with the slit along the axis of the pair, while AS 207 (an unresolved binary in these observations), V2508 Oph and PX Vul were observed with the slit perpendicular to the horizon (vertical mode).

The HIRES spectra were reduced using the facility "makee" reduction script written by Tom Barlow. Reduction includes bias-correction, flat-fielding, spectral extraction, sky subtraction, wavelength calibration, and heliocentric radial velocity corrections. This procedure worked well for single stars, but not for the components of AS 205 whose spectra overlap. In that case, the component spectra were determined by fitting two Gaussians to each one-dimensional cut in the spatial direction of the two-dimensional spectra. The FWHM of the best fit Gaussians were 0.″4; the seeing was quite good and the 1.″2 pair is reasonably well resolved. These extracted compo-

nent spectra were then assigned the wavelength solution of the combined system as determined by makee. Portions of the extracted spectra for our sources are shown in Figure 6.1.

6.3 Analysis

Calibrated 2.2 μm KI visibilities (§6.2.2) and de-reddened SEDs (§§6.2.3–6.2.4) for our sample are shown in Figures 6.2–6.5. V^2 values are plotted as a function of $u - v$ radius, $r_{\rm uv}$, and SEDs use units of λF_λ. The SEDs were constructed from our measured $UBVRIJHK$ photometry, corrected for binarity in the case of AS 207 and AS 205 (Table 6.3; §6.3.1.1), and de-reddened using the A_V values in Table 6.1. Figures 6.2–6.5 also include longer-wavelength (> 3 μm) photometry from the literature.

Measured 2.2 μm KI visibilities and broadband SEDs constrain the sizes and temperatures of inner disks around the observed sources. However, the near-IR stellar flux contribution to both the SEDs and visibilities must be removed before modeling the circumstellar component. We determine the stellar properties of our sample in §6.3.1.1 based on our spectroscopy and photometry, and use Kurucz models to determine stellar fluxes at near-IR wavelengths (see Figures 6.2–6.5; Table 6.4). Removing the stellar contributions, we are left with the circumstellar components of the visibilities and SEDs.

We model these circumstellar components in terms of 1) a geometrically flat accretion disk and 2) a flared, two-layer, irradiated disk with a puffed-up inner wall (§6.3.3; as in Eisner et al. 2004). For each source, we compute a grid of models for varying inner disk sizes and temperatures, and find the "best-fit" model for which the χ^2 between the model and the data is minimized. SEDs and visibilities computed for the best-fit models are shown in Figures 6.2–6.5, and best-fit inner disk sizes and temperatures are listed in Table 6.5. Longer-wavelength photometry from the literature is used to qualitatively constrain disk flaring (§6.3.4), although it is not used in our disk model-fitting.

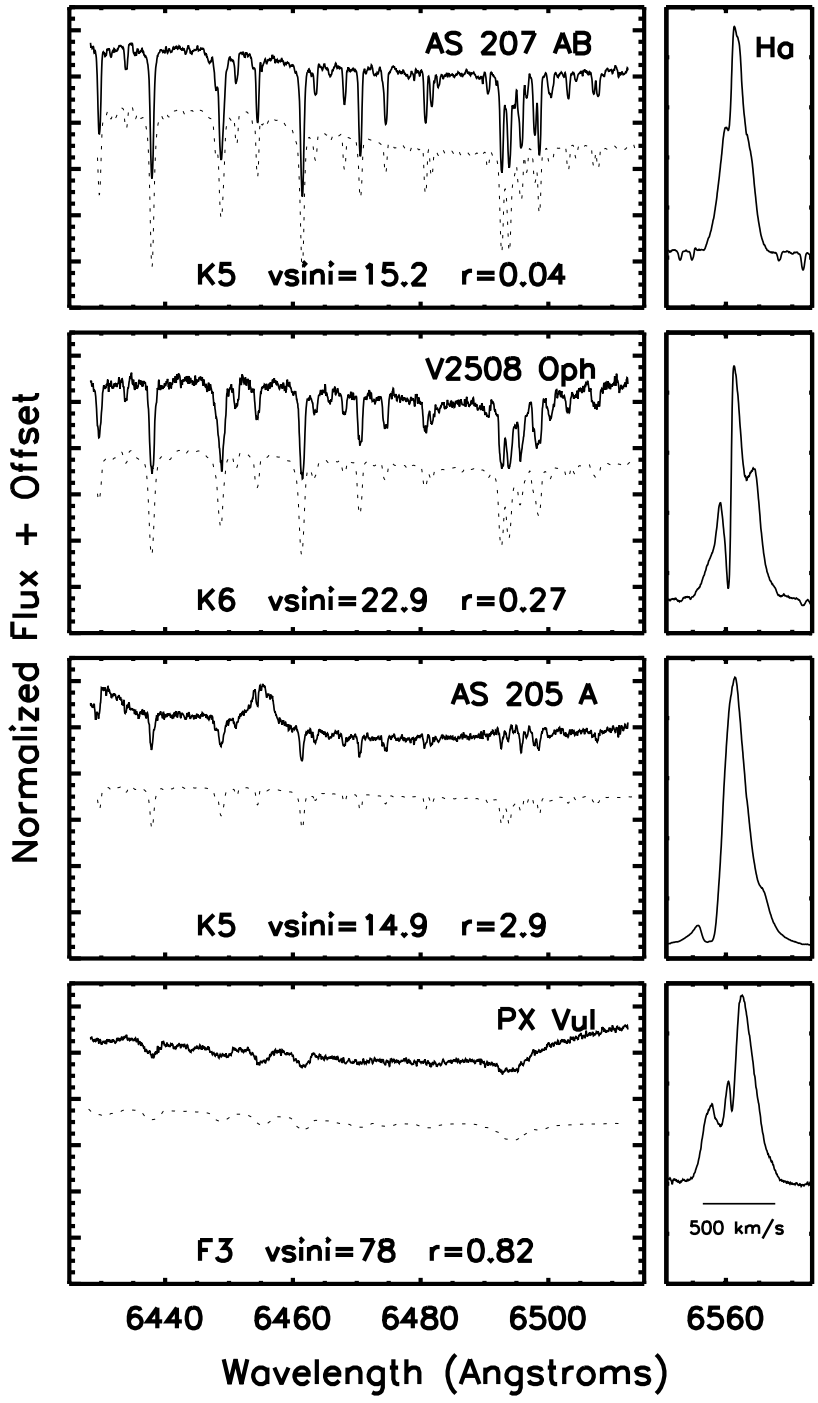

Figure 6.1 Portions of the Keck/HIRES spectra within the R-band (left), and Hα emission profiles (right); both panels have the same wavelength scale. The best fit dwarf standards, rotationally broadened and optically veiled, are shown as dashed lines for comparison. The strong, broad Hα emission profiles suggest all stars are accreting.

In order to compare our derived inner disk sizes with those expected from magnetospheric accretion theory, we use veiling values and shorter wavelength photometry to constrain mass accretion rates (§6.3.1.2) and thereby determine magnetospheric truncation radii (§6.3.1.3). Inferred $v \sin i$ values allow estimates of disk co-rotation radii (§6.3.1.4) for comparison purposes.

6.3.1 Stellar and Accretion Properties

6.3.1.1 Stellar Properties

We determined radial velocities, rotational velocities, spectral types, and continuum excesses for our sample from optical spectra (Table 6.1), following White & Hillenbrand (2004). Radial velocities and $v\sin i$ values are estimated by fitting a parabola to the peak of the cross-correlation functions, derived using dwarf stars of similar spectral type. The spectral types and the optical veiling levels at ~ 6500 Å and ~ 8400 Å (defined as $r_{R,I} = F_{\rm excess}/F_{\rm photosphere}$) are established simultaneously by comparisons with artificially veiled dwarf standards[2]. For the binary AS 205, spectral types are determined for both components from spatially-resolved spectra. In this discussion, we focus on AS 205A, but analysis of AS 205B, itself resolved into a spectroscopic binary, is included in Appendix 6.7. The binary AS 207 is spatially unresolved in the spectral data, preventing extraction of individual components. However, the large flux ratio for the AS 207 components (Table 6.3) suggests that the spectral type of the system is dominated by that of AS 207A. AS 207A, V2508 Oph, and AS 205A have mid-K spectral types, while PX Vul is hotter, with a spectral type of F3.

Since the optical photometry does not resolve the components of AS 205 and AS 207 (§6.2.4), we measure flux ratios from adaptive optics or spectroscopic observations and use the spectral types for the components to determine flux ratios at wavelengths where the pairs are spatially unresolved. For AS 205, the two Gaussian fits to echelle spectra (§2.4) provide a direct measure of the flux ratios at R and I bands of 0.16

[2]The lines used to measure spectral types and veilings are not gravity dependent, and thus dwarf standards are suitable even though they have higher surface gravities than our T Tauri sample (see White & Hillenbrand 2004, for further discussion).

and 0.24, respectively. The independently determined spectral types then provide estimates of flux ratios for the spatially unresolved UBV measurements. For AS 207, the two components are unresolved in the echelle spectra and we employ a less direct procedure. We assume that the spatially-resolved J-band measurement (§6.2.3) probes the photosphere of each component, and then predict flux ratios at the shorter, spatially unresolved wavelengths using the measured spectral type for AS 207A (K5) and an assumed spectral type of M3 for the secondary. The companion's spectral type is consistent with both the observed J-band flux ratio and the cooler spectral types assigned from near-infrared spectroscopy and photometry for the composite system (Doppmann et al. 2003; Geoffray & Monin 2001).

Stellar temperatures are assigned based on measured spectral types assuming a dwarf temperature/spectral type relation (e.g., Hillenbrand & White 2004). Extinctions and stellar luminosities are determined by comparing the veiling-corrected $R-I$ fluxes to those expected from Kurucz models most similar in temperature, assuming $\log g = 4$ (appropriate for pre-main sequence stars aged 1-10 Myr; e.g., Piorno Schiavon et al. 1995), the extinction relation of Steenman & Thé (1991), and the distances listed in Table 6.1. Stellar radii are estimated from the luminosities and temperatures using the Stefan-Boltzmann equation. Temperatures, luminosities, radii, and extinctions for these stars are listed in Table 6.4. We estimate that the assumed stellar temperatures are accurate to $\pm$100 K, while luminosities, radii, and extinction estimates are uncertain by $\sim 20-30\%$.

Stellar masses and ages are estimated by comparing the luminosities and temperatures with the predictions of pre-main sequence evolutionary models (Siess et al. 2000)[3]. These comparisons lead to masses near 1 $M_\odot$ for the 3 K-type stars, and 2.0 $M_\odot$ for the F3 star. Stellar ages range from 0.6 to 6.9 Myr (Table 6.4). While considerable uncertainties in pre-main sequence evolutionary models may lead to large errors in absolute ages, the relative ages are more secure. Including adopted uncertainties of 100 K for stellar temperature and 30% for stellar luminosity, AS 207A

[3]We prefer evolutionary models of Siess et al. (2000) because they span a larger range of stellar masses than those of Baraffe et al. (1998), and are more consistent with measured dynamical masses than D'Antona & Mazzitelli (1997) models.

and V2508 Oph appear to be the youngest stars in the sample, while AS 205A is somewhat older, and PX Vul is older still. We note that the apparent spread in ages may also correspond to different accretion histories for different sources, which could lead to variations in the birthline for pre-main sequence models; thus, the relative ages should be treated with some caution.

6.3.1.2 Mass Accretion Rates

Relative accretion rates for our sample are constrained qualitatively by Hα emission lines in our spectra (Figure 6.1). Equivalent widths of Hα and full-widths at 10% of the peak are listed in Table 6.1. These strong, broad profiles suggest on-going accretion in all sources (e.g., White & Basri 2003), with relatively smaller accretion rates for AS 207A and V2508 Oph.

Quantitative estimates of mass accretion rates are calculated from the accretion luminosity generated by infalling material (Gullbring et al. 1998):

$$\dot{M} = \frac{L_{\rm acc} R_*}{GM_*(1 - R_*/R_{\rm inner})}. \tag{6.1}$$

Here, $L_{\rm acc}$ is the accretion luminosity, R_* is the stellar radius, M_* is the stellar mass, and $R_{\rm inner}$ is the inner disk radius. We adopt values of $R_{\rm inner}$ from Table 6.5 (using puffed-up inner disk sizes determined from combined V^2+SED analysis; see §6.3.3); these are inner radii of the dust disks, and may be somewhat larger than the inner gas radii relevant for this formula (as discussed in §6.5.2), which would consequently lead to larger inferred mass accretion rates.

The accretion luminosity, $L_{\rm acc}$, is estimated by applying a bolometric correction factor to a flux excess measured over a limited wavelength range. We calculate accretion luminosities using two methods, one based on measured veiling at R-band (e.g., Hartigan & Kenyon 2003; White & Hillenbrand 2004), and the other based on measured U-band excess emission (Gullbring et al. 1998). For the first method, R-band excess luminosities are calculated from the measured veilings and then converted into accretion luminosities using a bolometric correction of 35. The bolometric correction

Table 6.4. Inferred Stellar and Accretion Properties

Source	T_* (K)	L_* ($L_\odot$)	R_* ($R_\odot$)	A_v (mag)	M_* ($M_\odot$)	τ_* (Myr)	$L_{\rm acc}$ ($L_\odot$)	$\dot{M}$ ($M_\odot$ yr^{-1})	$R_{\rm mag}$ (AU)	$R_{\rm corot}$ (AU)	$F_{*,K}$ (Jy)	$F_{{\rm D},K}$ (Jy)
AS 207A	4400	2.7	2.9	1.6	1.2	1.1	0.4	3.2×10^{-8}	0.13	0.09	0.59	0.27
V2508 Oph	4200	3.3	3.5	3.5	0.9	0.6	1.6	2.3×10^{-7}	0.11	≤ 0.07	0.82	0.45
AS 205A	4400	1.3	2.0	3.6	1.2	3.2	13.0	7.2×10^{-7}	0.03	≤ 0.07	0.27	2.12
PX Vul	6600	13.7	2.9	2.0	1.9	6.9	25.0	1.3×10^{-6}	0.04	≤ 0.03	0.13	0.46

References. — Stellar parameters, accretion luminosities and rates, and magnetospheric and co-rotation radii determined using high-resolution optical spectra and $UBVRI$ photometry (§6.3.1). Stellar and disk fluxes at 2.2 μm ($F_{*,K}$, $F_{{\rm D},K}$) determined using Kurucz models (with measured T_*, R_*, and adopted distances from Table 6.1) and de-reddened observed photometry (§6.3.2). As discussed in §6.3.1, we estimate that T_* is uncertain by $\pm$100 K, L_*, R_*, A_v, $R_{\rm mag}$, and $R_{\rm corot}$ are uncertain by $\sim 30\%$, $L_{\rm acc}$ and $\dot{M}$ are uncertain by a factor of 2-3, and $F_{*,K}$ and $F_{{\rm D},K}$ have error bars of $\sim 30 - 50\%$. The uncertainties on M_* and τ_* are more difficult to ascertain since they depend on pre-main sequence evolutionary models; however, we estimate that the relative uncertainties for these parameters are $\sim 30 - 50\%$.

factor is highly uncertain, and probably introduces uncertainties of a factor of ~ 3 in the computed accretion luminosities. We also calculate the accretion luminosity from the observed U-band excess luminosity (L_U) following Gullbring et al. (1998):

$$\log(L_{\rm acc}/L_\odot) = 1.09^{+0.04}_{-0.18}\log(L_U/L_\odot) + 0.98^{+0.02}_{-0.07}. \quad (6.2)$$

Although the accretion luminosities calculated using Equation 6.2 use a smaller bolometric correction than for the first method (due to the assumed high temperature of the accretion excess; Calvet & Gullbring 1998), the large photometric uncertainties for our U-band data (Table 6.2) introduce errors of a factor of ~ 2. We find that accretion estimates based on U-band fluxes are typically higher than those computed from R-band measurements, although the two estimates are consistent to within a factor of 2. Since the accretion luminosities estimated from both methods have large error bars, we adopt the mean of the two values in our analysis. Inferred accretion luminosities for our sample range from 0.4 $L_\odot$ to 25.0 $L_\odot$, and are listed in Table 6.4.

Using these adopted values for $L_{\rm acc}$, we calculate mass accretion rates from Equation 6.1. For our sample, $\dot{M}$ is between 3.2×10^{-8} $\rm M_\odot$ $\rm yr^{-1}$ and 1.3×10^{-6} $\rm M_\odot$ $\rm yr^{-1}$ (Table 6.4). The large uncertainties for $L_{\rm acc}$ lead to accretion rates that are probably uncertain by a factor of 2-3.

6.3.1.3 Magnetospheric Radii

The expected radius of magnetospheric truncation, $R_{\rm mag}$, is determined by the balance of forces between infalling (accreting) material and the stellar dipole field (Königl 1991):

$$\frac{R_{\rm mag}}{R_*} = 2.27\left[\frac{(B_0/1\ {\rm kG})^4(R_*/{\rm R}_\odot)^5}{(M_*/{\rm M}_\odot)(\dot{M}/10^{-7}{\rm M}_\odot\ {\rm yr}^{-1})^2}\right]^{1/7}. \quad (6.3)$$

With the stellar parameters determined in §6.3.1.1, the accretion rates calculated in §6.3.1.2, and assuming a typical magnetic field strength for T Tauri stars of 2 kG (Johns-Krull et al. 2003), we calculate $R_{\rm mag}$ for our sample. Our values for $R_{\rm mag}$ range from 0.03 to 0.13 AU (Table 6.4). Propagating the assumed uncertainties for

R_*, M_*, and $\dot{M}$, and adopting an uncertainty of 30% for B_0, we estimate that the magnetospheric radii are uncertain by $\sim 30\%$.

6.3.1.4 Co-Rotation Radii

The co-rotation radius is the radius at which the Keplerian orbital period in the disk equals the stellar rotation period. We derive co-rotation radii for stars with $v \sin i$ measurements (Table 6.1) according to:

$$R_{\rm co-rotation} = (GM_*)^{1/3} \left(\frac{R_*}{v}\right)^{2/3} \leq (GM_*)^{1/3} \left(\frac{R_*}{v \sin i}\right)^{2/3}. \quad (6.4)$$

Here, M_* is the stellar mass, R_* is the stellar radius, $v \sin i$ is the projected rotational velocity of the star, and i is the inclination of the system. For AS 207A, where there is a reported photometric period, $\tau = 6.53$ days (Shevchenko & Herbst 1998; Bouvier 1990), the inclination (and hence the co-rotation radius) can be determined explicitly. For the remaining sources, without known rotation periods (Shevchenko & Herbst 1998), we derive upper limits. Co-rotation radii and upper limits range from 0.03 to 0.09 AU, and are listed in Table 6.4. Propagating the uncertainties in M_*, R_*, and $v \sin i$ (assuming stellar mass and radius are uncertain by $\sim 30\%$), we estimate that the derived co-rotation radii are uncertain by approximately 20%.

6.3.2 Near-IR Stellar and Excess Fluxes

The measured 2.2 μm visibilities and near-IR SEDs contain information about inner circumstellar disks as well as the central stars, and distinguishing the stellar and excess fluxes is crucial to accurate modeling of the disks. Because the stellar SED peaks closer to 2.2 μm for our current sample than for the hotter stars analyzed in Eisner et al. (2004), this step is especially critical here. In this Section, we discuss our procedure for removing the stellar component from the V^2 and SED data, and in §6.3.3, we model the circumstellar component and determine disk parameters.

The measured SED at near-IR wavelengths is simply the sum of the stellar and

disk fluxes. Our 2.2 μm visibilities are given by

$$V^2_{\rm meas} = \left(\frac{F_* V_* + F_{\rm D} V_{\rm D}}{F_* + F_{\rm D}}\right)^2 \approx \left(\frac{F_* + F_{\rm D} V_{\rm D}}{F_* + F_{\rm D}}\right)^2, \tag{6.5}$$

where F_* is the stellar flux, $V_* \approx 1$ are the visibilities due to the unresolved central star, $F_{\rm D}$ is the circumstellar disk flux, and $V_{\rm D}$ are the visibilities due to the disk. A knowledge of the stellar flux at near-IR wavelengths is critical for modeling the circumstellar components of both the 2.2 μm visibilities and the near-IR SEDs. This flux can be estimated using the stellar parameters from §6.3.1.1 and extrapolating the veiling-corrected flux measured at optical wavelengths using a Kurucz model. The excess 2.2 μm flux due to the compact circumstellar disk is the difference between the de-reddened observed flux and the Kurucz model. These 2.2 μm stellar and excess fluxes are listed in Table 6.4.

The inferred stellar and excess fluxes are somewhat uncertain, leading to uncertainties in the derived disk parameters. For AS 205A and PX Vul, where the excess flux dominates the emission, uncertainties in the relative fluxes will have a small effect on disk parameters. However, when the stellar and excess fluxes are comparable, as for AS 207A and V2508 Oph, there can be significant errors in the fitted disk sizes. For example, 30% errors in 2.2 μm stellar flux lead to size errors of 25% and 23% for AS 207A and V2508 Oph, but only 2% and 7% for AS 205A and PX Vul.

In addition to the central star and circumstellar disk, there may be other contributions to the visibilities and SEDs. Emission on scales between the ~ 5 mas KI fringe spacing and the ~ 50 mas field of view, for example, due to thermal or scattered emission from residual envelopes, will be resolved out and will lower the overall measured visibilities and lead to larger inferred sizes. If the extended emission has a similar spectrum to the star, as expected for scattering from large dust grains, it will not affect the SED. Extended emission is difficult to constrain, since observations that can resolve faint emission on angular scales smaller than 50 mas are virtually nonexistent. However, previous analysis of the visibilities and SEDs of more luminous Herbig Ae/Be stars indicates small ($\lesssim 1\%$) contributions from extended emission on

$\lesssim 1''$ scales (Eisner et al. 2004). For KI, which has a field of view of only 50 mas, we expect the contribution from extended emission for our less luminous T Tauri star sample to be even smaller.

Near-IR emission may also arise from hot gas in accretion shocks at the stellar photosphere (e.g., Calvet & Gullbring 1998; Gullbring et al. 2000), or hot optically thin gas in the inner disk (interior to the dust truncation radius; e.g., Akeson et al. 2005). Since these hot gas components are compact compared to emission from the circumstellar dust disk, they would tend to raise the visibilities compared to those predicted by our Equation 6.5; i.e., lead to smaller inferred disk sizes. In contrast, for the measured SEDs hot gas would contribute extra emission, leading to *larger* inferred disk sizes. We expect that the fraction of near-IR emission from an 8000 K accretion shock (Calvet & Gullbring 1998) will be relatively small compared to peak emission from a 1000-2000 K disk. However, emission from hot gas may cause a measurable effect on the 2.2 μm visibilities and near-IR SEDs for sources with extremely high accretion rates (see §6.4.3).

In the analysis below, we assume that near-IR emission from extended dust or hot gas is insignificant compared to the stellar and disk emission. Thus, we model the SED using a Kurucz stellar atmosphere plus thermal emission from a disk, and use Equation 6.5 to model the measured visibilities.

6.3.3 Modeling Inner Disk Structure

Equipped with the stellar and circumstellar contributions to the visibilities and SEDs (§6.3.2), we fit the circumstellar components using the two simple disk models described in detail by Eisner et al. (2003, 2004): 1) a geometrically flat accretion disk with a temperature profile $T(R) \propto R^{-3/4}$ (Lynden-Bell & Pringle 1974), truncated at an inner radius, $R_{\rm in}$; and 2) a flared, irradiated, two-layer disk (Chiang & Goldreich 1997) incorporating a puffed-up inner disk wall at $R_{\rm in}$ (Dullemond et al. 2001). The main difference between the two models is the angle of incidence of stellar radiation: for the flat disk, stellar radiation is incident at glancing angles, while the puffed-up

inner disk and flared outer surface intercept starlight at more normal angles, leading to additional disk heating. For the second model, the near-IR emission is dominated by the puffed-up inner rim, and the emission appears essentially ring-like at the 2.2 μm wavelength of our interferometric observations. While the geometrically-thin disk model assumes blackbody emission, we assume the opacity for the puffed-up inner disk model is due to astronomical silicate dust (Draine & Lee 1984).

For each model, the parameters relevant for the inner disk structure are the inner radius, $R_{\rm in}$, and the temperature of the disk at the inner radius, $T_{\rm in}$. Temperatures at other disk radii are specified by these parameters and the assumed temperature profiles for the disk models. The V^2 and SED data (and associated error bars) used in the modeling are shown in Figures 6.2-6.5. We use only $RIJHK$ photometry, and de-veil the RI fluxes, so that the data traces only the inner disk, uncontaminated by hot accretion excess emission which can dominate at shorter wavelengths.

With the limited amount of data available (2-4 visibilities, and 5 photometric points for each source), we consider only face-on disk models here. As discussed in Eisner et al. (2004), including inclination in the models may affect the results. Unless the baseline position angle corresponds with the major axis of an inclined disk, the size inferred from V^2 measurements for a face-on model would be underestimated with respect to the inferred size for an inclined model. Similarly, the face-on assumption would lead to an underestimate of disk size from SED data, since a face-on disk produces more near-IR flux than an inclined disk of the same size. Further interferometric observations, probing a range of position angles, are necessary to constrain the parameters of inclined disk models. However, assuming our sources are not close to edge-on (reasonable given that the central stars are un-obscured), inclination effects will not substantially alter the results presented here for face-on disk models.

We fit our 2.2 μm KI visibilities and SED data simultaneously and determine the best-fit parameter values, $R_{\rm in}$ and $T_{\rm in}$, by calculating χ^2 for models over a grid of inner radii and temperatures. In practice, we fit for the directly observable angular (rather than linear) size of the inner radius, $\theta_{\rm in}$; best-fit values are converted to linear sizes using the distances in Table 6.1. We consider $\theta_{\rm in}$ ranging from 0.1 to 10 mas

in increments of 0.01 mas (spanning the approximate angular resolution of KI), and $T_{\rm in}$ ranging from 1000 to 2500 K in 100 K increments (bracketing values expected for dust sublimation; e.g., Salpeter 1977; Pollack et al. 1994). For each model, we calculate the χ^2 of the combined V^2+SED dataset, where each data point is weighted by its measurement uncertainty, and we find the inner disk size and temperature for which χ^2 is minimized. 1-σ uncertainties on the best-fit parameters are determined in the standard way (e.g., Eisner et al. 2004). Best-fit parameters, 1-σ uncertainties, and reduced χ^2 values are listed in Table 6.5. Puffed-up inner disk models generally provide small χ^2 values (indicating good fits to the data), with inner disk sizes and temperatures ranging from 0.12 to 0.32 AU and 1000 to 1800 K, respectively. In contrast, flat disk models fit the data poorly, and suggest smaller inner disk sizes (0.02-0.22 AU) and higher temperatures (1400-2400 K).

The poor fits of flat disk models to the data are consistent with previous observations which showed that sizes determined from near-IR interferometry are often larger than those determined from SED modeling (e.g., Akeson et al. 2000; Millan-Gabet et al. 2001; Eisner et al. 2003). We investigate this issue here by fitting the visibility and SED data separately. For the SEDs, we use the same procedure and parameter grid as for the combined analysis. For the visibilities, where we have fewer data points, we fit only for $\theta_{\rm in}$, assuming the value of $T_{\rm in}$ determined from the combined analysis. The best-fit parameter values, uncertainties, and reduced χ^2 values are included in Table 6.5. We note that for the small numbers of visibility measurements, the reduced χ^2 are often very small, indicating poor constraints on the models. The results indicate that the V^2 or SED data individually can be fit reasonably well with either model, although the puffed-up inner disk model provides somewhat lower χ^2 values for the SED fits. For most sources, the inner size for flat disk models inferred from the visibilities is ≥ 5 times larger than inferred from the SEDs. The puffed-up inner disk models, in contrast, find best-fit sizes from the V^2 or SEDs generally consistent within the 1σ uncertainties (Table 6.5).

From the SEDs alone, we cannot distinguish between flat and puffed-up inner disk models, but combined V^2+SED analysis shows that puffed-up inner disk models are

Table 6.5. Disk Parameters from Near-IR Interferometry and SEDs

Source	Flat Disks χ^2_r	Flat Disks $R_{\rm in}$ (AU)	Flat Disks $T_{\rm in}$ (K)	Flared, Puffed-Up Disks χ^2_r	Flared, Puffed-Up Disks $R_{\rm in}$ (AU)	Flared, Puffed-Up Disks $T_{\rm in}$ (K)
Combined V^2+SED Results						
AS 207A	1.070	$0.04^{+0.01}_{-0.02}$	1500^{+300}_{-100}	0.208	$0.23^{+0.11}_{-0.10}$	1000^{+200}_{-100}
V2508 Oph	1.409	$0.02^{+0.17}_{-0.01}$	2400^{+100}_{-1300}	0.981	$0.12^{+0.10}_{-0.10}$	1500^{+900}_{-300}
AS 205A	3.729	$0.07^{+0.01}_{-0.01}$	1900^{+100}_{-100}	6.072	$0.14^{+0.01}_{-0.01}$	1900^{+100}_{-100}
PX Vul	3.049	$0.22^{+0.01}_{-0.03}$	1400^{+100}_{-100}	1.072	$0.32^{+0.01}_{-0.04}$	1500^{+100}_{-100}
V^2-only Results						
AS 207A	0.010	$0.17^{+0.04}_{-0.05}$	1500	0.010	$0.25^{+0.06}_{-0.07}$	1000
V2508 Oph	0.003	$0.10^{+0.04}_{-0.03}$	2400	0.003	$0.20^{+0.04}_{-0.13}$	1500
AS 205A	0.211	$0.07^{+0.01}_{-0.01}$	1900	0.224	$0.13^{+0.01}_{-0.01}$	1900
PX Vul	0.234	$0.23^{+0.01}_{-0.01}$	1400	0.234	$0.34^{+0.03}_{-0.02}$	1500
SED-only Results						
AS 207A	0.473	$0.04^{+0.01}_{-0.02}$	1500^{+300}_{-100}	0.327	$0.23^{+0.11}_{-0.23}$	1000^{+300}_{-100}
V2508 Oph	0.969	$0.02^{+0.03}_{-0.01}$	2400^{+100}_{-800}	0.870	$0.07^{+0.08}_{-0.07}$	1900^{+600}_{-500}
AS 205A	6.851	$0.06^{+0.01}_{-0.01}$	2000^{+200}_{-100}	4.796	$0.23^{+0.01}_{-0.03}$	1600^{+100}_{-100}
PX Vul	1.341	$0.05^{+0.03}_{-0.01}$	2400^{+100}_{-400}	0.842	$0.21^{+0.06}_{-0.04}$	1800^{+200}_{-200}

References. — Columns 2-4 list the reduced χ^2 values, inner radii, and inner temperatures for best-fit flat accretion disk models. Columns 5-7 list χ^2_r, $R_{\rm in}$, and $T_{\rm in}$ for best-fit puffed-up inner disk models. Results are shown for fits to combined V^2+SED datasets as well as V^2 and SEDs individually. For the V^2-only fits, we assumed the best-fit temperature from the combined V^2+SED analysis, fitting only for $R_{\rm in}$.

preferred (Table 6.5). Qualitatively, this additional constraint comes from the spatially resolved information contained in the V^2 data. While near-IR SEDs constrain both the temperature and size of the inner disk, these parameters are degenerate with the spatial and temperature profiles, and thus SED fits are not unique; one can find a suitable fit for either the geometrically thin or puffed-up inner disk models by varying $T_{\rm in}$ and $R_{\rm in}$. Combining SEDs with even a limited amount of interferometric data, we can measure *directly* the size of the inner disk, thereby breaking the degeneracy inherent in SED-only modeling and enabling us to distinguish between puffed-up and geometrically flat inner disk models.

The measured sizes discussed above are determined directly from the data. Since we separated the circumstellar components of the visibilities and SEDs from the stellar contributions in §6.3.2, the measured disk sizes do not depend on stellar properties or disk accretion rates; i.e., $R_{\rm in}$ and $T_{\rm in}$ are chosen simply to provide the best fit to the observations. Thus, the inner disk structure for our best-fit models is fully specified by $R_{\rm in}$, $T_{\rm in}$, and the assumed temperature profiles. Below, we investigate whether the stellar and accretion luminosities in these sources can provide sufficient disk heating to match the measured inner radii and temperatures, providing an additional test of whether the measured sizes are consistent with the physical models.

For flat disk models, the expected temperature in the disk at 1 AU depends on heating by both stellar radiation and viscous dissipation of accretion energy (Lynden-Bell & Pringle 1974),

$$T_{\rm 1AU} = \left[2.52 \times 10^{-8} \left(\frac{R_*}{\rm R_\odot} \right)^3 T_*^4 + 5.27 \times 10^{10} \left(\frac{M_*}{\rm M_\odot} \right) \left(\frac{\dot{M}}{10^{-5}\,\rm M_\odot\,yr^{-1}} \right) \right]^{1/4}. \quad (6.6)$$

Thus, the expected disk temperature depends on T_*, R_*, M_*, and $\dot{M}$. Using the value of $T_{\rm 1AU}$ computed for our inferred stellar and accretion parameters (§6.3.1), we predict the radius in the disk where $T = T_{\rm in}$ (where $T_{\rm in}$ is determined from combined V^2+SED analysis),

$$\frac{R_{\rm flat}}{\rm AU} = \left(\frac{T_{\rm 1AU}}{T_{\rm in}} \right)^{4/3}. \quad (6.7)$$

For the passive disk model with a puffed-up inner wall, the expected radius where $T = T_{\rm in}$ depends on the total luminosity incident on the inner disk,

$$R_{\rm puffed-up} = \sqrt{\frac{L_* + L_{\rm acc}}{4\pi\sigma T_{\rm in}^4}(1+f)}. \quad (6.8)$$

Here, f is the ratio of the inner disk width to the inner radius, which we have assumed to be 0.10 (Dullemond et al. 2001). Equation 6.8 includes the effects of accretion luminosity, $L_{\rm acc}$, in addition to the stellar luminosity (Muzerolle et al. 2003).

Expected inner radii for the two models, with and without accretion heating, are listed in Table 6.6. We compare these predictions with our measured sizes: for the puffed-up inner disk model, we use sizes measured from V^2+SED data, while for the flat disk model, which provides poor fits to combined datasets, we use the inner disk sizes measured from V^2-only data. Measured inner disk sizes are roughly consistent with expectations for puffed-up inner disk models based on the stellar parameters determined in §6.3.1.1. Moreover, for the high-accretion rate source AS 205A, the predicted size is more consistent with the measured size when accretion luminosity is included, demonstrating the importance of accretion in the disk structure for this object. In contrast, for AS 207A, V2508 Oph, and PX Vul, the predicted sizes of puffed-up inner disk models with $\dot{M} = 0$ are compatible with the measured sizes (Table 6.6), suggesting that stellar irradiation is the dominant effect in puffing up the inner disk edges. Expected sizes for the flat disk model are smaller than measured values for all sources except AS 205A. These results are compatible with the fact that the puffed-up inner disk models generally fit the visibility and SED data better than the flat disk models.

The best-fit inner disk sizes (Table 6.5) are larger than both the magnetospheric and co-rotation radii calculated in §6.3.1 (Table 6.4). We illustrate this graphically in Figure 6.6, where we plot the 2.2 μm brightness distributions for our best-fit puffed-up inner disk models, and indicate the positions of magnetospheric and co-rotation radii with dotted and dashed lines, respectively. The discrepancy between measured sizes and magnetospheric/co-rotation radii is relatively small for some sources ($\lesssim 2$),

Table 6.6. Measured versus Predicted Inner Disk Sizes

Source	Flat Disks			Flared, Puffed-Up Disks		
	$R_{\rm in,meas}$ (AU)	$R_{\rm in,\dot{M}=0}$ (AU)	$R_{\rm in,\dot{M}\neq 0}$ (AU)	$R_{\rm in,meas}$ (AU)	$R_{\rm in,\dot{M}=0}$ (AU)	$R_{\rm in,\dot{M}\neq 0}$ (AU)
AS 207A	$0.17^{+0.04}_{-0.05}$	0.03	0.04	$0.23^{+0.11}_{-0.10}$	0.26	0.28
V2508 Oph	$0.10^{+0.04}_{-0.03}$	0.02	0.03	$0.12^{+0.10}_{-0.10}$	0.13	0.16
AS 205A	$0.07^{+0.01}_{-0.01}$	0.01	0.07	$0.14^{+0.01}_{-0.01}$	0.05	0.17
PX Vul	$0.23^{+0.01}_{-0.01}$	0.06	0.15	$0.32^{+0.01}_{-0.04}$	0.27	0.46

References. — Measured sizes ($R_{\rm in,meas}$) taken from Table 6.5, compared to expectations for disk models based on inferred inner disk temperatures and stellar parameters. For the puffed-up inner disk models, we use the sizes measured from combined V^2+SED analysis, while for the flat disk models, where models generally provide poor fits to the V^2 and SED values simultaneously, we use measured sizes from V^2-only analysis. Expected inner disk sizes for the flat and puffed-up disk models are calculated from Equations 6.7–6.8, assuming no accretion ($R_{\rm in,\dot{M}=0}$) and using the inferred accretion rates from Table 6.1 ($R_{\rm in,\dot{M}\neq 0}$).

and large for others (> 5). The magnitude of these discrepancies depends to some extent on our assumptions. However, more realistic models including inclined disks and potentially lower stellar magnetic fields would actually exacerbate the differences between measured sizes and magnetospheric radii (magnetic fields substantially higher than the assumed 2 kG are unlikely; Johns-Krull et al. 2003).

6.3.4 Large-Scale Disk Structure

In §6.3.3, we modeled our $RIJHK$ photometry and 2.2 μm visibilities, and determined inner disk radii and temperatures for our sample. These values of $R_{\rm in}$, $T_{\rm in}$ also provide the normalization of the temperature profiles (for our two simple models) in the outer disk regions. Here, we combine our measurements and modeling of the inner disk with longer-wavelength photometry (3-100 μm; Weaver & Jones 1992; Jensen & Mathieu 1997; Prato et al. 2003; Koresko 2002) which probes larger disk radii. Due to source variability and multiple sources within the large IRAS beam (as seen in 2MASS images), the uncertainties in this long-wavelength photometry are likely $\gtrsim 10\%$. Despite these uncertainties, the long-wavelength fluxes still yield rough constraints on outer disk structure.

We quantify disk flaring by how the height of the disk increases with radius: $H/R \propto R^{\xi}$. For a flat disk, $\xi = -1$, while for a fully flared disk in hydrostatic equilibrium, $\xi = 2/7$ (Chiang & Goldreich 1997). These two extremes correspond to the flat and puffed-up disk models used above. However, dust settling and/or grain growth could result in other values for ξ (Dullemond & Dominik 2004a,b). Here, we also consider the case of a somewhat, but not fully, flared disk with $\xi = 1/10$. Comparison of the un-flared, somewhat flared, and fully flared models with the data give a qualitative measure of the degree of flaring. Inclination effects, which are not included in our face-on models, will also suppress the long-wavelength flux (due to the smaller projected surface area), mimicking the effects of flatter disks. Thus, we do not attempt to determine ξ exactly, instead maintaining a qualitative approach.

The outer disk geometry, as illustrated by the long-wavelength photometry, seems

to vary from source to source (Figures 6.2–6.5). In some sources (AS 207A, PX Vul), flatter outer disks are consistent with the data, while other objects (V2508 Oph, AS 205A) require significant outer disk flaring to explain the data.

6.4 Results for Individual Sources

Figures 6.2–6.5 show the flat (solid lines) and puffed-up (dotted lines) disk models that provide the best fits to combined V^2+SED datasets. For each source see Table 6.5 for best-fit $R_{\rm in}$, $T_{\rm in}$, and reduced χ^2 values of these models. In general, puffed-up inner disk models with inner temperatures ranging from 1000-1800 K provide good fits to the data, while flat disk models provide poor fits to the SED and V^2 data.

6.4.1 AS 207A

AS 207A shows a weak near-IR excess and a mass accretion rate lower than other sources in our sample. The visibility and SED data are more consistent with the predictions of a cooler, puffed-up inner disk model than with a flat disk model (χ^2_r = 0.21 versus 1.07; Figure 6.2). Best-fit inner disk sizes and temperatures are $\sim$ 0.25 AU and 1000 K for the puffed-up inner disk model. This size is approximately two times larger than the calculated magnetospheric and co-rotation radii (Figure 6.6).

The IRAS photometry for AS 207A is compatible with flat outer disk models. Although AS 207A has a binary companion, the steeply increasing flux ratio across J,H, and K (Table 6.3) suggests that the companion contributes little to the long-wavelength flux.

6.4.2 V2508 Oph

For V2508 Oph, a source with a relatively small accretion rate, the puffed-up disk model provides a better fit to our V^2 and SED data than the flat disk model (χ^2_r = 0.98, compared with 1.41). While the puffed-up inner disk size determined from the visibilities (0.20 AU) is somewhat larger than that determined from the SED (0.07

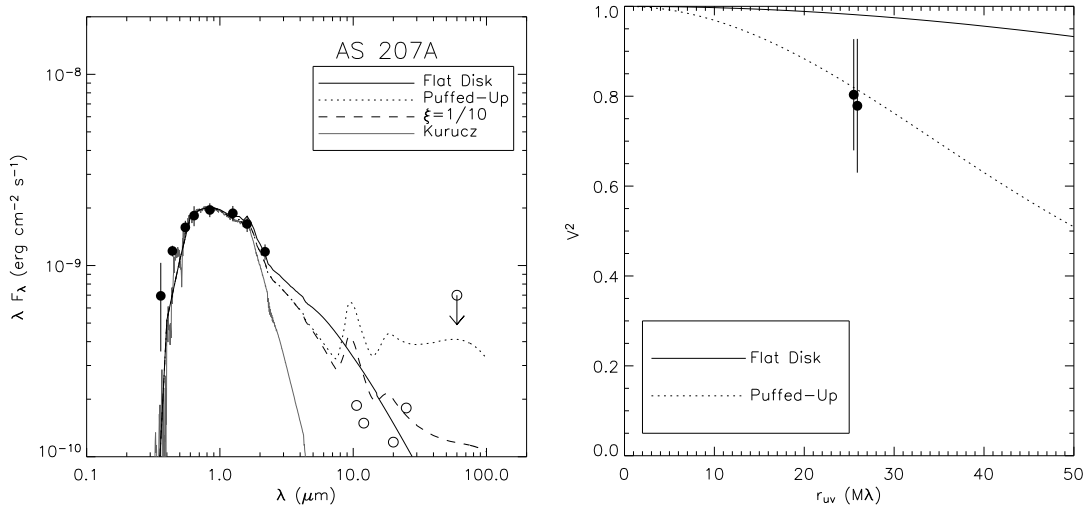

Figure 6.2 (left) Reddening-corrected fluxes for AS 207A from optical through near-IR wavelengths (filled circles), supplemented with longer-wavelength fluxes from the literature (open circles; Weaver & Jones 1992; Jensen & Mathieu 1997; Prato et al. 2003; Koresko 2002). Predicted SEDs for geometrically flat accretion disks (solid black line), and flared disks with puffed-up inner rims (dotted line), as well as the Kurucz model atmosphere with the stellar parameters determined in §6.3.1.1 (solid gray line), are also plotted. Only $RIJHK$ photometry, probing the star and inner disk, was used in the fits. We also plot the SED predicted by a flared disk model with an intermediate flaring index, $\xi = 1/10$ (dashed line). (right) Squared visibilities measured with KI, as a function of uv radius, along with the predictions of different models. The two curves are labeled as in the left panel: the solid black line indicates the model determined by fitting a flat accretion disk to the V^2+SED dataset, and the dotted line represents the V^2 for the best-fit puffed-up inner disk wall model. For AS 207A, the puffed-up inner disk model provides a superior fit to the data. The long-wavelength photometry is compatible with an un-flared outer disk.

AU), the discrepancy has $< 1\sigma$ significance, and the fit to the combined V^2+SED dataset produces a reasonable χ^2_r value (Figure 6.3; Table 6.5). Furthermore, the measured inner disk size agrees well with (but is slightly larger than) the magnetospheric truncation radius calculated in §6.3.1.3 and the upper limit on co-rotation radius determined in §6.3.1.4 (Figure 6.6). The long-wavelength photometry is compatible with an outer disk that is somewhat flared ($\xi \sim 1/10$).

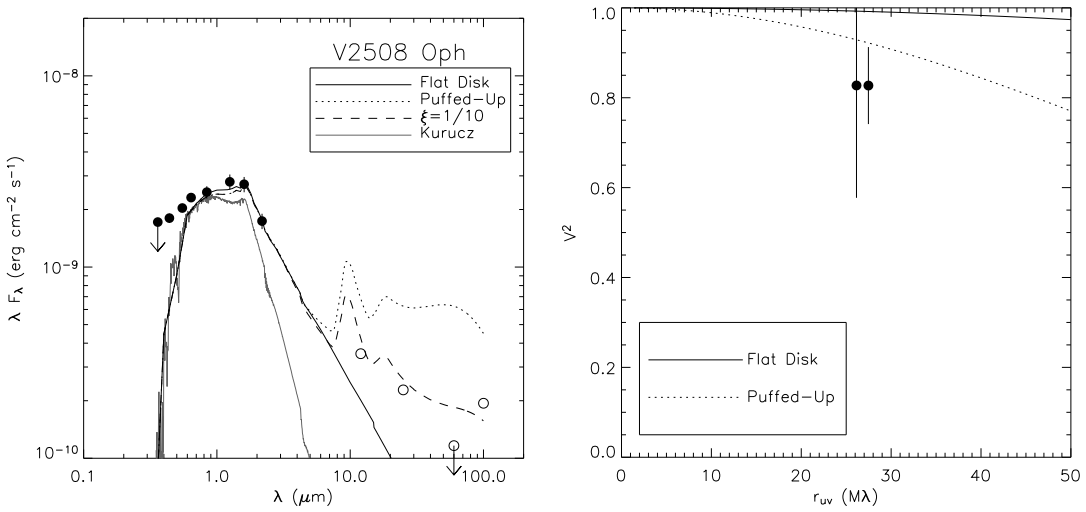

Figure 6.3 SEDs and squared visibilities for V2508 Oph, labeled as in Figure 6.2. For this source, the puffed-up inner disk model provides a superior fit to the SED and V^2 data. The IRAS photometry for this source is more consistent with a moderately flared disk model (with $\xi \sim 1/10$) than with a flat disk model.

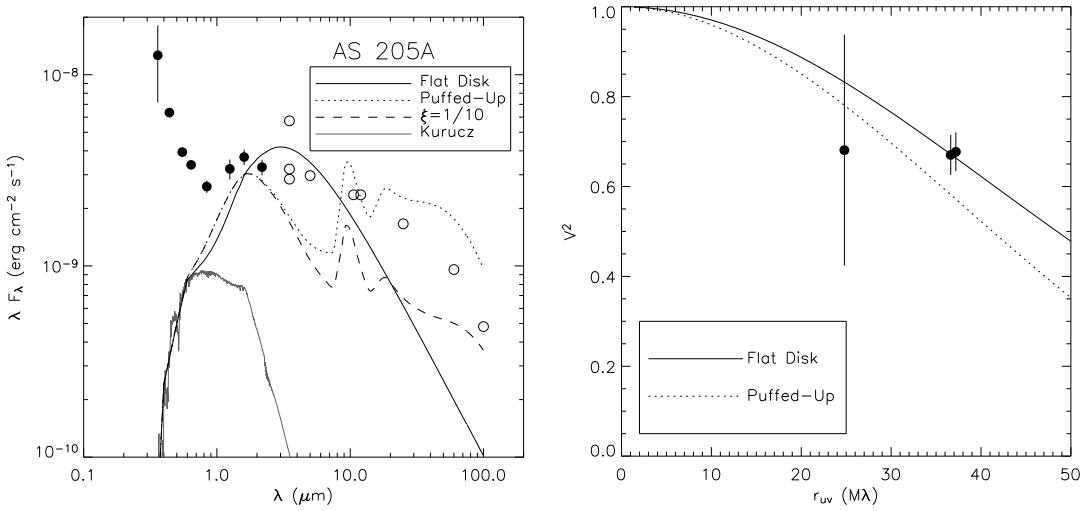

Figure 6.4 SEDs and squared visibilities for AS 205A, labeled as in Figure 6.2. For this source, the flat disk model provides a better fit than the puffed up inner disk model to the SED and V^2 data, although neither model fits very well. These poor fits are likely due to near-IR emission from hot accretion shocks that is not accounted for in our models. The fact that the long-wavelength photometry lies above the model predictions suggests that flaring and accretion heating are important in the outer disk.

6.4.3 AS 205A

Fits to the combined V^2+SED dataset have $\chi^2 \sim 4-6$, mainly due to the poor fit to the SED data. The flat accretion disk model provides a better fit to the combined V^2+SED dataset than the puffed-up inner disk model, but both fits are of poor quality so it is difficult to distinguish between them. The best-fit inner disk sizes range from 0.07 to 0.14 AU, and inner disk temperatures are $\sim$ 1900 K. These fitted inner disk sizes are significantly larger than the magnetospheric truncation radius computed in §6.3.1.3 and the upper limit on co-rotation radius calculated in §6.3.1.4 (Figure 6.6).

We suggest that the poor fits to the SED data for this source ($\chi^2_r \gg 1$; Table 6.5) are due to near-IR emission from an accretion shock, which has not been included in our simple models. As discussed in §6.3.2, sources with very high accretion rates may produce substantial near-IR emission from hot accretion shocks; this hot, compact emission would lead to larger inferred sizes from the SED but smaller inferred sizes from the V^2 measurements. This is consistent with our results for the accretion-dominated source AS 205A ($L_{\rm acc}/L_{\rm star} \sim 10$), the only object in our sample for which model fits to the SED predict larger sizes than fits to the visibilities.

Neither the flat disk model nor the flared, puffed-up inner disk model reproduces the far-IR emission well. For the flat disk model, this discrepancy is most likely due to disk flaring, which is ignored in the model. While the flared disk model fits better, the measured 3-5 μm fluxes are substantially larger than predicted by the model. Given the extremely high inferred accretion rate for AS 205A, we suggest that viscous dissipation of accretion energy may lead to disk-heating, and thus additional puffing that is not included in the model.

6.4.4 PX Vul

The puffed-up inner disk model provides a good fit to the SED and visibility data for PX Vul ($\chi^2_r = 1.09$). In contrast, the flat disk model provides a relatively poor fit to the combined dataset ($\chi^2_r = 3.10$; Figure 6.5). The best-fit size and temperature for the puffed-up inner disk model are $\sim$ 0.32 AU and 1500 K. Similar to AS 205A, this

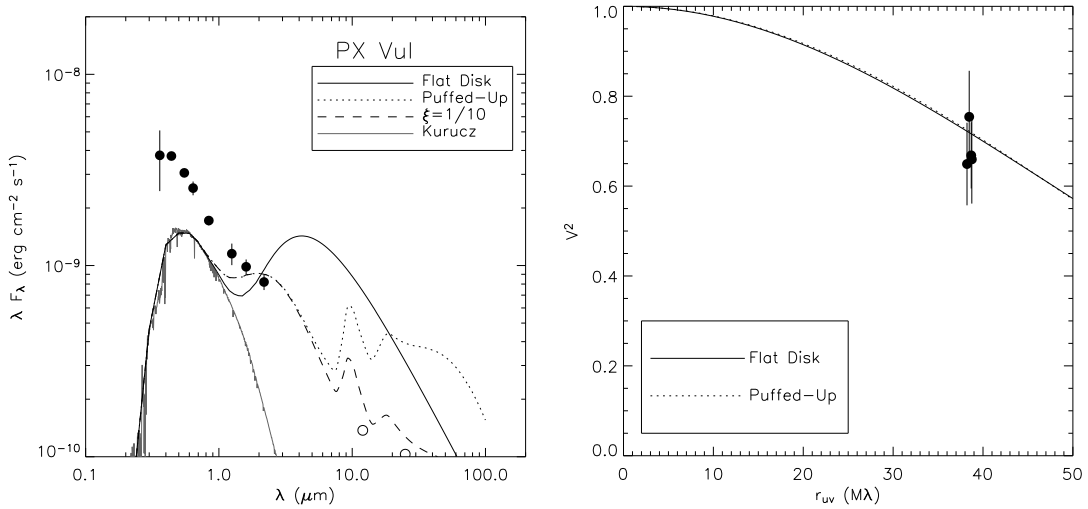

Figure 6.5 SEDs and squared visibilities for PX Vul, labeled as in Figure 6.2. For this source, the puffed-up inner disk model provides a superior fit to the SED and V^2 data. The long-wavelength photometry is compatible with an un-flared outer disk. Note that for this object, both models fit the V^2 data, but lead to significant deviations in the near-IR SEDs, while for other sources, the SEDs are similar but the V^2 predictions differ (Figures 6.2–6.4); this is due to the fact that we have more V^2 measurements for PX Vul, and the combined V^2+SED fits are therefore dominated by the interferometric rather than the photometric data.

source has a high mass accretion rate and displays substantial hot excess emission from an accretion shock. However, the ratio of accretion to stellar luminosity is only ~ 2 for PX Vul, and there seems to be little near-IR emission due to this hot excess; the SED is therefore fit well by our best-fit disk model. The magnetospheric truncation radius and the co-rotation radius determined for PX Vul (Table 6.4) are substantially smaller than the measured inner disk size. Comparison of the IRAS photometry with our models suggests that the outer disk may be moderately flared ($\xi < 1/10$).

6.5 Discussion

6.5.1 Emerging Properties of Inner Disks around T Tauri Stars

Inner sizes and temperatures of circumstellar disks around young stars have traditionally been determined by fitting disk models to SEDs (e.g., Beckwith et al. 1990; Hillenbrand et al. 1992; D'Alessio et al. 1999). However, recent interferometric observations of high-mass T Tauri and Herbig Ae/Be stars have shown that inner disks are often much larger than predicted by these SED models (Monnier & Millan-Gabet 2002; Eisner et al. 2004). Our new results presented in §6.4 confirm this trend for lower-mass T Tauri stars.

For AS 207A, V2508 Oph, and PX Vul, simple flat accretion disk models suggest much smaller sizes (when fit to SEDs) than those determined interferometrically. Models incorporating puffed-up inner walls and flared outer disks provide better fits to our V^2 and SED data than the simple flat disk models. This is consistent with previous studies of more massive Herbig Ae stars (Eisner et al. 2004; Leinert et al. 2004), and suggests that truncated disks with puffed-up inner walls describe lower-mass T Tauri stars in addition to more massive objects.

The one source in our sample for which the observed V^2 and SED values may be consistent with a simple flat accretion disk model is AS 205A, the object with the highest ratio of accretion to stellar luminosity. Recent observations of another accretion-dominated source, FU Ori, have shown a flat disk model to be appropriate (Malbet et al. 2005). Thus, the vertical structure of the inner disk may depend on the relative magnitude of stellar and accretion luminosities. However, as discussed in §6.4.3, a more complicated model that accounts for near-IR emission from accretion shocks is probably necessary to accurately fit the data for AS 205A, and we cannot rule out a puffed-up inner disk with our current analysis.

6.5.2 Dust Sublimation and Magnetospheric Truncation

The truncated disks around T Tauri and Herbig Ae stars may be explained by dust sublimation, which depends on the disk temperature and dust grain properties. An alternative truncation mechanism is magnetospheric disruption of the disk, which is expected to yield a range of inner disk truncation radii and temperatures depending on accretion rates and stellar magnetic fields (e.g., Kenyon et al. 1996). In reality, both mechanisms may be operative in T Tauri disks: optically-thick dust disks (which produce most of the observed near-IR emission) may be truncated by dust sublimation, while an optically-thin ionized gas component may be truncated closer to the star by the stellar magnetic field.

The calculated magnetospheric radii (§6.3.1.3; Table 6.4) are smaller than the puffed-up inner dust disk radii measured from the visibilities and SEDs (Table 6.5) for all sources in our sample, suggesting that magnetospheric truncation is not a viable mechanism for truncating the dust disks in our sample. Stronger magnetic fields are an unlikely way to reconcile these differences, especially for AS 205A and PX Vul, where $|\vec{B}_*| > 20$ kG would be required to bring the magnetospheric truncation radii into agreement with the measured sizes. Assuming that accreting disk material travels to $R_{\rm mag}$ in the midplane before being funneled along magnetic field lines onto the star, the fact that $R_{\rm in} > R_{\rm mag}$ for all sources suggests that the gaseous component of these disks extends further inward than the dust.

We speculate that dust disks are truncated by sublimation while gaseous material in the disk midplane extends all the way to $R_{\rm mag}$. The smaller discrepancies between $R_{\rm in}$ and $R_{\rm mag}$ for sources with lower accretion rates (Figure 6.6) are consistent with this scenario: accretional heating pushes the sublimation radius outward (Equation 6.8), leading to a larger measured inner dust disk size, while increased pressure from accreting material compresses the magnetospheric radius (Equation 6.3). For AS 207A and V2508 Oph, smaller accretion rates lead to magnetospheric truncation closer to the sublimation radii, consistent with the data. In contrast, the high accretion rates in AS 205A and PX Vul may lead to large dust sublimation radii and small

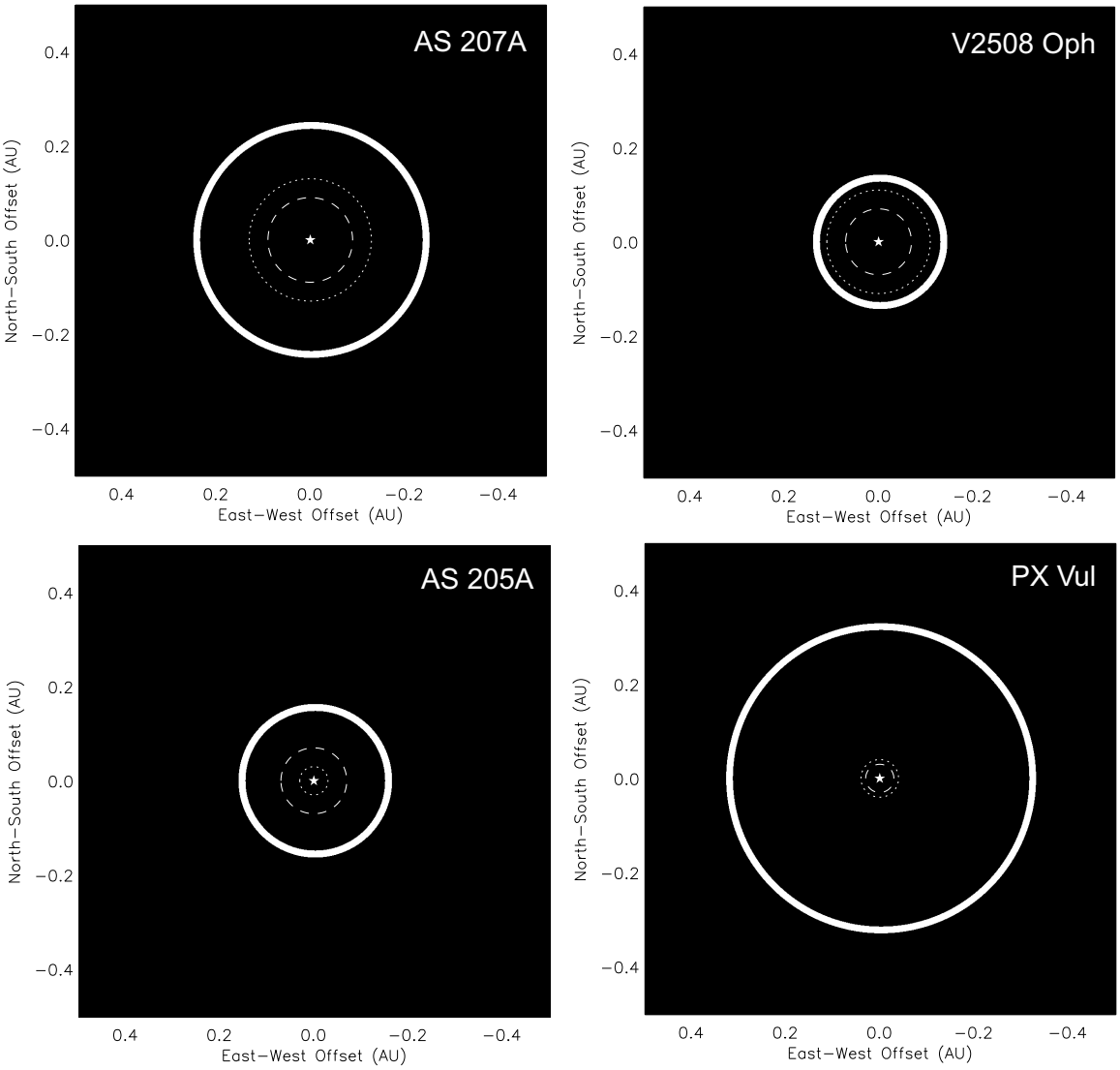

Figure 6.6 Images of the best-fit puffed-up inner disk models for our sample, with inner sizes and temperatures given in Table 6.5. Because the puffed-up inner rims dominate the 2.2 μm emission, the images appear ring-like. The magnetospheric truncation radii and (limits on) co-rotation radii (Table 6.4) are indicated by dotted and dashed lines, respectively. For AS 205A, V2508 Oph, and PX Vul, the plotted co-rotation radii are upper limits. The positions of the central stars are indicated with symbols.

magnetospheric radii, which could explain the larger differences between $R_{\rm in}$ and $R_{\rm mag}$ in these sources.

Under standard models of magnetospheric accretion, it is expected that $R_{\rm mag} \lesssim R_{\rm corot}$, since outside of co-rotation, the centrifugal barrier would prevent accretion of material above the disk midplane (Ghosh & Lamb 1979a,b; Kenyon et al. 1996; Shu et al. 1997). Moreover, the slow rotational velocities of T Tauri stars (compared to expectations for the collapse of rotating clouds; e.g., Hartmann & Stauffer 1989) are often explained by magnetic locking of the stellar rotation to the inner disk, which requires $R_{\rm mag} \approx R_{\rm corot}$ (e.g., Königl 1991; Shu et al. 1994). Figure 6.6 shows that our results are compatible with these models: $R_{\rm mag} \approx R_{\rm corot}$ for our sample. Although for V2508 Oph and AS 207A, the calculated (upper limits) on co-rotation radii are somewhat smaller than $R_{\rm mag}$, the estimates agree within adopted uncertainties. Thus, our results are consistent with magnetospheric truncation of the gaseous component of circumstellar disks, and magnetic locking of the stellar rotation and the inner (gaseous) disk edge.

6.5.3 Implications for Planet Formation

Our results indicate that dust disks around T Tauri stars are truncated within $0.1 - 0.3$ AU of the central stars. Since dust particles provide the building blocks for planetesimals, and ultimately planets, planet formation in these systems is unlikely interior to ~ 0.1 AU. However, our observations indicate that there *is* dust in the terrestrial planet forming region (i.e., $\lesssim 1$ AU). While our best-fit flat inner disk models predict temperatures near 1 AU between 280 and 500 K (Equation 6.7), too hot for ice condensation (e.g., Hayashi 1981), the puffed-up inner disk edges indicated by our data may cast a shadow over inner disk regions (e.g., Dullemond et al. 2001), leading to lower temperatures. Thus, the snowline may be located at smaller radii than predicted by flat inner disk models (e.g., Hayashi 1981; Sasselov & Lecar 2000). The location of the snowline has profound implications for the formation of planets, and snowlines at smaller radii may increase the efficiency of Earth-like

planet formation (e.g., Raymond et al. 2004).

Inner disk truncation provides a natural mechanism for halting planetary migration (e.g., Lin et al. 1996), and may therefore be linked with the observed period distribution of close-in extra-solar planets. Specifically, one expects migration to cease in a 2:1 resonance with the inner disk radius, corresponding to $0.63R_{\rm in}$ (Lin et al. 1996). Kuchner & Lecar (2002) argue that the disk density may drop precipitously within the dust sublimation radius, and that it is therefore the dust truncation radius that is important for halting migration. For the measured inner dust radii of our sources, migrating planets would be halted between 0.08 and 0.20 AU. While some extra-solar planets are found at these radii, there is a relative dearth of planets between $\sim 0.06 - 0.6$ AU, and most close-in planets are "piled-up" near $0.03 - 0.04$ AU (e.g., Udry et al. 2003). Thus, our measured inner dust disk sizes are larger than expected based on the exo-planet period distribution.

This discrepancy suggests that the gaseous components of disks extend further toward the star than the dust components, and that planetary migration halts in resonances with these gaseous truncation radii as argued by Lin et al. (1996). Gaseous material within the dust disk truncation radius is also consistent with the discrepancy between measured sizes and calculated magnetospheric radii discussed above. Assuming our inferred magnetospheric radii correspond to the inner edges of gaseous disks, we predict resonant orbits between 0.02 and 0.08 AU from the central star, compatible with the observed pile-up location for migrating exo-planets.

An alternate explanation for the apparent discrepancy between resonant orbits predicted by the dust truncation sizes and those actually observed is that the observed exo-planet period distribution is due to migration that occurred in an earlier evolutionary stage, when smaller disk truncation radii led to smaller resonant orbits. Observations of larger samples, spanning a range of inner radii, are necessary to address this issue properly.

6.6 Conclusions

We have observed three 1 $M_\odot$ T Tauri stars and one $2M_\odot$ T Tauri star with the Keck Interferometer to constrain the structure of the innermost regions of their circumstellar disks. High-resolution near-IR adaptive optics images, optical photometry, and optical spectra aided in the analysis of the interferometry data, and enabled us to estimate various properties of the systems, including mass accretion rates and co-rotation radii.

The main result of our analysis is that inner disks around solar-mass T Tauri stars appear similar to those around higher-mass T Tauri and Herbig Ae stars. Specifically, the observations for most sources are more consistent with puffed-up inner disk models than with geometrically flat accretion disk models.

We tested the theory of magnetospheric accretion by comparing our measured inner dust disk radii with calculated co-rotation and magnetospheric truncation radii. All measured sizes are larger than the magnetospheric and co-rotation radii. Moreover, the difference between measured sizes and inferred magnetospheric/co-rotation radii seems to increase with accretion rate: the discrepancy is small for AS 207A and V2508 Oph, but large for AS 205A and PX Vul. We suggest that accretional heating leads to dust sublimation at radii larger than $R_{\rm mag}$. Since higher accretion rates cause larger sublimation radii but smaller magnetospheric radii, this hypothesis can explain our results. Thus, gaseous disks may extend inward to $R_{\rm mag}$, while dust disks are truncated further out by sublimation.

Comparison of the observed inner disk sizes with the period distribution of extra-solar planets provides support for the hypothesis that gaseous disks extend further inward than dust disk truncation radii, since our measured inner disk sizes predict 2:1 resonances (which could halt migration) farther from the star than observed for extra-solar planets. In contrast, inferred magnetospheric radii predict resonant orbits that are compatible with the observed semi-major axis distribution of exo-planets.

Acknowledgments: The near-IR interferometry data presented in this paper were obtained with the Keck Interferometer (KI), which is supported by NASA. We wish

to thank the entire KI team for making these observations possible. Observations were carried out at the W.M. Keck Observatory, which is operated as a scientific partnership among California Institute of Technology, the University of California, and NASA. The Observatory was made possible by the generous financial support of the W.M. Keck Foundation. The authors wish to recognize and acknowledge the cultural role and reverence that the summit of Mauna Kea has always had within the indigenous Hawaiian community. We are most fortunate to have the opportunity to conduct observations from this mountain. This publication makes use of data products from the Two Micron All Sky Survey, which is a joint project of the University of Massachusetts and the Infrared Processing and Analysis Center, funded by the National Aeronautics and Space Administration and the National Science Foundation. 2MASS science data and information services were provided by the Infrared Science Archive at IPAC. This work has used software from the Michelson Science Center at the California Institute of Technology. J.A.E. acknowledges support from a Michelson Graduate Research Fellowship.

6.7 Appendix: Spectroscopic Binary AS 205B

The Keck/HIRES spectrum of AS 205B (Figure 6.7; §6.2.5) showed it to be a double-lined spectroscopic binary, making AS 205 a hierarchical triple. Since the components of AS 205B, labeled Ba and Bb, are of similar brightness, slowly rotating, and reasonably well separated in velocity, their properties can be determined somewhat independently. We use a technique similar to that described in §6.3.1.1, but tailored to fit the components of a spectroscopic binary.

Radial velocities, rotational velocities, spectral types, and continuum excesses for the components of AS 205B are determined from the optical spectra. Radial velocities and $v \sin i$ values are estimated by fitting the two peaks of the cross-correlation function. AS 205Ba and Bb have radial velocities of -0.30 ± 0.46 km s^{-1} and -17.71 ± 1.11 km s^{-1}, respectively. Both have projected rotational velocities below our measurement limits ($v \sin i_{Ba} \leq 5.9$ km s^{-1}, $v \sin i_{Bb} \leq 10.2$ km s^{-1}); the larger limit for

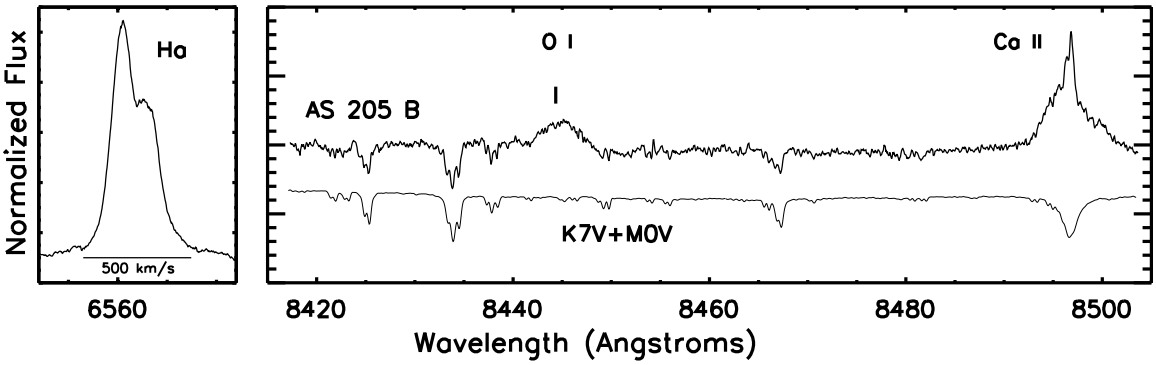

Figure 6.7 Portions of the Keck/HIRES spectrum of the double-lined spectroscopic binary AS 205B at Hα and within the I-band; both panels have the same wavelength scale. The strong, broad Hα, OI 8446 Å, and Ca II 8496 Å emission features suggest on-going accretion. The photospheric features are best matched by combining K7 and M0 dwarfs plus an optical excess (see Appendix 6.7).

AS 205Bb is a consequence of its fainter features. The flux ratio of the components, their spectral types, and the continuum excess of the system (defined here as $r = F_{excess}/(F_{Ba}+F_{Bb})$) are determined simultaneously by comparisons with synthetic spectroscopic binaries, generated by combining dwarf standards at the appropriate velocities. The best fit is determined by minimizing the root-mean-squared difference between AS 205B and the synthetic binary spectra over several temperature-sensitive regions. The components have spectral types of K7±1 (AS 205Ba) and M0±1 (AS 205Bb), and AS 205Ba is slightly brighter ($[F_{Ba}/F_{Bb}]_R = 1.52 \pm 0.12$, $[F_{Ba}/F_{Bb}]_I = 1.38 \pm 0.11$). The optical veiling of the system ($r_R = 0.83 \pm 0.12$, $r_I = 0.60 \pm 0.09$) suggests on-going accretion, although it is not possible to determine if this is onto the primary, the secondary or both. A high accretion rate is also consistent with the strong and broad Hα emission (EW= -42.6 Å; 10% width = 384 km s^{-1}) .

We estimate the visual extinction and luminosity of each component using the relative fluxes of the spectroscopic binary components at R and I in combination with spectral types, veiling, and the total AS 205B fluxes determined in §6.3.1.1. We determine visual extinctions of 3.9 mag and 3.4 mag, and luminosities of 0.44 $L_\odot$ and 0.26 $L_\odot$ for AS 205Ba and Bb, respectively. Comparison of the effective temperatures (4000 K, 3800 K) and luminosities with the Siess et al. (2000) pre-main sequence

evolutionary models yields stellar masses of 0.74 $M_{\odot}$ and 0.54 $M_{\odot}$ and ages of 5.1 Myr and 5.4 Myr for AS 205Ba and Bb, respectively. Given the uncertainties, all three components of the AS 205 system appear to be coeval.

Chapter 7

Distribution of Circumstellar Disk Masses in the Young Cluster NGC 2024[1]

We determine the distribution of circumstellar disk masses in the young (~ 0.3 Myr) cluster NGC 2024 by imaging a $2\farcm5 \times 2\farcm5$ region in λ3mm continuum emission to an RMS noise level of ~ 0.75 mJy beam^{-1} with the Owens Valley Millimeter Array. The mosaic encompasses 147 K-band sources as well as the molecular ridge seen previously in dust continuum emission. We detect 10 point-like sources in λ3mm continuum emission above the level of 5σ within the unit gain region of the mosaic. One of these sources corresponds to the near-IR source IRS 2, an early B-type star. Two other sources are tentatively associated with low-mass near-IR cluster members, and the remaining 7 sources have no K-band counterparts. Assuming the millimeter continuum point sources represent emission from circumstellar disks and/or envelopes, then $\sim 6\%$ of the total population (infrared and millimeter sources) in the NGC 2024 mosaic has a circumstellar mass in excess of ~ 0.06 M$_\odot$. We obtain further constraints on the average circumstellar disk mass by considering the mean millimeter continuum flux observed toward a sample of 140 K-band sources that likely have stellar masses $\lesssim 1 - 2$ M$_\odot$. While none of these sources are detected individually above the 3σ limit of ~ 0.035 M$_\odot$, the ensemble of sources are detected in the mean at the 5σ level with a mean disk mass of ~ 0.005 M$_\odot$. Compared to the older (~ 2 Myr) cluster

[1]This chapter has been published previously as Eisner & Carpenter (2003).

IC 348, NGC 2024 contains a higher frequency of massive disks/envelopes and has a higher mean disk mass by a factor of 2.5 ± 1.3 among K-band sources, suggesting that the mean circumstellar mass is decreasing with cluster age. We also compare the results for the NGC 2024 and IC 348 clusters to those for the lower-density Taurus star forming region. Finally, we compare our detection limits with the minimum mass estimate for the proto-solar nebula, and discuss possible implications for planet formation.

7.1 Introduction

In recent years, high resolution millimeter, infrared, and optical images have provided direct evidence for the existence of circumstellar disks on scales of $\sim$ 100–1000 AU around young stars (e.g., Koerner & Sargent 1995; Dutrey et al. 1996; Padgett et al. 1999; O'Dell & Wong 1996). These disks are the likely birth-sites for planets, and determination of the ubiquity, masses, and evolutionary timescales of circumstellar disks will place constraints on the timescales and mechanisms of planet formation.

While direct imaging has provided concrete evidence for a limited number of circumstellar disks, high resolution observations are difficult to obtain for large ensembles of objects. Therefore, indirect tracers of circumstellar disks are commonly utilized to infer disk evolution. The most common tracer is the presence of near-infrared (near-IR) emission in excess of that expected from the stellar photosphere. Indeed, the ubiquity of near-IR excesses around young stars in Taurus (see, e.g., Strom et al. 1989) provided early indications that disks are common around young solar-mass stars. More recently, JHKL photometric surveys of rich clusters spanning a range of ages detected near-IR excesses for at least 50% of solar mass stars at an age of $\sim$ 1 Myr, but for fewer than 10% of stars with ages from 3–10 Myrs (e.g., Haisch et al. 2001).

The main limitation of near-IR surveys is that the excess emission traces only the hot ($>$ 1000 K), inner ($\sim$ 0.1 AU) disk regions around solar-mass stars. Moreover, the emission is usually optically thick. Therefore, near-IR surveys provide no direct

constraints on the reservoir of cold dust located at larger radii where planets are expected to form. To study this cooler material, observations at longer wavelengths, in particular millimeter (mm) and sub-millimeter (sub-mm) wavelengths, are necessary. Since the mm and sub-mm emission is optically thin, the observed flux provides a direct measure of mass.

Several investigators have carried out comprehensive single-dish mm and sub-mm continuum surveys toward regions of star formation comprising loose aggregates of stars: Taurus (Beckwith et al. 1990; Osterloh & Beckwith 1995; Motte & André 2001), ρ Ophiuchi (André & Montmerle 1994; Nuernberger et al. 1998; Motte et al. 1998), Lupus (Nuernberger et al. 1997), Chamaeleon I (Henning et al. 1993), Serpens (Testi & Sargent 1998), and MBM 12 (Itoh et al. 2003; Hogerheijde et al. 2002). About 20%–30% of stars aged $\sim$ 1 Myr appear to possess circumstellar disks with masses greater than $\sim$ 0.01 $M_\odot$, comparable to the minimum mass of the pre-solar nebula (Weidenschilling 1977; Hayashi 1981), and the median disk mass is $\lesssim$ 0.004 $M_\odot$.

Expanding millimeter continuum surveys to include rich clusters allows the determination of accurate statistics on the frequency and evolution of disk masses as a function of both stellar mass and age. Also, since most stars in the Galaxy form in rich clusters (Lada et al. 1991, 1993; Carpenter 2000), understanding disk formation and evolution in cluster environments is a vital component in our general understanding of how stars and planets form. The main challenge to observing rich clusters at mm-wavelengths is that very high angular resolution is required to resolve individual sources and to distinguish compact disk emission from the more extended emission of the molecular cloud. Single-aperture mm-wavelength telescopes lack sufficient angular resolution, and to date, only two rich clusters have been observed with mm-wavelength interferometers: the Orion Nebula cluster (Mundy et al. 1995; Bally et al. 1998), and IC 348 (Carpenter 2002). These observations have detected *no* massive disks with 3σ upper limits ranging from $\sim$ 0.025–0.17 $M_\odot$.

Here, we present a mm-wavelength interferometric survey of NGC 2024, a young, deeply embedded stellar cluster in the Orion molecular cloud. In addition to improving the statistics on circumstellar disks in clusters, these observations enable a

comparison between relatively young (NGC 2024; $\sim$ 0.3 Myr) and old (Orion Nebula cluster and IC 348; $\sim$ 1-2 Myr) clusters, which places constraints on the timescales for disk evolution. In the next section, we describe the NGC 2024 region and discuss the stellar and protostellar populations. The observations and results are presented in §7.3 and §7.4, and we derive constraints on the circumstellar disk masses in §7.5. Finally, we compare the results for NGC 2024 to those for the IC 348, Orion Nebula cluster, and Taurus regions, and discuss the implications for disk evolution in rich clusters.

7.2 The NGC 2024 Cluster

NGC 2024 is a young HII region embedded in the L1630 (Orion B) molecular cloud. Distance estimates to the Orion region range from $\sim 360 - 480$ pc (Anthony-Twarog 1982; Brown et al. 1994, and references therein), and the distance to the stellar group containing NGC 2024 has been estimated to be 415 pc based on ubvy photometric and Balmer line measurements of 11 B-stars (Anthony-Twarog 1982). We adopt this distance of 415 pc.

Grasdalen (1974) originally identified the brightest infrared source in the region, IRS 2, which has a luminosity of $\sim 10^6$ $L_\odot$ and is a suspected early B-type star. IRS 2 was subsequently resolved into two sources, IRS 2 and IRS 2b (Jiang et al. 1984). Recently, Bik et al. (2003) estimated a spectral type of $\sim$O8 for IRS 2b, and suggested that it is the dominant source of ionizing flux for the HII region.

NGC 2024 also contains a cluster of lower mass stars, originally identified by Barnes (1989). Lada et al. (1991) identified 309 sources with $m_K < 14$ within the NGC 2024 cluster, and Lada (1999) computed a stellar density of $\rho \approx 400$ stars pc^{-3}. Meyer (1996) obtained J-,H-, and K-band photometry for 233 cluster members. L-band photometry (and new JHK measurements) for 142 of these stars by Haisch et al. (2000) indicates near-IR excess emission for $\geq 86 \pm 8\%$ of sources. Thus, a large fraction of the NGC 2024 cluster members have at least a small amount ($\sim 10^{-6}$ $M_\odot$) of hot (> 1000 K) associated circumstellar material, presumably distributed in inner

circumstellar disks.

The age of the NGC 2024 cluster has been estimated at $\sim$ 0.3–0.5 Myr (Meyer 1996; Ali 1996), using spectroscopic and photometric data to place cluster members in an HR diagram and then inferring the age from pre-main sequence evolutionary tracks by D'Antona & Mazzitelli (1994). For comparison, the same technique yields ages of $\sim$ 1 and 2 Myr for the Orion Nebula cluster and IC 348, respectively (Hillenbrand 1997; Luhman et al. 1998; Luhman 1999). While the absolute ages of the three clusters are uncertain due to limitations of the pre-main sequence evolutionary tracks, the relative ages are more secure. To further clarify the relative ages of the three clusters, we re-calculate the ages in a consistent way using published data compiled by Hillenbrand, Meyer & Carpenter (2003). We place cluster members with masses between 0.1 and 1 $M_{\odot}$ on an HR diagram, and infer the ages from the pre-main sequence tracks of D'Antona & Mazzitelli (1997). We compute logarithmic ages (in years) of 4.2 ± 0.9, 5.5 ± 0.8, and 6.2 ± 0.7 for NGC 2024, the Orion Nebula cluster, and IC 348, respectively. The relative youth of NGC 2024 is also supported by the fact that the cluster remains deeply embedded within the molecular cloud, in contrast to both the Orion Nebula cluster and IC 348 where the extinction to the cluster members is substantially less (Hillenbrand 1997; Luhman et al. 1998; Luhman 1999). In the remainder of the discussion, we adopt an age of 0.3 Myr for NGC 2024.

Meyer (1996) estimated the masses for NGC 2024 cluster members using near-IR spectroscopy for 19 sources, and a photometric method based on de-reddening sources to the expected locus of T Tauri stars in color-color diagrams for an additional 72 sources. The resulting mass distribution is statistically consistent with a Miller-Scalo IMF. Figure 7.1 shows a color-magnitude diagram for NGC 2024 (based on data from Meyer 1996). Although near-IR excess emission, age uncertainties, and binarity complicate the interpretation of this diagram, the observed colors and magnitudes are consistent with most stars in NGC 2024 having masses of $\sim$ 0.1–1 $M_{\odot}$. While some sources ($\sim$ 10%) may have sub-stellar masses, spectroscopic observations are required to confirm this speculation.

We examined the K-band UKIRT image from Meyer (1996), and found 147 point-

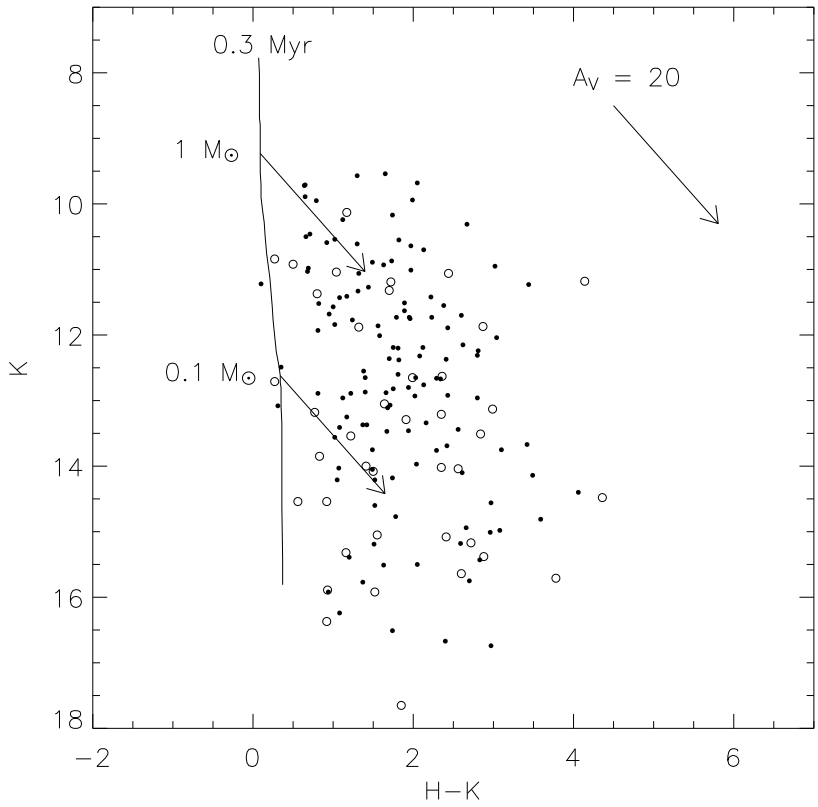

Figure 7.1 Color-magnitude diagram for the stars in the NGC 2024 cluster (based on data from Meyer 1996). We also plot the isochrone for stars of age 0.3 Myr (D'Antona & Mazzitelli 1997), and the extinction vectors (Cohen et al. 1981) for a 1 $M_\odot$ star and a 0.1 $M_\odot$ star, assuming $A_V = 20$. Sources that lie within the unit gain contour of our OVRO mosaic (see Figure 7.2) are indicated by filled circles, while open circles represent cluster members that lie outside of the unit gain region.

like sources within the region we observed at OVRO (see §7.3). We astrometrically calibrated the UKIRT image using the 2MASS Point Source Catalog, and the residuals of the astrometric fit of the UKIRT image are $0\farcs1$. The astrometric uncertainty of the 2MASS coordinates is $\lesssim 0\farcs2$, and thus the positions of the infrared sources are known to within a fraction of the OVRO beam size ($\sim 2''$; see §7.3).

In addition to the young stellar population traced by near-IR emission, NGC 2024 also contains a population of deeply embedded objects, invisible at near-IR wavelengths, but traced by mm and sub-mm wavelength emission. Several strong, compact λ3mm continuum sources, labeled FIR 1-7 (Mezger et al. 1988, 1992), are detected in the ridge of mm emission that coincides with the prominent dust lane

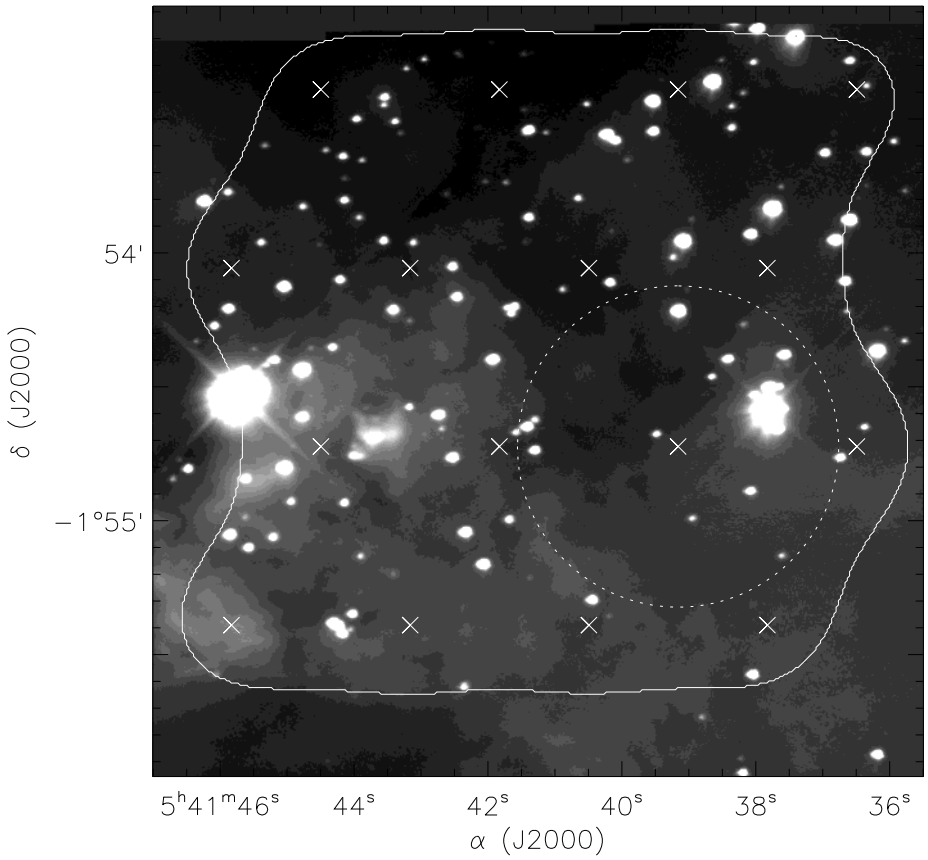

Figure 7.2 Pointing positions for the OVRO mosaic ("X" symbols), plotted over a K-band image of the NGC 2024 cluster from Meyer (1996). The FWHM of the OVRO primary beam at the observed frequency (100 GHz) is indicated by the dotted circle in the lower-right corner, and the unit gain contour of the map is shown by the solid curve.

in NGC 2024. While these compact sources were originally interpreted as dense ($n_{\rm H} \sim 10^{14} - 10^{15}$ m^{-3}), cold ($T \sim 15 - 20$ K) protostellar condensations (Mezger et al. 1988, 1992), subsequent observations yielded evidence that at least some of the sources are actually embedded protostars or young stellar objects (e.g., Moore et al. 1989; Richer et al. 1989; Chandler & Carlstrom 1996).

7.3 Observations

We mosaicked a $2\farcm5 \times 2\farcm5$ region toward the NGC 2024 cluster in the λ3mm continuum with the OVRO millimeter array between January, 2002 and April, 2003. Continuum

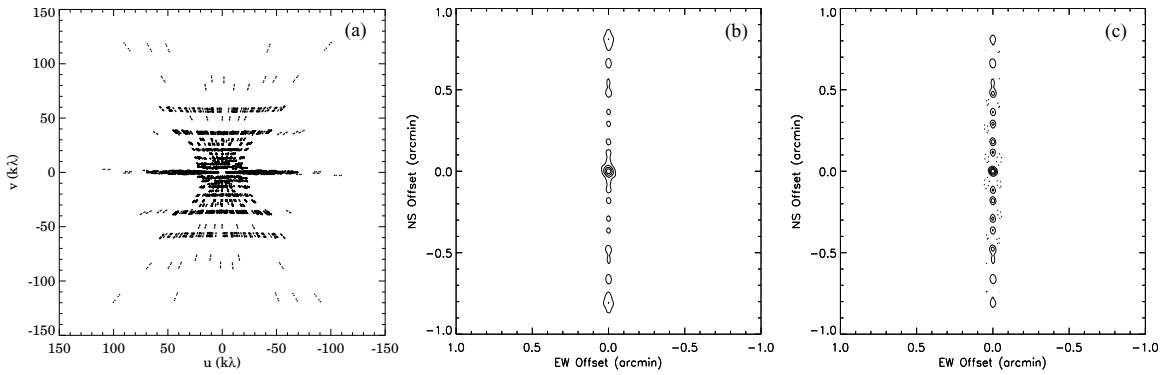

Figure 7.3 (a) uv coverage of the OVRO observations of NGC 2024. (b) Resultant beam after weighting the complete OVRO data set using a robust parameter of 0.5. (c) The OVRO beam for only uv spacings > 20 kλ. The contour increments in panels (b) and (c) are 0.2, positive contours are indicated by solid lines, and negative contours are indicated by dotted lines.

data were recorded simultaneously in four 1-GHz bandwidth channels centered at 99.46, 97.96, 102.46, and 103.96 GHz. As shown in Figure 7.2, the mosaic consists of sixteen pointing centers. Five separate array configurations provided baselines between 15 and 483 meters, and the uv coverage of the observations is shown in Figure 7.3a.

We calibrated the amplitudes and phases of the data with the blazar J0530+135: $(\alpha, \delta)_{\rm J2000} = (5^{\rm h}30^{\rm m}56\overset{\rm s}{.}4, +13^\circ31'55\overset{''}{.}2)$. We estimated the flux for J0530+135 using Neptune and Uranus as primary flux calibrators, and 3C84 and 3C273 as secondary calibrators. Since we obtained data over two separate observing seasons, and since J0530+135 may be variable, we estimated the flux for each season. For observations up to May, 2002, we determined a mean flux of 2.23 Jy, with an RMS dispersion of 0.16 Jy, as computed from observations on 21 separate nights in which both J0530+135 and flux calibrators were observed. For the observations that began in September 2002, we computed a mean flux of 1.97 Jy, with an RMS dispersion of 0.11 Jy, based on observations on 5 nights in which both J0530+135 and flux calibrators were observed. All data reduction and calibration were performed using the OVRO software package MMA (Scoville et al. 1993).

We mosaicked the sixteen individual pointings into a single image, then deconvolved and CLEANed the mosaic using the MIRIAD package (Sault et al. 1995). We

averaged the data using robust weighting (with a robustness parameter of 0.5) in order to obtain a good balance between sensitivity and angular resolution. Based on observations of circumstellar disks in Taurus, which find disk diameters $\lesssim$ 300 AU (Dutrey et al. 1996), we expect that disks in NGC 2024 (at a distance of 415 pc) will have angular scales of $\lesssim 0\farcs7$. In order to directly observe this compact disk emission, which is effectively point-like at the angular resolution of these observations, we resolved out the extended emission in the OVRO mosaic by using only longer-baseline data. Experimenting with different uv spacing cutoffs, we minimized the RMS noise of the map by eliminating all data with uv spacings < 20 kλ.

Because NGC 2024 is at low declination, the uv coverage is often sparse in the north-south direction, and thus beam artifacts in the north-south direction may contain up to 50% as much flux as the main beam. Figures 7.3b and c show the synthesized beams corresponding to the full uv coverage of the mosaic, and only uv spacings > 20 kλ, respectively. The FWHM of the core of the beam using all our OVRO data is $3\farcs84 \times 3\farcs22$ at a position angle of $-28.5°$, and the FWHM of the beam core for only outer spacings is $2\farcs53 \times 2\farcs13$ at a position angle of $-44.2°$

7.4 λ3mm Continuum Emission

The mosaic produced from all of our robust-weighted NGC 2024 data is shown in Figure 7.4. The unit gain region of the mosaic encompasses a $2\farcm5 \times 2\farcm5$ area, as indicated by the solid contour. We detect the previously known mm sources FIR 2-6 (Mezger et al. 1988) and IRS 2 (Wilson et al. 1995), as well as extended emission from the molecular ridge (e.g., Chandler & Carlstrom 1996). The horizontal emission regions labeled "NCP" and "SCP" in Figure 7.4 correspond spatially to the free-free emission regions observed in VLA centimeter continuum maps (Crutcher et al. 1986; Gaume et al. 1992).

We calculate the RMS of the image in $0\farcm5 \times 0\farcm5$ sub-regions after removing the strong point source emission using CLEAN. The "intrinsic" RMS noise in the mosaic is ~ 0.6 mJy, calculated for a $0\farcm5 \times 0\farcm5$ region in the northwest corner of the map that

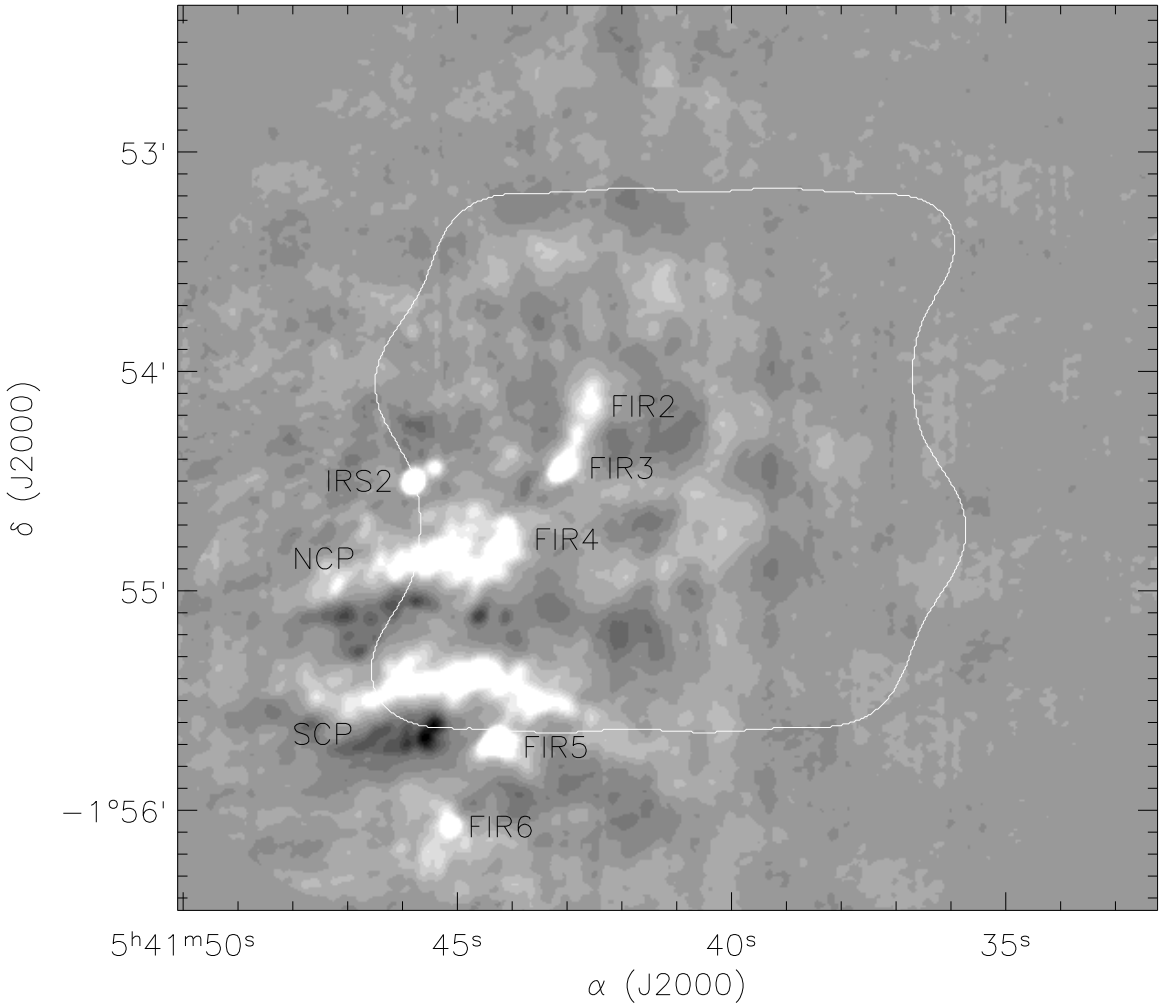

Figure 7.4 The NGC 2024 star forming region, imaged in λ3mm continuum with the Owens Valley Millimeter Array (greyscale). All of the OVRO data were used to create this image, and the angular resolution is $3\farcs84 \times 3\farcs22$. The unit gain region of the mosaic encompasses a $2\farcm5 \times 2\farcm5$ area, as indicated by the solid contour, and the average RMS of the residuals within the unit gain contour is ~ 1.3 mJy. We have labeled the previously detected sub-mm sources FIR 2-6 (Mezger et al. 1988) and IRS 2 (Wilson et al. 1995). Also, the horizontal emission regions labeled NCP and SCP correspond spatially to the free-free emission regions observed in VLA centimeter continuum maps (Crutcher et al. 1986; Gaume et al. 1992). While it is difficult to distinguish FIR 4 from NCP in this image, FIR 4 is clearly visible in Figure 7.5.

is free of any strong emission. Some regions of the image with more extended emission and sidelobe artifacts (which we could not CLEAN adequately) have an RMS as high as ~ 3 mJy, and the mean RMS across the mosaic is 1.3 mJy.

Figure 7.5 shows the OVRO mosaic produced from data with uv spacings > 20 kλ. The extended emission seen in Figure 7.4 is mostly resolved out, and the overall sensitivity is significantly improved. Specifically, the RMS sensitivity within a $0\farcs5 \times 0\farcs5$ region in the northwest corner of the mosaic shown in Figure 7.5 is ~ 0.5 mJy (compared to ~ 0.6 mJy for Figure 7.4). The local RMS in $0\farcs5 \times 0\farcs5$ sub-regions varies from $0.5 - 1$ mJy across the image, and the mean RMS for the mosaic is 0.75 mJy. Since Figure 7.5 represents such a dramatic improvement over Figure 7.4 in terms of RMS noise and distinctness of the point sources, we will use this outer spacings map in the remainder of the analysis.

In Figure 7.5, we detect emission above the 5σ level (where sigma is determined locally, as described in the preceding paragraphs) from the compact sources FIR 2-6 and IRS 2, as well as several faint new sources. We choose this detection threshold since < 0.01 out of the $\sim 6,000$ independent pixels within the unit gain contour are expected to have noise spikes above the 5σ level (assuming Gaussian noise). Positions, measured fluxes, sizes, and estimated masses (see §7.5 below) for all of the compact sources are listed in Table 7.1. Since the extended emission from the NCP and SCP structures is not completely resolved out of Figure 7.5, no sources observed toward the NCP and SCP are included. Since some of the weaker sources listed in Table 7.1 may represent peaks of the underlying extended emission or beam artifacts due to imperfect cleaning, rather than true point sources, they should be treated with some caution.

For each source in Table 7.1, we fit 2-D elliptical Gaussians to the emission to determine fluxes, positions, and sizes. For three weak sources, the Gaussian fits did not converge, and for these we determine the peak flux, and quote the position of the pixel in which the peak flux occurs. From the fitted sizes listed in Table 7.1, FIR 2, FIR 3, and source #7 appear to be somewhat resolved. Since we expect typical disks in NGC 2024 to be unresolved in the OVRO image (§7.3), these resolved sources

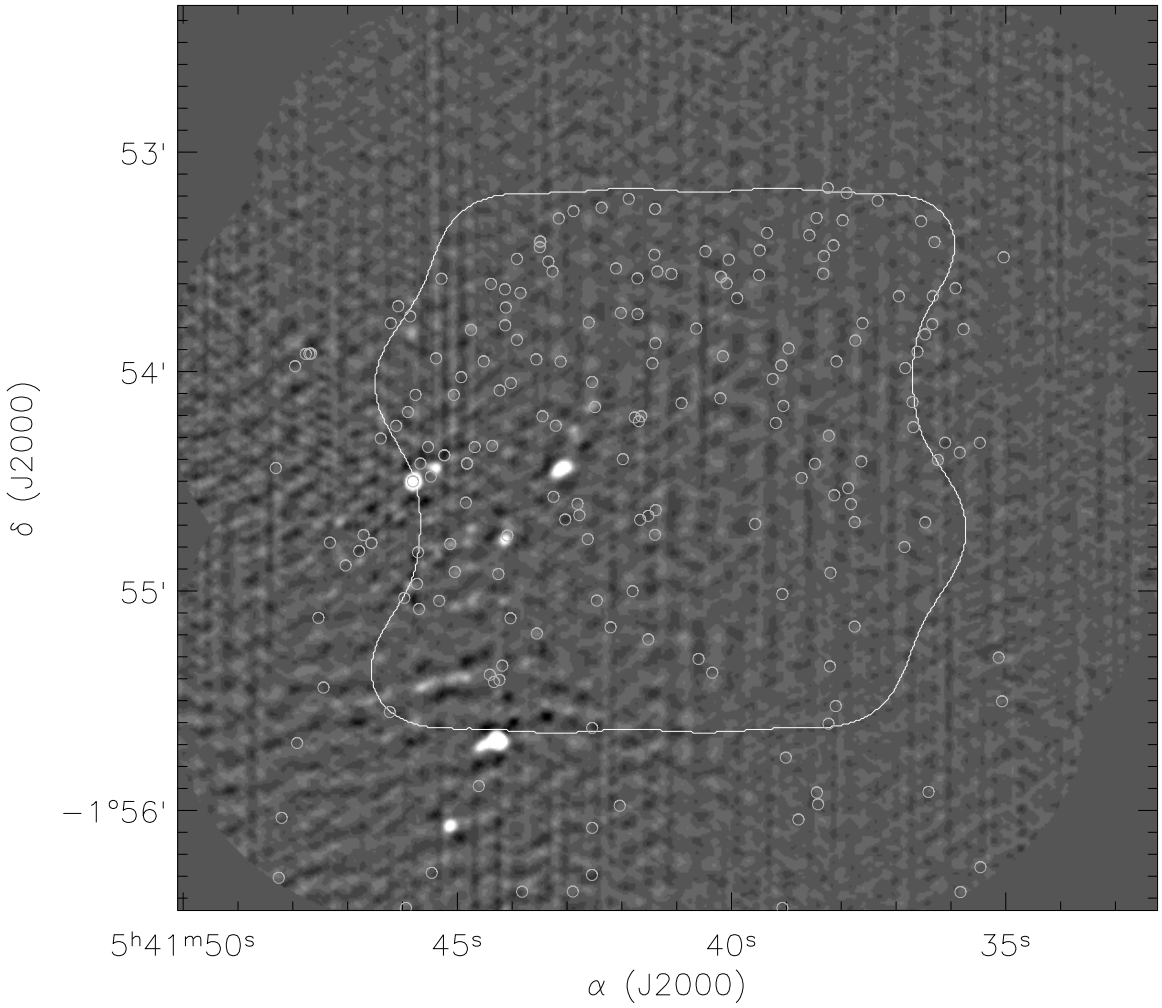

Figure 7.5 The NGC 2024 star forming region, imaged in λ3mm continuum with the Owens Valley Millimeter Array (greyscale). This image is constructed from measurements with a uv radius > 20 kλ, and the resultant angular resolution is $2\farcs53 \times 2\farcs13$. The unit gain contour is indicated by a solid line, and the average RMS of the residuals within the unit gain contour is 0.75 mJy. The positions of near-IR sources detected at K-band (Meyer 1996) are indicated with open circles.

Table 7.1. Sources detected in λ3mm continuum with OVRO

ID	Source Name	α (J2000)	δ (J2000)	FWHM	PA (°)	S_ν (mJy)[a]	M_{circ} ($M_\odot$)	
1	FIR 2	05 41 42.59	-01 54 9.21	$3\farcs43 \times 2\farcs39$	-49.5	5.07 ± 0.76	0.08	
2	...	05 41 42.83	-01 54 14.48			6.19 ± 0.76	0.10	
3	FIR 3	05 41 43.11	-01 54 26.15	$3\farcs63 \times 2\farcs26$	-34.5	34.22 ± 0.93	0.53	
4	FIR 4	05 41 44.13	-01 54 45.58	$2\farcs10 \times 2\farcs80$	-143.1	15.41 ± 0.86	0.24	
5	...	05 41 44.23	-01 55 2.72	$2\farcs42 \times 1\farcs91$	-0.5	4.26 ± 0.73	0.07	$*$
6	...	05 41 44.67	-01 55 1.83			4.82 ± 0.73	0.07	$*$
7	...	05 41 45.04	-01 55 4.33	$3\farcs23 \times 2\farcs41$	-20.9	4.23 ± 0.73	0.07	
8	...	05 41 45.41	-01 54 26.39	$2\farcs54 \times 2\farcs35$	24.8	15.23 ± 1.10	0.24	
9	IRS 2	05 41 45.80	-01 54 29.71	$1\farcs94 \times 2\farcs17$	36.5	111.17 ± 1.10	1.71	
10	...	05 41 45.83	-01 53 49.37	$2\farcs25 \times 2\farcs88$	5.9	5.93 ± 0.88	0.09	
11	FIR 5	05 41 44.33	-01 55 40.98	$2\farcs79 \times 2\farcs47$	-164.5	81.97 ± 0.87	1.27	†
12	...	05 41 44.48	-01 55 41.33			16.67 ± 0.87	0.27	†
13	FIR 6	05 41 45.14	-01 56 4.22	$2\farcs54 \times 2\farcs06$	-40.1	58.55 ± 1.32	0.90	†

References. — †–These sources lie outside of the unit gain contour, and have been scaled by the inverse gain; $*$–These sources are probably artifacts due to imperfect cleaning of extended emission; a–Uncertainties are 1σ, where σ is the locally-determined RMS. .

likely represent envelopes, large disks, or other extended structures.

We now restrict our attention to the mm-wavelength fluxes observed toward the known K-band cluster members within the unit gain contour. For these 147 pre-determined pixel positions, ~ 0.2 sources are expected to show emission above the 3σ level from Gaussian noise, and we therefore use a 3σ detection level of 2.25 mJy for individual K-band sources. We note that for the entire mosaic, ~ 10 pixels within the unit gain contour are expected to show noise spikes above the 3σ level, which is why we used a 5σ detection limit above.

Figure 7.6a shows the distribution of mm-wavelength fluxes observed toward K-band sources in NGC 2024. Several K-band sources have corresponding λ3mm fluxes above the 3σ level. One of these sources is IRS 2, an early-type B star previously detected by several investigators (e.g., Grasdalen 1974; Wilson et al. 1995). Two other detected sources, FIR 2 and 4, correspond roughly with the positions of near-IR cluster members. However, the peak of the mm emission for FIR 2 is $\sim 1\farcs6 \pm 0\farcs3$ away from the position of the infrared cluster member, and FIR 4 is $\sim 0\farcs7 \pm 0\farcs3$ away from the nearby infrared cluster member. The other source in Figure 7.6a above the 3σ level is part of the NCP extended structure, and the extreme negative source with

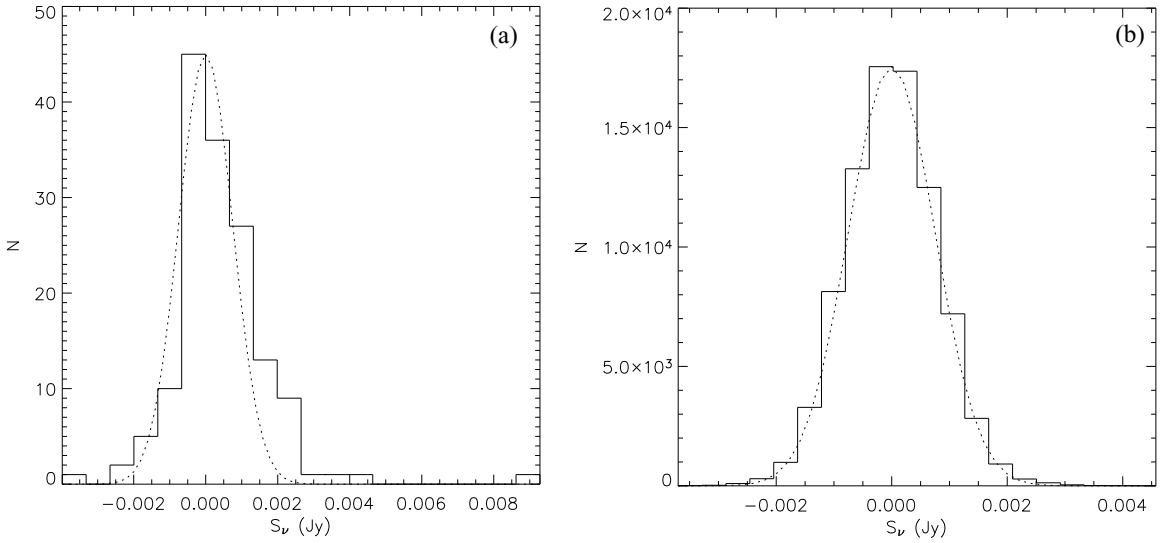

Figure 7.6 (a) Frequency distribution of λ3mm continuum fluxes measured toward the low-mass NGC 2024 K-band cluster members within the unit gain contour of the OVRO mosaic (histogram). IRS 2 is off the scale of the plot at ~ 0.1 Jy. The three sources with fluxes > 2.5 mJy correspond to slight offsets from FIR 2 and 4 (§7.4) and to part of the NCP structure. The extreme negative source with $F \sim -4$ mJy is actually tracing a sidelobe artifact. (b) Frequency distribution of λ3mm continuum fluxes for all pixels within the unit gain contour of the high-angular resolution OVRO map (Figure 7.5), where the bright (> 3.75 mJy) point sources listed in Table 7.1 have been removed using CLEAN (histogram). In both panels, the frequency distribution expected for Gaussian noise with a mean of zero and an RMS of 0.75 mJy is indicated by a dotted line.

$F \sim -4$ mJy is actually tracing a sidelobe artifact. We exclude these sources, as well as the high-mass stars IRS 1 and IRS 2b, in order to examine the distribution of λ3mm fluxes observed toward the remaining 140 "typical" low-mass cluster members.

The observed distribution of λ3mm fluxes shown in Figure 7.6a is different from that expected for pure Gaussian noise with a mean of zero and an RMS of 0.75 mJy in that the fluxes are skewed toward positive values. Weighting the observed fluxes by the locally measured RMS of the image, we determine an RMS of the distribution of 0.94 mJy, with a mean of 0.32 mJy, and a standard deviation of the mean of 0.06 mJy. This positive bias is significant since the noise in the OVRO map is consistent with a Gaussian distribution about a mean of zero (see Figure 7.6b). Specifically, the distribution of fluxes observed toward all pixels within the unit gain contour of the OVRO mosaic (with the strong point sources listed in Table 7.1 removed using

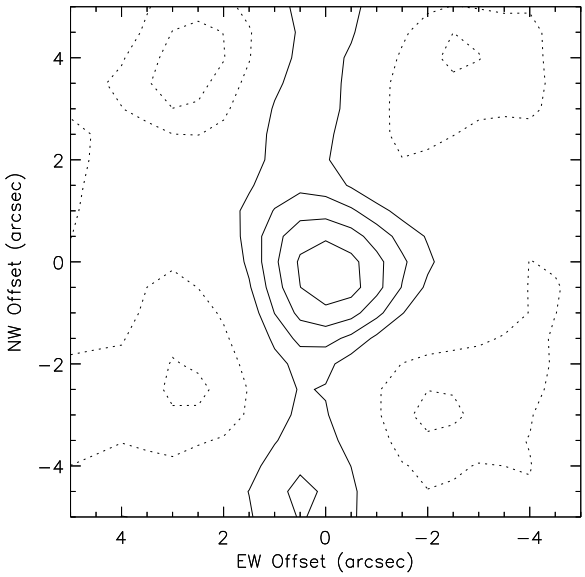

Figure 7.7 OVRO image created by averaging $10'' \times 10''$ images toward the positions of known low-mass K-band cluster members in NGC 2024. The bright sources listed in Table 7.1 were removed using CLEAN before shifting and co-adding the images. The contour increment is given by the standard deviation of the mean for the flux distribution (0.06 mJy; §7.4). Negative contours are represented by dotted lines and positive contours are represented by solid lines. The FWHM of the emission, as well as the negative features, are consistent with the OVRO beam shown in Figure 7.3c. We also note that the emission is centered at (0,0), corresponding to the mean position of K-band sources. None of the individual stars used to create this image were detected at the $\geq 3\sigma$ level, although the sources are detected in the mean at the $\sim 5\sigma$ level. Assuming this compact emission originates from circumstellar disks, the average disk mass for the ensemble of K-band sources is ~ 0.005 $M_{\odot}$.

CLEAN) has a mean of -7.6×10^{-5} mJy and a standard deviation of 0.78 mJy. Comparison of Figures 7.6a and 7.6b suggests that the bias in the distribution of fluxes observed toward K-band sources represents real underlying emission.

The positive bias is also illustrated in Figure 7.7, which shows an "average" image of the 3mm flux observed toward K-band sources, obtained by averaging $10'' \times 10''$ images centered around each object. The bright point sources listed in Table 7.1 were removed using CLEAN before shifting and co-adding the images. Figures 7.6a and 7.7 both exhibit a positive bias at the $\sim 5\sigma$ confidence level. Moreover, the FWHM of the emission in Figure 7.7 is consistent with a point source centered at the mean position of the K-band sources, including negative features that closely resemble the negative

features of the OVRO beam (Figure 7.3c). Based on Figure 7.7, the possibility that the positive bias in Figure 7.6a is due to extended cloud emission is unlikely because the average image is centered and is clearly point-like (whereas we would expect cloud emission to be extended and randomly distributed). Thus we conclude that the positive bias observed in Figures 7.6a and 7.7 probably represents underlying weak mm-wavelength emission from point sources, and that the mean flux for the ensemble is 0.32 ± 0.06 mJy.

7.5 Circumstellar Masses

The λ3mm continuum sources listed in Table 7.1 represent thermal dust emission, as opposed to optically-thin free-free emission from hot plasma, because the $\nu^{-0.1}$ frequency dependence of free-free emission would imply higher fluxes in cm-wavelength VLA images from Gaume et al. (1992) than were actually observed. These authors imaged NGC 2024 at λ1.3cm with an RMS noise level of ~ 0.6 mJy, and detected emission only from IRS 2, NCP, and SCP. For the weakest object in Table 7.1, which has a λ3mm flux of 4.23 mJy, the implied λ1.3cm flux for optically-thin free-free emission would be 4.90 mJy, easily detectable in the Gaume et al. (1992) image. In addition, although IRS 2 is detected in the λ1.3cm image with $S_\nu = 19$ mJy, the measured λ3mm flux of 111.17 mJy is much higher than that predicted for optically-thin free-free emission, indicating that at least some of the λ3mm emission is due to dust.

The mass of circumstellar material (dust + gas, assuming a standard ISM gas to dust ratio) can be estimated from the observed flux in the OVRO λ3mm continuum image following Hildebrand (1983):

$$M_{\rm circumstellar} = \frac{S_\nu d^2}{\kappa_\nu B_\nu(T_{\rm dust})}. \tag{7.1}$$

Here, ν is the observed frequency, S_ν is the observed flux, d is the distance to the source, $\kappa_\nu = \kappa_0(\nu/\nu_0)^\beta$ is the mass opacity, $T_{\rm dust}$ is the dust temperature, and B_ν is the Planck function. We assume $d = 415$ pc (Anthony-Twarog 1982), $\kappa_0 = 0.02$ cm^2

g^{-1} at 1300 μm, $\beta = 1.0$ (Hildebrand 1983; Beckwith et al. 1990), and $T_{\rm dust} = 20$ K (see discussion in Carpenter 2002). Uncertainties in the assumed values of these parameters (notably κ) imply that the derived masses are uncertain (in an absolute sense) by at least a factor of 3 (e.g., Pollack et al. 1994). For the sources detected in our mosaic, we derive circumstellar masses ranging from 0.07 to 1.71 $M_\odot$. The 5σ mass detection limit is ~ 0.06 $M_\odot$, although this limit varies by $\sim 20\%$ across the mosaic.

The OVRO observations alone do not have the angular resolution or kinematic information necessary to determine whether the circumstellar material is distributed in circumstellar disks or envelopes, or combinations of the two. If any of our λ3mm continuum sources are also detected in the infrared, the observed mm-wavelength dust emission probably arises in flattened distributions since, for spherical distributions of material the columns of dust implied by the mm-wavelength flux would completely block out any near-IR emission (see, e.g., Beckwith et al. 1990). For even the weakest source in Table 7.1, the implied extinction for a spherical mass distribution would exceed 300 magnitudes. In contrast, de-reddening the sources in Figure 7.1 to the 0.3 Myr isochrone yields extinction estimates of $\lesssim 50$ magnitudes for the infrared sources in NGC 2024. Therefore, the millimeter emission detected toward any K-band sources probably originates from flattened spatial distributions, probably disks, and not from envelopes of gas and dust.

NGC 2024 contains 147 K-band detected cluster members and 10 mm continuum sources within the unit gain region of our OVRO mosaic. As discussed in §7.4, one of the mm sources corresponds to the K-band source IRS 2, an early B-type star where the dust temperature could be substantially hotter than the 20 K used in Equation 7.1. Since this would lead to a correspondingly lower circumstellar dust mass, the visual extinction argument presented above does not necessarily apply, and we cannot rule out circumstellar envelope emission for IRS 2. Since the main goal of this study is to determine the frequency of disk masses around low mass stars, we exclude IRS 2, and by the same argument, we also exclude IRS 1 and IRS 2b from our analysis (Garrison 1968; Bik et al. 2003). We also exclude two K-band sources that correspond

spatially with mm emission from NCP and a negative sidelobe artifact (§7.4).

Of the remaining sample of 151 low-mass objects within the unit gain contour (9 mm and 142 near-IR), the mm sources FIR 2 and FIR 4 are tentatively associated with K-band cluster members (§7.4), leaving 149 unique sources. Since the associations of K-band sources with FIR 2 and 4 are tentative, the quoted fraction of near-infrared sources with disks should be considered an upper limit. None of the remaining 140 K-band sources within the OVRO mosaic, which most likely have stellar masses $\lesssim$ 1-2 $M_\odot$ (see Figure 7.1), have been detected in the λ3mm continuum at the locally-determined 3σ noise level or greater. Therefore, the fraction of low-mass K-band cluster members in NGC 2024 with a disk mass $\gtrsim 0.035$ $M_\odot$ is at most 1.4%. However, millimeter emission has been detected for the *ensemble* of K-band sources with a mean flux of 0.32 ± 0.06 mJy (§7.4; Figures 7.6 and 7.7). Since the emission is compact, and centered on the K-band sources, we suggest that the mm-wavelength emission originates in disks. Using the assumptions in Equation 7.1, this mean flux implies an average circumstellar disk mass for the ensemble of low-mass near-IR cluster members of 0.005 ± 0.001 $M_\odot$.

7.6 Discussion

Excluding the massive stars (see §7.5), the frequency of circumstellar masses (in disks and/or envelopes) greater than 0.06 $M_\odot$ in NGC 2024 is $\sim$ 6% (9/151). Although K-L color excesses for NGC 2024 cluster members suggest that 86 ± 8% of the stars have circumstellar disks (Haisch et al. 2000), these two estimates of the disk fraction are not necessarily contradictory, since the near-IR emission probes trace material ($\sim 10^{-6}$ $M_\odot$) within $\sim$ 0.1 AU of the star, while millimeter emission traces massive ($\gtrsim 0.035$ $M_\odot$) outer circumstellar material.

We compare our results for NGC 2024 with an analogous λ3mm continuum survey of IC 348 (Carpenter 2002). Although the IC 348 survey contains shorter uv spacings than the NGC 2024 mosaic, and samples $\sim$ 2 times larger spatial scales, this does not affect the comparison since no emission (compact or extended) was detected in IC 348.

NGC 2024 and IC 348 are similar in that each cluster contains on the order of 300 stars (Lada et al. 1991; Herbig 1998), the spectral types of the most massive stars are comparable (∼O8 for NGC 2024, B0 for IC 348), and the stellar mass distributions are consistent with a Miller-Scalo IMF (Meyer 1996; Luhman et al. 1998). The primary difference between the two clusters is that NGC 2024 is more deeply embedded within the molecular cloud and younger than IC 348 (see §7.2). No λ3mm continuum sources were detected in IC 348 with a 3σ upper limit of 0.025 $M_\odot$ out of a sample of 95 known infrared cluster members. In contrast, $\sim$ 6% of cluster members in NGC 2024 are surrounded by more than 0.06 $M_\odot$ of material (which could be distributed in disks, envelopes, or combinations of the two). Using the Fisher Exact Test, the probability that these two measurements are drawn from the same distribution is 1.5%. Moreover, the average disk mass for the ensemble of low-mass stars in NGC 2024 is 0.005 ± 0.001 $M_\odot$, compared to 0.002 ± 0.001 $M_\odot$ in IC 348. Assuming that the differences between NGC 2024 and IC 348 are due to temporal evolution, these observations indicate that massive disks/envelopes dissipate on timescale $\lesssim$ 2 Myr, and that the average disk mass decreases by a factor of 2.5 ± 1.3 between $\sim$ 0.3 and 2 Myr [2].

The NGC 2024 results can also be compared with the disk masses in the Orion Nebula cluster, which have been computed from both λ3.5mm (Mundy et al. 1995) and λ1.3mm continuum observations (Bally et al. 1998). At λ3.5mm, a 3σ upper limit of 5.7 mJy was derived for the flux observed above the level of the expected free-free emission for a sample of 33 proplyds in the Orion Nebula cluster. Using Equation 7.1 with the same assumptions as in §7.5, this translates into a 3σ upper limit on disk mass of 0.17 $M_\odot$. An upper limit on the *average* disk mass for these 33 sources is 0.03 $M_\odot$. The λ1.3mm results yield a 3σ upper limit of 0.047 $M_\odot$ for five proplyd sources. The lack of massive disks in the Orion Nebula cluster is similar to the results for NGC 2024 and IC 348.

In contrast to NGC 2024, IC 348, and the Orion Nebula cluster, a large fraction of

[2] Another possible explanation for the higher observed flux in NGC 2024 relative to IC 348 is that one or more of the assumed quantities in Equation 7.1 (e.g., temperature or opacity) is different in the two regions. Regardless of the underlying factors, our measurement suggests disk evolution between $\sim$ 0.3 and 2 Myr.

the stars in Taurus show evidence for massive circumstellar disks. We have compiled a sample of 164 stars in Taurus that have been observed at millimeter wavelengths, including sources observed by Beckwith et al. (1990), Osterloh & Beckwith (1995), and Motte & André (2001). All detected sources included in the sample are $\geq 90\%$ concentrated within the $\sim 11''$ beams of the various surveys. We also compiled K-band magnitudes for the sample, either from the literature or from 2MASS. Approximately 21% of the sample sources show evidence for circumstellar disks with masses $\gtrsim 0.01$ $M_\odot$.

In NGC 2024, $\sim 6\%$ of cluster members have circumstellar masses greater than ~ 0.06 $M_\odot$. In Taurus, the percentage of sources with > 0.06 $M_\odot$ of circumstellar material is $\sim 3\%$, and the probability that the two samples are drawn from the same distribution is 75.9%. Based on these results, we cannot statistically distinguish between the frequencies of sources with circumstellar masses > 0.06 $M_\odot$ in NGC 2024 and Taurus. However, if we compare the observed mm fluxes for only low-mass K-band sources, where the millimeter emission likely originates in circumstellar disks, we find a possible difference. The fraction of near-IR cluster members in NGC 2024 with circumstellar disks $\gtrsim 0.035$ $M_\odot$ is $\leq 1.4\%$. In contrast, $\sim 5\%$ of objects in Taurus have circumstellar disks > 0.035 $M_\odot$. Follow-up observations of the Taurus sources at high angular resolution show that the dust usually lies in compact flattened distributions, and not in massive envelopes (e.g., Dutrey et al. 1996; Looney et al. 2000). Moreover, these objects are quite bright at K-band, and if placed at the distance of NGC 2024, would be detectable in the UKIRT K-band image for visual extinctions < 50 mag. Thus, despite the fact that NGC 2024 is younger than Taurus, the fraction of K-band sources with massive disks is lower. The probability that the frequencies of massive disks around K-band sources in Taurus and NGC 2024 are drawn from the same distribution is $\leq 8.5\%$.

In summary, the NGC 2024 and IC 348 clusters combined contain at most 2 K-band sources out of a total of 239 observed, or $\leq 0.8\%$, that are associated with millimeter continuum emission characteristic of massive circumstellar disks ($M > 0.035$ $M_\odot$). In comparison, 5% of the sources in Taurus contain such disks. These combined

results suggest that the rich cluster environments may not be conducive to forming large, massive circumstellar disks. Scally & Clarke (2001) showed that massive disks in rich clusters may be inhibited by photo-evaporation or tidal disruption due to close encounters with massive stars, with photo-evaporation as the dominant effect. Although the ionizing flux from the massive stars in NGC 2024 will be highly attenuated by the extinction in the dense core, these effects may help to explain the lack of massive disks.

The derived upper limits on circumstellar disk masses in NGC 2024 and IC 348 can be compared with the minimum mass needed to form a system like our own Solar System. Summing the mass contained in Solar planets, and assuming a standard ISM gas to dust ratio, the minimum mass of the proto-solar nebula is ~ 0.01 $M_\odot$ (Weidenschilling 1977; Hayashi 1981). This reflects primarily the matter needed to form Jupiter. The true mass of the proto-solar nebula may have been higher than this minimum estimate, depending on the efficiency of conversion of proto-solar dust and gas into planets. The average disk mass determined for K-band sources in NGC 2024, 0.005 ± 0.001 $M_\odot$, is comparable to the expected mass of the proto-solar nebula. Although uncertainties in the assumed values of the parameters used in Equation 7.1 imply that the derived masses are uncertain by at least a factor of 3, our data indicate that the average star in NGC 2024 possesses a disk massive enough to form a planet with $M \lesssim M_{\rm Jupiter}$.

In contrast, the 3σ upper limits on disk mass in both NGC 2024 and IC 348 rule out the existence of disks massive enough to form planets with several Jupiter masses. Our results therefore imply either that the formation of massive planets (i.e., several Jupiter masses) is relatively rare in NGC 2024 and IC 348, or that the aggregation of dust grains into planetesimals (and eventually planets) has already occurred within ~ 1 Myr, depleting the disks of small grains that OVRO would see in emission. The timescale for giant planet formation via core accretion is thought to be $\sim 10^6 - 10^8$ years (e.g., Pollack et al. 1996), and thus it is unlikely that planets of several Jupiter masses have formed by this method around most of the stars in NGC 2024 (which has an age of $\sim 3 \times 10^5$ years). A possible implication of this might be

that giant planets do not form in rich clusters. A recent survey of the 47 Tuc cluster failed to detect any planets (where they expected to find ~ 17; Gilliland et al. 2000), providing some support for this possibility. An alternative explanation is that the core accretion model for giant planet formation is not operating in NGC 2024. Giant planet formation through gravitational instabilities in circumstellar disks requires only $\sim 10^3 - 10^5$ years (e.g., Boss 1998), and might provide a viable explanation for quick massive planet formation in NGC 2024.

7.7 Conclusions

We have imaged the central $2\farcm5 \times 2\farcm5$ region of NGC 2024 in λ3mm continuum emission with the OVRO millimeter-wavelength interferometer. The mosaic encompasses 147 K-band detected cluster members and the molecular ridge seen previously in dust continuum emission. We detected 10 point sources within the unit gain region of the OVRO mosaic above the 5σ level (where $\sigma \sim 0.75$ Jy). One of the millimeter sources is coincident with the early B-type star IRS 2. Two other millimeter sources, FIR 2 and FIR 4, are near to but not exactly coincident with infrared cluster members. No millimeter emission was detected toward the other low-mass infrared cluster members above the 3σ level of 2.25 mJy. The mean λ3mm flux toward the ensemble of K-band sources is 0.32 ± 0.06 mJy.

We use the λ3mm fluxes to estimate the circumstellar dust masses assuming that the millimeter-wavelength emission is optically thin, with a temperature of 20 K, and adopting a mass opacity coefficient of $\kappa = 0.02$ cm^2 g^{-1} at 1.3 mm. With these assumptions, the circumstellar mass (dust plus gas) ranges from 0.07 to 1.71 $M_\odot$ for the 10 detected sources. The 3σ upper limit to the circumstellar mass around the individual K-band sources (excluding the tentative associations with FIR 2 and FIR 4) is ~ 0.035 $M_\odot$, and the average mass for the ensemble of low-mass K-band sources is 0.005 ± 0.001 $M_\odot$. These results show that at the age of the NGC 2024 cluster (~ 0.3 Myr; Meyer 1996), $\sim 6\%$ of cluster members have massive ($\gtrsim 0.06$ $M_\odot$) circumstellar structures (disks and/or envelopes), and many of the sources may

possess low-mass circumstellar disks.

We compare our results to a similar millimeter continuum survey of IC 348 (Carpenter 2002). None of the 95 cluster members observed in IC 348 were detected in the millimeter continuum above the 3σ level of 0.025 $M_\odot$ in IC 348. In contrast, we detect more than $\sim$ 0.06 $M_\odot$ of circumstellar material around $\sim$ 6% of cluster members in NGC 2024. Moreover, the average disk mass around a typical low-mass K-band source in NGC 2024 is 2.5 ± 1.3 times higher than in IC 348. Thus, there may be some evolution of circumstellar disks and/or envelopes on $\sim$ 1 Myr timescales.

The fraction of circumstellar disks more massive than $\sim$ 0.035 $M_\odot$ around near-IR cluster members is at most 0.8% in NGC 2024 and IC 348 combined, suggesting that massive disks are either very rare, or non-existent, in rich cluster environments. In contrast, $\sim$ 5% of the sources in Taurus have circumstellar disks more massive than 0.035 $M_\odot$, even though Taurus is older than, or of similar age to, the rich clusters. This may imply different physical mechanisms for disk formation and evolution in clustered versus isolated star forming regions.

The average disk mass of $\sim$ 0.005 $M_\odot$ for the ensemble of K-band sources is comparable to the minimum mass of material necessary to form the proto-solar nebula, which implies that many objects in NGC 2024 possess disks massive enough to form planets with the approximate mass of Jupiter. However, the 3σ limit of 0.035 $M_\odot$ on the masses of circumstellar disks in NGC 2024 suggests that high-mass planets (several Jupiter masses) may have either already formed (thus depleting the disks of small grains), or may never form in this cluster.

Acknowledgments. JAE is supported by a Michelson Graduate Research Fellowship. JMC acknowledges support from Long Term Space Astrophysics Grant NAG5-8217 and the Owens Valley Radio Observatory, which is supported by the National Science Foundation through grant AST-9981546. This publication makes use of data products from the Two Micron All Sky Survey, which is a joint project of the University of Massachusetts and the Infrared Processing and Analysis Center, funded by the National Aeronautics and Space Administration and the National Science Foundation. 2MASS science data and information services were provided by the Infrared

Science Archive (IRSA) at IPAC.

Chapter 8

Distribution of Circumstellar Disk Masses in the Orion Nebula Cluster[1]

We determine the distribution of circumstellar disk masses in the young ($\sim$ 1 Myr) Orion Nebula cluster by imaging a $2\farcm5 \times 2\farcm5$ region in $\lambda 3$ mm continuum emission to an RMS noise level of ~ 1.75 mJy beam^{-1} with the Owens Valley Millimeter Array. The mosaic encompasses 337 K-band sources in addition to the well-known Trapezium stars. With the exception of the massive BN object, no 3 mm continuum emission is detected toward any of these near-IR cluster members above the level of 5σ. However, considering the low-mass near-IR cluster members as an ensemble, and stacking the observed fluxes toward each source (which may contain noise and signal), an average disk is detected at approximately the 3σ level. Under standard assumptions for the dust opacity, dust temperature, and distance to Orion, the average disk flux corresponds to a circumstellar mass of ~ 0.005 $M_\odot$, comparable to the minimum mass solar nebula. Comparison of these results with similar surveys of younger and older clusters is used to constrain the evolutionary timescales of massive circumstellar disks.

[1]This chapter is based on a manuscript in preparation by J. Eisner and J. Carpenter.

8.1 Introduction

Over the last two decades, high resolution millimeter, infrared, and optical images have provided direct evidence for the existence of circumstellar disks on scales of $\sim$ 0.1–1000 AU around young stars (e.g., Koerner & Sargent 1995; Dutrey et al. 1996; Padgett et al. 1999; O'Dell & Wong 1996; Eisner et al. 2004). Circumstellar disks are the likely birth-sites for planetary systems, and determining their ubiquity, properties, and lifetimes is crucial for constraining the timescales and mechanisms of planet formation. The mass distribution of protoplanetary disks is especially important since only disks more massive than ~ 0.01 $M_\odot$, the minimum-mass protosolar nebula (Weidenschilling 1977), can form planetary systems like our own solar system. The frequency and lifetimes of these massive disks thus constrain formation scenarios for protosolar systems.

While direct imaging at optical through near-IR wavelengths has provided concrete evidence for a limited number of circumstellar disks (e.g., O'Dell & Wong 1996), and observations of near-IR excess emission have shown statistically that most young stars with ages less than a few million years still possess inner circumstellar disks (e.g., Strom et al. 1989; Haisch et al. 2001), these studies did not constrain the disk mass distribution. To probe the bulk of the disk mass, which resides in cooler, outer disk regions, observations of optically-thin millimeter emission are needed.

Several investigators have carried out comprehensive single-dish mm and sub-mm continuum surveys toward regions of star formation comprising loose aggregates of stars: Taurus (Beckwith et al. 1990; Osterloh & Beckwith 1995; Motte & André 2001), ρ Ophiuchi (André & Montmerle 1994; Nuernberger et al. 1998; Motte et al. 1998), Lupus (Nuernberger et al. 1997), Chamaeleon I (Henning et al. 1993), Serpens (Testi & Sargent 1998), and MBM 12 (Itoh et al. 2003; Hogerheijde et al. 2002). About 20%–30% of stars aged $\sim$ 1 Myr appear to possess circumstellar disks with masses greater than ~ 0.01 $M_\odot$, comparable to the minimum mass of the pre-solar nebula (Weidenschilling 1977; Hayashi 1981), and the median disk mass is $\lesssim 0.004$ $M_\odot$.

Expanding millimeter continuum surveys to include rich clusters allows the de-

termination of accurate statistics on the frequency and evolution of disk masses as a function of both stellar mass and age. Also, since most stars in the Galaxy form in rich clusters (Lada et al. 1991, 1993; Carpenter 2000; Lada & Lada 2003), understanding disk formation and evolution in cluster environments is a vital component in our general understanding of how stars and planets form. The main challenge to observing rich clusters at mm-wavelengths is that very high angular resolution is required to resolve individual sources and to distinguish compact disk emission from the more extended emission of the molecular cloud. Single-aperture mm-wavelength telescopes lack sufficient angular resolution, and to date, only three rich clusters have been observed with mm-wavelength interferometers: the Orion Nebula cluster (Mundy et al. 1995; Bally et al. 1998), IC 348 (Carpenter 2002), and NGC 2024 (Eisner & Carpenter 2003).

These observations have detected *no* massive disks with 3σ upper limits ranging from ~ 0.025–0.17 $M_\odot$. However, the large numbers ($\gtrsim 100$) of young stars included in the surveys of IC 348 and NGC 2024, when treated as ensembles, allow estimates of the mean masses of disks around cluster members. The mean disk mass for low-mass stars in NGC 2024 is 0.005 ± 0.001 $M_\odot$, comparable to the minimum mass of the protosolar nebula (and somewhat higher than the mean mass of IC 348, 0.002 ± 0.001 $M_\odot$), consistent with earlier findings that many disks aged $\lesssim 1$ Myr still possess massive circumstellar disks.

Here, we present a new mm-wavelength interferometric survey of the Orion Nebula cluster (ONC), a young, deeply embedded stellar cluster that includes the bright, massive Trapezium stars. The Trapezium region contains hundreds of stars within several arcminutes (Figure 8.1), and pre-main-sequence evolutionary models (e.g., D'Antona & Mazzitelli 1994) fitted to spectroscopic and/or photometric data indicate that most stars are less than approximately one million years old (e.g., Prosser et al. 1994; Hillenbrand 1997). Moreover, the spread in these stellar ages seems to be $\lesssim 1$ Myr. Our OVRO observations thus provide a snapshot of millimeter emission around a large number of roughly coeval young stars.

With the large number of stars in the ONC, one can investigate the correlation of

Figure 8.1 A $7' \times 7'$ JHK mosaic of the Orion Nebula cluster from VLT/ISAAC (courtesy of Mark McCaughrean and the European Southern Observatory). The bright, hot Trapezium stars are seen toward the center of the image.

disk properties with stellar and/or environmental properties. Previous investigations of near-IR excess emission have explored the dependence of inner disk properties on stellar mass, age, and environment (e.g., Hillenbrand et al. 1998; Lada et al. 2000). For example, the fraction of stars in Orion exhibiting near-IR excess emission seems largely independent of stellar age and mass, although there are indications of a paucity of disks around very massive stars (Hillenbrand et al. 1998; Lada et al. 2000). In addition, the inner disk fraction may decrease at larger cluster radii (Hillenbrand et al. 1998). To explore how the properties of the massive outer disk component correlate with such stellar and environmental properties, millimeter observations of cool, optically-thin dust emission are necessary.

The ONC has been previously observed in the mm-wavelength continuum by several investigators. Mundy, Looney, & Lada (1995) set a 3σ upper limit on circum-

stellar dust of 0.17 $M_\odot$ within a 45″ field containing 33 proplyds. Bally et al. (1998) observed two 30″ fields offset by $60-100''$ from the cluster center, and set a 3σ upper limit of 0.047 $M_\odot$ for five proplyds. Our survey represents an improvement over this previous work because our map contains more than three times as many sources as the previous surveys, enabling an improvement of $\sqrt{3}$ in statistics for the existence and mean mass of circumstellar disks. Moreover, the comparable sensitivity of our survey with the previous surveys of IC 348 and NGC 2024 allows a more direct comparison between relatively young (NGC 2024; 0.3 Myr), intermediate (Orion Nebula cluster; 1 Myr), and old (IC 348; 2 Myr) clusters, enabling constraints on timescales for disk evolution.

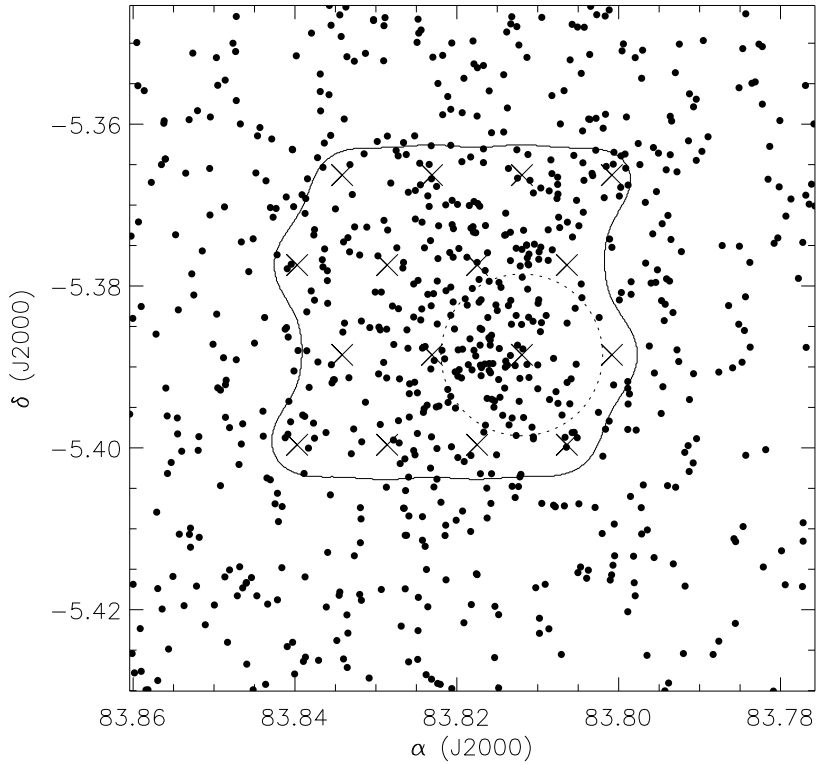

Figure 8.2 Pointing positions for the OVRO mosaic ("X" symbols), plotted over the positions of K-band sources in the ONC (points). These K-band source positions are from Hillenbrand & Carpenter (2000), and have been registered to the 2MASS astrometric grid. The unit gain contour of the mosaic (solid line) and the primary beam of an OVRO antenna (dotted line) are also indicated.

8.2 Observations and Data Reduction

We mosaicked a $2\farcm5 \times 2\farcm5$ region toward the ONC in $\lambda 3$ mm continuum with the OVRO millimeter array between August, 2003 and March, 2004. Continuum data were recorded using the new COBRA correlator, providing a total of 8 GHz of bandwidth centered at 100 GHz. Two different configurations of the 6-element array provided baselines between 35 and 240 meters. As shown in Figure 8.2, the mosaic consists of sixteen pointing centers. For observations in a given night, the mosaic was observed in its entirety once or twice (depending on the length of the track), with equal integration time (and hence equal sensitivity) for each pointing position.

We calibrated the amplitudes and phases of the data with the blazar J0530+135: $(\alpha, \delta)_{\rm J2000} = (5^{\rm h}30^{\rm m}56\fs4, +13^\circ31'55\farcs2)$. Three minute observations of J0530+135 were interleaved with sixteen minute integrations on the target mosaic. We estimated the flux for J0530+135 using Neptune and Uranus as primary flux calibrators, and 3C84 and 3C273 as secondary calibrators. Since we obtained data over a long time-span, and J0530+135 is variable, we estimated the flux for each array configuration. For observations in the less extended "E" configuration (spanning August-September 2003), we calculate a mean flux of 2.91 Jy, with an RMS of 0.21 Jy. For observations in the "H" configuration (spanning December, 2003-March, 2004), we determine a flux of 2.08 Jy and an RMS of 0.14 Jy. All data calibration was performed using a suite of IDL routines developed for the MIR software package.

We mosaicked the sixteen individual pointings into a single image, robustly weighted the data (using a robust parameter of 0.5), then de-convolved and CLEANed the mosaic using the MIRIAD package (Sault et al. 1995). Since we are primarily interested in compact disk emission, we eliminate uv spacings shorter than 35 kλ in order to avoid contamination from bright extended emission. This cutoff was chosen to be the value for which the RMS background noise in the CLEANed image is minimized. We note that previous analyses of the ONC have also eliminated data with uv spacings < 35 kλ (Felli et al. 1993; Bally et al. 1998) to filter out the extended emission in the region.

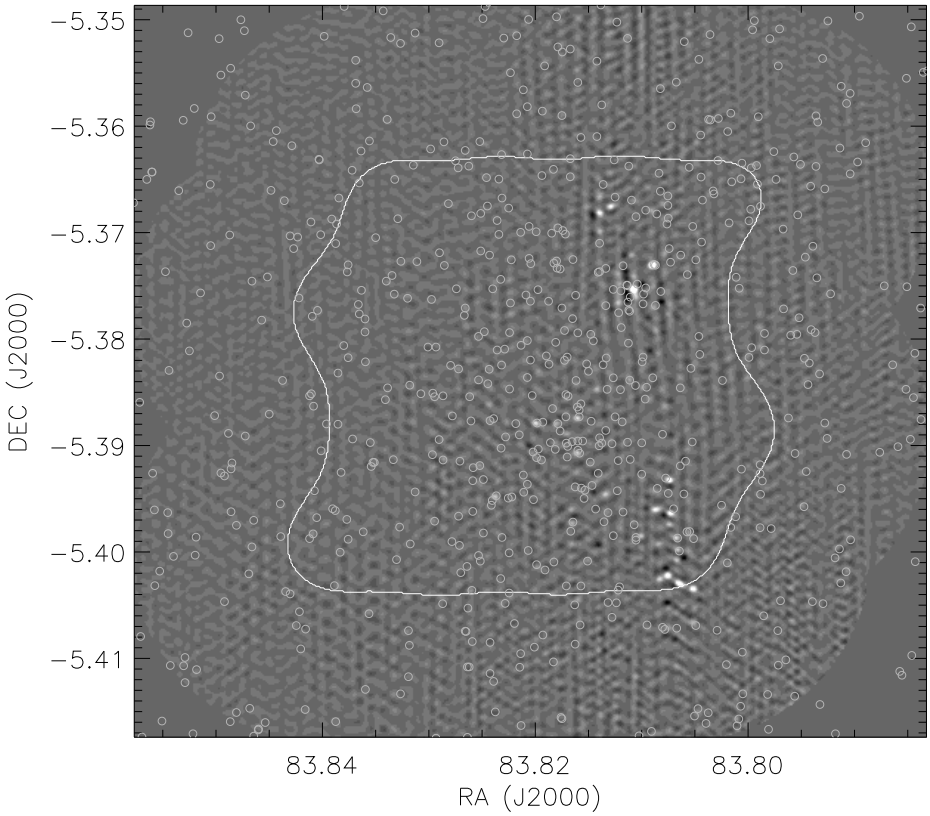

Figure 8.3 The Orion Nebula cluster, imaged in $\lambda 3$ mm continuum with the Owens Valley Millimeter Array (greyscale). Only data observed on long baselines ($r_{uv} > 35$ kλ) were used to create this image, and the angular resolution is $1\farcs9 \times 1\farcs5$. The unit gain region of the mosaic encompasses a $2\farcm5 \times 2\farcm5$ area, as indicated by the solid contour, and the average RMS of the residuals within the unit gain contour is ~ 1.75 mJy.

The mosaic produced from our robust-weighted data with $r_{uv} > 35$ kλ is shown in Figure 8.3. The unit gain region of the mosaic encompasses a $2\farcm5 \times 2\farcm5$ area, as indicated by the solid contour. The angular resolution of the mosaic is $1\farcs9 \times 1\farcs5$. The mean RMS residuals within the unit gain contour of the mosaic, calculated from a residual image after CLEANing of strong point sources, is 1.75 mJy. However, the RMS varies across the mosaic, because of varying amounts of sidelobe emission from point sources and extended emission that were not removed by CLEAN. We calculate the RMS of the image in $0\farcs5 \times 0\farcs5$ sub-regions, and find values ranging from 0.88 mJy to 2.34 mJy. Despite these large variations in RMS, the noise across the mosaic is largely Gaussian, as illustrated by Figure 8.4.

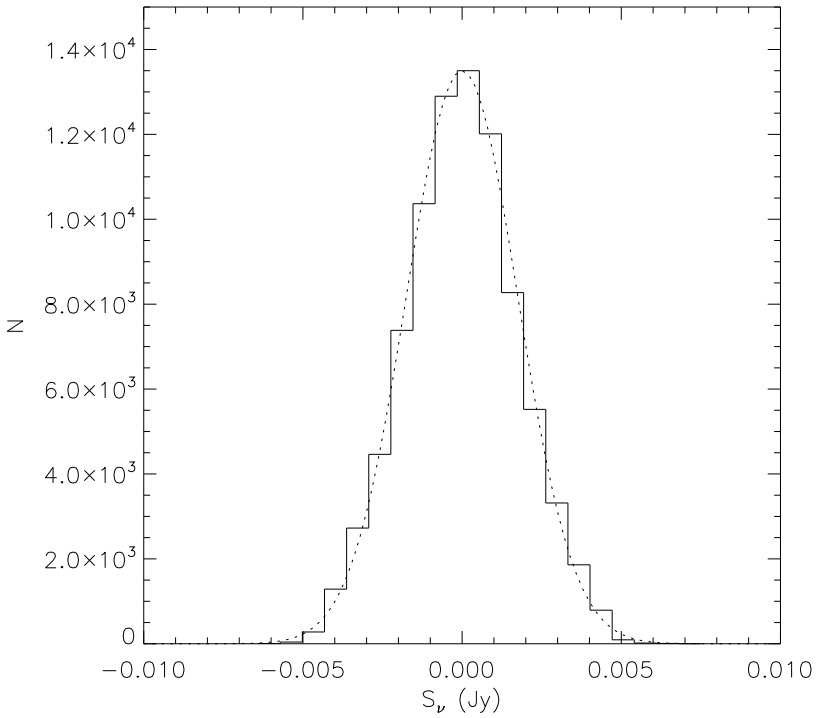

Figure 8.4 Distribution of 3 mm continuum fluxes for all pixels within the unit gain contour (solid line), and the frequency distribution expected for Gaussian noise with a mean of zero and a standard deviation of 1.75 mJy (dotted line). The agreement between the measured and Gaussian distributions suggests that the noise in the OVRO mosaic is represented well by Gaussian statistics.

8.3 Results

Within the unit gain contour of the OVRO mosaic (Figure 8.3), we detect the well-known BN object (Becklin & Neugebauer 1967), as well as twenty-six other sources without known infrared counterparts, in 3 mm continuum emission above the 5σ level (where σ is determined locally in $0\farcs5 \times 0\farcs5$ sub-regions). We expect less than one pixel in our mosaic to have a noise spike at $\geq 5\sigma$, and thus these detections probably correspond with real emission. Detected sources are listed in Table 8.1 (the BN object corresponds with "MM1" in the table).

We now restrict our attention to the mm-wavelength fluxes observed toward the known K-band cluster members within the unit gain contour (including the BN object). For these 337 pre-determined pixel positions, ~ 0.4 sources are expected to show emission above the 3σ level from Gaussian noise, and we therefore use a 3σ

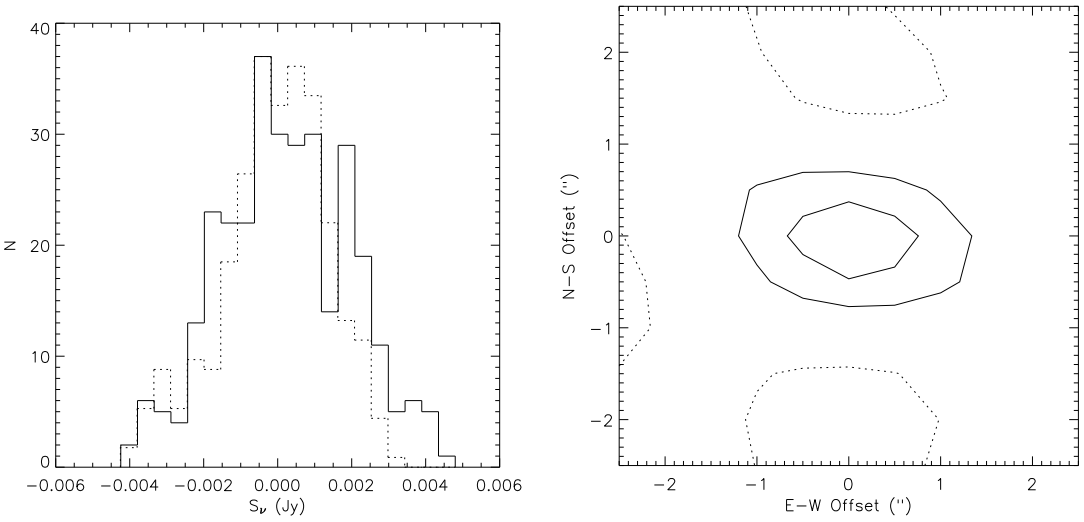

Figure 8.5 (left) Histogram of 3 mm continuum fluxes observed toward positions of 313 near-IR cluster members in the ONC (solid line) and the fluxes observed toward 313 random positions within the unit gain contour (dotted line). The flux distribution for near-IR sources is biased to positive values with respect to the noise distribution. (right) Average image, obtained by stacking the 3 mm continuum emission observed toward each of the 313 low-mass near-IR sources. Contour levels are -1σ (dotted line), +1σ, and 2σ (solid lines). For the ensemble, an average disk is detected at a significance of 2.9σ, and exhibits a compact morphology centered on the origin. In addition, the average image shows negative emission that resembles sidelobe features in the OVRO beam, suggesting that the average emission is point-like.

detection level for individual K-band sources. Since the 3σ value varies across the mosaic, we use a locally-determined 3σ estimate, as in §8.2. We note that for the entire mosaic, $\sim$ 10 pixels within the unit gain contour are expected to show noise spikes above the 3σ level, which is why we used a 5σ detection limit above.

From Figure 8.3, we see that no near-IR sources are coincident with $\geq$ 5σ 3 mm emission (with the exception of the BN object). However, we do observe 3 mm emission above the 3σ level near to several K-band objects. We estimate relative positional uncertainties between the millimeter and near-IR observations by considering the centroiding uncertainty for millimeter sources ($\sim 0.5\theta_{\rm beam}$/signal-to-noise $\approx 0\farcs3$) and the uncertainty in the near-IR source positions ($\sim 0\farcs3$), and find that the relative astrometric uncertainty is $\sim 0\farcs4$. There are several candidates for which weak millimeter emission is coincident with near-IR emission within the positional uncertainties; we list these sources in Table 8.1. However, we caution that these

associations may be spurious: emission from nearby millimeter sources not properly CLEANed may produce side-lobe emission close to near-IR source positions, creating false 3σ detections. While the relative lack of negative features $< -3\sigma$ compared to positive features $> 3\sigma$ (~ 5 versus 15) in the residual image suggests that sidelobe emission may not be a dominant contaminant, further observations are necessary to improve image quality and signal-to-noise, and test whether the near-IR sources listed in Table 8.1 are actually massive disks.

In order to examine the flux distribution for "typical" low-mass stars in the ONC, we remove all sources that show fluxes with absolute values larger than 3σ. In this way, we remove sources that may be coincident with positive or negative side-lobes from other nearby sources, as well as the potential detections listed in Table 8.1. Figure 8.5 shows the distribution of mm-wavelength fluxes observed toward 313 K-band sources in the ONC, none of which are detected individually above the 3σ level. The bright point sources visible in Figure 8.3 were removed using CLEAN before computing this histogram.

We also plot the flux distribution measured for 313 randomly selected pixels within the unit gain contour, to give an idea of the noise. The 3 mm flux distribution observed for near-IR cluster members is biased to positive values compared to the noise distribution determined from random pixels. Thus, it appears that while none of these K-band objects are detected in 3 mm continuum emission above the 3σ level, there may be weak emission below the 3σ level from circumstellar disks. The mean flux observed for the ensemble of near-IR cluster members is 0.25 mJy, and the standard deviation in the mean is 8.65×10^{-5} Jy. The significance of the positive bias in Figure 8.5 is thus 2.9σ.

This positive bias is also illustrated in the right panel of Figure 8.5, which shows an average image of the 3 mm flux observed toward K-band sources, obtained by averaging $10'' \times 10''$ images centered around each object. The "average" disk is detected at a significance of $\sim 2.9\sigma$. In addition, the FWHM of the emission in Figure 8.5 is consistent with a point source, including negative features that resemble the negative features of the OVRO beam. Thus we conclude that the positive bias observed in

Table 8.1. Sources detected in $\lambda 3$ mm continuum with OVRO

ID	α (J2000)	δ (J2000)	S_ν (mJy)	Offset ($''$)
OVRO $> 5\sigma$ detections without near-IR counterparts				
MM1[†]	05 35 14.092	-05 22 22.63	66.58	
MM2	05 35 14.125	-05 22 04.63	9.99	
MM3	05 35 14.561	-05 22 19.63	9.67	
MM4	05 35 14.527	-05 22 31.13	70.45	
MM5	05 35 14.862	-05 22 35.63	14.91	
MM6	05 35 15.063	-05 22 03.13	26.03	
MM7	05 35 15.297	-05 22 05.13	26.80	
MM8	05 35 13.724	-05 23 35.63	36.10	
MM9	05 35 13.690	-05 23 46.63	28.75	
MM10	05 35 13.723	-05 23 50.63	14.51	
MM11	05 35 14.025	-05 23 45.63	26.79	
MM12	05 35 13.523	-05 23 59.13	15.56	
MM13	05 35 13.556	-05 24 02.63	15.43	
MM14	05 35 13.489	-05 24 10.63	40.82	
MM15	05 35 13.757	-05 24 08.13	36.92	
MM16	05 35 13.924	-05 24 09.13	18.35	
MM17	05 35 13.958	-05 23 57.13	11.72	
MM18	05 35 14.360	-05 23 54.63	16.02	
MM19	05 35 15.163	-05 23 40.63	15.31	
MM20	05 35 15.364	-05 23 05.13	12.52	
MM21	05 35 15.799	-05 23 14.63	19.70	
MM22	05 35 15.799	-05 23 26.63	18.59	
MM23	05 35 15.933	-05 23 45.63	10.31	
MM24	05 35 15.933	-05 23 50.13	11.94	
MM25	05 35 16.302	-05 23 16.63	11.30	
MM26	05 35 16.737	-05 23 16.63	19.12	
MM27	05 35 17.808	-05 23 10.13	9.34	
OVRO $> 3\sigma$ detections with potential near-IR counterparts				
NIR1	05 35 13.556	-05 23 55.13	18.92	0.34
NIR2	05 35 14.628	-05 23 01.63	8.88	0.15
NIR3	05 35 17.674	-05 23 41.13	16.68	0.34
NIR4	05 35 18.009	-05 23 30.63	5.90	0.45
NIR5	05 35 18.244	-05 24 13.13	6.31	$\lesssim 0.4$

Note. — MM1 corresponds to the massive BN object, which does have a counterpart at H and K bands (e.g., Becklin & Neugebauer 1967).

Figure 8.5 probably represents underlying weak mm-wavelength emission from point sources.

The mass of circumstellar material (dust + gas, assuming a standard ISM gas to dust ratio of 100) is related to the 3 mm continuum flux. Assuming the emission is optically-thin, and following Hildebrand (1983),

$$M_{\rm circumstellar} = \frac{S_\nu d^2}{\kappa_\nu B_\nu(T_{\rm dust})}. \tag{8.1}$$

Here, ν is the observed frequency, S_ν is the observed flux, d is the distance to the source, $\kappa_\nu = \kappa_0(\nu/\nu_0)^\beta$ is the mass opacity, $T_{\rm dust}$ is the dust temperature, and B_ν is the Planck function. We assume $d = 480$ pc (Genzel et al. 1981), $\kappa_0 = 0.02$ cm^2 g^{-1} at 1300 μm, $\beta = 1.0$ (Hildebrand 1983; Beckwith et al. 1990), and $T_{\rm dust} = 20$ K (see discussion in Carpenter 2002). Uncertainties in the assumed values of these parameters (notably κ) imply that the derived masses are uncertain (in an absolute sense) by at least a factor of 3 (e.g., Pollack et al. 1994).

With these assumptions, the masses of detected sources in our OVRO mosaic (Table 8.1) range from 0.12 to 1.44 M$_\odot$. However, since some of these objects may be massive stars (e.g., the BN object), the millimeter flux may contain substantial contributions from free-free emission or optically-thin emission from dust substantially hotter than the assumed 20 K. Thus, these masses should be treated as upper limits in some cases. In contrast, for the 313 known low-mass K-band sources our assumptions should be valid, and the conversion from 3 mm flux into mass is more reliable. The mean circumstellar mass among the 313 low-mass K-band sources within the unit gain contour of our OVRO mosaic is 0.005 ± 0.002 M$_\odot$.

The OVRO observations alone do not have the angular resolution or kinematic information necessary to determine whether the circumstellar material is distributed in disks or envelopes, or combinations of the two. However, for the sample of near-IR cluster members, the observed mm-wavelength dust emission probably arises in flattened distributions since, for spherical distributions of material the columns of dust implied by the mm-wavelength flux would cause extinctions $A_V \gtrsim 300$ mag, which

would completely block out any near-IR stellar emission (see, e.g., Beckwith et al. 1990). Thus, the mean circumstellar mass of 0.005 ± 0.002 $M_\odot$ probably represents the mean disk mass for the K-band-detected low-mass stars in the ONC.

8.4 Discussion

Our observations did not find large millimeter fluxes toward the positions of near-IR cluster members in the ONC, implying a lack of very massive disks ($\gtrsim 0.2$ $M_\odot$). While there are five candidate cluster members which may be associated with 3 millimeter continuum emission at the 3σ level, these may be chance coincidences with sidelobe artifacts rather than actual associations (§8.3). Thus, at most 1.5% of the near-IR cluster members of the ONC have disk masses higher than ~ 0.1 $M_\odot$. Although K-L color excesses of ONC members suggest that $80 \pm 7\%$ of the stars have circumstellar disks (Lada et al. 2000), these two estimates of the disk fraction are not necessarily contradictory, since the near-IR emission probes trace material ($\sim 10^{-6}$ $M_\odot$) within ~ 0.1 AU of the star, while the millimeter emission traces massive ($\gtrsim 0.1$ $M_\odot$) outer circumstellar material.

We compare our results for the ONC with analogous 3 mm continuum surveys of NGC 2024 (Eisner & Carpenter 2003) and IC 348 (Carpenter 2002). NGC 2024 and IC 348, are somewhat less dense than the ONC, but still each contain on the order of 300 stars (Lada et al. 1991; Herbig 1998). In addition, spectroscopically-determined masses in the ONC (Hillenbrand 1997) and IC 348 (Luhman 1999), and estimated masses from color-magnitude diagrams in NGC 2024 (Meyer 1996; Eisner & Carpenter 2003) indicate similar stellar mass ranges in the three clusters, although the spectral types of the most massive stars are somewhat cooler in NGC 2024 ($\sim$O8) and IC 348 (B0) than in Orion. Comparison of the disk mass distributions can provide insights into disk evolution, since the three clusters have apparently different ages. NGC 2024 is more deeply embedded within the molecular cloud and probably younger then the ONC, which is in turn younger than IC 348 (Meyer 1996; Ali 1996; Hillenbrand 1997; Luhman et al. 1998; Luhman 1999).

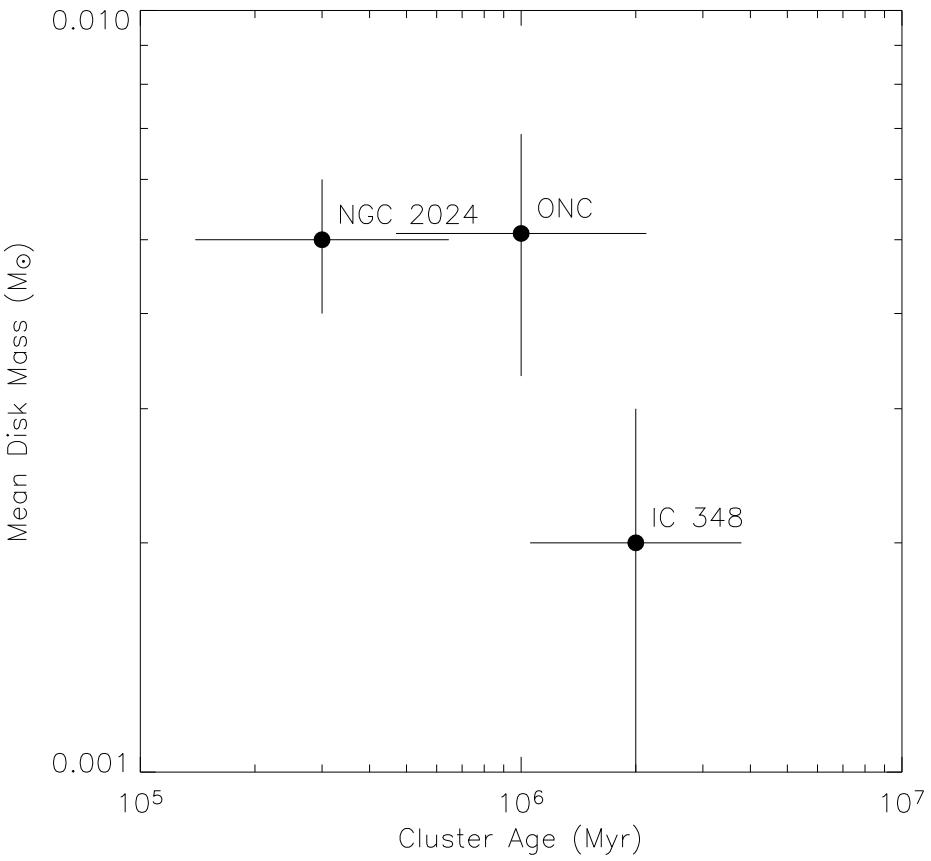

Figure 8.6 Average disk mass as a function of age for the NGC 2024, ONC, and IC 348 clusters. The disk masses are taken from this work, Eisner & Carpenter (2003), and Carpenter (2002), and estimated cluster ages and uncertainties are from Meyer (1996), Ali (1996), Hillenbrand (1997), Luhman et al. (1998), and Luhman (1999).

The average disk masses for "typical" low-mass stars in the three regions is plotted as a function of cluster age in Figure 8.6. In NGC 2024, the mean disk mass is 0.005 ± 0.001 $M_\odot$ (Eisner & Carpenter 2003), compared to 0.005 ± 0.002 in the ONC, and 0.002 ± 0.001 $M_\odot$ in IC 348 (Carpenter 2002). In addition, the fraction of objects detected in millimeter emission (without near-IR counterparts) is higher in NGC 2024 ($\sim 6\%$) and the ONC ($\lesssim 10\%$) than in IC 348 (0%). Assuming that the differences between NGC 2024, the ONC, and IC 348 are due to temporal evolution, these observations indicate that massive disks/envelopes dissipate on timescales $\lesssim 2$ Myr, and that the average disk mass decreases by a factor of 2.5 ± 1.3 between ~ 0.3 and 2 Myr.

It is important to keep in mind that the total millimeter emission is sensitive to

dust grain properties in addition to total dust mass. For example, dust grains larger than the observing wavelength emit inefficiently compared to small dust grains, and the millimeter flux therefore depends on dust grain properties in addition to the total mass. Thus, observed evolution in the millimeter flux may indicate that one or more of the assumed quantities in Equation 8.1 (e.g., temperature or opacity) is different in the three regions. Regardless of the underlying factors, our measurements suggest disk evolution between ~ 0.3 and 2 Myr. However, future measurements of the disk mass distributions in clusters will decrease the uncertainties in Figure 8.6, enabling more concrete constraints on the evolutionary timescales of massive disks.

Acknowledgments. JAE is supported by a Michelson Graduate Research Fellowship. JMC acknowledges support from Long Term Space Astrophysics Grant NAG5-8217 and the Owens Valley Radio Observatory, which is supported by the National Science Foundation through grant AST-9981546. This publication makes use of data products from the Two Micron All Sky Survey, which is a joint project of the University of Massachusetts and the Infrared Processing and Analysis Center, funded by the National Aeronautics and Space Administration and the National Science Foundation. 2MASS science data and information services were provided by the Infrared Science Archive (IRSA) at IPAC.

Chapter 9

Summary and Future Prospects

Circumstellar disks are an integral part of the processes of star and planet formation: young stars are surrounded by massive, rotating disks of dust and gas, which supply a reservoir of material that may be incorporated into planets, accreted onto the central star, or ejected in powerful winds. In this dissertation, I have described high angular resolution observations of these dust- and gas-rich disks around young stars, and I used these data to constrain processes related to star and planet formation. In this chapter, I summarize my results and discuss several exciting prospects for future investigations.

9.1 Class I Protostars: Circumstellar Evolution and Accretion

I presented new scattered light images at 0.9 μm and OVRO 1.3 mm continuum images of five Class I protostars in the Taurus star forming region, and I analyzed these data in conjunction with broadband spectral energy distributions and 8-13 μm spectra from the literature using a Monte Carlo radiative transfer code. I fit several classes of models for the circumstellar dust distributions, including pure disks, pure envelopes, and combinations of disks and envelopes, simultaneously to the combined imaging+SED datasets, and I showed that models incorporating *both* massive envelopes and embedded disks provide better fits than either pure disks or pure envelopes. For the best-fitting disk+envelope models, I determined mass accretion rates,

centrifugal radii, outer radii, envelope and disk masses, and source inclinations. The inferred disk+envelope geometries, high mass infall rates ($\sim 10^{-6}$ $M_\odot$ yr^{-1}), and large disk masses ($\gtrsim 0.1$ $M_\odot$), all suggest that Class I sources are at an evolutionary stage intermediate to spherical collapsing clouds and fully assembled young stars surrounded by geometrically thin, rotating disks. Moreover, the inferred mass accretion rates, which pertain to the transfer of material from the envelope onto the disk, are larger than accretion rates tracing infalling material from the disk onto the central protostar. These discrepant accretion rates, and the high disk masses for our best fit models, argue in favor of non-stationary accretion from the disk onto the central star, perhaps as a result of periodic gravitational instabilities.

There are several areas in which future work can enhance our understanding of Class I sources. Perhaps most importantly, more detailed and physically realistic models must be developed, which can explain simultaneously a variety of observations. In the analysis described in this dissertation, I suggested several potential improvements to the models, which will hopefully be implemented in the future. For example, the inclusion of large-scale distributions of tenuous dust, in addition to the dense disk+envelope distributions included in our models, may be necessary to fit multi-wavelength imaging data well. In addition, more detailed, physically-motivated models of the radial and vertical density profiles for disk+envelope models will enable better constraints on physical properties of the circumstellar dust distributions.

In addition to improvement of the models, new astronomical instruments will provide powerful new measurements of the dust and gas distributions around Class I objects. By providing direct constraints on the circumstellar geometries and compositions, these new observations will remove ambiguities in the models, and allow a clearer picture of the dust and gas around Class I sources. New millimeter interferometers including the SMA, CARMA, and ALMA, will provide spatially and kinematically resolved images of Class I objects, which will enable direct measurements of disk density, temperature, and velocity profiles. Sensitive new infrared telescopes like the *Spitzer Space Telescope*, and new mid-IR interferometers such as the Large Binocular Telescope Interferometer, will enable observations of Class I sources close in

wavelength to the peak flux, helping to constrain the structure of the inner regions of the circumstellar dust distributions. Finally, mid-IR spectroscopic observations with *Spitzer* will allow new constraints on the mineralogy and particle size distribution of dusty and icy material around these objects. The more complete picture of Class I sources allowed by these new observations and improved models will help to establish firmly the evolutionary stage of this class of objects.

9.2 Inner Disk Structure: Planet Formation and Disk Accretion

While previous modeling of circumstellar disks had been based largely on spatially unresolved spectral energy distributions (e.g., Bertout et al. 1988), the new near-IR interferometry data presented in this thesis has enabled *direct* observations of inner disk regions within $\sim 0.1 - 1$ AU of the central stars. Using the Palomar Testbed Interferometer and the Keck Interferometer, I measured directly the inner disk sizes, inclinations, and temperatures for a sample of young stars spanning a range of stellar masses (Eisner et al. 2003, 2004, 2005).

I discovered that inner disks around young stars are generally inclined, and possess inner holes approximately 0.1-1 AU in radius. Using the interferometry data in conjunction with photometry and spectroscopy, I showed that disks around lower-mass stars ($\lesssim 5$ $M_\odot$) probably have puffed-up inner disk walls, while higher-mass stars may have geometrically flat inner disks; thus, it appears that the detailed structure of the inner disk depends on stellar and/or accretion properties in these systems. Comparison of the inner disk geometries to outer disk morphologies inferred from millimeter interferometric observations of a few sources (e.g., Corder et al. 2005) demonstrated that the disks around these stars are not significantly warped (Eisner et al. 2004). Finally, I used these interferometric and ancillary data to investigate the inner disk truncation mechanism, and showed the the dusty component is likely truncated by sublimation, while the gaseous component may extend inward to the magnetospheric

radius (Eisner et al. 2005). Moreover, the truncation radius of the gaseous component is consistent with expectations based on the observed orbits of short-period extra-solar planets, which may have halted their inward migration in resonances with the inner disk.

With new near- and mid-IR interferometers coming on-line, and the advent of sensitive infrared telescopes like *Spitzer Space Telescope* and SOFIA, the future prospects for studying inner disk structure are very exciting. One obvious improvement over current work is to obtain larger samples, and to supplement the near-IR interferometric observations described in this dissertation with longer-wavelength interferometry. The Very Large Telescope Interferometer has already produced interferometric measurements of protoplanetary disks at 10 μm (e.g., Leinert et al. 2004; van Boekel et al. 2004). In the near future, the Large Binocular Telescope Interferometer and the Keck Interferometer will also enable interferometric measurements from 3-25 μm.

With larger samples of young stars, observed interferometrically at several wavelengths and supplemented by high quality photometric and spectroscopic measurements, one can obtain a better understanding of inner disk structure, disk accretion, and planet formation around typical young stars. Another exciting prospect is a more detailed determination of the temperature structure of disks in the terrestrial region, with clear implications for the location of the snowline (e.g., Hayashi 1981), and thus Earth-like planet formation. Finally, in the future I hope to monitor several young star+disk systems to search for time-variations in inner disk structure, due to changes in the stellar magnetic field, variable mass accretion rates (e.g., Shu et al. 1997), or hydrodynamic fluctuations in the puffed-up inner disk wall (Dullemond et al. 2003).

9.3 Disk Masses: Disk Evolution and Giant Planet Formation

I used the Owens Valley Millimeter Array to determine the distribution of circumstellar disk masses in the young ($\sim 0.3-1$ Myr) clusters NGC 2024 and the Orion Nebula

cluster. These observations encompassed hundreds of young stars in these clusters, and enabled an investigation of the circumstellar disk mass distributions. The mean disk masses observed for the ensembles of known low-mass near-IR sources in each cluster is ~ 0.005 $M_\odot$ (probably uncertain by a factor of ~ 3 due to uncertainties in converting millimeter flux into mass), comparable to the estimated minimum mass solar nebula, ~ 0.01 $M_\odot$. Thus, it appears that many stars aged less than about 1 Myr may possess disks with sufficient mass to form planetary systems like our own. However, in the older (~ 2 Myr) cluster IC 348, the mean disk mass is ~ 2.5 times lower (Carpenter 2002), suggesting that the mean circumstellar mass is decreasing with cluster age, and that disks massive enough to form solar-system-like planetary systems may disperse on timescales of 1-2 Myr. Finally, comparison of these observations of young stars in rich clusters with results for the lower-density Taurus star forming region indicate that there are statistically significant differences in the distributions of massive disks in the two environments. Since most young stars form in rich clusters (e.g., Lada & Lada 2003), understanding the properties of disks in rich clusters is crucial for understanding disk properties and evolution, and giant planet formation, in general.

The enhanced sensitivity of new sub-millimeter interferometers, including the SMA, CARMA, and eventually ALMA, will enable us to detect directly large numbers of disks more massive than the 0.01 $M_\odot$ "minimum-mass solar nebula" (Weidenschilling 1977), greatly improving our understanding of the ubiquity of potential precursors to analogs of our solar system. Moreover, surveys of several rich stellar clusters of different ages will constrain better the evolutionary timescales of massive circumstellar disks. Another improvement that is possible with these new telescopes is to follow up detected sources at multiple wavelengths, to distinguish between the effects of disk dispersal and coagulation of dust grains into larger bodies like planetesimals; while these processes produce degenerate effects for single-wavelength observations, dust grain growth would produce changes in spectral index that could be detected with multi-wavelength data. Finally, with the enhanced sensitivity and spectral bandwidths of new instruments, one can observe the gas content of disks as

a function of age, in parallel with the dust evolution.

While millimeter observations provide an excellent probe of the dust content in young disks, infrared observations are much more sensitive for older disks, where dust masses as small as $\sim 10^{-6}$ $M_{\oplus}$ can be detected (e.g., Mamajek et al. 2004). Using the enhanced sensitivity of *Spitzer* at mid- and far-IR wavelengths, and the mid-IR nulling capability of instruments like Keck Interferometer, LBTI, and MMT/BLINC, low levels of infrared dust emission can be detected. By combining millimeter and mid- to far-IR observations of sources spanning a range of ages, one can place firm constraints on the evolutionary timescales of disk material, with important implications for planet formation theories.

Bibliography

Adams, F. C., Lada, C. J., & Shu, F. H. 1987, ApJ, 312, 788

—. 1988, ApJ, 326, 865

Akeson, R. L., Ciardi, D. R., van Belle, G. T., Creech-Eakman, M. J., & Lada, E. A. 2000, ApJ, 543, 313

Akeson, R. L., Walker, C. H., Wood, K., Eisner, J. A., Scire, E., Penprase, B., Ciardi, D. R., van Belle, G. T., Whitney, B., & Bjorkman, J. E. 2005, ApJ, 622, 440

Ali, B. 1996, PhD thesis, The Ohio State University, Ohio, USA

André, P. & Montmerle, T. 1994, ApJ, 420, 837

André, P., Ward-Thompson, D., & Barsony, M. 1993, ApJ, 406, 122

Anthony-Twarog, B. J. 1982, AJ, 87, 1213

Appenzeller, I., Jankovics, I., & Oestreicher, R. 1984, A&A, 141, 108

Augereau, J. C., Lagrange, A. M., Mouillet, D., & Ménard, F. 1999, A&A, 350, L51

Bèland, S., Boulade, O., & Davidge, T. 1988, Bulletin d'information du telescope Canada-France-Hawaii, 19, 16

Balbus, S. A. & Hawley, J. F. 1991, ApJ, 376, 214

Bally, J., Testi, L., Sargent, A., & Carlstrom, J. 1998, AJ, 116, 854

Baraffe, I., Chabrier, G., Allard, F., & Hauschildt, P. H. 1998, A&A, 337, 403

Barsony, M., Koresko, C., & Matthews, K. 2003, ApJ, 591, 1064

Bate, M. R., Bonnell, I. A., Clarke, C. J., Lubow, S. H., Ogilvie, G. I., Pringle, J. E., & Tout, C. A. 2000, MNRAS, 317, 773

Becklin, E. E. & Neugebauer, G. 1967, ApJ, 147, 799

Beckwith, S. V. W. & Sargent, A. I. 1993, in Protostars and Planets III, 521–541

Beckwith, S. V. W., Sargent, A. I., Chini, R. S., & Guesten, R. 1990, AJ, 99, 924

Beichman, C. A., Myers, P. C., Emerson, J. P., Harris, S., Mathieu, R., Benson, P. J., & Jennings, R. E. 1986, ApJ, 307, 337

Bell, K. R. & Lin, D. N. C. 1994, ApJ, 427, 987

Benson, P. J. & Myers, P. C. 1989, ApJS, 71, 89

Bertout, C., Basri, G., & Bouvier, J. 1988, ApJ, 330, 350

Bigay, J. H. & Garnier, R. 1970, A&AS, 1, 15

Bik, A., Lenorzer, A., Kaper, L., Comerón, F., Waters, L. B. F. M., de Koter, A., & Hanson, M. M. 2003, A&A, 404, 249

Blake, G. A. & Boogert, A. C. A. 2004, ApJ, 606, L73

Blandford, R. D. & Payne, D. G. 1982, MNRAS, 199, 883

Boden, A. F., Colavita, M. M., van Belle, G. T., & Shao, M. 1998, in Proc. SPIE Vol. 3350, p. 872-880, Astronomical Interferometry, Robert D. Reasenberg; Ed., 872–880

Bodenheimer, P. & Pollack, J. B. 1986, Icarus, 67, 391

Born, M. & Wolf, E., eds. 1999, Principles of optics : electromagnetic theory of propagation, interference and diffraction of light

Boss, A. P. 1997, Science, 276, 1836

—. 1998, ApJ, 503, 923

Bouvier, J. 1990, AJ, 99, 946

Brittain, S. D., Rettig, T. W., Simon, T., Kulesa, C., DiSanti, M. A., & Dello Russo, N. 2003, ApJ, 588, 535

Brown, A. G. A., de Geus, E. J., & de Zeeuw, P. T. 1994, A&A, 289, 101

Brown, D. W. & Chandler, C. J. 1999, MNRAS, 303, 855

Burrows, C. J., Stapelfeldt, K. R., Watson, A. M., Krist, J. E., Ballester, G. E., Clarke, J. T., Crisp, D., Gallagher, J. S., Griffiths, R. E., Hester, J. J., Hoessel, J. G., Holtzman, J. A., Mould, J. R., Scowen, P. A., Trauger, J. T., & Westphal, J. A. 1996, ApJ, 473, 437

Butler, R. P., Marcy, G. W., Fischer, D. A., Brown, T. M., Contos, A. R., Korzennik, S. G., Nisenson, P., & Noyes, R. W. 1999, ApJ, 526, 916

Butner, H. M., Evans, N. J., Lester, D. F., Levreault, R. M., & Strom, S. E. 1991, ApJ, 376, 636

Calvet, N. & Gullbring, E. 1998, ApJ, 509, 802

Cameron, A. G. W. 1973, Icarus, 18, 407

—. 1978, Moon and Planets, 18, 5

Canto, J., Rodriguez, L. F., Calvet, N., & Levreault, R. M. 1984, ApJ, 282, 631

Carpenter, J. M. 2000, AJ, 120, 3139

—. 2002, AJ, 124, 1593

Carr, J. S., Tokunaga, A. T., Najita, J., Shu, F. H., & Glassgold, A. E. 1993, ApJ, 411, L37

Cassen, P. & Moosman, A. 1981, Icarus, 48, 353

Chandler, C. J. & Carlstrom, J. E. 1996, ApJ, 466, 338

Chandler, C. J. & Richer, J. S. 2000, ApJ, 530, 851

Chandler, C. J., Terebey, S., Barsony, M., Moore, T. J. T., & Gautier, T. N. 1996, ApJ, 471, 308

Chavarria-K., C., de Lara, E., Finkenzeller, U., Mendoza, E. E., & Ocegueda, J. 1988, A&A, 197, 151

Chiang, E. I. & Goldreich, P. 1997, ApJ, 490, 368

—. 1999, ApJ, 519, 279

Chini, R. 1981, A&A, 99, 346

Cohen, J. G., Persson, S. E., Elias, J. H., & Frogel, J. A. 1981, ApJ, 249, 481

Colavita, M., Akeson, R., Wizinowich, P., Shao, M., Acton, S., Beletic, J., Bell, J., Berlin, J., Boden, A., Booth, A., Boutell, R., Chaffee, F., Chan, D., Chock, J., Cohen, R., Crawford, S., Creech-Eakman, M., Eychaner, G., Felizardo, C., Gathright, J., Hardy, G., Henderson, H., Herstein, J., Hess, M., Hovland, E., Hrynevych, M., Johnson, R., Kelley, J., Kendrick, R., Koresko, C., Kurpis, P., Le Mignant, D., Lewis, H., Ligon, E., Lupton, W., McBride, D., Mennesson, B., Millan-Gabet, R., Monnier, J., Moore, J., Nance, C., Neyman, C., Niessner, A., Palmer, D., Reder, L., Rudeen, A., Saloga, T., Sargent, A., Serabyn, E., Smythe, R., Stomski, P., Summers, K., Swain, M., Swanson, P., Thompson, R., Tsubota, K., Tumminello, A., van Belle, G., Vasisht, G., Vause, J., Walker, J., Wallace, K., & Wehmeier, U. 2003, ApJ, 592, L83

Colavita, M. M. 1999, PASP, 111, 111

Colavita, M. M., Wallace, J. K., Hines, B. E., Gursel, Y., Malbet, F., Palmer, D. L., Pan, X. P., Shao, M., Yu, J. W., Boden, A. F., Dumont, P. J., Gubler, J., Koresko, C. D., Kulkarni, S. R., Lane, B. F., Mobley, D. W., & van Belle, G. T. 1999, ApJ, 510, 505

Colavita, M. M. & Wizinowich, P. L. 2003, in Interferometry for Optical Astronomy II. Edited by Wesley A. Traub. Proceedings of the SPIE, Volume 4838, pp. 79-88 (2003)., 79–88

Corcoran, M. & Ray, T. P. 1997, A&A, 321, 189

Corder, S., Eisner, J., & Sargent, A. 2005, ApJ, 622, L133

Corporon, P. 1998, Ph.D. Thesis

Corporon, P. & Lagrange, A.-M. 1999, A&AS, 136, 429

Crutcher, R. M., Henkel, C., Wilson, T. L., Johnston, K. J., & Bieging, J. H. 1986, ApJ, 307, 302

D'Alessio, P., Calvet, N., & Hartmann, L. 2001, ApJ, 553, 321

D'Alessio, P., Calvet, N., Hartmann, L., Lizano, S., & Cantó, J. 1999, ApJ, 527, 893

D'Antona, F. & Mazzitelli, I. 1994, ApJS, 90, 467

—. 1997, Memorie della Societa Astronomica Italiana, 68, 807

de Lara, E., Chavarria-K., C., & Lopez-Molina, G. 1991, A&A, 243, 139

de Winter, D., van den Ancker, M. E., Maira, A., Thé, P. S., Djie, H. R. E. T. A., Redondo, I., Eiroa, C., & Molster, F. J. 2001, A&A, 380, 609

Doppmann, G. W., Jaffe, D. T., & White, R. J. 2003, AJ, 126, 3043

Draine, B. T. & Lee, H. M. 1984, ApJ, 285, 89

Draine, B. T. & Malhotra, S. 1993, ApJ, 414, 632

Duchêne, G., Bouvier, J., Bontemps, S., André, P., & Motte, F. 2004, A&A, 427, 651

Dullemond, C. P. & Dominik, C. 2004a, A&A, 417, 159

—. 2004b, A&A, 421, 1075

Dullemond, C. P., Dominik, C., & Natta, A. 2001, ApJ, 560, 957

Dullemond, C. P., van den Ancker, M. E., Acke, B., & van Boekel, R. 2003, ApJ, 594, L47

Dutrey, A., Guilloteau, S., Duvert, G., Prato, L., Simon, M., Schuster, K., & Menard, F. 1996, A&A, 309, 493

Edwards, S., Cabrit, S., Strom, S. E., Heyer, I., Strom, K. M., & Anderson, E. 1987, ApJ, 321, 473

Edwards, S., Hartigan, P., Ghandour, L., & Andrulis, C. 1994, AJ, 108, 1056

Efstathiou, A. & Rowan-Robinson, M. 1991, MNRAS, 252, 528

Eiroa, C., Garzón, F., Alberdi, A., de Winter, D., Ferlet, R., Grady, C. A., Cameron, A., Davies, J. K., Deeg, H. J., Harris, A. W., Horne, K., Merín, B., Miranda, L. F., Montesinos, B., Mora, A., Oudmaijer, R., Palacios, J., Penny, A., Quirrenbach, A., Rauer, H., Schneider, J., Solano, E., Tsapras, Y., & Wesselius, P. R. 2001, A&A, 365, 110

Eiroa, C., Oudmaijer, R. D., Davies, J. K., de Winter, D., Garzón, F., Palacios, J., Alberdi, A., Ferlet, R., Grady, C. A., Cameron, A., Deeg, H. J., Harris, A. W., Horne, K., Merín, B., Miranda, L. F., Montesinos, B., Mora, A., Penny, A., Quirrenbach, A., Rauer, H., Schneider, J., Solano, E., Tsapras, Y., & Wesselius, P. R. 2002, A&A, 384, 1038

Eisner, J. A. & Carpenter, J. M. 2003, ApJ, 598, 1341

Eisner, J. A., Hillenbrand, L. A., White, R. J., Akeson, R. L., & Sargent, A. I. 2005, ApJ, 623, 952

Eisner, J. A., Lane, B. F., Akeson, R. L., Hillenbrand, L., & Sargent, A. 2003, ApJ, 588, 360

Eisner, J. A., Lane, B. F., Hillenbrand, L., Akeson, R., & Sargent, A. 2004, ApJ, 613, 1049

Elsasser, H. & Staude, H. J. 1978, A&A, 70, L3+

Eritsyan, M. A., Hovhannessian, R. K., & Hovhannessian, E. R. 2002, Astrophysics, 45, 25

Felli, M., Churchwell, E., Wilson, T. L., & Taylor, G. B. 1993, A&AS, 98, 137

Fukagawa, M., Hayashi, M., Tamura, M., Itoh, Y., Hayashi, S. S., Oasa, Y., Takeuchi, T., Morino, J., Murakawa, K., Oya, S., Yamashita, T., Suto, H., Mayama, S., Naoi, T., Ishii, M., Pyo, T., Nishikawa, T., Takato, N., Usuda, T., Ando, H., Iye, M., Miyama, S. M., & Kaifu, N. 2004, ApJ, 605, L53

Galli, D. & Shu, F. H. 1993a, ApJ, 417, 220

—. 1993b, ApJ, 417, 243

Gammie, C. F. 1996, ApJ, 457, 355

Garrison, R. F. 1968, PASP, 80, 20

Gaume, R. A., Johnston, K. J., & Wilson, T. L. 1992, ApJ, 388, 489

Genzel, R., Reid, M. J., Moran, J. M., & Downes, D. 1981, ApJ, 244, 884

Geoffray, H. & Monin, J.-L. 2001, A&A, 369, 239

Ghez, A. M., Neugebauer, G., & Matthews, K. 1993, AJ, 106, 2005

Ghosh, P. & Lamb, F. K. 1979a, ApJ, 232, 259

—. 1979b, ApJ, 234, 296

Gilliland, R. L., Brown, T. M., Guhathakurta, P., Sarajedini, A., Milone, E. F., Albrow, M. D., Baliber, N. R., Bruntt, H., Burrows, A., Charbonneau, D., Choi, P., Cochran, W. D., Edmonds, P. D., Frandsen, S., Howell, J. H., Lin, D. N. C.,

Marcy, G. W., Mayor, M., Naef, D., Sigurdsson, S., Stagg, C. R., Vandenberg, D. A., Vogt, S. S., & Williams, M. D. 2000, ApJ, 545, L47

Goldreich, P. & Ward, W. R. 1973, ApJ, 183, 1051

Gomez, M., Whitney, B. A., & Kenyon, S. J. 1997, AJ, 114, 1138

Goodman, A. A., Benson, P. J., Fuller, G. A., & Myers, P. C. 1993, ApJ, 406, 528

Grady, C. A., Perez, M. R., Talavera, A., McCollum, B., Rawley, L. A., England, M. N., & Schlegel, M. 1996, ApJ, 471, L49+

Grady, C. A., Woodgate, B., Bruhweiler, F. C., Boggess, A., Plait, P., Lindler, D. J., Clampin, M., & Kalas, P. 1999, ApJ, 523, L151

Grasdalen, G. L. 1974, ApJ, 193, 373

Gullbring, E., Calvet, N., Muzerolle, J., & Hartmann, L. 2000, ApJ, 544, 927

Gullbring, E., Hartmann, L., Briceno, C., & Calvet, N. 1998, ApJ, 492, 323

Haisch, K. E., Lada, E. A., & Lada, C. J. 2000, AJ, 120, 1396

—. 2001, AJ, 121, 2065

Hartigan, P. & Kenyon, S. J. 2003, ApJ, 583, 334

Hartmann, L. 1998, Accretion processes in star formation (Accretion processes in star formation / Lee Hartmann. Cambridge, UK ; New York : Cambridge University Press, 1998. (Cambridge astrophysics series ; 32) ISBN 0521435072.)

Hartmann, L. & Kenyon, S. J. 1985, ApJ, 299, 462

—. 1987, ApJ, 312, 243

—. 1996, ARA&A, 34, 207

Hartmann, L., Kenyon, S. J., & Calvet, N. 1993, ApJ, 407, 219

Hartmann, L. & Stauffer, J. R. 1989, AJ, 97, 873

Hayashi, C. 1981, Progress of Theoretical Physics, 70, 35

Hayward, T. L., Brandl, B., Pirger, B., Blacken, C., Gull, G. E., Schoenwald, J., & Houck, J. R. 2001, PASP, 113, 105

Henning, T., Pfau, W., Zinnecker, H., & Prusti, T. 1993, A&A, 276, 129

Herbig, G. H. 1960, ApJS, 4, 337

—. 1998, ApJ, 497, 736

Herbig, G. H. & Kameswara Rao, N. 1972, ApJ, 174, 401

Herbst, W. & Shevchenko, V. S. 1999, AJ, 118, 1043

Herbst, W., Warner, J. W., Miller, D. P., & Herzog, A. 1982, AJ, 87, 98

Hernández, J., Calvet, N., Briceño, C., Hartmann, L., & Berlind, P. 2004, AJ, 127, 1682

Hildebrand, R. H. 1983, QJRAS, 24, 267

Hillenbrand, L. A. 1997, AJ, 113, 1733

Hillenbrand, L. A. & Carpenter, J. M. 2000, ApJ, 540, 236

Hillenbrand, L. A., Strom, S. E., Calvet, N., Merrill, K. M., Gatley, I., Makidon, R. B., Meyer, M. R., & Skrutskie, M. F. 1998, AJ, 116, 1816

Hillenbrand, L. A., Strom, S. E., Vrba, F. J., & Keene, J. 1992, ApJ, 397, 613

Hillenbrand, L. A. & White, R. J. 2004, ApJ, 604, 741

Hiltner, W. A. & Johnson, H. L. 1956, ApJ, 124, 367

Hogerheijde, M. R. 2001, ApJ, 553, 618

Hogerheijde, M. R., Jayawardhana, R., Johnstone, D., Blake, G. A., & Kessler, J. E. 2002, AJ, 124, 3387

Hogerheijde, M. R. & Sandell, G. 2000, ApJ, 534, 880

Hogerheijde, M. R., van Dishoeck, E. F., Blake, G. A., & van Langevelde, H. J. 1997, ApJ, 489, 293

—. 1998, ApJ, 502, 315

Hollenbach, D. J., Yorke, H. W., & Johnstone, D. 2000, Protostars and Planets IV, 401

Ishii, M., Tamura, M., & Itoh, Y. 2004, ApJ, 612, 956

Itoh, Y., Sugitani, K., Fukuda, N., Nakanishi, K., Ogura, K., Tamura, M., Marui, K., Fujita, K., Oasa, Y., & Fukagawa, M. 2003, ApJ, 586, L141

Jensen, E. L. N. & Mathieu, R. D. 1997, AJ, 114, 301

Jiang, D. R., Perrier, C., & Lena, P. 1984, A&A, 135, 249

Johns-Krull, C. M., Valenti, J. A., & Gafford, A. D. 2003, in Revista Mexicana de Astronomia y Astrofisica Conference Series, 38–44

Keene, J. & Masson, C. R. 1990, ApJ, 355, 635

Kenyon, S. J., Calvet, N., & Hartmann, L. 1993a, ApJ, 414, 676

Kenyon, S. J. & Hartmann, L. 1987, ApJ, 323, 714

—. 1995, ApJS, 101, 117

Kenyon, S. J., Hartmann, L. W., Strom, K. M., & Strom, S. E. 1990, AJ, 99, 869

Kenyon, S. J., Whitney, B. A., Gomez, M., & Hartmann, L. 1993b, ApJ, 414, 773

Kenyon, S. J., Yi, I., & Hartmann, L. 1996, ApJ, 462, 439

Kessler-Silacci, J. E., Hillenbrand, L. A., Blake, G. A., & Meyer, M. R. 2005, ApJ, 622, 404

Klahr, H. & Bodenheimer, P. 2004, in Revista Mexicana de Astronomia y Astrofisica Conference Series, 87–90

Koerner, D. W. & Sargent, A. I. 1995, AJ, 109, 2138

Königl, A. 1991, ApJ, 370, L39

Koresko, C. D. 2002, AJ, 124, 1082

Kuchner, M. J. & Lecar, M. 2002, ApJ, 574, L87

Kusaka, T., Nakano, T., & Hayashi, C. 1970, Progress of Theoretical Physics, 44, 1580

Lada, C. J. 1987, in IAU Symp. 115, Star Forming Regions, ed. M. Peimbert & J. Jugaku (Dordrecht: Reidel), 1

Lada, C. J., Depoy, D. L., Merrill, K. M., & Gatley, I. 1991, ApJ, 374, 533

Lada, C. J. & Lada, E. A. 2003, ARA&A, 41, 57

Lada, C. J., Muench, A. A., Haisch, K. E., Lada, E. A., Alves, J. F., Tollestrup, E. V., & Willner, S. P. 2000, AJ, 120, 3162

Lada, C. J. & Wilking, B. A. 1984, ApJ, 287, 610

Lada, E. A., Strom, K. M., & Myers, P. C. 1993, in Protostars and Planets III, 245–277

Ladd, E. F., Fuller, G. A., Padman, R., Myers, P. C., & Adams, F. C. 1995, ApJ, 439, 771

Lai, D. 1999, ApJ, 524, 1030

Landolt, A. U. 1992, AJ, 104, 340

Larson, R. B. 1969, MNRAS, 145, 271

Laughlin, G. & Bodenheimer, P. 1994, ApJ, 436, 335

Lay, O. P., Carlstrom, J. E., Hills, R. E., & Phillips, T. G. 1994, ApJ, 434, L75

Leinert, C., van Boekel, R., Waters, L. B. F. M., Chesneau, O., Malbet, F., Köhler, R., Jaffe, W., Ratzka, T., Dutrey, A., Preibisch, T., Graser, U., Bakker, E., Chagnon, G., Cotton, W. D., Dominik, C., Dullemond, C. P., Glazenborg-Kluttig, A. W., Glindemann, A., Henning, T., Hofmann, K.-H., de Jong, J., Lenzen, R., Ligori, S., Lopez, B., Meisner, J., Morel, S., Paresce, F., Pel, J.-W., Percheron, I., Perrin, G., Przygodda, F., Richichi, A., Schöller, M., Schuller, P., Stecklum, B., van den Ancker, M. E., von der Lühe, O., & Weigelt, G. 2004, A&A, 423, 537

Lin, D. N. C., Bodenheimer, P., & Richardson, D. C. 1996, Nature, 380, 606

Liu, W. M., Hinz, P. M., Hoffmann, W. F., Brusa, G., Miller, D., & Kenworthy, M. A. 2005, ApJ, 618, L133

Looney, L. W., Mundy, L. G., & Welch, W. J. 2000, ApJ, 529, 477

Lucas, P. W., Blundell, K. M., & Roche, P. F. 2000, MNRAS, 318, 526

Lucas, P. W. & Roche, P. F. 1998, MNRAS, 299, 699

Luhman, K. L. 1999, ApJ, 525, 466

Luhman, K. L., Rieke, G. H., Lada, C. J., & Lada, E. A. 1998, ApJ, 508, 347

Lynden-Bell, D. & Pringle, J. E. 1974, MNRAS, 168, 603

Malbet, F., Berger, J.-P., Colavita, M. M., Koresko, C. D., Beichman, C., Boden, A. F., Kulkarni, S. R., Lane, B. F., Mobley, D. W., Pan, X. P., Shao, M., van Belle, G. T., & Wallace, J. K. 1998, ApJ, 507, L149

Malbet, F., Lachaume, R., Berger, J., Colavita, M. M., Di Folco, E., Eisner, J. A., Lane, B. F., Millan-Gabet, R., Ségransan, D., & Traub, W. A. 2005, ArXiv Astrophysics e-prints

Malfait, K., Bogaert, E., & Waelkens, C. 1998, A&A, 331, 211

Mamajek, E. E., Meyer, M. R., Hinz, P. M., Hoffmann, W. F., Cohen, M., & Hora, J. L. 2004, ApJ, 612, 496

Mannings, V. 1994, MNRAS, 271, 587

Mannings, V., Koerner, D. W., & Sargent, A. I. 1997, Nature, 388, 555

Mannings, V. & Sargent, A. I. 1997, ApJ, 490, 792

—. 2000, ApJ, 529, 391

Marcy, G. W. & Butler, R. P. 2000, PASP, 112, 137

Marsh, K. A., Silverstone, M. D., Becklin, E. E., Koerner, D. W., Werner, M. W., Weinberger, A. J., & Ressler, M. E. 2002, ApJ, 573, 425

Mathis, J. S., Rumpl, W., & Nordsieck, K. H. 1977, ApJ, 217, 425

Mayor, M. & Queloz, D. 1995, Nature, 378, 355

McCaughrean, M. J. & O'Dell, C. R. 1996, AJ, 111, 1977

Meeus, G., Waters, L. B. F. M., Bouwman, J., van den Ancker, M. E., Waelkens, C., & Malfait, K. 2001, A&A, 365, 476

Merrill, P. W. & Burwell, C. G. 1950, ApJ, 112, 72

Meyer, M. R. 1996, Ph.D. Thesis

Mezger, P. G., Chini, R., Kreysa, E., Wink, J. E., & Salter, C. J. 1988, A&A, 191, 44

Mezger, P. G., Sievers, A. W., Haslam, C. G. T., Kreysa, E., Lemke, R., Mauersberger, R., & Wilson, T. L. 1992, A&A, 256, 631

Michelson, A. A. 1920, ApJ, 51, 257

Millan-Gabet, R., Schloerb, F. P., & Traub, W. A. 2001, ApJ, 546, 358

Millan-Gabet, R., Schloerb, F. P., Traub, W. A., Malbet, F., Berger, J. P., & Bregman, J. D. 1999, ApJ, 513, L131

Miroshnichenko, A., Ivezić , Ž., Vinković , D., & Elitzur, M. 1999, ApJ, 520, L115

Monnier, J. D. & Millan-Gabet, R. 2002, ApJ, 579, 694

Monnier, J. D., Tuthill, P. G., Ireland, M. J., Cohen, R., & Tannirkulam, A. 2004, American Astronomical Society Meeting Abstracts, 205,

Moore, T. J. T., Chandler, C. J., Gear, W. K., & Mountain, C. M. 1989, MNRAS, 237, 1P

Mora, A., Merín, B., Solano, E., Montesinos, B., de Winter, D., Eiroa, C., Ferlet, R., Grady, C. A., Davies, J. K., Miranda, L. F., Oudmaijer, R. D., Palacios, J., Quirrenbach, A., Harris, A. W., Rauer, H., Cameron, A., Deeg, H. J., Garzón, F., Penny, A., Schneider, J., Tsapras, Y., & Wesselius, P. R. 2001, A&A, 378, 116

Moriarty-Schieven, G. H., Wannier, P. G., Keene, J., & Tamura, M. 1994, ApJ, 436, 800

Moriarty-Schieven, G. H., Wannier, P. G., Tamura, M., & Keene, J. 1992, ApJ, 400, 260

Motte, F. & André, P. 2001, A&A, 365, 440

Motte, F., André, P., & Neri, R. 1998, A&A, 336, 150

Mouillet, D., Larwood, J. D., Papaloizou, J. C. B., & Lagrange, A. M. 1997, MNRAS, 292, 896

Mundy, L. G., Looney, L. W., & Lada, E. A. 1995, ApJ, 452, L137+

Muzerolle, J., Calvet, N., Hartmann, L., & D'Alessio , P. 2003, ApJ, 597, L865

Myers, P. C., Fuller, G. A., Mathieu, R. D., Beichman, C. A., Benson, P. J., Schild, R. E., & Emerson, J. P. 1987, ApJ, 319, 340

Myers, P. C., Heyer, M., Snell, R. L., & Goldsmith, P. F. 1988, ApJ, 324, 907

Myers, P. C. & Ladd, E. F. 1993, ApJ, 413, L47

Najita, J., Carr, J. S., Glassgold, A. E., Shu, F. H., & Tokunaga, A. T. 1996, ApJ, 462, 919

Nakazato, T., Nakamoto, T., & Umemura, M. 2003, ApJ, 583, 322

Natta, A., Grinin, V., & Mannings, V. 2000, Protostars and Planets IV, 559

Natta, A., Palla, F., Butner, H. M., Evans, N. J., & Harvey, P. M. 1993, ApJ, 406, 674

Natta, A., Prusti, T., Neri, R., Wooden, D., Grinin, V. P., & Mannings, V. 2001, A&A, 371, 186

Natta, A. & Whitney, B. A. 2000, A&A, 364, 633

Nuernberger, D., Brandner, W., Yorke, H. W., & Zinnecker, H. 1998, A&A, 330, 549

Nuernberger, D., Chini, R., & Zinnecker, H. 1997, A&A, 324, 1036

O'Dell, C. R. & Wong, K. 1996, AJ, 111, 846

Ohashi, N., Hayashi, M., Kawabe, R., & Ishiguro, M. 1996, ApJ, 466, 317

Oke, J. B., Cohen, J. G., Carr, M., Cromer, J., Dingizian, A., Harris, F. H., Labrecque, S., Lucinio, R., Schaal, W., Epps, H., & Miller, J. 1995, PASP, 107, 375

Osorio, M., D'Alessio, P., Muzerolle, J., Calvet, N., & Hartmann, L. 2003, ApJ, 586, 1148

Osterloh, M. & Beckwith, S. V. W. 1995, ApJ, 439, 288

Oudmaijer, R. D., Palacios, J., Eiroa, C., Davies, J. K., de Winter, D., Ferlet, R., Garzón, F., Grady, C. A., Cameron, A., Deeg, H. J., Harris, A. W., Horne, K., Merín, B., Miranda, L. F., Montesinos, B., Mora, A., Penny, A., Quirrenbach, A., Rauer, H., Schneider, J., Solano, E., Tsapras, Y., & Wesselius, P. R. 2001, A&A, 379, 564

Oudmaijer, R. D., van der Veen, W. E. C. J., Waters, L. B. F. M., Trams, N. R., Waelkens, C., & Engelsman, E. 1992, A&AS, 96, 625

Padgett, D. L., Brandner, W., Stapelfeldt, K. R., Strom, S. E., Terebey, S., & Koerner, D. 1999, AJ, 117, 1490

Papaloizou, J. C. & Savonije, G. J. 1991, MNRAS, 248, 353

Papaloizou, J. C. B. & Terquem, C. 1999, ApJ, 521, 823

Park, S. & Kenyon, S. J. 2002, AJ, 123, 3370

Piétu, V., Dutrey, A., & Kahane, C. 2003, A&A, 398, 565

Piorno Schiavon, R., Batalha, C., & Barbuy, B. 1995, A&A, 301, 840

Pollack, J. B., Hollenbach, D., Beckwith, S., Simonelli, D. P., Roush, T., & Fong, W. 1994, ApJ, 421, 615

Pollack, J. B., Hubickyj, O., Bodenheimer, P., Lissauer, J. J., Podolak, M., & Greenzweig, Y. 1996, Icarus, 124, 62

Prato, L., Greene, T. P., & Simon, M. 2003, ApJ, 584, 853

Prosser, C. F., Stauffer, J. R., Hartmann, L., Soderblom, D. R., Jones, B. F., Werner, M. W., & McCaughrean, M. J. 1994, ApJ, 421, 517

Rafikov, R. R. 2004, AJ, 128, 1348

—. 2005, ApJ, 621, L69

Raymond, S. N., Quinn, T., & Lunine, J. I. 2004, Icarus, 168, 1

Reipurth, B. & Zinnecker, H. 1993, A&A, 278, 81

Richer, J. S., Hills, R. E., Padman, R., & Russell, A. P. G. 1989, MNRAS, 241, 231

Rodriguez, L. F., D'Alessio, P., Wilner, D. J., Ho, P. T. P., Torrelles, J. M., Curiel, S., Gomez, Y., Lizano, S., Pedlar, A., Canto, J., & Raga, A. C. 1998, Nature, 395, 355

Safronov, V. S. 1969, Evolyutsiya Doplanetogo Oblake i Obrazovanie Zemli i Planet; English translation, Evolution of the Protoplanetary Cloud and Formation of the Earth and the Planets, NASA TTF-677 (Nauka, Moscow, 1969, p. 45.)

Saito, M., Kawabe, R., Kitamura, Y., & Sunada, K. 2001, ApJ, 547, 840

Salpeter, E. E. 1977, ARA&A, 15, 267

Sasselov, D. D. & Lecar, M. 2000, ApJ, 528, 995

Sault, R. J., Teuben, P. J., & Wright, M. C. H. 1995, in ASP Conf. Ser. 77: Astronomical Data Analysis Software and Systems IV, 433–+

Scally, A. & Clarke, C. 2001, MNRAS, 325, 449

Scoville, N. Z., Carlstrom, J. E., Chandler, C. J., Phillips, J. A., Scott, S. L., Tilanus, R. P. J., & Wang, Z. 1993, PASP, 105, 1482

Semenov, D., Pavlyuchenkov, Y., Schreyer, K., Henning, T., Dullemond, C., & Bacmann, A. 2004, ArXiv Astrophysics e-prints

Shakura, N. I. & Sunyaev, R. A. 1973, A&A, 24, 337

Shevchenko, V. S., Grankin, K. N., Ibragimov, M. A., Kondratiev, V. B., Melnikov, S. Y. U., Petrov, P. P., Shcherbakov, V. A., & Vitrichenko, L. A. 1994, in ASP Conf. Ser. 62: The Nature and Evolutionary Status of Herbig Ae/Be Stars, 43–+

Shevchenko, V. S. & Herbst, W. 1998, AJ, 116, 1419

Shevchenko, V. S., Ibragimov, M. A., & Chenysheva, T. L. 1991, Soviet Astronomy, 35, 229

Shevchenko, V. S. & Vitrichenko, E. A. 1994, in ASP Conf. Ser. 62: The Nature and Evolutionary Status of Herbig Ae/Be Stars, 55–+

Shu, F., Najita, J., Galli, D., Ostriker, E., & Lizano, S. 1993, in Protostars and Planets III, 3–45

Shu, F., Najita, J., Ostriker, E., Wilkin, F., Ruden, S., & Lizano, S. 1994, ApJ, 429, 781

Shu, F. H. 1977, ApJ, 214, 488

Shu, F. H., Adams, F. C., & Lizano, S. 1987, ARA&A, 25, 23

Shu, F. H., Shang, H., Glassgold, A. E., & Lee, T. 1997, Science, 277, 1475

Siess, L., Dufour, E., & Forestini, M. 2000, A&A, 358, 593

Simon, M., Dutrey, A., & Guilloteau, S. 2000, ApJ, 545, 1034

Skrutskie, M. F., Meyer, M. R., Whalen, D., & Hamilton, C. 1996, AJ, 112, 2168

Smith, B. A. & Terrile, R. J. 1984, Science, 226, 1421

Steenman, H. & Thé, P. S. 1991, Ap&SS, 184, 9

Strom, K. M., Strom, S. E., Breger, M., Brooke, A. L., Yost, J., Grasdalen, G., & Carrasco, L. 1972, ApJ, 173, L65+

Strom, K. M., Strom, S. E., Edwards, S., Cabrit, S., & Skrutskie, M. F. 1989, AJ, 97, 1451

Strom, K. M., Strom, S. E., & Vrba, F. J. 1976, AJ, 81, 320

Strom, S. E., Grasdalen, G. L., & Strom, K. M. 1974, ApJ, 191, 111

Struve, O. & Rudkjøbing, M. 1949, ApJ, 109, 92

Su, K. Y. L., Rieke, G. H., Misselt, K. A., Stansberry, J. A., Moro-Martin, A., Stapelfeldt, K. R., Werner, M. W., Trilling, D. E., Bendo, G. J., Gordon, K. D., Hines, D. C., Wyatt, M. C., Holland, W. S., Marengo, M., Megeath, S. T., & Fazio, G. G. 2005, ArXiv Astrophysics e-prints

Sylvester, R. J., Dunkin, S. K., & Barlow, M. J. 2001, MNRAS, 327, 133

Sylvester, R. J. & Skinner, C. J. 1996, MNRAS, 283, 457

Tamura, M., Gatley, I., Waller, W., & Werner, M. W. 1991, ApJ, 374, L25

Terebey, S., Shu, F. H., & Cassen, P. 1984, ApJ, 286, 529

Terebey, S., Vogel, S. N., & Myers, P. C. 1989, ApJ, 340, 472

Terquem, C. & Bertout, C. 1996, MNRAS, 279, 415

Testi, L., Natta, A., Shepherd, D. S., & Wilner, D. J. 2003, A&A, 403, 323

Testi, L. & Sargent, A. I. 1998, ApJ, 508, L91

Thompson, A. R., Moran, J. M., & Swenson, G. W. 1986, Interferometry and synthesis in radio astronomy (New York, Wiley-Interscience, 1986, 554 p.)

Troy, M., Dekany, R. G., Brack, G., Oppenheimer, B. R., Bloemhof, E. E., Trinh, T., Dekens, F. G., Shi, F., Hayward, T. L., & Brandl, B. 2000, in Proc. SPIE Vol. 4007, p. 31-40, Adaptive Optical Systems Technology, Peter L. Wizinowich; Ed., 31–40

Udry, S., Mayor, M., & Santos, N. C. 2003, A&A, 407, 369

Ulrich, R. K. 1976, ApJ, 210, 377

van Boekel, R., Min, M., Leinert, C., Waters, L. B. F. M., Richichi, A., Chesneau, O., Dominik, C., Jaffe, W., Dutrey, A., Graser, U., Henning, T., de Jong, J., Köhler, R., de Koter, A., Lopez, B., Malbet, F., Morel, S., Paresce, F., Perrin, G., Preibisch, T., Przygodda, F., Schöller, M., & Wittkowski, M. 2004, Nature, 432, 479

Vieira, S. L. A., Corradi, W. J. B., Alencar, S. H. P., Mendes, L. T. S., Torres, C. A. O., Quast, G. R., Guimarães, M. M., & da Silva, L. 2003, AJ, 126, 2971

Vink, J. S., Drew, J. E., Harries, T. J., & Oudmaijer, R. D. 2002, MNRAS, 337, 356

Vink, J. S., Drew, J. E., Harries, T. J., Oudmaijer, R. D., & Unruh, Y. C. 2003, A&A, 406, 703

Vinković, D., Ivezić, Ž., Miroshnichenko, A. S., & Elitzur, M. 2003, MNRAS, 346, 1151

Vogt, S. S., Allen, S. L., Bigelow, B. C., Bresee, L., Brown, B., Cantrall, T., Conrad, A., Couture, M., Delaney, C., Epps, H. W., Hilyard, D., Hilyard, D. F., Horn, E., Jern, N., Kanto, D., Keane, M. J., Kibrick, R. I., Lewis, J. W., Osborne, J., Pardeilhan, G. H., Pfister, T., Ricketts, T., Robinson, L. B., Stover, R. J., Tucker, D., Ward, J., & Wei, M. Z. 1994, in Proc. SPIE Instrumentation in Astronomy VIII, David L. Crawford; Eric R. Craine; Eds., Volume 2198, p. 362, 362–+

Walker, M. F. 1972, ApJ, 175, 89

Walter, F. M. 1986, ApJ, 306, 573

Watson, D. M., Kemper, F., Calvet, N., Keller, L. D. Furlan, E., Hartmann, L., Forrest, W. J., Chen, C. H., Uchida, K. I., Green, J. D., Sargent, B., Sloan, G. C., Herter, T. L., Brandl, B. R., Houck, J. R., Najita, J., D'Alessio, P., Myers, P. C., Barry, D. J., Hall, P., & Morris, P. W. 2004, ApJS, 154, 391

Weaver, W. B. & Jones, G. 1992, ApJS, 78, 239

Weidenschilling, S. J. 1977, Ap&SS, 51, 153

Weinberger, A. J., Becklin, E. E., Schneider, G., Smith, B. A., Lowrance, P. J., Silverstone, M. D., Zuckerman, B., & Terrile, R. J. 1999, ApJ, 525, L53

Weingartner, J. C. & Draine, B. T. 2001, ApJ, 548, 296

White, G. J., Liseau, R., Men'shchikov, A. B., Justtanont, K., Nisini, B., Benedettini, M., Caux, E., Ceccarelli, C., Correia, J. C., Giannini, T., Kaufman, M., Lorenzetti, D., Molinari, S., Saraceno, P., Smith, H. A., Spinoglio, L., & Tommasi, E. 2000, A&A, 364, 741

White, R. J. & Basri, G. 2003, ApJ, 582, 1109

White, R. J. & Hillenbrand, L. A. 2004, ApJ, 616, 998

Whitney, B. A. & Hartmann, L. 1992, ApJ, 395, 529

Whitney, B. A., Kenyon, S. J., & Gomez, M. 1997, ApJ, 485, 703

Whitney, B. A., Wood, K., Bjorkman, J. E., & Cohen, M. 2003a, ApJ, 598, 1079

Whitney, B. A., Wood, K., Bjorkman, J. E., & Wolff, M. J. 2003b, ApJ, 591, 1049

Wilson, T. L., Mehringer, D. M., & Dickel, H. R. 1995, A&A, 303, 840

Wolf, S. 2003, Computer Physics Communications, 150, 99

Wolf, S. & Henning, T. 2000, Computer Physics Communications, 132, 166

Wolf, S., Padgett, D. L., & Stapelfeldt, K. R. 2003, ApJ, 588, 373

Wood, K., Wolff, M. J., Bjorkman, J. E., & Whitney, B. 2002, ApJ, 564, 887

Wurm, G., Blum, J., & Colwell, J. E. 2001, Phys. Rev. E, 64, 046301

Yorke, H. W., Bodenheimer, P., & Laughlin, G. 1995, ApJ, 443, 199

Young, C. H., Shirley, Y. L., Evans, N. J., & Rawlings, J. M. C. 2003, ApJS, 145, 111